Unravelling the early responses to KrasG12D activation in the adult lung epithelium

Liam Sean Hill

Thesis submitted for the award of PhD

May 2024

The European Cancer Stem Cell Research Institute

School of Biosciences
Cardiff University

Table of Contents

List of Figures

List of Tables

List of Supplemental Movies

List of Abbreviations

A

AAH	Adenomatous atypical hyperplasia
AAV	Adeno-associated virus
AdCre	Ad5-CMV-iCre
ADI	Alveolar differentiation intermediate
AEP	Airway epithelial progenitor
ALI	Air-Liquid interface
ALK	Anaplastic lymphoma kinase
ANOVA	Analysis of Variance
ATI	Alveolar type 1 cell
ATII	Alveolar type 2 cell
a.u.	Arbitrary units

B

BADJ	Bronchoalveolar ductal junction
BASC	Bronchoalveolar stem cell

C

CD	Cluster of Differentiation
CFTR	Cystic fibrosis transmembrane conductance regulator
CGRP	Calcitonin gene-related peptide
CM	Conditioned media
COPD	Chronic obstructive pulmonary disease

D

DAG	Diacyl Glycerol
DAMP	Damage-associated molecular patterns
DATPs	Damage associated transient progenitor
DEN	Diethyl nitrosamine
DEph	Drosophila Eph homolog
DMEM	Dulbecco's modified eagle medium
DNA	Deoxyribose nucleic acid
DPI	Days post induction
DPP	Decapentaplegic

E

E	Embryonic day
EDAC	Epithelial defence against cancer
EGFR	Epidermal growth factor receptor
EH	Epithelial hyperplasia
EpCAM	Epithelial cell adhesion molecule
Eph	Erythropoietin-producing hepatoma receptor
Ephrin	Eph-family receptor interacting proteins
ERK	Extracellular regulated kinase

F

F-actin	Filamentous actin
FAK	Focal adhesion kinase
FBS	Foetal bovine serum
FFPE	Formalin fixed paraffin embedded
FIJI	FIJI is Just ImageJ
FOV	Field of view

G

G-CSF Granulocyte colony stimulating factor
GAP GTPase activating protein
GDP Guanosine diphosphate
GEF Guanine exchange factor
GEMM Genetically engineered mouse model
GM-CSF Granulocyte-macrophage colony stimulating factor
GRB2 Growth factor receptor bound protein 2
GSC Germline stem cells
GTP Guanosine triphosphate

H-L

H&E Haematoxylin and Eosin
HRAS Harvey Rat sarcoma
IL Interleukin
IPF Idiopathic pulmonary fibrosis
KRAS Kirsten Rat Sarcoma
KRT Cytokeratin
LL Left lobe
LMP Low melting point agarose
LUAD Lung adenocarcinoma

M-O

M+ Minute heterozygous loss of function
MAPK Mitogen associated protein kinase
MDCK Madin-Darby Canine Kidney
MEK MAPK/ERK kinase
MIP Maximum intensity projection
MLCK Myosin light chain kinase
MLI Mean linear intercept
MTT 3-(4,5-dimethylthiazol-2-yl)-2,5-diphenyltetrazolium
NRAS Neuroblastoma RAS
NSCLC Non-small cell lung cancer
OCT Optimal Cutting Temperature
OD Optical Density

P

PAMP Pathogen associated molecular patterns
PanIN Pancreatic intra-epithelial neoplasia
PATS Pre-alveolar transitional state
PBS Phosphate buffered saline
PCLS Precision cut lung slices
pcw Post conception week
PDAC Pancreatic ductal adenocarcinoma
PFA Paraformaldehyde
PFU Particle forming unit
PIP2 Phosphatidylinositol (4,5)-bisphosphate
PIP2 Phosphatidylinositol (3,4,5)-trisphosphate
PLC ε Phospholipase C epsilon
PNEC Pulmonary neuroendocrine cell
Pro-SPC Pro-surfactant protein C

Q

qPCR Real time quantitative polymerase chain reaction

R

R.T. Room temperature
RA Right accessory lobe
RAF Rat fibroma
RFP Red fluorescent protein
RI Right inferior lobe
RM Right middle lobe
ROI Region of interest
RS Right superior lobe
RSK Ribosomal S6 kinase
RTK Receptor tyrosine Kinase

S

S1P Sphingosine-1-phosphate
SCLC Small cell lung cancer
SD Standard deviation
SEM Standard error of the mean
SFK Src family kinase
SOS Son of sevenless

T-Y

TNFα Tumour necrosis factor alpha
UV Ultraviolet
VNC Ventral nerve cord
WT Wild-type
YAP Yes associated protein

Abstract

Our lung epithelium is continuously exposed to a harsh external environment, accumulating tissue damage, infections, and harmful mutations that may have the potential to drive cancer. Activating mutations in KrasG12D are responsible for around 30% of lung cancers, with patients frequently diagnosed at later stages. At early timepoints, KrasG12D mutant cells have been shown to be eliminated from adult tissues such as the pancreas by a conserved process known as cell competition. In the lung, it is not clear if cell competition has a role in shaping the pre-neoplastic lung epithelium, or even how KrasG12D drives cancer in the distal lung epithelium.

Using a well-established model of tumorigenesis in mouse lungs, cell competition was not found to regulate the lung epithelium at early timepoints post KrasG12D expression. Instead, alveolar cells that express KrasG12D undergo morphological changes that are reminiscent of transition cell state changes found in fibrotic lung disease. We identify that KrasG12D expressing alveolar type II cells undergo cellular differentiation via Krt8+ cell states, becoming less spherical and more squamous in morphology. Furthermore, pro-inflammatory recruitment of innate immune cells to the alveoli further drives differentiation of non-transformed cells *ex vivo*. We identify a positive correlation between the level of KrasG12D expressing cells and Krt8 expression *in vivo* in early adenomatous tissue. Thus, KrasG12D mutant cells in lung are subject to differentiation driven by conserved injury remodelling pathways in the alveoli. Whether or not these cell state changes are pro-tumorigenic or are an attempt to offset tumorigenesis is not yet clear, however, further elucidation of processes identified in this thesis could provide a novel marker to identify early stage disease for better detection and intervention.

Acknowledgements

I wish to extend my sincerest thanks to my supervisor Dr. Catherine Hogan for all the guidance and support you've provided in this PhD project, especially for always pushing me to do good science, and supporting my passion for lung research.

The skills I have developed during the process have largely been the result of keeping great company in the Hogan lab, in particular, my thanks and gratitude go to Dr Beatriz Salvador Barbero, Dr Markella Alatsatianos, my fellow PhD student Joshua D'Ambrogio, Dr Anna Richards, Dr Carmen Velasco Martinez, and Dr Charley Lovatt. My thanks also extend to Dr Renata Jurkowska and her lab for being an excellent support network and fellow lung researchers during my project. I am grateful to Professor Matthew Smalley for permitting me valuable time to write this thesis whilst in his lab.

Starting a PhD at the height of the COVID-19 pandemic was difficult, with training and learning opportunities limit by restrictions until the middle of 2021. Therefore, I would like to thank the teams at the Transgenic Unit, Bioimaging Hub, and my dear colleagues at ECSCRI for making this experience so enjoyable and worthwhile. Over the course of my PhD, I have been lucky to supervise great students who have helped me develop further, especially Ellis Jones and Daisy Moyers whose work helped to make this thesis – Diolch yn fawr iawn both.

Finally, I want to thank my parents and family for always encouraging and supporting my endeavours in life. To my friends, thank you for putting up with my sporadic absences and always believing in me. Last but not least, thank you Roman for your never ending support and encouragement at this time of my life.

1 Introduction.

1.1. The Mammalian Lung.

1.1.1. Origins of the lung.

The mammalian lungs are a complex branched organ that ensures efficient gaseous exchange of oxygen into the blood from the lungs, and carbon dioxide out of the blood. In development, two primitive lung buds arise from the foregut endoderm at 4-7 post-conception weeks (pcw) in human lungs, and between E9-E12 (embryonic day) in mice (Fig 1.1Ai), which eventually give rise to the left and right lung lobes (Nikolić et al. 2018; Dean and Cheong 2023). From here, the buds undergo successive branching events during the pseudoglandular stage of development (5-17 pcw; E12-15,Fig 1.1 Ai), giving rise to the core structure of the airway tree (Nikolić et al. 2018). By the end of this developmental stage, the preliminary airway tree is formed of 20 generations of branches generated from distinct morphological branching types referred to as domain branching, planar bifurcation, and orthogonal bifurcation (Metzger et al. 2008; Mullassery and Smith 2015). Domain branching arises when a new tip erupts from the stalk of an existing branch (Fig 1.1 B), setting the primary architecture of tertiary and quaternary branches. Orthogonal and planar bifurcation (Fig 1.1 C-D) is the process of tip branching either in the anterior-posterior plane (planar; Fig 1.1C), or rotated 90˚ from the previous branching plane (orthogonal; Fig 1.1D) (Mullassery and Smith 2015).

From 16-26 pcw and E15-E17, the epithelial tree is mostly established and the canalicular stage of organogenesis occurs. Here, further branching occurs that prepares for alveolar expansion and development, existing airways expand, and epithelial cell fate determination via epithelial-mesenchymal interactions is initiated (Nikolić et al. 2018; Lim et al. 2023). Following this, sacculation begins at 26-36 pcw in humans, and from E17.5 to the first few days of postnatal life in mice (Nikolić et al. 2018; Akram et al. 2019). Primitive air sacs that formed at the later end of the canalicular stage from distal lung tips begin to dilate and form early alveolar sacs (Desai et al. 2014; Nikolić et al. 2018; Dean and Cheong 2023). At the end of development resides the most important stage: alveologenesis, where the air sacs formed in previous stages increase in surface area, migrate into position, and cluster with other migrating cells to expand and septate (Akram et al. 2019). This stage occurs from 36 pcw and continues to around 3 years after birth in humans, and begins from birth to around postnatal day 20 in mice (Nikolić et al. 2018).

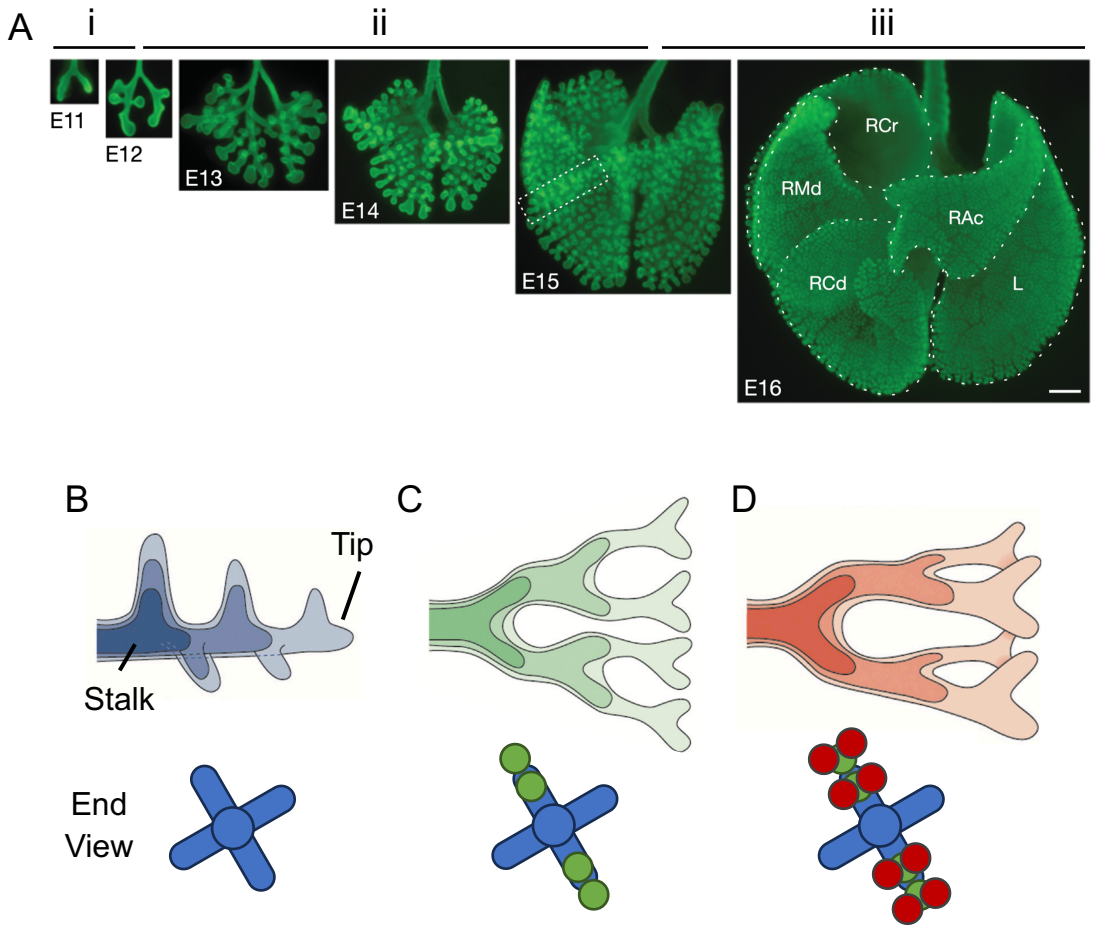

Figure 1. 1 Branching morphogenesis programmes in the developing lung.

A) *In situ* staining of E-Cadherin in mouse embryonic lungs across the (**i)** embryonic stage (embryonic day; E11-12), **(ii)** pseudoglandular stage (E12-E15), **(iii)** and canalicular stage (E15-E16). Scale bar, 500 μm. **B)** Domain branching refers to branches that erupt from existing branches. **C)** Planar Bifurcation refers to division of branches in the anterior-posterior plane. **D)** Orthogonal bifurcation occurs 90˚ from the previous plane of branching tips. Adapted from (Metzger et al. 2008; Varner and Nelson 2017).

1.1.2. Structure and comparative anatomy.

Developmental processes underpinning the broad patterning of the lung are similar between mouse and humans. However, in adult tissues, differences between mouse and human lungs are abundant and need to be considered in lung research. Human lungs have five lobes: three right lobes and two left lobes. Branching in the pattern described before can be seen for 23 to 26 generations in human lungs, before they reach terminal bronchioles, and then respiratory airways; distinct niches in larger mammals where small alveoli are interspersed between rows of cuboidal cells (Basil and Morrisey 2020). Mice also possess five lung lobes, instead with one larger left lobe, and four right lobes: the right superior, right middle, right inferior, and the smallest, right accessory lobe which wraps around the bottom of the heart. Mouse airways branch for 13 generations (Basil and Morrisey 2020) and terminate abruptly in structures referred to as the bronchioalveolar ductal junction (BADJ).

In human lungs, distinct cricoid cartilage rings can be observed far into the intrapulmonary airways where they provide structural support and prevent collapse. In mice, these are only present around the trachea and extrapulmonary bronchi (Fig 1.2) (Danopoulos et al. 2019; Basil and Morrisey 2020). Submucosal glands are present in the major airways of humans and mice, and function to regulate ion concentration, and roles in host defence against invading pathogens (Ostedgaard et al. 2020). In humans, sub-mucosal glands are present throughout most of the extrapulmonary airways and the large-medium bronchioles (Fig 1.2), however mouse submucosal glands are only found in the trachea (Innes and Dorin 2001). The distribution of epithelial cells along the proximal-distal axis of the lung contains distinct patches of epithelial cells that link structure to function. However, this is where mice and humans greatly diverge. Due to this, the only semi-comparable regions of the mouse and human lungs are the mouse trachea which is similar to large airways in humans, and the alveoli.

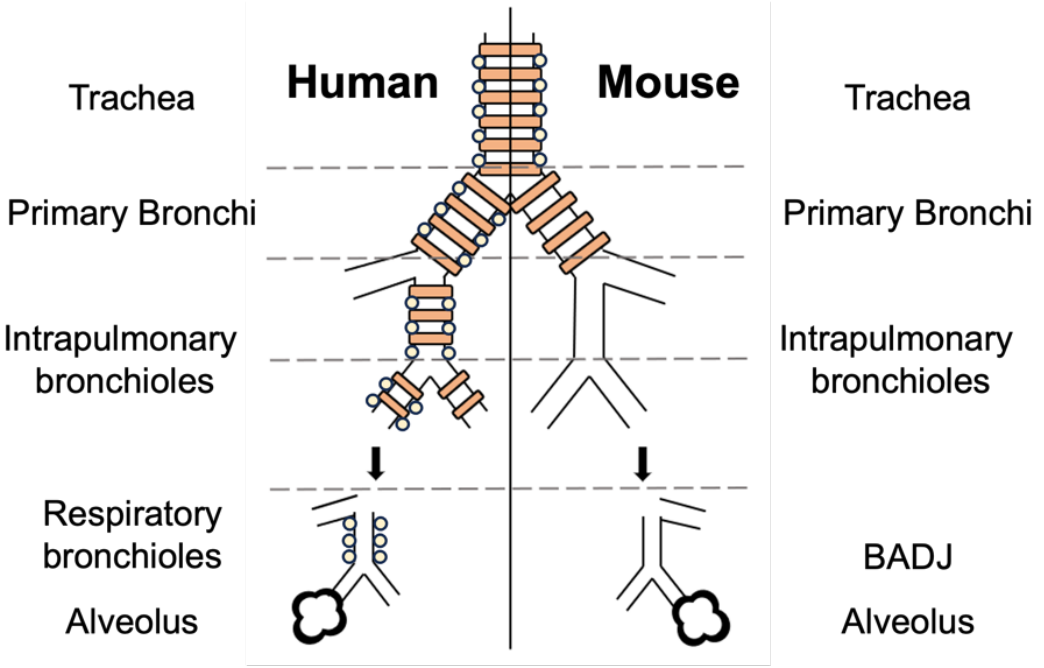

Figure 1. 2 Comparative anatomy of the respiratory tree between humans and mice.

Structural differences between human and mice are important to understand and consider in lung research. The most similar structures between both species are the trachea: both are surrounded by cricoid cartilage (orange rings) and contain submucosal glands (yellow circles). In humans, both cartilage and submucosal glands are present deep into the conductive airways, towards the terminal bronchioles, then only submucosal glands are present in the respiratory bronchioles. In mice, cartilage is only present in the extrapulmonary bronchi, and not in the intrapulmonary airways. Bronchioles are not comparable to humans as they possess different proportions of cells, particularly club cells which are the dominant cell type in mice. Mouse airways terminate abruptly at the bronchioalveolar ductal junction (BADJ), where terminal airways open into alveolar space. Alveolar regions of human and mouse lung are similar. Figure adapted from (Danopoulos et al. 2019).

1.1.3. Epithelial cell types of the adult lung.

1.1.3.1. Proximal airways.

The lung epithelium is continuous from the trachea down to the gas exchange surface; therefore, regions are not distinctly isolated within the tissue as can be said about other organs. However, the lung epithelium can be broken into approximate regions based upon the expression and ratio of different cell types, at different levels of the airways. Functionally the trachea forms the second line of defence after the nasal passageway in both human and mouse lungs. Here, frequent cell types are the basal cells, goblet cells, ciliated cells, tuft cells, pulmonary neuroendocrine cells, and ionocytes (Fig 1.3A) (Meng et al. 2023).

Basal cells are small cuboidal cells that are secured to the basement membrane of proximal airways and are identifiable by their expression of cytokeratin 5 and cytokeratin 14 (KRT5 and KRT14), in addition to transformation-related protein 63 (TRP63) (Rock et al. 2009; Watson et al. 2015). Basal cells have been shown to be the principal stem cell of the airway as they are able to divide asymmetrically to produce other differentiated luminal cells such as club cells, tuft cells, ionocytes, and neuroendocrine cells (Rock et al. 2009; Watson et al. 2015; Davis and Wypych 2021). In humans, basal cells are expressed along the entire airway epithelium down to the terminal bronchioles, whereas in mice, basal cell expression is limited strictly to the extrapulmonary bronchi and the trachea (Wu et al. 2022).

Club cells (previously known as Clara cells) are a secretory, non-ciliated cell type that is present across the entire lung epithelium, and are one of the most prevalent cell types found in the murine lung (Hewitt and Lloyd 2021). They are typically characterised by expression of *Scgb1a1*, and are known to be both self-renewing cells, and progenitor cells for ciliated and goblet cells in the lung (Rawlins et al. 2009), and have even been shown to replenish lost basal cells upon airway injury (Tata et al. 2013).

Ciliated cells are an abundant columnar epithelial cell that project hair-like cilia into the airway lumen. Organised beating of cilia moves mucous proximally in the lungs as part of the mucociliary escalator (Davis and Wypych 2021). Ciliated cells arise from *Scgb1a1* positive club cells post birth, steadily increasing in population size over the first 3 months of post-natal growth (Rawlins et al. 2009). Experimental evidence suggests that ciliated cells also derive from basal cells as a result of differentiation from club cell intermediates (Watson et al. 2015). In air liquid interface culture, ciliated cells arise around 14 days post exposure to air, where mucociliary

action can be observed and quantified (Lee et al. 2020). Ciliated cells are characterised by their expression of Foxj1 and acetylated tubulin, which are required for cilia development and function respectively (Rawlins et al. 2009; Watson et al. 2015). In mice and in human airways, ciliated cells are present throughout, though in mice, population numbers decrease compared to humans in intrapulmonary airways (Fig 1.3 A-C).

Goblet cells are the mucous producing cells of the airways that work in conjunction with ciliated cells during mucociliary clearance. Like ciliated cells, goblet cells derive from club cells (Kim et al. 2019) and their presence can be highlighted by staining for MUC5A and MUC5B.Ciliated cell function is linked to protection against inhaled particles and microbes, and their dysfunction is recorded in many respiratory diseases like asthma, COPD and cystic fibrosis (Davis and Wypych 2021). In humans, goblet cells are some of the most abundant secretory cell types in the proximal airways, though this is not the case in mice where their appearance is more rare (Fig 1.3 C) (Hewitt and Lloyd 2021).

Aside from these main four cell types in the proximal lung, there are relatively misunderstood and under-researched cell types that contribute to lung epithelial function in mice and humans. Tuft cells are a poorly understood, rare chemosensory cell, located primarily in the trachea, but can be found in the proximal airways of rodents and humans (Davis and Wypych 2021; Hewitt and Lloyd 2021). They are believed to play a role in mediating communication between neuronal and immune pathways as they do in the gut (Davis and Wypych 2021). Pulmonary neuroendocrine cells (PNECs) are another rare cell type in the lung, but their function is clearer than tuft cells. They serve as resident epithelial-nerve cells that respond to airway signals to stimulate immune responses (Davis and Wypych 2021). They can be identified based on their expression of calcitonin gene-related peptide (CGRP) and are known to secrete various chemicals that interact with epithelial and immune cell types. They are present in airways as single cells or clustered masses known as neuroepithelial bodies which are usually found adjacent to the BADJ (Noguchi et al. 2020). The final rare cell type is the recently identified pulmonary ionocyte, which express high levels of cystic fibrosis transmembrane conductance regulator gene (*CFTR)* (Meng et al. 2023). They were found to be present in 1-2% of cells isolated from human bronchial epithelial cells and present in mouse tracheal epithelial cells (Plasschaert et al. 2018), and are believed to play key roles in regulating lung fluid pH, viscosity and clearance rate from the airways (Yuan et al. 2023).

1.1.3.2. Alveolar epithelial cells.

The alveolar epithelium comprises of two main cell types: the large, flat, squamous epithelial type 1 pneumocytes (ATI), and the small cuboidal type 2 pneumocytes (ATII; Fig 1.3 D). ATI cells make up the vital structure known as the primary gas exchange surface. They make up the bulk of the alveolar tissue, covering over 95% of the surface area of the alveoli (Chan and Liu 2022). ATI cells are closely associated to the endothelial plexus on their basal side, in order to provide a short distance for gas exchange (Meng et al. 2023). ATII cells on the other hand are nestled between ATI cells and have been shown to present multiple apical surfaces into alveolar spaces (Konkimalla et al. 2022). ATII cells cover only around 5% of the gas exchange surface but make up around 60% of the cells in the lung alveoli (Wang et al. 2007).The primary function of ATII cells under homeostasis is to produce surfactant that maintains inflation of alveoli, however, there are now many articles that show a role for ATII cells in restoring alveolar cell populations in response to injury and repair (Desai et al. 2014; Xie et al. 2022), and that they exhibit remarkable migratory abilities to replenish injured regions (Chioccioli et al. 2024).

There are several cell markers which can be utilised to distinguish ATI and ATII cells. ATI cells can be identified by high expression of Pdpn, Ager, Hopx, and Cav1, whereas ATII cells can be identified broadly by expression of Pro-surfactant protein C (Pro-SPC) and LAMP3 (Choi et al. 2020; Juul et al. 2023). These are conserved markers in the lung epithelium of humans and mice.

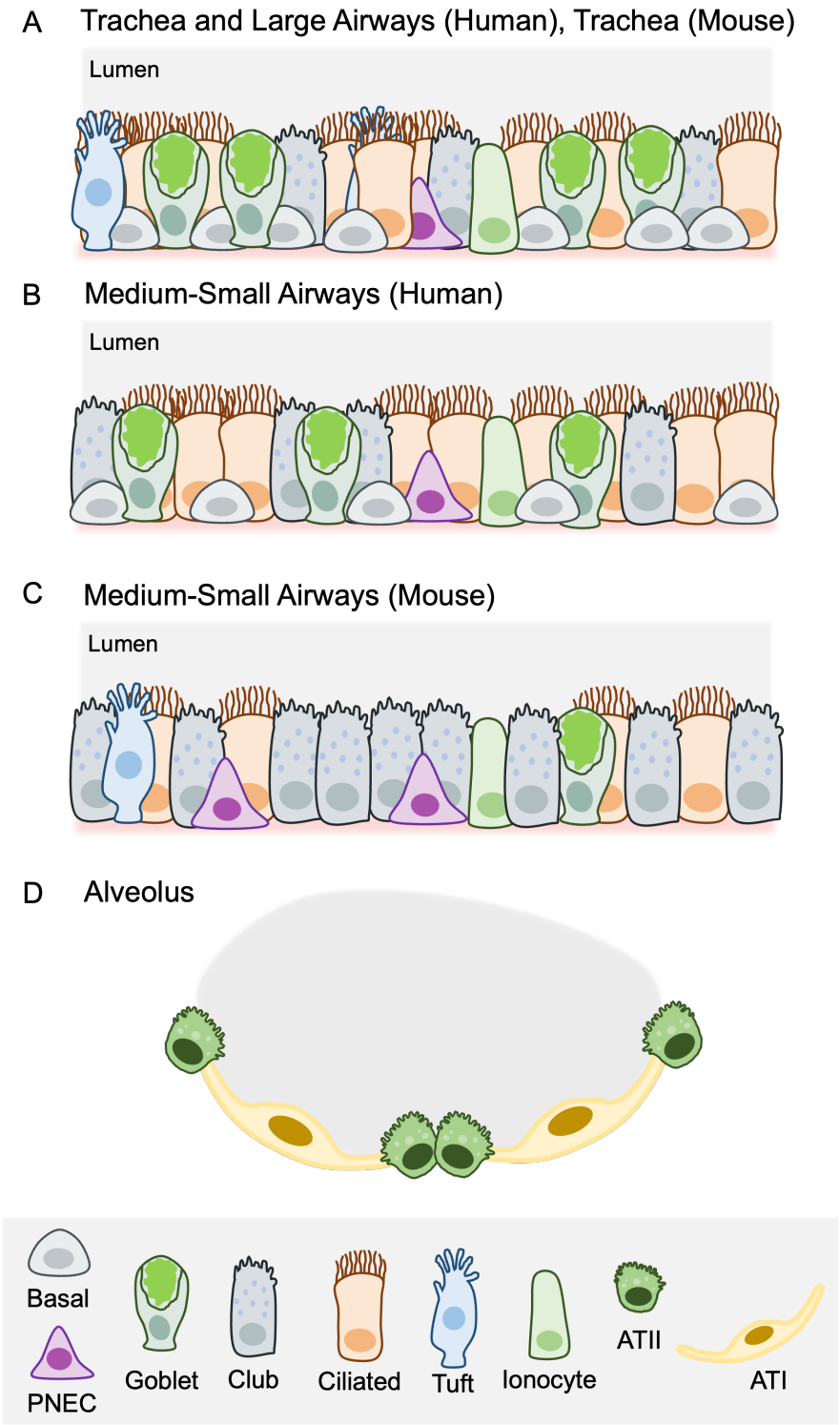

Figure 1. 3 Distribution of cell types define regions of the lung epithelium.

Lungs are patterned along the proximal-distal axis based on the expression of numerous cell types that relate to the function and requirement of the anatomy. **A)** Mice and humans have most similarity in the trachea and human large airways, containing bulk of basal cell populations, more mucus producing cells, and ciliated cells to form the mucociliary escalator. **B, C)** Divergence in patterning in medium-small airways as mice do not possess basal cells here and club cells become the predominant cell type in mice. **(D)** Epithelia at the alveolus are similar, except for the scale of which cells form the gas exchange surface.

1.1.4. Homeostasis and lung stem cell populations.

Lungs have a relatively slow turnover rate of cells in homeostasis; however, they are extremely responsive to epithelial injury and utilise resident epithelial cells to restore the airway epithelium. As was alluded to in the previous section, basal cells appear to be the hierarchical cell of the proximal airways in the lung and are able to give rise to all cell types of the bronchioles either directly, or by producing intermediate progenitor cells.

Naphthalene is an aromatic hydrocarbon that specifically ablates non-ciliated club cells in the bronchiolar epithelium. Lineage tracing of Krt14 basal cells in mouse trachea revealed that club cells ablated in naphthalene injury are replenished by basal cell progenitors in clonal patches (Hong et al. 2004). Within these clonal patches, lineage-tagged cells stained positive for markers of basal cell fate (Krt14), club cell fate (CC10) and ciliated cell fate (acetylated tubulin), suggesting that basal cells self-renew whilst also giving rise to differentiated cell types. Basal cells were found to be a heterogeneous population of cells, consisting of a self-renewing population that maintain basal cell populations (Fig 1.4 A), and a luminal precursor population of basal cells that express low levels of the luminal differentiation marker cytokeratin 8 (Krt8; (Watson et al. 2015). Krt8 positive precursor cells first differentiate into clubs cells, which are capable of self-renewal, then acquire the necessary conditions to develop further into ciliated cells (Watson et al. 2015). Further evidence from lineage tracing mouse models identified the presence of labelled PNECs, tuft cells, and ionocytes alongside labelled basal cells, club cells and ciliated cells, characterising them as direct descendants of basal cells in the proximal airways (Montoro et al. 2018).

In other parts of the lung, particularly the mouse lung, basal cells are less frequent and are therefore less likely to play a major role in lung cell homeostasis. Scgb1a1+ club cells are reported to act as airway progenitor cells in mice, giving rise to ciliated cells in steady-state homeostasis. Club cells were shown to partially contribute to sulphur-dioxide injured trachea, contributing to ciliated and club cell replenishment in denuded tracheae (Rawlins et al. 2009). Further models using injury have elucidated that WNT-RYK signalling in club cells repressed goblet cell differentiation pathways, and that disruption of this regulation can lead to goblet cell hyperproliferation in injury mouse models, and in chronic obstructive pulmonary disease (COPD) (Kim et al. 2019). These works support a role for bronchiolar club cells in replenishing major cell types of the respiratory tree in steady state homeostasis and in lung repair. Investigations into the potential roles of basal cells as airway progenitor cells in humans revealed that mature airway cells such as ciliated,

goblet, club and basal cells could be derived from human induced-pluripotent stem cell models (Dye et al. 2015; Konishi et al. 2016), suggesting that basal cells are a conserved progenitor cell for the proximal airways in humans and mice.

More distally in the airways, specifically the BADJ, are a population of dual positive Pro-SPC+/ Scgb1a1+ cells that are proposed to be epithelial progenitors of the distal lung epithelium (Fig 1 .4 B). Early work in mice identified that these so-called bronchioalveolar stem cells (BASC) were resistant to bronchiolar and alveolar injury, and possessed markers of stemness such as Sca-1 and CD34 (Kim et al. 2005). In a similar study using *Scgb1a1* Cre- confetti mice, rare naphthalene resistant cells in the BADJ were shown to clonally expand to reconstitute lost club cell populations (Chen et al. 2012). Furthermore, isolation and culture of club cells alone can give rise to many different cell types of the mid-proximal airway, whereas culture of proposed BASC predominantly gives rise to ATII and club cells in culture, demonstrating that these distal airway cells carry out progenitor roles for the distal airways as well as the alveoli.

More recent studies have identified that in homeostasis, BASC populations remain stable over a longer period that has not yet been determined and demonstrate that BASC populations are responsive to different models of injury (Liu et al. 2019b). As has been described previously, naphthalene injury drove expansion of labelled BASC cells into bronchial epithelial cell types, labelling club cells and some ciliated cells. Bleomycin has been used as the go-to model of murine pulmonary fibrosis. Lungs express low levels of the bleomycin-inactivating enzyme bleomycin hydrolase and are therefore more susceptible to the toxic side effects of the antibiotic which drives low grade inflammation, immune cells recruitment to the lung, and alveolar cell injury (Hay et al. 1991; Moeller et al. 2008). Bleomycin injury was shown to drive expansion of BASCs distally into the alveoli, replenishing ATI and ATII cells and restoring the epithelial barrier (Liu et al. 2019b).

During development, the mature alveolar cell types are produced from bipotent progenitor cells that, through acquisition or loss of mature cell gene expression, produce either ATI or ATII cells (Desai et al. 2014). This study further highlighted that in the steady state post-natal mouse lung, lineage-labelled ATII cells can give rise to ATI cells and replenish alveoli over time as a result of EGFR stimulation from dying ATI cells (Fig 1.4 B). Whether or not the entire ATII cell population or just a subset are capable of this differentiation response to ATI cell loss is unclear. More recent work identified that a subset of ATII cells termed airway epithelial progenitors (AEP) characterised in mice as Axin2+, Wnt responsive cells, and in humans as Tm4sf1 positive cells that are capable of replenishing mature cells

of the alveoli in organoid models (Zacharias et al. 2018). EpCAM+, HTII-280+ cells sorted from adult human lungs were also shown to form self-renewing ATII cell spheres, where all cells express the surface market HTII-280, but not cytoplasmic Pro-SPC, suggesting a heterogeneous population of mature and naïve ATII cells (Barkauskas et al. 2013).

In summary, characterisation of lung epithelial cells not limited to the studies presented here have identified the dynamic relationship between multipotent progenitor cells across the lung epithelium, and the mature cell types that they can give rise to in order to maintain epithelial homeostasis and barrier function. There are three core cells that are proposed to hold the greatest potential in the lung, these are basal cells, distal lung SPC+ club cells, and alveolar progenitor cells. More recently, investigations into the response of these epithelial populations to injury and early pathogenesis have highlighted the importance of tight regulation of repair pathways in the lung.

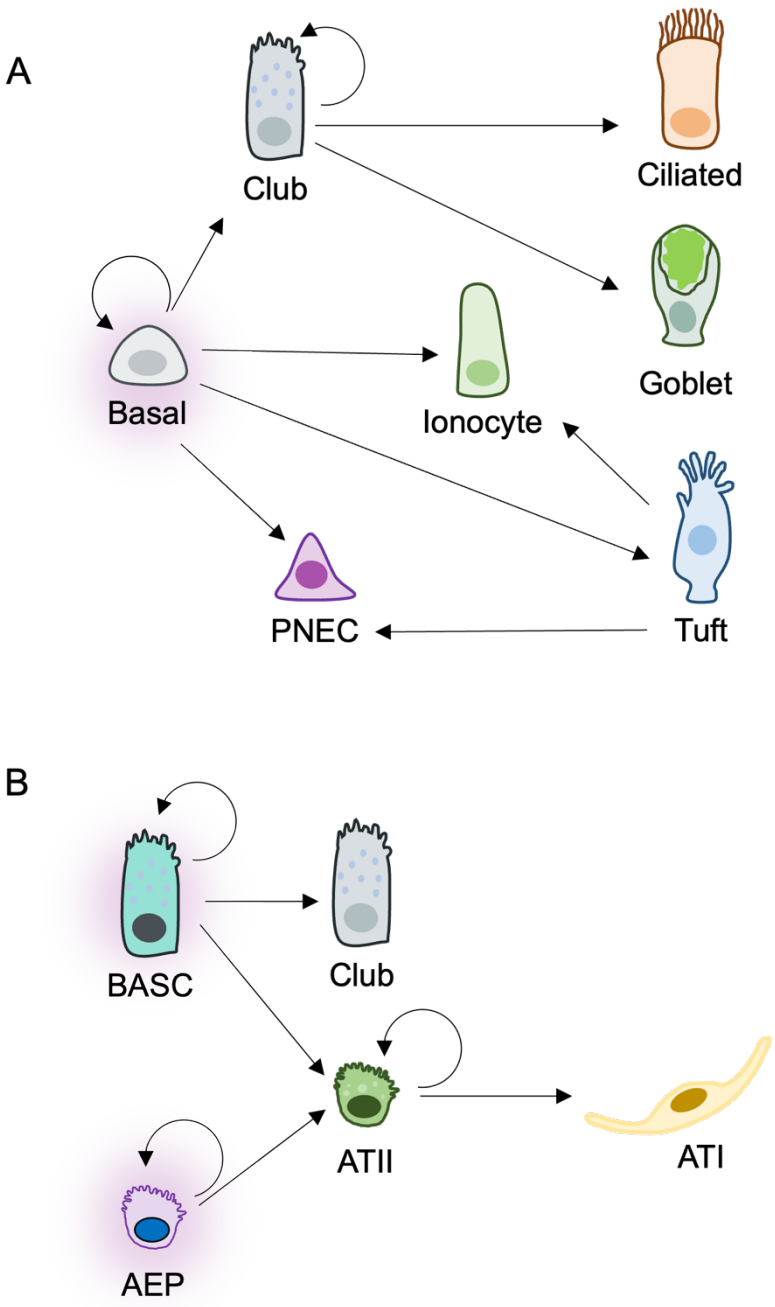

Figure 1. 4 Progenitor and stem cell relationships in the lung.

A) Basal cells are the conserved progenitor cell for most cell types of the proximal airways. Aside from self-renewal, they can directly give rise to club cells, pulmonary neuroendocrine cells (PNEC), ionocytes, and tuft cells. Club cells form an intermediate cell type that can give rise to goblet cells and ciliated cells. **B)** In the distal airways, a subset of pro-SPC positive club cells termed bronchioalveolar stem cells (BASC) can self-renew, give rise to standard club cells or ATII cells. A population of alveolar epithelial progenitors in the distal lung self-renew and give rise to ATII cells. ATII cells are the established progenitor of adult alveoli and either self-renew or give rise to ATI cells. AEP = airway epithelial progenitors.

1.1.5. Lung innate immunity.

Aside from epithelial cells, the lung contains components of immune system that reside in the tissue to provide a swift, localised response to tissue wounding. The immune system is broadly divided into the adaptive immune system which forms the long term response to insult and infection, and the innate immune system, which includes cells that are typically long-lived and self-renewing that act as first responders. The innate immune system stems from myeloid cells in the bone marrow, differentiating further into the granulocytes, dendritic cells, monocytes, and myeloid-derived suppressor cells. The adaptive immune response spans from differentiated lymphoid cells, giving rise to natural killer cells, B cells in the bone marrow, and T cells in the thymus. Adaptive immune responses are coordinated based on interactions and early responses from the innate immune system, and resident epithelial cells in the lung.

1.1.5.1. Granulocytes.

Granulocytes contain cytoplasmic granules that are released upon cell activation. This class of cells refers to neutrophils, eosinophils, basophils, and mast cells, which reach maturity in the bone marrow during haematopoiesis (Tavares et al. 2020). In health, granulocytes act to halt invading pathogens, however, inappropriate and prolonged activation contributes to many allergic responses such as asthma and other pulmonary diseases (Leitch et al. 2008). Neutrophils are recruited through chemokines such as CXCL1, CXCL2, IL1α, and CCL2, and are regulated by macrophage secretion of granulocyte-macrophage colony stimulation factor (GM-CSF), granulocyte colony stimulating factor (G-CSF), and TNF-α (Graf et al. 2023). Basophils are the least abundant granulocyte, share characteristics with mast cells, and are relatively short lived cells. Their primary function is to contribute to allergic inflammation in the skin, respiratory and gastrointestinal tract, and secrete pro-inflammatory substances such as cytokines, proteases, and histamine (Karasuyama et al. 2018). Similarly, mast cells are found in connective tissue and mucosal surfaces and are implicated in the curation of appropriate immune responses to tissue damage or invading pathogens. They are a key source of TNF-α, and IL-6 which is necessary for activation of neutrophils (Virk et al. 2016). Dysregulation of mast cells is implicated in many pulmonary disorders. Eosinophils are the final type of granulocyte, and account for less than 5% of circulating leukocytes. They have proposed roles in producing important cytokines such as IL-4, can modulate adaptive immunity by

activation of T cells (Leitch et al. 2008). They are short lived cells, surviving for up to 12 hours in circulation, a feature that aims to reduce their destructive capacity in tissues.

1.1.5.2. Dendritic cells.

Dendritic cells are antigen presenting immune cells that recognise target antigens and present them to T-cells to instigate the adaptive immune response. There are two types of pulmonary dendritic cell: the conventional dendritic cells which are important for mucosal immune response in the upper and lower respiratory tracts, and plasmacytoid dendritic cells which express toll-like receptors and regulate tolerance and immunity in the small airways (Graf et al. 2023). Dendritic cells function in response to environmental stimuli, utilising an array of surface and intracellular receptors that recognise cytokines, pathogen associate molecular patterns (PAMPs) and damage associated molecular patterns (DAMPs) (Wculek et al. 2020).

1.1.5.3. Monocytes and Macrophages.

Monocytes are long-lived effector cells that can give rise to tissue resident macrophages or dendritic cells. They are recruited to the site of infection or injury to replenish other resident macrophage populations (Luster et al. 2005). Macrophages can be polarised to M1 or M2 phenotypes, which are classically associated with inflammatory and anti-inflammatory/wound repair pathways respectively. M1 macrophages typically secrete cytokines that drive inflammation such as IL-1β, IL-6, IL-8, and TNF-α in response to foreign pathogens, and M2 macrophages secrete cytokines that are typically anti-inflammatory like CCL22, IL-4, IL-13 and IL-10 (Graf et al. 2023). There are two types of tissue resident macrophage in the lung, the alveolar macrophage which resides in the alveolar airspaces, and the interstitial macrophage which reside in the lung parenchyma.

In homeostasis, alveolar macrophages are key immunoregulators of other alveolar immune cells and the epithelium. Alveolar macrophages activate regulatory T-cells (Treg) through TGF-β and retinoic acid signalling, which are important cells for limiting immune response to prevent pathological events (Ardain et al. 2020). Alveolar macrophages are reported to secrete cytokines and chemokines that recruit other immune cells to the lung, including IL-6, RANTES, TNF-α and G-CSF (Ardain et al. 2020). In tissue injury, alveolar macrophage populations are bolstered by monocyte derived macrophage populations which have a greater inflammatory response than

resident counterparts and as such are a promising target for reducing inflammatory signatures in fibrotic lung disease (Graf et al. 2023).

Interstitial macrophages are a more poorly described set of macrophages in the lung, located outside of airways, and outside of the blood. Their function is still believed to be primarily as a phagocyte, though evidence suggests that they may have additional capabilities as antigen presenting cells, and immunoregulatory cells (Schyns et al. 2018). Compared to the self-renewing alveolar macrophages, interstitial populations appear to be more dependent on monocyte influx at steady state, expressing genes like *Maf* and *Mafb* that function to repress self-renewal (Ardain et al. 2020). Thus, the lungs possess an impressive resumé of resident lung cells that assist in reacting to tissue insult, and present interesting candidates for dysregulated tissue homeostasis in lung disease.

1.1.6. Aberrant repair pathways in lung fibrosis.

Chronic respiratory diseases affect both adults and children globally. They encompass diseases such as asthma, chronic obstructive pulmonary disease (COPD), emphysema, idiopathic pulmonary fibrosis (IPF), and lung cancer. An overarching feature of these pathologies is aberrant epithelial wound healing, tissue hypersensitivity, and failure to resolve inflammatory processes, subsequently leading to chronic disease. IPF is rapidly progressing disease resulting in irreversible pulmonary dysfunction, scarring, and poor prognosis of around 2-5 years post diagnosis (Wang and Tang 2020). IPF is recognised by histological presence of interstitial pneumonia, fibroblast foci, alveolar cell hyperplasia, impaction of airway architecture, and presence of epithelial-lined cysts called 'honeycombs' in the distal epithelium (Adams et al. 2020). In recent years, detailed studies into mouse models of IPF have uncovered aberrant cellular populations that are thought to underpin pathogenesis of chronic lung disease (Choi et al. 2020; Kobayashi et al. 2020; Strunz et al. 2020). These aberrant populations, named differently in each study, identify conserved transitional cell intermediate states that exploit alveolar epithelial cell plasticity and the potential of progenitor cells to change in response to damage and other stimuli. These states are detailed in the following sections.

1.1.6.1. Pre-Alveolar type 1 Transitional Cell states (PATS)

In culture, ATII cells spontaneously differentiate into ATI cells. Single cell transcriptomic analysis of ATII-fibroblast co-cultured organoids identified known cell states that represent ATII cells (*Sftpc*), and ATI cells (*Ager*), but also a novel population of cells that express *Cldn4* and *Krt19* and *SFN* (Kobayashi et al. 2020). These unique cells were further divided into two subsets: *Ctgf*+ cells enriched for *Ctgf, Clu, Sox4* and *Actn1*, and another referred to as *Lgals3*+ cells, enriched for *Lgals3, Csrp1, S100a14,* and *Cldn18*. Furthermore, transcriptional markers of ATI cells in this population such as *Ager, Emp2,* and *Hopx* suggest a hierarchical relationship between damaged ATII cells, Lgals3+ cells, and ATI cells. As such, this cell profile was referred to as a 'pre-alveolar type-1 transitional cell state' (PATS; (Kobayashi et al. 2020). PATS were observed *in vivo* following bleomycin injury, expressing CLDN4, SFN, KRT19 and LGALS3 as was found spontaneously in organoid cultures. PATS cells were morphologically elongated compared to ATII cells and exhibited temporal expression of CLDN4 at early stages, CLDN4/LGALS3 at middle stages of PATS, and LGALS3 positive at late stage PATS. PATS was surprisingly accompanied by upregulation of several interesting signalling pathways including, TGF-β, p53,

senescence signatures and DNA damage. Interestingly, PATS could be observed in human IPF lungs, indicating a conserved hierarchical relationship preserved between mice and humans.

1.1.6.2. Damage Associated Transient Progenitors (DATP)

Complementing Kobayashi et al. (2019) was a study that identified inflammatory signals as the main driver of ATII cell transitional states. At the peak of bleomycin injury, multiple subsets of ATII cells can be distinguished based on distinct characteristics. These are the standard ATII cell population (*Sftpc* and *Sftpa1*), homeostatic population (*Acly, Hmgcr* and *Hmgcs1*), cycling ATII cells (*Mki67, Cdk1,* and *Cenpa*), and another aberrant population of cells referred to as damage-associated transient progenitors (DATPs), which express a spectrum of signatures that are reminiscent of those observed in PATS (Choi et al. 2020).

Broadly, DATPs were found to express *Cldn4, Krt8, Ndrg1, Sprr1a,* low levels of the ATI cells markers *Pdpn, Hopx* and *Cav1*, increased *p53* signalling, cell cycle arrest (*Cdkn1a* and *Cdkn2a*), and hypoxia signatures (*Hif1*α and *Ndrg1*). The authors identified that in response to bleomycin, interstitial macrophage populations increase drastically and localise to ATII cells in the alveoli, where they upregulate expression of *IL-1*β. Using IL-1 receptor deficient mice, Choi et al. (2020) demonstrated that IL-1β signalling is required for DATP formation, and that stimulation of macrophage populations with granulocyte macrophage colony stimulating factor (GM-CSF), bolsters IL-1β production and colony formation of organoid cultures. IL-1β was subsequently identified to promote increased HIF-1α mediated changes in glycolysis metabolism that are required for DATP transition. Finally, 80% of DATP were shown to be derived from ~ 15% of ATII cells that express high levels of Il1r1, which are epigenetically primed to respond to IL-1β signalling in alveolar repair. As in PATS, DATPs were observed in human lung samples, highlighting that chronically high inflammation restrains DATPs in their un-resolved state, maintaining a non-functional population of cells in alveoli that can also be observed in lung tumour samples. This highlights that transitional states arising in the lung are not restricted to pulmonary fibrosis, but instead are a result of dysregulated immune responses in chronic inflammation.

1.1.6.3. KRT8+ Alveolar Differentiation Intermediates (ADI)

Finally, a third study identified an aberrant population of cells that appear ~ 10-14 days following exposure to bleomycin, and possessed similar features of ATI cells, but lacked canonical markers that define the pneumocyte populations, therefore naming them alveolar differentiation intermediates (ADI; (Strunz et al. 2020). Single cell sequencing of lungs revealed the characteristic expression of KRT8 in these aberrant cell types, alongside pro-fibrogenic signatures like *Areg, Hbegf, Lgals3,* and *Itgb6*, in addition to enrichment for signatures pertaining to epithelial-mesenchymal transition, senescence, p53, MYC, TNFA, and oxidative phosphorylation. Mapping of interaction networks between KRT8 ADI and other cells in the lung highlighted key interaction networks between macrophage populations and capillary endothelial cells, alluding to the findings of DATP which imply interstitial macrophages as drivers of differentiation states. Not-surprisingly, KRT8+ ADI signatures were observed in human IPF samples, as well as in acute respiratory distress syndrome, influenza-A infected lungs, and other interstitial lung disease patients.

To conclude, damage incurred to the ATI cell population drives innate immune responses in the alveoli. Interstitial macrophages secrete IL-1β, in turn, inducing Hif1α mediated changes in primed ATII cell populations that lead to increased p53 signalling, self-renewal arrest, and transcriptional changes that correspond with differentiation states. Characteristically, these include Cldn4, KRT8, Lgals3 and SFN (Choi et al. 2020; Kobayashi et al. 2020; Strunz et al. 2020). In culture, these differentiation states resolve into fully mature ATI cells (Kobayashi et al. 2020), however chronic inflammation and the sustained IL-1β signalling this brings prevents resolution *in vitro* and *in vivo* (Fig 1.5), instead contributing to respiratory disease as non-functional tissue (Choi et al. 2020; Strunz et al. 2020). Many of these processes such as p53 signalling, aberrant proliferation, glycolysis metabolism, senescence and DNA damage repair are found in cancer, implying that disease initiation in the lung could be utilising conserved and normal lung repair pathways that become dysregulated? in the early tumour niche.

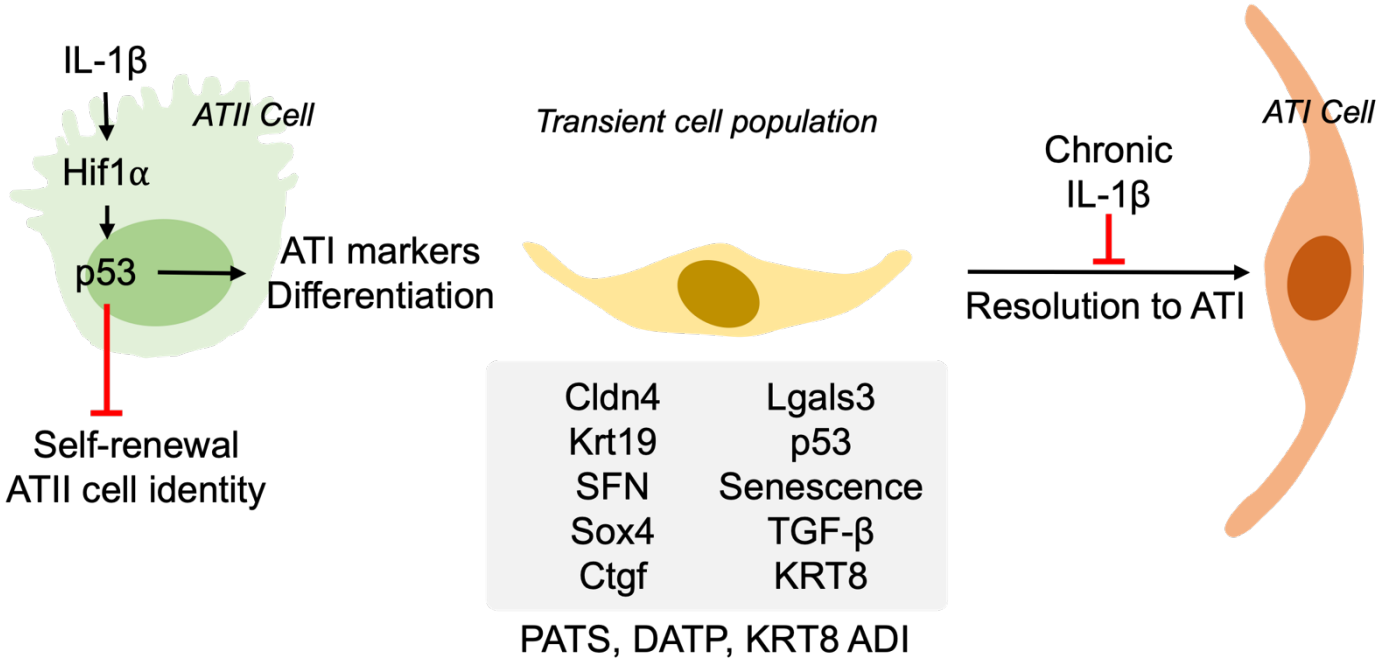

Figure 1. 5 Transient progenitor populations in fibrosis.

Several studies have identified a core transitional cell state induced by Hif1α mediated regulation of ATII cell self-renewal. Increased p53 signalling leads to loss of ATII cell identity and the subsequent acquisition of a core package of signatures, including senescence pathways and p53 signalling. In the absence of chronic inflammatory signals, transient cell types resolve into functional ATI cells. However, signals from innate immune cells such as IL-1β prevents resolution, and further promotes differentiation. Pre-Alveolar Transition State (PATS; Damage Associated Transient Progenitors (DATP) KRT8+ Alveolar Differentiation Intermediates (KRT8+ ADI).

1.2. Lung Cancer.

1.2.1. Incidence and prognosis.

Lung cancer is the 2nd most common cancer in both males and females (CRUK 2024) and is considered to be the greatest cause of cancer deaths worldwide (Yeddula et al. 2015; Padhye et al. 2019; Ferone et al. 2020). Between 2016 and 2018 48,459 new cases were diagnosed in the UK. Diagnosis is often carried out by chest X-ray or CT scan, though practitioners may perform lung function tests or biopsy to aid diagnoses (Macmillan Cancer Support 2024). Lung cancer is split into two major subgroups: small cell lung cancer (SCLC) and non-small cell lung cancer (NSCLC). NSCLC is further divided into lung adenocarcinoma (LUAD), lung squamous cell carcinoma, and large cell carcinoma. Surgical resection of early-stage disease provides the best prognosis for patients, with 10-year or more survival rates at 10% (CRUK 2024). Mortality and poor 10 year survival is due in part to late presentation of disease at time of diagnosis with 48.1% of cases diagnosed as stage IV, and 20.6% as Stage III in Wales, and similarly across the other nations of the UK (CRUK 2024). Currently, risk factors understood to drive pathogenesis of lung cancer include smoking, environmental factors such as air pollution and ozone, occupational exposure to particulate matter, microplastics and detergents, as well as poor diet, chronic illness and other lifestyle choices (Malhotra et al. 2016; Celebi Sözener et al. 2020; Hill et al. 2023).

1.2.2. Small cell lung cancer.

SCLC accounts for ~15% of lung cancers and is characterised by high proliferation, high incidence of metastases to the brain, lymph nodes, bone, liver and adrenal glands, and poor overall survival with 70% of cases presenting at stage with extensive disease (Rudin et al. 2021). Tobacco use appears to be the single greatest contributing risk factor in SCLC, contributing to 95% of SCLC cases. SCLCL is predominantly characterised as a neuroendocrine cell-derived disease in the central lung, driven by the ubiquitous loss of *TP53* and *RB1* tumour suppressor genes (George et al. 2015). Researchers have also shown that SCLC can be derived from AT2 cells that have lost *Rb1* and *Trp53* to some extent as well as directed club cell induction (Sutherland et al. 2011; Ferone et al. 2020).

1.2.3. Non-small cell lung cancer.

NSCLC accounts for the remaining ~85% of lung cancer cases. A large proportion of NSCLC is driven by tobacco smoke (20-fold increase), though other factors increase risk of developing NSCLC such as second-hand smoke, Radon exposure, non-infectious respiratory conditions and chronic illness (Malhotra et al. 2016). The most prominent mutations that drive NSCLC are activating mutations in the Kirsten rat sarcoma (*KRAS*) gene which is found in around 30% of NSCLC cases (Johnson et al. 2001; Adderley et al. 2019; Chevallier et al. 2021). Mutations in *RAS* are associated with history of smoking (Ferrer et al. 2018), though not limited to this group alone. Smoking-induced *KRAS* mutations are more frequently $KRAS^{G12C}$ (~40%) or $KRAS^{G12V}$ (~19%) and are associated with more complex genomic signatures with a higher frequency of co-mutations in the *TP53* and *STK11* (Ferrer et al. 2018; Ghimessy et al. 2020; Judd et al. 2021). On the other hand, LUAD is still the most frequent cancer in never smokers (Couraud et al. 2012), and activating $KRAS^{G12D}$ are the most frequent *KRAS* mutation in never smokers (Ghimessy et al. 2020; Judd et al. 2021).

Second to *KRAS* mutant NSCLC in smoker groups are mutations in epidermal growth factor receptor (*EGFR*), which account for 13% of NSCLC cases. However, *EGFR* mutations account for ~ 58% of NSCLC found in never smokers (Sun et al. 2007). Evidence suggests that risk factors that contribute to *EGFR* mutant disease in never smokers include occupational exposure, indoor and outdoor air pollutants, previous history of lung disease, and dietary factors (Sun et al. 2007). Another driver of NSCLC is alteration to the anaplastic lymphoma kinase (*ALK)* gene such as amplifications, fusions and rearrangements, and activating mutations, which lead to aberrant downstream activation of signalling pathways such RAS/MAPK, PI3K/AKT, and JAK/STAT pathways (Shreenivas et al. 2023). *ALK* alterations account for ~ 3-7% of cases of NSCLC, particularly LUAD subtype (Shreenivas et al. 2023).

A study performed in 2015 identified frequent co-mutations that are associated with *KRAS*-driven NSCLC. *KRAS*-driven NSCLC produces three distinct genetic subtypes based on expression of co-mutations and associated factors such as immune markers, gene enrichment, and expression of PD- L1. *STK11* and *KEAP1* mutations are associated with low levels of immune markers, and mostly immune inert tumours, show low expression of PD-L1 and are associated with poor prognosis NSCLC (Skoulidis et al. 2015; Di Federico et al. 2021). *KRAS* mutant NSCLC expressing mutant *TP53* is characterised by active inflammation and adaptive immune resistant tumour phenotype (Skoulidis et al. 2015). The final subtype includes

tumours that possess inactivated CDKN2A/B, plus low thyroid transcription factor 1 (TTF-1), over-expression of which is associated with a better prognosis in stages 1, III and IV non-squamous cell NSCLC (Kim et al. 2018).

1.2.4. RAS-MAPK Pathway.

The Mitogen Activated Protein Kinase (MAPK) refers to a well characterised signalling family that are activated in response to the binding of mitogens and growth factors to membrane bound receptor tyrosine kinases (RTK). Ligands binding to respective receptors induce dimerization, and subsequent trans-phosphorylation of intracellular tyrosine kinase domains, which permits the recruitment and binding of adaptor proteins such as GRB2 (growth factor receptor-bound protein 2) and guanine exchange factors (GEFs) like SOS (son of sevenless; Fig 1.6) (Zenonos and Kyprianou 2013). Post-translational prenylation of cytosolic RAS tethers and localises it to the plasma membrane, making it available for binding to SOS (Konstantinopoulos et al. 2007). There are three RAS family members, KRAS, HRAS (Harvey rat sarcoma) and NRAS (Neuroblastoma rat sarcoma) which are widely expressed in tissues, and knockout studies have revealed that KRAS is the only member of the RAS family required for embryogenesis (Downward 2003). Activation of RAS is required for downstream signalling to occur. This is carried out by GEFs which alter RAS protein conformation and lowers affinity for guanine-diphosphate (GDP), to permit binding of guanine-triphosphate (GTP) which is more abundant in the cell (Simanshu et al. 2017).

Activation of RAS initiates recruitment of RAF to the plasma membrane, inducing RAS nanoclustering, and permitting the formation of RAF dimer complexes that permit allosteric transactivation by phosphorylation (Lavoie and Therrien 2015). Three RAF paralogs exist, ARAF, BRAF and RAF1, each containing highly conserved regions that are important for maintenance of inactive states, membrane recruitment during activation, and kinase domains (Desideri et al. 2015). RAF phosphorylates MAPK/ERK kinase (MEK), which in turn activates extracellular regulated kinase (ERK; Fig 1.6). Roles for ERK include regulating cell proliferation through its effectors JUN and FOS, cell survival via regulation of pro- and anti-apoptotic factors, cell motility via interactions with ribosomal S6 kinase (RSK), myosin light chain kinase (MLCK) and cortactin, as well as its role in regulating cell motility by mediating focal adhesion turnover by regulating focal adhesion kinase (FAK; (Lavoie et al. 2020). Though ERK and MAPK pathway activity is not limited to these roles, it is clear to see how regulation of RAS activity is of vital importance for normal cell behaviour.

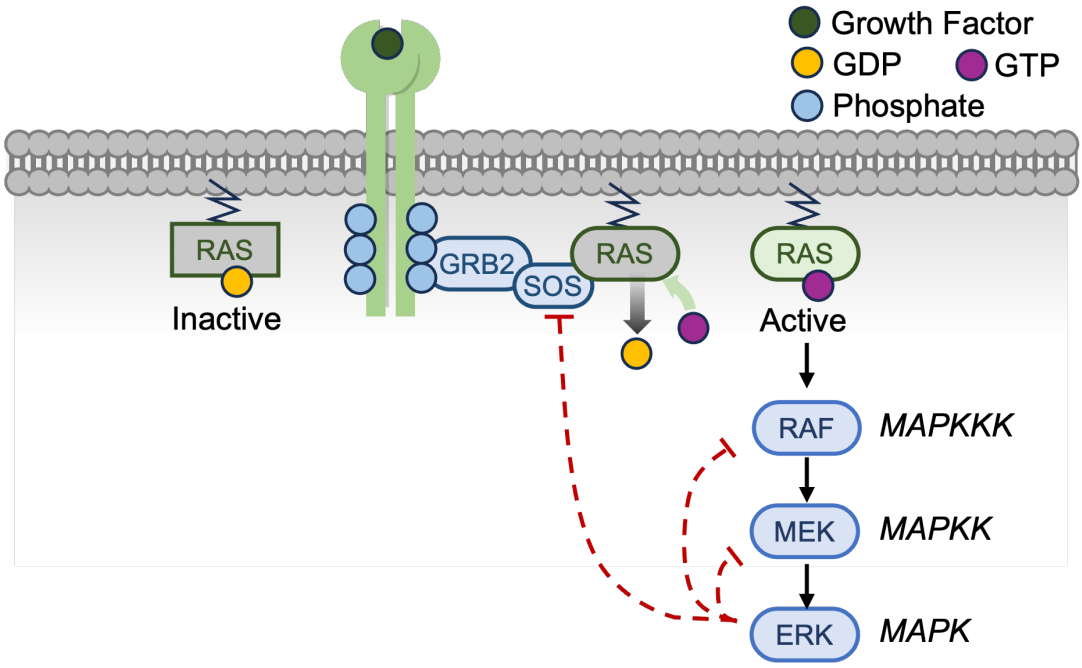

Figure 1. 6 Activation of RAS MAP Kinase signalling cascade.

Activation of prenylated RAS located at the plasma membrane starts by the binding of a ligand such as a growth factor, mitogen or integrin to the receptor tyrosine kinase (RTK) at the cell surface. Ligand binding induces dimerisation of RTKs, subsequently leading to transphosphorylation of intracellular domains, and permitting the docking of adaptor proteins like GRB2 and GEFs such as SOS. RAS association with SOS induces a conformational change which promotes dissociation of GDP form RAS, permitting GTP binding and activation of RAS. Activated RAS is involved in many pathways, but most famously drives signalling of the MAP kinase pathway, through RAF (MAPK kinase kinase; MAPKKK), MEK (MAPK kinase; MAPKK) and ERK (MAPK). One key function of ERK is it's auto-inhibitory feedback loop to upstream pathway members such as MEK, RAF and SOS. Once bound to GTP, RAS cannot unbind it without biochemical intervention due to its abundance in the cell.

Abundance of GTP in cytosol, unfavourable re-binding of GEFs to RAS-GTP, and low intrinsic GTPase activity means that de-activation of the MAPK pathway by RAS requries intervention from other sources (Simanshu et al. 2017). GTPase-activating proteins (GAPs) such as Neurofibromin type 1 (NF1) and Ras GTPase-activating-like protein IQGAP1 (IQGAP1), promote GTPase activity of RAS, driving the hydrolysis of RAS-bound GTP into GDP, ultimately leading to the cessation of RAS signalling (Vigil et al. 2010). KRAS mutations are frequent in the MAPK pathway, with single-base missense mutations prevailing above others (Huang et al. 2021). These frequently arise at codon 12 (Glycine 12; G12), codon 13 (G13), or at codon 61 (Glutamine 61; Q61). These common mutation sites are associated with altered GTPase activity of KRAS, showing slight reduction in RAS intrinsic GTPase activity, but demonstrating the significant impact on GAP stimulated GTP hydrolysis (Hunter et al. 2015). Therefore, lack of RAS inactivation leads to the constitutive activation of the RAS pathway, and aberrant signalling outputs that become dysregulated and contribute to tumorigenesis (Fig 1.7).

Of course, RAS is not only involved the RAS/MAPK pathway, other roles for RAS in pathways such as the PI3K/AKT/mTORC signalling pathway. Here, RAS binds to the p110 subunit of PI3K, leading to PI3K activation and promoting conversion of phosphatidylinositol 4,5-bisphosphate (PIP2) to phosphatidylinositol 3,4,5-triphosphate (PIP3). PIP3 promotes phosphorylation of AKT by PDK1, which then translocates to the nucleus to regulate processes such as proliferation, apoptosis and metabolic processes (Huang et al. 2021). RAS further promotes the conversion of RAL-GDP to RAL-GTP by RalGDS (Huang et al. 2021). RAL-GTP activates phospholipase D1 and Rac-Cell division cycle 42 (CDC42) which are associated with endocystosis and cell cycle progression respectively (Downward 2003; Huang et al. 2021). RAS can also stimulate the RAC-GEF TIAM1 to activate processes associated with cell-cell adhesion, cell-matrix adhesion, migration and cell cycle progression (Mack et al. 2011). Finally, RAS can activate phospholipase Cε (PLCε), which functions to convert PIP2 into diacyl glycerol (DAG) and inositol triphosphate (IP3) which are used in the cell to promote secondary messenger transduction via Ca^{2+} and PKC (Downward 2003; Huang et al. 2021). In summary, RAS is involved in may cellular processes that if deregulated, contribute to several hallmarks of cancer. As such, understanding how core pathways become dysregulated in oncogenic settings is vital to determine interventions and targets for therapy.

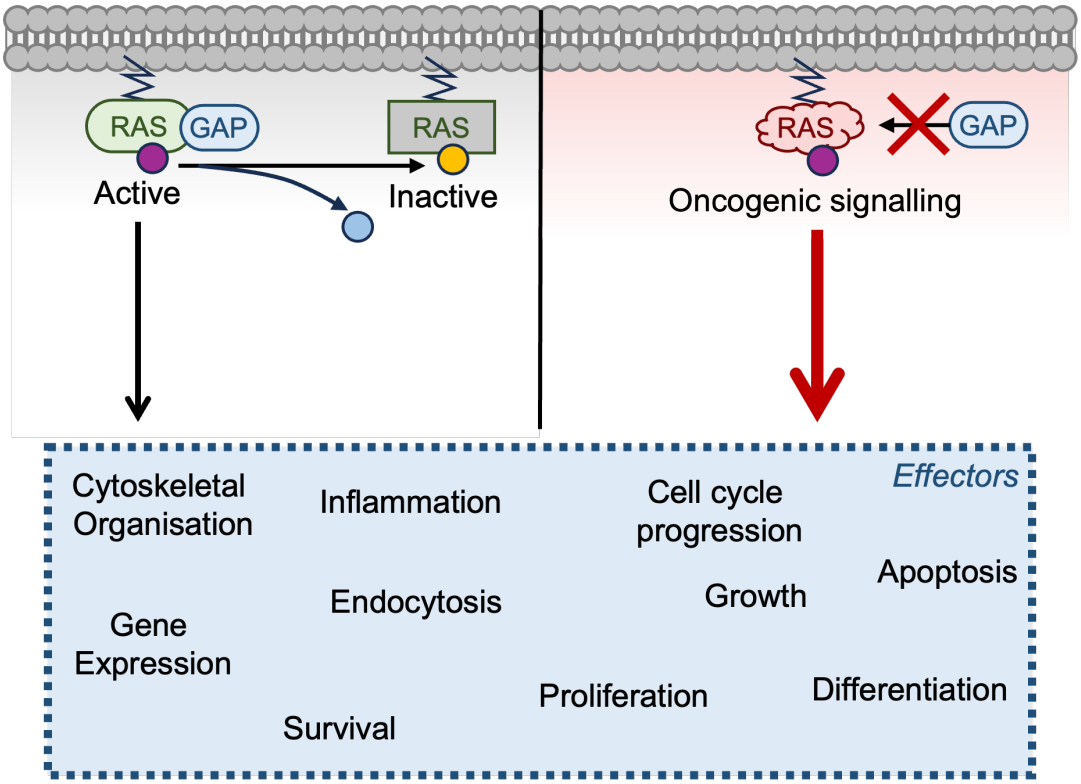

Figure 1. 7 Inactivation of RAS requires GAP-assisted hydrolysis of GTP to GDP.

In its active state (left panel), RAS mediates key cellular process that if deregulated could become harmful to the cell. As such GTPase activating proteins (GAPs) like NF1 and IQGAPI promote the intrinsic GTPase activity of RAS, hydrolysing RAS-bound GTP to GDP, inactivating the pathway. Oncogenic KRAS (right panel) has altered GTPase intrinsic activity and altered binding to GAP subsequently affecting stimulated GTP hydrolysis. As a result, RAS effectors become dysregulated and continue signalling aberrantly.

1.2.5. Cell of origin and mutational landscape.

A large body of research has focussed on trying to identify the cell of origin that contributes to LUAD. Research suggests that cancer arises from many different cell types following expression of certain mutations such as oncogenic KRAS. Early work established the well-known model of inducing KrasG12D in mice by delivering adenoviral Cre recombinase either intranasally or intratracheally (Jackson et al. 2001; Meuwissen et al. 2001; DuPage et al. 2009). From KrasG12D induction alone, three types of hyperplastic tissue were identified; atypical adenomatous hyperplasia (AAH) which closely resembles early human lesions, epithelial hyperplasia (EH) wherein bronchial epithelial cells proliferate in the distal lung, and adenomas, which are mixed lesions that distort or obliterate alveolar space in the distal lung by 6-12 weeks post induction (Jackson et al. 2001; Meuwissen et al. 2001). Further abrogation of p53, a potent tumour suppressor led to a more malignant adenocarcinoma phenotype in late time-point animals (Jackson et al. 2005). Further investigation into what cell types were giving rise to these lesions revealed a complex pattern of cell types that can conditionally derive LUAD-like disease. Generally, oncogenic Kras expression leads to the appearance of CC10 positive papillary structures in EH, pro-SPC positive adenoma lesions in alveolar regions, and distinct overlapping double positive sites in adjacent serial sections (Jackson et al. 2001).

As was discussed previously, BASC which exhibit both SPC and CC10 positivity were the likely culprits for this (Kim et al. 2005). These cells were shown to increase shortly after KrasG12D induction, and later exhibit differentiation into alveolar lineage cells (Kim et al. 2005). Furthermore, this study also showed that enriching BASCs with prior naphthalene exposure increased the tumour number, and area in mice at 6 weeks post KrasG12D induction. Another study linked aberrant regulation of RAS-PI3K signalling to tumour progression, finding that PI3K inhibition reduced tumour burden and proliferation. They found that BASCs exhibited greater levels of p110α and phosphorylated AKT (Yang et al. 2008) This provided evidence to suggest that BASCs contribute to LUAD.

Refinements to mouse models in recent years have complicated our understanding of tumour cell biology in the lung. Using tamoxifen inducible cre recombinase expressed in club cells (*Scgb1a1*-Cre^{ERT}) or ATII cells (*Sftpc*-Cre^{ERT}), it was shown that KrasG12D activation in these cell types alone is sufficient to drive hyperplasia of the lung between 8-15 weeks post induction (Xu et al. 2012; Rosigkeit et al. 2021). expression of KrasG12D via *Scgb1a1*-Cre resulted in bronchiolar hyperplasia at the BADJ, and some Pro-SPC negative adenomas in the alveoli, and

Sftpc-Cre^{ERT} induction of KrasG12D led to hyperplasia in the alveoli, but not the BADJ. This was further supported using adenoviral cre recombinase that only targets either ATII cells (Ad5-SPC-Cre) or club cells (Ad5-CC10-Cre) (Sutherland et al. 2014). Tumour histology between the two adenoviral constructs appeared distinct; Ad5-SPC-Cre drove an expected AAH, adenocarcinoma phenotype in the distal lung, and AD5-CC10-Cre drove focal hyperplasia, EH, and papillary hyperplasia of the more proximal and terminal bronchiolar epithelial cells. Furthermore, Ad5-SPC Cre could not drive hyperplasia in the BADJ, similar to what was observed by Xu et al. (2012).The authors note that in their study they observe the presence of CC10/SPC positive hyperplasia in Ad5-CC10-Cre mice, but not in Ad5-SPC-cre inoculated mice and suggest either that BASC expression of SPC is too low for Ad5-SPC-Cre infection, or that dual positive cells are not the cell of origin for LUAD. Furthermore, loss of TP53 in mice alongside cell specific expression of KrasG12D does not limit malignancy, to specific regions as was observed in the presence of Tp53 (Sutherland et al. 2014). In summary, these findings illuminated that development of LUAD from a specific cell of origin is largely context dependent, that BASCs do not contribute to tumour initiation, and that ATII cells are like the predominant cell of origin in distal LUAD.

Since this discovery, more evidence for ATII cells as the cell of origin has been uncovered. Isolating ATII cells from mice and inducing oncogenic KrasG12D expression increased the percentage of proliferating ATII cells per organoid at 2-weeks post induction (Dost et al. 2020). Transplantation of KrasG12D-ATII cells into injured mice led to the formation of AAH *in vivo* at 4 weeks post implantation, demonstrating their potential to drive disease in the alveoli. Interestingly, transformed ATII cells displayed dedifferentiation phenotypes, upregulating developmental gene signatures such as *Hmga2, Sox9* and *Ly6a*, whilst reducing gene expression of mature ATII cell markers like *Lyz2, Sftpc, Sftpd, Cd74* and *Nkx2-1* (Dost et al. 2020). This finding was shown to be conserved between murine alveolar organoids and human derived organoid models in the same study, fortifying the phenotype as an early tumour initiation phenotype.

1.3. Cell Competition.

1.3.1. Somatic mutations in normal tissues.

As a consequence of aging, tissues acquire somatic mutations. However, the fact that not everyone will develop cancer in their lifetime implies that homeostatic mechanisms exist that restrict tumorigenesis at the onset of mutation. Furthermore, having more cells and a longer lifetime is not a direct causative factor in cancer development (Peto et al. 1975; Leroi et al. 2003). Somatic mutations in normal tissues have been analysed in depth in multiple organs including the skin, oesophagus, endometrium, colon, lung, and bladder (Martincorena and Campbell 2015; Martincorena et al. 2015; Martincorena et al. 2018; Lee-Six et al. 2019; Martincorena 2019; Lawson et al. 2020; Moore et al. 2020; Yoshida et al. 2020). What is evident from these studies is that positive selection of particular mutations does not necessarily confer an oncogenic phenotype. Incidence of known driver mutations appears to be a rare event amidst a patchwork of somatic mutants that will not drive tissue-specific tumorigenesis (Lee-Six et al. 2019). However, the reality is that these seemingly rare mutations have the power to drive tumorigenesis over time. What occurs in the epithelium to shape the mutational landscape? And how does the body's innate regenerative capacity fail in ageing to permit clonal expansion and subsequent tumour development?

1.3.2. Elimination of cells to maintain tissue homeostasis.

This mechanism was first described in the *Drosophila melanogaster* wing disc, whereby slow growing clones expressing heterozygous mutations in the ribosomal protein *Minute* (*M*+) were eliminated from the tissue at developmental timepoints, and present only in small numbers in the adult wing (Morata and Ripoll 1975). This elimination of mutant, misplaced, or damaged cells describes a process now referred to as cell competition. For a process to be regarded as cell competition, there must be a population of cells that are removed from the epithelium, termed 'Losers', and subsequently a 'Winner' population that remain in the tissue as the dominant cell type. Though Losers are typically associated with mutated or damaged cells such as those expressing prominent oncogenes (Hogan et al. 2009; Kajita et al. 2010; Chiba et al. 2016), competitive elimination can result in healthy non-transformed cells being removed from the tissue, and dominant mutant cells take on the winner role (de la Cova et al. 2004; Moreno and Basler 2004). This process is referred to as super competition, and potentially suggests a role for cell competition in regulating the early

stages of tumorigenesis. Different phenotypes occur for different loser phenotypes, including induction of cell death, basal extrusion, apical extrusion, and induction of differentiation, likely owing to context within tissues.

1.3.2.1. Induction of cell death within the epithelium.

Following the initial findings, *M+* cells were observed to be eliminated from the wing disc by JNK-dependent apoptotic cell death (Moreno et al. 2002). Later, a similar finding was observed using a three-clone model of tracking clonal dynamics in the wing disc, finding that *M+* cells are outcompeted by sister cells that have a growth advantage (de la Cova et al. 2004). Further to this, this study identified that expression of the *Drosophila* growth regulator dMyc induces elimination of sister clones in the same compartment by apoptosis. Advancing on this phenotype, dosage of dMyc was shown to be a key factor in determining winner or loser status. When cells that express equal levels of dMyc were juxtaposed, no elimination was observed. However, when cells expressed double the amount of dMyc than their neighbours, they outcompeted them by inducing JNK-dependent cell death (Moreno and Basler 2004).

The role of JNK-induced apoptosis in *Drosophila* was further cemented by a study that showed that loss of the tumour suppressor APC in the fly intestine drives not only tumorigenesis, but elimination of WT clones that surround APC-/- clusters (Suijkerbuijk et al. 2016). Scribble is another driver of cell competition in *Drosophila*, driving loser phenotype in *Scribble* mutant cells when surround by WT cells, leading to JNK-induced apoptosis (Brumby and Richardson 2003). However, JNK-induced apoptosis does not appear to be a conserved mechanism in mammalian epithelia. In MDCK co-culture, scribble knock-down led to competition and loss of mutant clones by apoptosis. However, activation of JNK was not observed, and selective inhibition of JNK did not result in loss of competition phenotypes, instead suggesting that p38 MAPK drives competition-mediated apoptosis in mammalian cells (Norman et al. 2012).

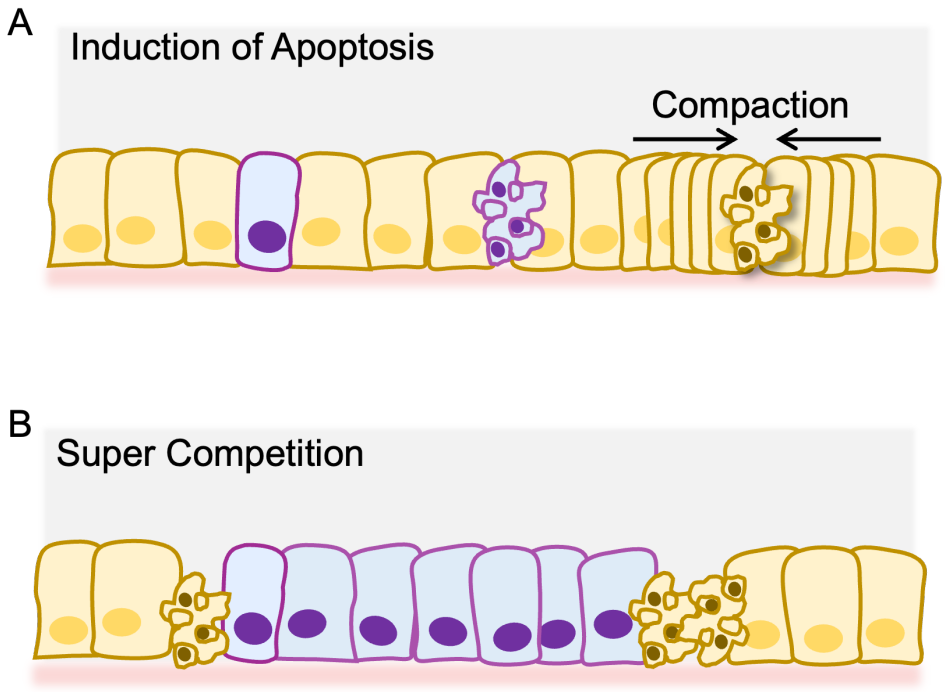

Figure 1. 8 Induction of cell death during tissue homeostasis.

During developmental processes, mutated or mis-specified cells are eliminated from the epithelium by induction of cell death. **A)** When loser cells (blue) are selected for elimination, surrounding WT cells induce JNK-mediated apoptosis to maintain a functional epithelial barrier. If epithelial tissues become overcrowded, cell death may be induced to prevent bucking or loss of integrity. **B)** Where cells acquire mutations that confer a selective advantage over their neighbours (blue), surrounding normal cells can be outcompeted by induction of cell death in a process known as super competition.

1.3.2.2. Extrusion of cells from the epithelium.

A second prominent mechanism of cell elimination is the physical extrusion of cells from the epithelium by neighbouring cells. Early work identified that when exposed to ultra-violet (UV) light, many cells are eliminated from epithelia both *in vitro* and *in vivo* by extrusion (Rosenblatt et al. 2001). Subsequent studies identified that apoptotic signals from dying cells induced conversion of the bioactive lipid sphingosine to sphingosine-1-phosphate (S1P), which functions to reorganise the cytoskeletal network of the dying cell and its neighbouring cells to prepare for contractile extrusion (Slattum et al. 2009; Gu et al. 2011). Apical extrusion is driven by a contractile actin-myosin ring around the basolateral surface of the cell destined for extrusion, which requires RhoGEF-RhoA-ROCK coordination to occur (Slattum et al. 2009). When induced in a tissue ubiquitously expressing mutant KrasV12, induction of cell death surprisingly led to the basal extrusion of loser cells (Slattum et al. 2014). KrasV12 expression was found to degrade levels of S1P, which led to improper localisation of extrusion machinery and the preferential extrusion of dying cells basally (Fig 1.9 A). Once extruded basally, KrasV12 mutant cells were shown to partially dedifferentiate and contribute to the development of cancer-like masses in zebrafish embryos suggesting that failure to extrude properly could underpin disease initiation (Gu et al. 2015; Fadul et al. 2021)

Interestingly, the oncogene expression on loser/winner cell fate appears inconsistent, driving different responses in different systems. When expressed at low numbers in an otherwise non-transformed MDCK monolayer, (H)RasV12 mutant cells were mostly apically extruded by WT neighbours, remained viable, and formed multicellular aggregates on top of the monolayer (Hogan et al. 2009). Further investigation found that RasV12 cells increase in height, accumulate F-actin at the Ras-Ras cell interface, and rely on contractile mechanics such as myosin-II phosphorylation and actin polymerisation similarly to Rosenblatt et al. (2001) (Hogan et al. 2009). In the remaining population of cells that did not extrude, basal protrusions were found underneath WT neighbours as well as fortification of E-cadherin junctions (Fig 1.9 B). Similar results were achieved when vSrc was expressed in MDCK cells, leading to extrusion of Src-expressing cells, independently of apoptosis, increased cell height, and reliance of contractile machinery (Kajita et al. 2010). Other drivers of cell extrusion in this fashion include constitutively active yes associated protein (YAP) 5SA (Chiba et al. 2016), loss of functional Scribble (Norman et al. 2012), and Erbb2 mutant cells (Leung and Brugge 2012). These studies all demonstrated that apical

extrusion is a non-cell autonomous responses to oncogene activation and relies on interactions between the transformed cells and the surrounding normal epithelium.

A potential explanation for this discrepancy was suggested by Slattum et al. (2014) as an effect of acute versus constitutive expression of Ras oncogene in the epithelium. In their study, KrasV12 is constitutively expressed throughout the monolayer culture, and extrusion is induced by UV-stimulated apoptosis (Slattum et al. 2014). Conversely, Hogan et al. (2009) generated co-cultures of WT MDCK and inducible HrasV12 cells in the ratio of 100:1 respectively, leading to spontaneous apical extrusion of HrasV12 mutant cells from the monolayer. The latter model focusses on interactions between transformed cells and their WT neighbours, whereas the Slattum model is modelling the effect of driving apoptosis in an already mutant field of cells. As such, the study of the interactions between WT cells and potentially tumorigenic mutant cells in an epithelium has branched off into its own subset of cell competition, termed Epithelial Defence Against Cancer (EDAC).

EDAC refers to the specific competition that arises in epithelial tissues, largely to suppress mutant cell expansion in early tumorigenesis. Initial findings such as those pertaining to HrasV12, and vSrc are associated with his phenotype, as failure to extrude from the epithelium leads to more invasive hallmarks (Hogan et al. 2009; Kajita et al. 2010). These attributes have been observed in mammalian tissues, including the pancreas, lung, mammary gland, and small intestine (Sasaki et al. 2018; Hill et al. 2021; Shirai et al. 2022). Attenuation of EDAC in these tissues, either by driving inflammatory process (Sasaki et al. 2018) or by interfering with cell competition drivers (Hill et al. 2021) leads to the onset of pre-malignant lesions that could contribute to disease initiation.

1.3.2.3. Induction of differentiation.

The final notable method of cell competition is the induction of loser cell terminal differentiation. This phenotype was originally observed in the *Drosophila* germline stem cell (GSC) niches. Here, loss of function of the JAK-STAT inhibitor *Suppressor of cytokine signalling 36E* (*socs36E*) led to a reduced number of GSCs and an increased number of somatic cells in the *Drosophila* testis (Issigonis et al. 2009). Later on, a study identified that WT cells in the *Drosophila* midgut were capable of inducing differentiation of *M+* intestinal stem cells with reduced growth capacity into cells that lack the intestinal stem cell marker *Delta* (Kolahgar et al. 2015).

Induction of differentiation has been further explored in mammalian tissues that exhibit a stratified tissue morphology such as the skin and the oesophagus. Cells

in the epidermis expressing a greater amount of COL17a had a competitive advantage of their lesser collagen XVII expressing cells, leading to their symmetrical cell division and subsequent expulsion of neighbouring cells from the stem cell layer of the epidermis (Liu et al. 2019a). In the oesophagus, low dose ionising radiation resulted in the increased differentiation of basal stem cells at early timepoints. When mutant p53 was introduced into the basal stem cell layer, low dose ionising radiation conferred a competitive growth advantage over p53 WT cells, leading to the expansion and colonisation of the oesophageal epithelium with p53 mutant clones (Fernandez-Antoran et al. 2019). Also in the oesophageal epithelium, cells harbouring the notch1-inhibitory mutant of Maml1 drive differentiation and stratification of normal cells out of the basal layer, subsequently expanding in the epithelium (Alcolea et al. 2014). Finally in the mature embryonic epidermis, Mycn+/- mutant cells are eliminated from the basal layer and stratify into the terminally differentiated layers by the symmetrical division of WT cells laterally in the basal layer (Ellis et al. 2019).

The implication of these studies is that competition and its mechanisms are regulated by the tissue, stage of development, and arrangement of neighbouring cells. In developing tissues, the predominant mode of cell elimination trends towards induction of cell death in the first instance, coinciding with a higher capacity for replenishing cells at this time point. In more mature tissues, elimination must not interfere with the tissue's function, compromise barrier function or exhaust stem cell pools. Therefore, mechanisms that more carefully shape the tissue around aberrant cell populations are required, such as differentiation, extrusion of cells before apoptosis, or extrusion of cells that may pose threats to the epithelial barrier.

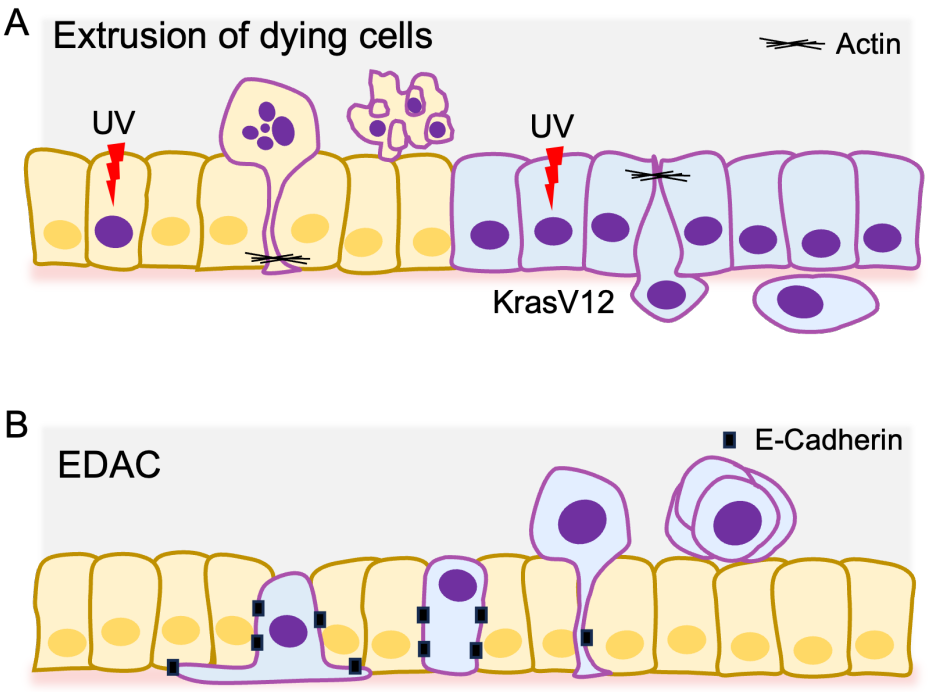

Figure 1. 9 Cell competive elimination by extrusion mechanisms.

In some tissues, induction of cell death may not be a preferred method of maintaining homeostasis. **A)** when presented with DNA damaging stimuli such as ultraviolet light (UV), cells are apically squeezed out from the epithelium via contraction of actin-myosin in adjacent normal cells. Once extruded these cells die by apoptosis. In tissues that harbour oncogenic mutations such as KrasV12 (blue cells), the polarity of extrusion flips to basal extrusion, whereby cells partially differentiate and survive in the tissue. **B)** On the other hand, when surrounded by WT cells, some oncogenic-mutated cells will be apically extruded from epithelia via destabilisation of junctional complexes, and contraction of surrounding epithelial cells. Once extruded, these cells survive and form aggregates on top of the epithelium. A small proportion of these cells upregulate their E-cadherin junctional complexes, and are retained in the epithelium, where they extend basal protrusions underneath their WT neighbours.

1.3.3. Cell competition in cancer.

Previous investigation of cell competition and its pertinence to disease initiation has revealed a dual role for relative 'fitness' sensing in epithelial tissues, where loser cells are determined by their energy efficiency, growth rate, polarity relative to the surrounding neighbourhood of cells. This can be deemed tumour suppressive. In instances where mutation confers a competitive advantage and drives tumorigenesis, cell competition is seen as tumour promoting. Therefore, context is critical to determine to outcomes of competition in disease. What does this mean for competition that occurs in tissue that already harbours disease, where competition does not dictate initiation, but progression? Do cells that harbour cancerous mutations have the ability to lower the 'fitness' of the WT epithelium? Several studies have highlighted the conserved role for key competition pathways in cancer progression, suggesting roles in colorectal cancer, hepatocellular carcinoma, oesophageal cancer, and in glioblastoma.

A group of studies published in Nature in 2021 described how loss of *APC* in colorectal cancer is accompanied by an increased expression of WNT antagonists like *Notum* which promotes differentiation of WT intestinal stem cells, cessation of normal crypt proliferation, and dominance of APC mutant stem cells in the colon (Flanagan et al. 2021; van Neerven et al. 2021; Yum et al. 2021). This was observed across several systems, including mouse and human organoids and i*n vivo.* In competition organoid models, cancer cells derived from intestinal tumours were shown to induce apoptotic elimination and extrusion of WT cells in mixed mouse organoids (Krotenberg Garcia et al. 2021). Inhibition of apoptosis with a pan-caspase inhibitor eliminated the competitive advantage tumour cells possessed and permitted the growth of WT cells in the organoid. WT cells in mixed organoids were enriched for JNK pathway signalling, inhibition of which led to neutralisation of WT cell out-competition (Krotenberg Garcia et al. 2021). These studies show that tumour cells in the gut act as supercompetitors by influencing neighbouring WT cells to exhaust stem cell pools, and become outcompeted based on cell competition phenotypes that are conserved between *Drosophila* and mammals (Moreno et al. 2002; Moreno and Basler 2004; Vincent et al. 2011; Suijkerbuijk et al. 2016).

In the liver, hepatocellular tumours were shown to be surrounded by normal hepatocytes that expressed a greater activation of YAP/TAZ signalling. Experimental manipulation of YAP/TAZ in the normal tissue revealed the importance of a signalling differential between the tumour and surround normal tissue; relatively increased YAP/TAZ in normal peritumoral liver, and relatively decreased YAP/TAZ in the tumour.

Complete knockout of YAP/TAZ had no anti-tumorigenic effect (Moya et al. 2019). A similar scenario was also demonstrated using human glioblastoma cell lines. Glioblastoma cells that stably overexpressed YAP were able to outcompete vector controls that express basal levels of Yap *in vitro* in co-culture assays and spheroid assays by inducing apoptotic cell death (Liu et al. 2019c). The importance of relative fitness is the fundamental concept in cell competition, but usually refers to the juxtaposition of genetically and physically WT cells competing with altered cells. Surprisingly only a handful of studies have asked how two populations of cells that both are altered react in competitive scenarios.

Oesophageal cancer can be induced using diethyl nitrosamine (DEN), which expresses a myriad of mutations in the epithelium that drives cancer over time. Strikingly, across tumorigenesis, many lesions are lost from the oesophageal epithelium, leaving behind few large tumours. Investigation at 30 days post induction revealed that early lesions are driven from the epithelium by expansion of mutated clones in adjacent tissue (Colom et al. 2021). Moreover, later stages tissues were less polyclonal and exhibited positive selection for mutations in *Notch1* in adjacent tissues, and *Atp2a2* in tumours. These results suggest a standard competition phenotype between opposed populations, where one population possesses a competitive edge of another, leading to a dominant winner population in a tumour.

Interestingly, clonal competition does not appear to be the sole outcome when two populations harbouring different mutations are opposed. In *Drosophila* eye disc, mosaic expression of RasV12, Src64B or co-expression of both alongside WT cells leads to small lesions of hyperplasia that never invade into the adjacent ventral-nerve codes (VNC). However, mosaic expression of RasV12 alongside Sr64B clones introduces a synergistic effect which drives aggressive tumour invasion of both mutant populations into the VNC (Enomoto et al. 2021). This mechanism was shown to rely on Ras driven Delta/Notch signalling in Src mutant cells, leading to E-cadherin junctional remodelling, inhibition of cell death, and invasion into the basement membrane. These studies demonstrate further that competition is a broad term for context dependent population dynamics that can be either tumour suppressive or promoting.

1.3.4. A conserved role for oncogenic Ras as a driver of loser cell fate.

Work performed by our lab and others has identified a mechanism by which Ras mutant cells are designated as loser cells and are subsequently eliminated from the epithelium in a tumour suppressive role. As was alluded to previously, when present in low numbers throughout the epithelium, cells expressing oncogenic HrasV12 are eliminated from the monolayer by apical extrusion and cytoskeletal changes mediated by Cdc42 and ROCK in RasV12 cells (Hogan et al. 2009). Cells that are not extruded in monolayer co- cultures extend basal protrusions underneath their WT neighbours, using mechanisms distinct from apically extruding cells. Further exploration of why HrasV12 mutant cells are designated loser cells in WT co-culture found that the initial stage of competition requires repulsion and segregation away from WT neighbours by conserved EphA2 signalling (Porazinski et al. 2016). Using a modified wound healing assay, WT MDCK cells were shown to repel HrasV12 mutant cells, inducing accumulation of F-actin and significantly reducing individual cell area in HrasV12 cells. Inhibition of myosin-II or Src family kinase (SFK) reduced Ras segregation and contractility, and depletion of E-cadherin led to a loss of repulsion. This phenotype was only observed when HrasV12 cells were opposed to WT cells, and not in Ras-Ras confrontations.

Exploration into segregation cues revealed that HrasV12 cells expressed increased levels of EphA2 gene and protein expression, in addition to increase phosphorylation of EphA2, and the EphA2-dependent phosphorylation of Src (Cheng et al. 2013). Knockdown of EphA2 resulted in the loss of cell repulsion in collision assays, reduced compaction and area remained unchanged. Finally, EphA2 was required for apical extrusion of HrasV12 cells in monolayer co-cultures, demonstrating that segregation of mutant cells requires phosphorylation of EphA2 on HrasV12 mutant cells, cytoskeletal re-arrangement, and myosin-II contraction for extrusion from the epithelium (Porazinski et al. 2016; Hill and Hogan 2017). This phenotype is conserved in the *Drosophila* wing imaginal disc, where the *Drosophila* EphA2 (DEph) is required for contraction and segregation of RasV12 expressing cells (Porazinski et al. 2016).

To explore the potential role of Ras-mutant cell competition at the onset of disease, the Hogan lab explored the role of cell competition at the early stages of pancreatic ductal adenocarcinoma (PDAC), of which over 90% of cases are driven by KrasG12D mutations (Morris et al. 2010). Inducing low numbers of KRasG12D mutant cells throughout the pancreatic epithelium was able to recapitulate the early stages of disease in a more representative way that's relevant to human disease initiation.

Indeed, across the first 5 weeks of expression a substantial number of KrasG12D mutant cells were eliminated from all compartments of the pancreatic epithelium in a manner dependent on normal-mutant cell interactions (Fig 1.10 A) (Hill et al. 2021). As was observed before, elimination of KrasG12D mutant cells appeared to be an imperfect process, with around 20% of the tissue still harbouring KrasG12D mutant cells at later timepoints. Using a mouse that contains a truncated and therefore non-functional *EphA2* gene (EphA2-/-), competitive elimination of KrasG12D mutants was neutralised (Fig 1.10 B), and no EphA2-associated phenotypes were observed including increased circularity, reduced inter-nuclear distance, and reduced cell volume. Furthermore, E-cadherin and p120 catenin junctional complexes at the interface of WT and KrasG12D mutant cells appeared to be destabilised in EphA2 WT pancreata (Fig 1.10 A), however E-cadherin junctions were fortified and increased in EphA2 deficient pancreata (Fig 1.10 B), suggesting a role for EphA2 in destabilising junctional complexes to permit elimination. Although loss of EphA2 did not worsen prognosis of animals, PDAC precursor lesions were more abundant at earlier timepoints in EphA2-/- animals (Fig 1.10 B). Overall, this suggests that at early timepoints, EphA2 regulates fate of KrasG12D mutant cells in the adult mouse pancreas, and functions to segregate mutant cells in preparation for elimination.

Most recently, it was found that cells that are not eliminated by 5 weeks, and therefore evade cell competition remain in the tissue and acquire a cell dormancy state (Salvador-Barbero et al. 2024). Dormancy is a reversible growth arrest which has implications in the early stages of tumorigenesis where tumour growth is not apparent (Min and Lee 2023). In post-competition pancreata, KrasG12D mutant cells exhibited decreased gene signatures associated with stemness and canonical Wnt signalling such as *Myc*, *Lgr5*, *Sox2*, *Nanog* and *Wnt3a*, in addition to an increase signature associated with non-canonical Wnt signalling such as *Wnt5a*, *Ror1, Ror2*, and *Jun*. In standard co-culture assays (Hogan et al. 2009), *Myc* knock-down as a proxy of dormancy led to a greater retention of HrasV12 mutant cells than in scramble controls. Non extruded cells were non-proliferative and displayed basal protrusions underneath WT neighbours. Inhibition of Wnt signalling with the porcupine inhibitor, WNT-974 rescued competitive elimination in *Myc* knock-down cultures and shows promise in driving further elimination of KrasG12D mutant cells *in vivo* at 5 weeks post induction. These findings suggest that a population of cells present in tissues are insensitive to competitive elimination cues, upregulate Wnt5a expression and enter a dormant state until the time is right to progress through tumorigenesis.

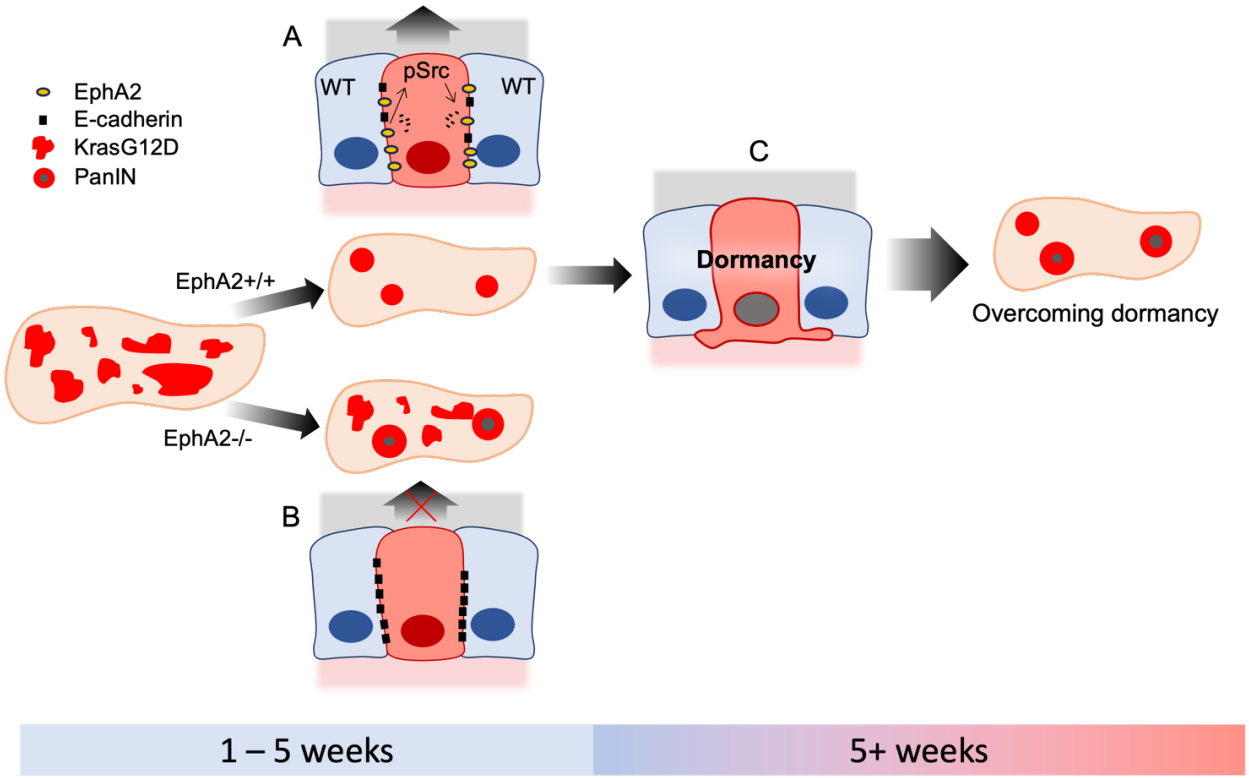

Figure 1. 10 KrasG12D mutant cells are eliminated from the pancreatic epithelium at early timepoints.

In the mouse pancreas, KrasG12D mutant cells which are known to drive disease, are eliminated via EphA2-dependent cell competitive interactions with surrounding WT cells. **A)** This is proposed to rely on EphA2-Src mediated re-organisation of the cytoskeleton and E-cadherin endocytosis. **B)** In EphA2 deficient mice, KrasG12D mutant cells are retained and develop into pre-neoplastic lesions earlier than EphA2WT pancreata. **C)** Retained KrasG12D mutant cells are found to be in a dormant state in the epithelium. Over time they acquire secondary and tertiary mutations that lead to development of pancreatic ductal adenocarcinoma.

1.3.5. A potential role for EphA2 signalling in early tumorigenesis.

EphA2 is an erythropoietin-producing human hepatocellular (Eph) receptor, which is part of the largest subfamily of RTKs. This family comprises 14 different Eph receptors which are further sub-categorised into 9 EphA (EpA1-8, EphA10) and 5 EphB (EphB1-5) receptors (Merlos-Suárez and Batlle 2008). Specific binding of Eph receptors to specific subclasses of ephrin ligand is determined by the receptor's ligand binding domain (Rohani et al. 2014), with EphA receptors preferentially binding to ephrin-A ligands, and EphB receptors preferentially binding ephrin-B ligands (Fig 1.11). Binding of membrane bound ligand to membrane bound receptor upon cell-to cell contact promotes the formation of higher order clusters, intracellular domain phosphorylation, and subsequent activation of several signaling pathways (Cowan and Henkemeyer 2001; Pasquale 2010; Lisabeth et al. 2013). In development, these processes include but are not limited to the segregation of different cellular populations and the formation of sharp boundaries (Cayuso et al. 2015; Cayuso et al. 2019), axonal guidance and repulsion cues in the developing spinal cord (Pasquale 2008; Lisabeth et al. 2013), patterning of branching morphogenesis in the mammary gland (Vaught et al. 2009), regulation of adult neo-angiogenesis, and the dorsoventral patterning of the developing foregut endoderm into the early oesophagus and trachea (Lewis et al. 2022). Unsurprisingly, Eph-ephrins have also been found in disease like cancer, but their specific functions are confounded from study to study and appear to be heavily context dependent.

As has been previously discussed, EphA2 functions as a tumour suppressor in the pancreatic epithelium following activation of KrasG12D (Hill et al. 2021). Under homeostasis, cells express basal levels of ligands and receptors that result in neutral competition outcomes. As a result of aberrant Ras signalling, EphA2 is transcriptionally upregulated in cells (Macrae et al. 2005), subsequently leading to increased EphA2-ephrinA1 binding and the ephrin-A1 dependent repulsion and elimination of Ras-mutant cells from otherwise WT epithelia (Porazinski et al. 2016; Hill and Hogan 2017; Hill et al. 2021). Further support for EphA2 as a tumour suppressor came from a study of lung adenocarcinoma which showed that EphA2 knockdown worsened prognosis and led to increased cell proliferation and survival *in vivo* by upregulation of Hedgehog signalling pathways (Yeddula et al. 2015). In spite of these studies, there appears to be a greater role for EphA2 as a tumour promoter in tumorigenesis and the formation of metastatic populations, with EphA2 overexpressed in lung cancer and correlating with poor survival (Amato et al. 2014).

In mice lacking functional EphA2, mammary tumorigenesis was reduced; exhibiting a lower number of proliferating cells, increased apoptosis, and reduced number of tumour lesions (Brantley-Sieders et al. 2008). Furthermore, pharmacological inhibition of EphA2 in EGFR mutant lung tumours led to reduced tumour growth and cancer cell viability, suggestive of EphA2's pro-survival role (Amato et al. 2014; Amato et al. 2016). In melanoma, EphA2 has been implicated in cell migration, tumour growth and poor prognosis (Udayakumar et al. 2011) Alternatively, ligand-independent AKT-mediated activation of EphA2 has been shown to increase cell migration and invasiveness *in vitro* (Miao et al. 2009; Hamaoka et al. 2016) and *in vivo* (Li et al. 2019; Mo et al. 2020).

Clinical studies have published data that suggests that the consequence of EphA2 overexpression is dependent on stage of disease, with high EphA2 corresponding to improved overall survival at early timepoints following surgical resection of lung cancer, but not later (Ishikawa et al. 2012). Therefore, it may well be the case that intact EphA2 at the onset of disease initiation is beneficial to provide biological barriers, repel and drive elimination of mutated cells from epithelia and restore homeostasis. In established disease high EphA2, along with ligand-independent signalling contribute to establishment of secondary disease and may prove to be promising targets for clinical intervention. Conversely, loss of ephrin ligand provides this receptor-ligand differential and has been shown to reduce metastatic disease progression in melanoma (Mo et al. 2020). What is unclear, is whether EphA2 provides a vital early tumour-suppressor role in the lung epithelium in the days following KrasG12D activation, as we previously observed in several model systems, including the mouse pancreas (Porazinski et al. 2016; Hill and Hogan 2017; Hill et al. 2021)

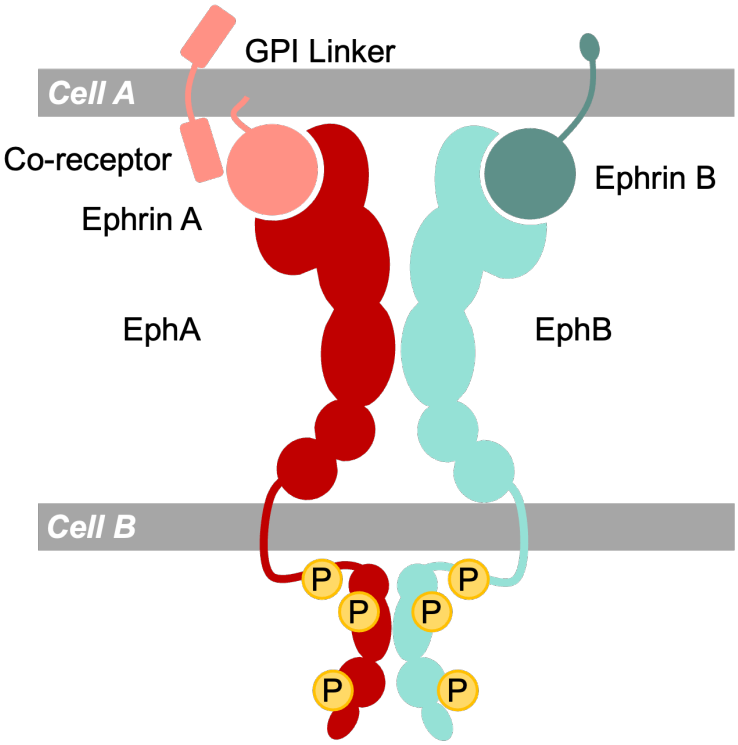

Figure 1. 11 Eph receptors form receptor-ligand complexes with ephrin ligands.

Eph-ephrin signalling requires cell-cell contact. Ephrin ligands bind to the ligand-binding domain of Eph receptors leading to higher-order clustering which permits activation of the intracellular tyrosine kinase domains by phosphorylation (yellow circles). EphA receptors are activated by ephrin A ligands preferentially, and EphB receptors by ephrin B ligands. Ephrin A ligands are tethered to the membrane by a GPI linker, possessing no cytosolic region for signal transduction. Instead, Ephrin A ligands rely on association of co-receptors. Ephrin B ligands contain a cytosolic domain which can permit signal transduction upon binding with Eph receptors.

1.4. Aims and Hypotheses.

Our understanding of the events following KrasG12D activation in the lung is incomplete. We know that activation of KrasG12D is sufficient and potent enough to drive disease in mice *in vivo* by 5 weeks post expression, and that progression is limited by endogenous expression of tumour suppressor genes. Our lab and others have demonstrated the power of cell competitive elimination of cells to shape the early tumour landscape in a conserved, predictable manner (Hogan et al. 2009; Porazinski et al. 2016; Sasaki et al. 2018; Hill et al. 2021; Shirai et al. 2022). However, whether competition shapes the lung epithelium in a cancer-relevant way has not yet been addressed. Therefore, my hypothesis was that EphA2-dependent cell competitive events between WT and KrasG12D mutant cells in the lung epithelium lead to the loss of most mutant cells from the tissue at early timepoints. The remaining cells that have evaded competitive elimination are sufficient to drive tumorigenesis.

I aimed to establish whether or not cell competitive elimination of KrasG12D mutant cells is conserved in the lung epithelium at expected timepoints. To do this I characterised the pattern of expression of KrasG12D mutant cells in lung epithelium and assessed cell competition phenotypes in an established model of lung cancer. To explore biological process in real time, I developed an e*x vivo* lung model which recapitulated these early stages in the alveolar lung. Finally, using this *ex vivo* system I investigated the role of lung repair pathways in response to oncogenic insult, potentially giving rise to the cell of origin for lung adenocarcinoma.

.

2 Methods and Materials

2.1 Experimental Animals

2.1.1 Animal husbandry

In this project, all experiments are performed using genetically modified murine models of human cancer. Animals were housed in conventional pathogen-free animal facilities and experiments were conducted in accordance with UK Home Office regulations (ASPA 1986 & EU Directive 2010) under the guidelines of Cardiff University Animal Welfare and Ethics Committee and under project licence granted to C Hogan (PP3616724). Animals were fed Standard Diet (Special Diet Service UK, expanded diet) and were given access to water *ad libitum*. Animals were maintained on a 12:12 hour light-dark schedule.

Experimental animals of at least 6 weeks old were selected based on their genotype for breeding either in trios of two females and one male, or pairs of one male and one female as required to maintain experimental stocks. At approximately 4 weeks of age, pups were weaned and separated according to their sex. At the time of weaning, ear biopsies were taken by animal technicians for identification and genotyping.

2.1.2 Genetic mouse models

This project makes use of two genetic mouse models: the *Kras*$^{LSL\text{-}G12D/+}$; *Rosa26*$^{LSL\text{-}tdRFP}$ (KrasG12D) mouse, and the *Kras*$^{LSL\text{-}G12D/+}$; *Rosa26*$^{LSL\text{-}tdRFP}$ *EphA2*$^{-/-}$ (EphA2$^{-/-}$) mouse. Cre recombinase delivered intranasally via Adenoviral Cre recombinase vector results in the cell infection, cre expression, and subsequent excision of LoxP flanked stop codons upstream of a Kras^{G12D} transgene, and a tandem-dimer red fluorescent protein (RFP) sequence, leading to expression of mutant Kras^{G12D} protein and an RFP reporter (Luche et al. 2007).

2.1.3 Breeding strategy

To remove the Pdx1 CreERT promoter from the mice, two females from the EphA2$^{-/-}$ strain were bred with a male wild-type C57B/6J mouse. Offspring from this litter were a mix of Pdx1 Cre negative and positive, with either wild-type (WT) or heterozygous (Het) expression of transgenes. Subsequent breeding of these litters with selected individuals from the EphA2$^{-/-}$ and KrasG12D colonies were used to generate Pdx1 Cre negative animals into the mouse colonies for lung experiments.

2.2 Genotyping

2.2.1 Ear biopsy

At time of weaning at approximately 4 weeks, ear biopsies were taken from mouse pups using a 2 mm ear punch (Harvard apparatus) for the purposes of individual and genotypic identification. Biopsies were stored at -20˚C until required.

2.2.2 DNA extraction

Ear biopsies were digested in 250 µl cell lysis buffer (VWR) containing 0.4 mg/ml Proteinase K (Roche) overnight at 37˚C with gentle agitation. Once cooled to room temperature (R.T.), protein precipitation solution was added, and samples centrifuged to remove debris at 16,000 x g for 15 minutes. DNA was precipitated into isopropanol (Thermofisher Scientific) before centrifuging once more and discarding the supernatant. DNA pellets were fully dried before being resuspended in 250 µl DNase and RNase free water (Ambion) and stored at 4˚C until required for PCR reaction.

Sample genotypes were then distinguished by polymerase chain reaction (PCR) using the primers described in Table 2.1. Master mixes were prepared according to manufacturer's protocols (PCR Biosystems). Reactions were carried out using Thermo Cycler T100 (BioRad) with standard lab protocol cycle times. Samples were loaded into 1.5% agarose gel and Images taken using GelDoc software (ImageLab) and genotypes were identified by size of PCR bands.

Table 2. 1 Primer Sequences for Genotyping PCR.

Due to proximity of Kras^{G12D} bands in heterozygous animals, the reaction is split into wild type (WT) and Mutant (Mut) and imaged separately.

Gene	Forward Primer (5'- 3')	Reverse Primer (5'- 3')	Product Size (bp)
Pdx1-Cre	CTGGACTACATCTTGAGTTGC	GGTGTACGGTCAGTAAATTTG	~500
Kras^{G12D}	WT: GTCGACAAGCTCATGCGGGTG	CCTTTACAAGCGCACGCAGACTGTAGA	WT ~ 500
	Mut: AGCTAGCCACCATGGCTTGAGTAAGTCTGCA		Mut ~600
EphA2^{tm1jrui}	TGTCACTTGCGAACAGTGCT	WT: CGCTATCACACTCAGCAGGA	WT ~ 400
		Mut: GTGGAGAGGCTTTTTGCTTC	Mut ~300
Rosa26^{tdRFP}	Forward 1: AAG GGA GCT GCA GTG GAG TA	AAGACCGCGAAGAGTTTGTCC	WT ~ 200
	Forward 2: TAAGCCTGCCCAGAAGACTCC		Hom ~300

2.3 Virus Preparation

2.3.1 T-REx^{TM}-239 cell culture

T-REx^{TM}-239 cell lines were gifted to us from the Parker lab at Cardiff University to produce concentrated virus from a commercially available Ad5-CMV-iCre recombinase virus (AdCre; Vector biolabs). Cells were defrosted by partially melting the frozen pellet by hand, then adding 1 mL of DMEM (10% FBS, pen/strep, 200 mM GlutaMAX) and plating into a CellBIND 25 cm^2 flask (Corning). Cells were allowed to settle for 30 minutes in an incubator, then media was exchanged for fresh DMEM overnight. The next day, cells were detached with 1 mL trypsin-EDTA (Sigma Aldrich) and added to a 175 cm^2 flask (Sarstedt) pre-coated with Poly-D-lysine for optimum attachment. For long term maintenance of cell stocks, 2 x 10^6 cells were first trypsinised, then centrifuged at 300 x g for 5 minutes and media removed. The cell pellet was resuspended in DMSO with 10% FBS and aliquoted into. 1 mL freezing tubes. Cells were slowly frozen in a Mr. Frosty (Corning) at -80˚C, before moving to liquid nitrogen for long term storage.

2.3.2 Preparing poly-D-lysine coated flasks

Poly-D-lysine was used to increase binding of T-Rex cells to culture flasks. First, poly-D-lysine (Gibco) was diluted to prepare a 50 µg/mL solution. For a 175 cm^2 flask, approximately 5 mL of matrix was used to distribute across the entire culture surface and left to dry at R.T. for 1 hour. Excess poly-D-lysine was removed from the flask and the surface rinsed three times with sterilised distilled water. Once rinsed, the flask was left open in a laminar hood for 2 hours to allow the coated surface to dry ready for culture.

2.3.3 Bulking up commercial virus

To bulk up the commercial virus, 6 x 10^6 T-Rex cells were seeded into 5 pre-coated 175 cm^2 flasks and maintained until they reached ~80% confluency. Virus was added to a multiplicity of infection (MOI) of 0.1. Cells were infected overnight then media changed for fresh DMEM. Media was changed when required until all cells were detached as a result of the cytopathic effect (CPE) – this took approximately 5 days post infection. Once full CPE had been observed, flasks were tapped to fully detach all cells. The supernatant was collected then pelleted at 300 x g for 5 minutes. Cells were resuspended in PBS to wash off media, and cells from all flasks combined.

Cells were pelleted once more, PBS removed, and pellet stored dry at -80˚C until caesium chloride purification.

2.3.4 Caesium chloride purification

Purification of AdCre was carried out with the help of Dr Andrew Robinson from the Parker lab. To begin, infected pellet was defrosted in a water bath and briefly centrifuged to collect all cells. The cell pellet was resuspended in 6 mL of PBS and an equal volume of tetrachloroethylene. Cells were lysed by vigorously shaking the solution by hand for around 30 seconds, ensuring all 3 layers were mixed. The cell solution was centrifuged at 13,000 x g and the top layer of supernatant removed to a 15 mL falcon.

Next, 2.5 mL of room temperature caesium chloride (CsCl; 1.4 g/mL in 100 mL 1X TD buffer; 10X table 2.2) was added to the ultracentrifuge tubes (Beckman Coulter; thin walled, ultra-clear) before an equal volume of 1.25 g/L CsCl was carefully layered on top. The virus solution was added carefully onto the CsCl layers, filling the ultracentrifuge to the top with PBS. Ultracentrifuge tubes were carefully balanced using a scale, then were centrifuged at 217,00 x g for 1.5 hours at R.T. After the first centrifugation, the virus layer will be observed as a band at the 2.5 mL mark in the tube (between the CsCl layers). Using a 21G 40 mm needle (BD) and a 5 mL syringe the virus layer was extracted by piercing the side of the ultracentrifuge tube. The extracted virus layer was next added carefully to 1.34 g/mL CsCl, then topped up with PBS and balanced as before. These tubes were centrifuged for 20 hours at 217,000 x g.

The next day, the virus layer was extracted in a minimal amount of volume, then added to a prepared membrane of a dialysis cassette (Slide-A-Lyzer, G2, Pierce 10K MWCO, VWR) in 2.5 L of dialysis buffer (1 mM Tris-HCl pH7.8, 135 mM NaCl, 1 mM $MgCl_2(H_2O)_6$, 10% glycerol) at 4˚C. After a couple of hours, dialysis cassettes were switched to fresh dialysis buffer and incubated overnight at 4˚C. The next day, the virus was removed from the cassettes and aliquoted into labelled 50 µL aliquots. To prevent loss of viral titre through repeated freeze-thaw cycles, viral aliquots were disposed of following two defrosts. Viral titre was confirmed by micro-BCA assay (ThermoFisher Scientific).

Table 2. 2 Reagents list for 10X TD buffer for CsCl purification. Stock was made to 1 L, buffered to pH 7.4 with 10N HCl.

Reagent	Supplier	Molecular Weight	Stock
NaCl	Sigma Aldrich	58.44	1.37 M
KCl	Sigma Aldrich	74.55	50 mM
$Na_2HPO_4*12H_2O$	Sigma Aldrich	358.14	7 mM
Tris-base	Sigma Aldrich	121.14	250 mM
10 N HCl	Sigma Aldrich	-	pH 7.4
H_2O	MilliQ	-	Σ 1 L

2.4 Experimental Induction of Animals

2.4.1 Induction and maintenance of Anaesthesia

Mice between the ages of 6-12 weeks were selected based on their genotype for experimental procedures and were pre-assessed for health according to weight change and suitability for experiment. They were then anaesthetised using inhaled isoflurane 3.5% until correction reflex was lost and breathing rate stabilised.
To induce expression of transgenes, mice were given 1 x 10^5, 1 x 10^7 or 1 x10^8 particle forming units (PFU) of Adenoviral cre recombinase (AdCre; Vector Biolabs) via intranasal instillation. Briefly, mice were gripped by the loose fur around their throat and were suspended an inch from the surface of a biosafety hood. Next, 50 µl total of virus re-suspended in PBS was pipetted dropwise onto a nasal opening until all solution had been inhaled. Once mice have adjusted to the instillation they were placed on their back on a heated pad until they recovered. Mice were then checked regularly for changes in health before they were culled at 2-, 5-, 7-, 35- and 70- days post induction.

2.5 Flow Cytometry

2.5.1 Isolation of epithelial cells from mouse lungs

Mice were culled by cervical dislocation, and thoracic cavity by making an incision along the ventral midline from the abdomen to the mandible. Skin and fascia were deflected, and front of ribcage removed. Next, the salivary glands were deflected and the infrahyoid musculature removed, revealing the cricoid cartilage of the trachea and the larynx. Lungs were briefly perfused with 5 mL ice cold PBS trans-cardially through the right ventricle of the heart. Lungs were removed intact with heart and trachea still attached, then were suspended in PBS on ice for transport from the animal facility.

Lungs were briefly rinsed in 70% ethanol, then in PBS to separate lobes (Fig.2.1a). In a small weighing boat on ice, lung lobes were minced into a homogenous paste using dissection scissors and placed into Eppendorf tubes on ice until digestion. Minced lungs were incubated at 37˚C for 2 hours in lung digestion buffer (RPMI media, 10% FBS, 150 U/mL Collagenase IA (Sigma-Aldrich), 0.25 mg/mL DNase I (Roche)) with frequent agitation and mechanical breakdown of larger pieces of tissue with a pipette. Digested samples were transferred to a 15 mL falcon tube through a 70 μM cell strainer (Miltenyl Biotech), then strainers were rinsed with 10 mL ice cold PBS (2% FBS). Samples were centrifuged at 300 x *g* for 5 minutes at 4˚C.once the supernatant was removed, the pellet was resuspended in 1 mL of Ammonium-Chloride Potassium (ACK) lysis buffer to lyse erythrocytes for 5 minutes at room temperature, then were centrifuged once more. The final pellet was resuspended in PBS (2% FBS) for counting and staining.

2.5.2 Cell staining for flow cytometry

Cell suspensions were counted, and 2 x 10^6 cells were taken for staining in 100 μL volumes. Cells were incubated with 0.2 mg/mL of each of the antibodies listed in Table 2.3 for 15 minutes, at room temperature and away from light. Cells were first rinsed with 2% FBS by centrifugation, then were resuspended in 500 μL of DAPI (0.1 ng/mL) in 2% FBS. Single cell suspensions were process using a BD LSRFortessa, with BD FACSDiva V. (BD Biosciences) software.

Table 2. 3 Antibodies used for flow cytometry.

Antibody	Product code	Supplier
FITC CD24	101805	Biolegend
APC CD45 (30-F11)	17-0451-83	eBioscience
PE-Cy7 CD31	25-0311082	eBioscience
BV711 EpCAM	118322	Biolegend

2.6 Precision Cut Lung Slices

2.6.1 Generating Precision cut lung slices

To generate viable precision-cut lung slices (PCLS), 2% low melting point agarose was prepared in HBSS (Gibco) (10 mM HEPES (Gibco); LMP agarose (VWR)), maintaining a temperature above 37˚C to prevent setting before instillation into the lung. Animals (WT and KrasG12D) were culled, and thoracic compartment exposed as previously described (2.5.1). The fascia surrounding the trachea was gently reflected and the trachea separated from the oesophagus by blunt dissection. Next, a 20G catheter needle was inserted into the trachea and fastened into place with a surgical knot. Once secured, the needle was retracted from the catheter and around 1 mL of molten LMP agarose was instilled slowly. Inflation was assumed to be optimal when the right accessory lobe presented a flick in the distal tip. Once satisfactory inflation had been achieved, ice was added to the thoracic cavity of the mouse for around 2 minutes until the LMP agarose set. The left lobe provides the greatest number of even slices so was gently removed from the mouse and placed in a 35 mm dish filled with LMP agarose on ice ensuring the lung remained afloat beneath the surface until solidified.

The vibratome used (LeicaV1200S) was set up accordingly, with the reservoir filled with HBSS (10 mM HEPES), and the ice bath topped up with ice frequently. The lung was cut out of the agarose disc and trimmed into a trapezoid as in the schematic below (yellow lines; Fig 2.2). The lung block was further trimmed so that the bottom end of the tissue was exposed and could be glued to the vibratome stage (Fig 2.2). The vibratome was set up to make 300 μM steps, oscillating through each cut at 0.1 mm/s. This ensured even cuts through the transverse plane of the lobe. Slices were collected from the middle two-thirds of the lung for size and shape consistency. Once a slice was cut, the lung was placed into ice cold high glucose DMEM (Gibco) supplemented with 10 mM GlutaMAX (Gibco) and 1% penicillin/ streptomycin (Sigma Aldrich) (hereby referred to as DMEM+) in a 24 well plate. Once all slices were cut, they were transferred to a fresh 24-well plate with pre-warmed DMEM+, then kept at 37˚C at 5% CO_2 for two hours. After 2 hours, the slices were washed twice with 1 mL DMEM+ in a fresh plate where they remain under sterile conditions for the remainder of their culture. 1 hour after this previous step the PCLS are ready for experimental procedures.

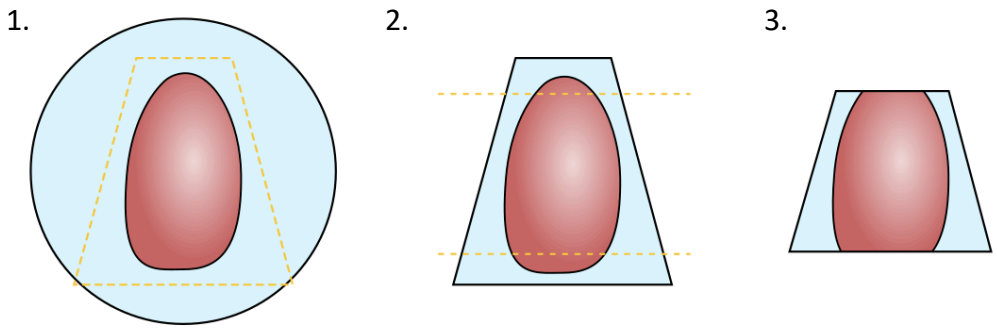

Figure 2. 1 Schematic for trimming lung lobe for vibratome slicing.

1) The left lung lobe is embedded in low melting-point agarose in a 35 mm culture dish. The lung is trimmed out of the agarose disc into a trapezoid to provide a better cutting surface. **2-3)** Cuts are made to expose the upper and lower parts of the tissue, providing a better surface to be superglued to the vibratome stage. Yellow dashes represent cutting lines for trimming tissue.

2.6.2 Infection of PCLS with Adenoviral cre recombinase

PCLS were first tested to see how much virus gives the optimum infection for stable expression of transgenes. After 2 hours post generation, they were taken to a level 2 pathogen suite for infection. To increase the opportunity for viral infection, media was removed from the wells to leave behind 200 µL. Here, viral concentrations were calculated so that 20 µL would deliver the desired titre in particle forming units. Slices were left to incubate for 1 hour in 200 µL DMEM+ and virus, then were topped up to 500 µL for overnight incubation. The next day, media containing virus was disposed of in Chemgene, and fresh DMEM+ added to the slices. From here they were cultured in a standard primary tissue culture suite and maintained in DMEM+ at 37˚C and 5% CO_2. Every other day, media was exchanged for fresh DMEM+ until end of experimental timepoints.

2.6.3 Assessing slice viability via MTT assay

To determine PCLS viability e*x vivo*, we utilised a standard MTT assay (Sigma Aldrich) according to manufacturer's instructions. MTT assay is a colorimetric assay that determines the metabolic activity of PCLS. This is due to the chemical reduction of yellow tetrazolium salt (3-(4,5- dimethylthiazol-2-yl)-2,5-diphenyltetrazolium bromide; MTT) to purple formazan crystals. These crystals are then solubilised in DMSO, then colorimetric changes quantified by CLARIOstar plate reader (BMG

Labtech) at 570 nm, the corrected at 690 nm. For this assay, similar sized PCLS were used to ensure optimal comparability between conditions.

2.6.4 PCLS KrasG12D-conditioned media transplantation

To interrogate the effect of KrasG12D activation on the surrounding tissue, conditioned media experiments were performed. At 5 DPI, culture media from WT or KrasG12D PCLS were taken from several wells of their respective plate and combined in a 15 mL tube. In lieu of a fresh media change, WT PCLS were incubated either with media taken from WT PCLS mixed 50:50 with fresh media (WT+CM(WT), or incubated with KrasG12D PCLS media, also mixed 50:50 with fresh media (WT+CM(KrasG12D). As a control, PCLS were included from WT or KrasG12D samples, and changed for fresh media as would be standard at 5 dpi (WT+F, KrasG12D+F). PCLS were cultured as standard until 7 dpi when they were fixed and processed for immunofluorescence. Conditioned media was not discarded to carry out dot blot analysis of inflammatory cytokines.

2.6.5 Mouse inflammatory cytokine dot blot array

To explore possible candidate signatures that were driving remodelling response, conditioned media was run on an inflammatory cytokine array blot (Abcam; ab133999) according to manufacturer's protocols. In brief, antibody array membranes were blocked for 2 hours at room temperature in 2 mL of the provided block buffer. 1mL was removed and replaced with 1 mL of the conditioned media from 2.8.5, then incubated overnight at 4˚C with agitation. Next, membranes were washed with a large volume of wash buffer I at R.T. for 45 minutes, followed by 2 more standard washes of 5 minutes at R.T, then 2 washed in wash buffer II for 5 minutes.

Next, membranes were incubated with 1 mL of 1X biotin-conjugated Anti-cytokine for 2 hours at RT, before washing 3 x 5 minutes with wash buffer I, and 2 x 5 minutes with wash buffer II. Membranes were then incubated with 2 mL HRP-conjugated streptavidin for 2 hours at R.T, before washing as before with wash buffers I and II. Membranes were transferred to a plastic sheet printed side up and incubated with 250 µL of chemiluminescence detection buffers provided for 2 minutes. Another sheet of plastic was used to sandwich the membranes before imaging with the GelDoc chemiluminescent detection system. In the first instance, 20 images were taken between 1 and 10 seconds, and an image was selected based on the most saturated sample on the blot.

Images were exported in FIJI for analysis by densitometry. Here, a circle ROI measurement was taken of the largest dot on the image. This was then used to measure integrated density of all targets on the array (table 2.4), blanks, and positive controls. Where no dot was visible, measurement was taken based on approximate spacing between previous and next sample to ensure all targets were accounted for. Data was normalised to mean positive control spots as reference targets for each blot, which was further normalised to positive control from WT+F array.

Table 2. 4 Cytokine targets from array blot.

Targets are printed in pairs across two rows. POS = positive control target, NEG = negative control, BLANK = no printing control

	A	B	C	D	E	F	G	H	I	J	K	L
1	POS	POS	NEG	NEG	BLANK	BLC	CD30 L	Eotaxin	Eotaxin 2	Fas Ligand	Fractalkine	GCSF
2	POS	POS	NEG	NEG	BLANK	BLC	CD30 L	Eotaxin	Eotaxin 2	Fas Ligand	Fractalkine	GCSF
3	GM-CSF	IFNG	IL-1A	IL-1B	IL-2	IL-3	IL-4	IL-6	IL-9	IL-10	IL-12 p40/p70	IL-12 p70
4	GM-CSF	IFNG	IL-1A	IL-1B	IL-2	IL-3	IL-4	IL-6	IL-9	IL-10	IL-12 p40/p70	IL-12 p70
5	IL-13	IL-17A	I-TAC	KC	Leptin	LIX	Lymphotactin	MCP-1	MCSF	MIG	MIP-1a	MIP-1g
6	IL-13	IL-17A	I-TAC	KC	Leptin	LIX	Lymphotactin	MCP-1	MCSF	MIG	MIP-1a	MIP-1g
7	RANTES	SDF-1a	TCA-3	TECK	TIMP-1	TIMP-2	TNFa	TNF RI	TNF RII	BLANK	POS	POS
8	RANTES	SDF-1a	TCA-3	TECK	TIMP-1	TIMP-2	TNFa	TNF RI	TNF RII	BLANK	POS	POS

2.7 Tissue Processing

2.7.1 Mouse dissection

Mice were sacrificed by a Schedule 1 approved method of killing i.e., cervical dislocation and were swiftly dissected following confirmation of death by permanent cessation of circulation. Mice were sprayed with 70% ethanol before an incision was made along the ventral midline, from the genital area to the base of the throat. The skin covering the ribcage was cut and parted, and the front of the ribcage removed.

To fix the lungs, the trachea was exposed and pinched off with forceps. Approximately 2 ml of 4% Paraformaldehyde (PFA; Sigma) was injected into the trachea to inflate the 5 lobes of the lung. Once satisfactory inflation was achieved, whole lungs were submerged in 4% PFA for 24 hours at 4˚C and were then washed and kept in 1xPBS.

2.7.2 Tissue embedding

Following fixation of the lungs, tissues were rinsed thoroughly with 1X PBS before the 5 lobes were separated for different tissue processing procedures.

2.7.3 Sucrose /OCT

For the main purpose of multi-stain immunofluorescence, right superior, right middle, and right inferior lobes were selected. Lobes were first cryoprotected by incubation at 4˚C in 30% Sucrose/ PBS for 24 hours, then gradually embedded in 30% sucrose OCT (optimal cutting temperature compound; 50:50), and finally 100% OCT. Once the tissues had gone through this sequence, they were transferred to Peel-A-Way™ embedding moulds (Merck) in OCT and stored at -80˚C until use.

2.7.4 Formalin fixed paraffin embedded (FFPE)

Left lung samples were embedded in paraffin wax by Cardiff University Bioimaging Hub according to standard procedures. Tissue blocks were sectioned to produce 6 µm sections, and haematoxylin and eosin staining was carried out to order by the bioimaging hub.

2.7.5 Preparing gelatin coated slides

Standard glass slides were coated in gelatin solution (5 g/L) to improve attachment of tissue sections. Gelatin powder was dissolved in 1L of heated, deionised water, ensuring that the temperature did not exceed 45˚C. Once fully dissolved, the gelatin solution was filtered with a 0.22 µm filter (Sartorius) and stored at 2-8˚C until needed. Before coating slides, the gelatin solution was gently heated to 37˚C and filtered again. Microscopy slides were dipped 3 to 5 times until completely coated, then were left to dry at R.T. for 48 hours.

2.7.6 Preparing Mowiol-488

Mowiol was used as a mounting agent for imaging. To prepare Mowiol, 12 g glycerol (Sigma) and 4.8 g Mowiol 4-88 (Calbiochem) were dissolved in 12 mL water and mixed overnight at R.T. Next, 24 mL of 0.2M Tris (pH 8.5) was added and the solution was heated to 50˚C with regular mixing until everything had dissolved. Solution was centrifuged for 15 minutes at 5000 x *g* to clarify before aliquoting. Aliquots were and protected from light and stored at -20˚C.

2.7.7 Cryosectioning

OCT embedded tissues were cut into sections of 10 µm thick using a Leica CM1860 UV cryostat. Blocks were first trimmed by taking thick sections until sufficient tissue was exposed from the block. For microscopy, 10 µM sections were cut and transferred either to gelatin-coated microscope slides, or later to uncoated Superfrost™ Plus Adhesion Slides (Thermofisher Scientific). The latter product was used instead of gelatin coated slides as a result of trial and error to find the best microscope slide to prevent losing sections. Once sectioned, slides were either used immediately, or were covered in aluminium foil for use the next day.

2.8 Immunohistochemistry

2.8.1 Immunofluorescence staining

Tissue sections were cut fresh prior to processing. Once fully dry, tissue was outlined using a hydrophobic barrier PAP pen (Vector Laboratories) before being washed in PBST solution (0.03% TritonX100, Sigma Aldrich) for 5 minutes. Tissue was permeabilised for 20 minutes in a solution of 0.5% PBST before being washed three times for 5 minutes in PBST. Tissue slices were blocked in PBST containing 10% foetal bovine serum (FBS) for 60 minutes at R.T. Samples were incubated in primary antibody (diluted in blocking solution and added to samples at concentrations referenced in table 2.5) overnight at 4˚C. The next day, samples were washed three times for 10 minutes in PBST. Samples were incubated with secondary antibodies (Table 2-5), and Phalloidin (1:500) for 1 hour at R.T., protected from light. Tissues were then washed and incubated with Hoechst (1:2000) for 15 minutes at R.T. Tissues were washed thoroughly with PBS before mounting a glass cover slide with Mowiol. Mounted slides were left to dry at R.T. overnight, or for 1-2 days at 4˚C. Antibodies were validated either from prior experience in the lab, or by comparison with no primary stained controls upon first usage, or with tissues where known antigens are expressed (positive control tissues).

2.8.2 Immunohistochemistry from paraffin embedded tissue

Paraffin sections were first de-waxed by submerging in 2 rounds of xylene for 1 minute each. Sections were then rehydrated by sequential decreasing ethanol sections (100%, 100%, 95%, 75%) for 30 seconds each. According to the antibody being stained, the appropriate antigen retrieval solution was pre-heated either in a pressure cooker or heat pad. For anti- Ki67 staining, sections were incubated for 5 minutes at pressure in Citrate buffer (10 mM, pH 6.0). Once cooled down, slides were washed in TBS-T (0.1% tween) 3 x 5 minutes. To remove endogenous peroxidases, sections were encircled with a PAP pen hydrophobic ring and were incubated in 3% hydrogen peroxide for 20 minutes at R.T, followed by 3 more washes in TBS-T. Tissues were blocked in 5% normal goat serum (NGS; Vector Laboratories) for 1 hour at R.T., followed by incubation with anti-Ki67 (ab16667, Table 2.5) overnight at 4˚C. For RFP IHC, samples were heated in fresh proteinase K solution (20 µg/ mL in TBS/T) and incubated in 1:500 anti-RFP (Rockland; Table 2.5). For anti-Krt8 (TROMA-I, DSHB), antigen retrieval was performed with citrate buffer for 20 minutes

in a heated pressure cooker. Anti-RFP and Anti-Krt8 IHC was carried out by Daisy Moyers, a Cardiff University undergraduate project student in the Hogan lab.

After primary incubation, slides were washed in 3 x 5 minutes, then incubated in secondary goat anti-rabbit HRP for 1 hour at R.T. Slides were washed three more times for 5 minutes. To expose protein in sections, DAB substrate kit (SK-4100) was prepared by adding reagents A: B:C to 5 mL of dH_2O in the ratio of 2 drops: 4 drops: 2 drops. Within 10 minutes of being prepared, slides were incubated in DAB for 2 minutes. Once satisfactory signal was achieved, DAB was neutralised in dH_2O, tissue counterstained for 30 seconds in haematoxylin, then rinsed thoroughly under running water for 5 minutes. Slides were dehydrated in gradually increasing ethanol gradients (75%, 95%, 100%, 100%) before another 2 rounds of dewaxing in fresh Xylene for 1 minute each. Sections were mounted with DPX and allowed to dry overnight.

2.8.3 Processing PCLS for immunofluorescence

At the end of experimental timepoint, tissues were washed briefly in PBS, then fixed in 4% paraformaldehyde for 30 minutes under a tissue culture hood. Following this, experiments were performed in non-sterile conditions. Next, PCLS were washed 3 x 10 minutes with PBS then permeabilised for 10 minutes in 0.5% Triton X100. PCLS were washed 3 x 10 minutes with 0.03% Triton X-100 prior to blocking with 10% FBS for 1 hour. Primary antibodies (Table 2.5) were incubated in 10% FBS overnight at 4˚C. The next day, samples were washed 3 x 10 minutes in 0.03% Triton X-100 then incubated with secondary antibodies for 1 hour at room temperature. Slices were mounted into glass-bottom 6-well plates, fitting technical replicates into the same well and using a small volume of Mowiol-488 to secure an 18 mm round glass cover slip over the slices. Plates were kept covered in foil and kept at 4˚C until imaging

2.8.4 Immunolabelling PCLS for live cell imaging

For live imaging of PCLS, slices were cultured in phenol-free DMEM (Gibco). Prior to imaging, PCLS were incubated for 1 hour at 37˚C in 1:500 APC CD45 (eBiosciences). Afterwards, PCLS were briefly rinsed in HBSS before securing to a glass bottom 6-well plate (MatTek) with 2% LMP. This was achieved by floating the slice into place with PBS, which was aspirated and replaced with agarose solution. As much agarose as possible was removed whilst still leaving enough to cover the slices. PCLS were gently pressed to the glass surface and placed on ice to solidify the agarose. 6 well plates were then topped off with standard culture media and samples transported to the live imaging microscope securely.

2.9 Microscopy

2.9.1 Immunofluorescence Microscopy

Image acquisition of immunofluorescence staining of tissue sections was carried out on a Zeiss LSM710 confocal microscope, using Zen Black software. Images were generally acquired using a 40X oil immersion objective lens, capturing 8-bit images with a frame size of 512 x 512 pixels with a frame averaging of 2. To capture airways for RFP analysis, tile scanning via convex hull sampling was carried out with a tile overlap of 10% for later stitching. To ensure enough cells were imaged, at least 10 airways were imaged, including bifurcating airways as individual airways. To sample as much of the tissue as possible for quantification, I made use of the positions function to sample at least 10 regions of interest per tissue section and aimed to image at least 3 sections per animal. Sampling via positions was carried out for analysis of cells in the distal lung in 2D sections, and similarly in PCLS stained for SPC, Ki67, Krt8, and RFP proteins. For PCLS samples, volumetric data was attained by imaging 2 x 2 tile scans with additional z-stack scanning for up to 40 µm depth. Where this was carried out, images are presented as maximum intensity projections. Z-scanning intervals were set to the value of 1 AU. After acquisition, tile scans were stitched using Zen Black software, and all images exported as .czi files for analysis.

For whole tissue scanning by immunofluorescence, the Olympus slide Scanner VS200 40X objective was used. Samples were located and scanned first in brightfield, so that scan area and focus points could be determined. Exposure was manually set for each slide using the DAPI and Cy5 and focus determined automatically.

2.9.2 Brightfield Microscopy

To image immunohistochemistry and H&E slides, I used the Olympus Slide Scanner VS200 20X objective for H&E, and 40X for immunolabelled slides. Slides were loaded into the slide tray and overview slides acquired at 4X magnification. Using these, scan areas were outlined to reduce scanning time and focus planes checked to cover the sample. Samples were scanned and exported as .vsi files.

2.9.3 Live-cell imaging

Live cell imaging was performed using a Zeiss Cell discoverer 7 with LSM900 series confocal scanhead. Prior to imaging, the CD7 was heated to 37˚C and CO_2 set to 5%

for culture conditions. PCLS ROI were detected with a 20X objective magnification, with a 2X additional magnification. Single tile 16-bit images were taken of selected ROI across PCLS samples. To encapsulate 3D aspects of the tissue, z stacks were defined as 10 sections above, and 10 sections below a region of interest's centre point. PCLS were imaged every 30 minutes for 12 hours. Timelapse movies were then compiled in FIJI and analysed in Imaris.

2.10 Image analysis

2.10.1 FIJI is Just Image J

Generally, file formats used in FIJI were .czi files directly imported from acquisition. Image channels were separated, then merged into composite files for observation of all channels of interest. Where presented as maximum intensity projections (MIPs), quantification was performed on optical sections, and projection was for presentation only.

Counting: counting was carried out on individual fields of view (512 px x 512 px) with the counting tool. First the Hoechst channel was counted for total number of cells, then this was overlayed with the next stain of interest. Where a stain of interest does not overlap or associate with a nucleus, it was not counted in the sample.

Integrated density: Positively stained cells were outlined in a freeform ROI and integrated density measured. Background intensity readings were not taken due to absence of background staining.

Analyse Particles: To generate cell masks and generate morphology data, I used the analyse particle function. First, RFP images were thresholded and made binary. Next, minimum area of detected particles was limited to 25 μm^2 to eliminate debris detection, and overlay mask was checked (Fig 2.4). From measurements, area, shape descriptors, and perimeter were selected.

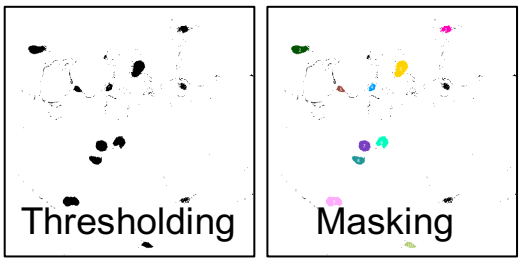

Figure 2. 2 Process of Analyse particles of alveolar RFP images.

Using Analyse particle's function, cells were selected for based on an area ≥25 μm^2. Overlay masks were generated to check number and selectivity of thresholding, then particles were measured for area, perimeter, roundness, and circularity.

2.10.2 QuPath

QuPath was used to view and handle large .vsi files generated from the Olympus slide scanner. To assist in quantifying positive cell populations, a grid showing squares that were 250 μm x 250 μm was overlaid on samples and a random number generator tool used to select 40 squares from the image. Cell detection algorithm in QuPath could detect haematoxylin-stained nuclei with minor adjustments to intensity parameters: threshold (0.15) and cell expansion (3 μm). This was validated by comparing manual and automated counts. For 35-dpi stratification of Krt8 and RFP imaging, ROI across the tissue were taken so that at least 10 regions of each category were taken. Serial section staining allowed similar regions to be sampled in both RFP and Krt8 sections. Positive cell detection parameters were established by Daisy Moyers (final year project student):

Table 2. 5 Parameters for positive cell detection in QuPath.

For RFP, cell detection was performed on IHC-DAB tissues, and for Krt8, immunofluorescence staining with Hoechst (DAPI) and Krt8 at 647 nm (Cy5). All other image analysis parameters were kept standard. Nuclei were detected using either Haematoxylin OD or DAPI OD.

	RFP	**Krt8**
Background Radius (µm)	5	5
Minimum Area (µm^2)	15	15
Maximum Area (µm^2)	55	55
Cell Expansion (µm)	3	3
Score department	Nucleus: DAB OD Mean)	Cell: Cy5 Mean
Threshold 1+	0.22	350

2.10.3 Imaris

Imaris (v9 Bitplane) was utilised to quantify 3D images generated from PCLS experiments. As with FIJI, .czi files were used as a standard file format. For quantification of RFP, Krt8 and Phalloidin, surfaces were generated with a surface smoothing factor of 1.4 µm, and background subtraction used on RFP and Krt8 surfaces for maximum size of 10 µM. Obvious cellular debris and fluorophore aggregates were filtered out by adjusting surface based on voxel size. Imaris Vantage was used to export cell morphological readouts of volume, sphericity, and area in excel for analysis.

To track cells in live imaging experiments, CD45 positive cells were detected as spots, then cell track sequences manually checked for consistency and fragmentation. Bright spots that could be misconstrued as immobile cells were removed, then displacement, velocity and track length exported from vantage for analysis.

Table 2. 6 List of antibodies and fluorescent probes used for Immunofluorescence.

Antibody Name	Dilution	Species	Supplier	Catalogue Number
Anti-E-Cadherin	1:100	Mouse	BD	610182
Anti-CC10	1:100	Mouse	Santa Cruz Biotechnologies	Sc-365992
Anti-RFP	1:500	Rabbit	Rockland	600-401-379
Anti-RFP	1:50	Goat	Rockland	200-101-379s
Anti-RFP	1:250	Rat	ProteinTech	SF8
Anti-Pro Surfactant Protein C	1:200	Rabbit	Abcam	Ab90716
Anti-F4/80	1:50	Rat	BD Pharmingen	565409
Phalloidin-647	1:500	-	Thermofisher	65906
Anti-Ki67	1:500	Rabbit	Abcam	Ab16667
Anti-Krt8	1:50	Rat	DSHB	TROMA I
APC CD45 (30-F11)	1:500	-	eBioscience	17-0451-83

Table 2. 7 Secondary Antibodies.

Antibody	Dilution	Fluorophore	Supplier	Catalogue Number
Donkey anti-Rat	1:1000	Alexa Fluor™ 488 nm	Thermofisher	A21208
Donkey anti-Rabbit	1:1000	Alexa Fluor™ 488 nm	Thermofisher	A21206
Goat anti-Rat	1:1000	Alexa Fluor™ 568 nm	Thermofisher	A11077
Goat anti-Rabbit	1:1000	Alexa Fluor™ 568 nm	Thermofisher	A11011
Donkey anti-Goat	1:1000	Alexa Fluor™ 568 nm	Thermofisher	A21447
Goat anti-Rabbit	1:1000	Alexa Fluor™ 647 nm	Thermofisher	A21244
Goat anti-Rat	1:1000	Alexa Fluor™ 647 nm	Thermofisher	A21247

2.11 Molecular Biology

2.11.1 RNA extraction

Mice were sacrificed via cervical dislocation, lungs briefly dissected and separated into left lung and right lung constituent lobes. lungs were placed in labelled Eppendorf tubes on dry ice for preservation of RNA quality and were stored at -80ºC until processing.

To extract total RNA from mouse lungs 10-20 mg tissue was placed into 2 mL tubes containing MP Biomedicals Lysing Matrix D Homogenisation beads (Fisher Scientific). 1 mL of Trizol reagent was added to each tube before samples were homogenised using an MP Biomedicals Fastprep-24 (6 m/s, 40 s). When samples were totally homogenised, 200 µL chloroform (Sigma) was added to the tube and mixed regularly for 15 minutes at room temperature.

After 15 minutes had elapsed, homogenates were centrifuged for 15 minutes at 13,000 RPM in a cold centrifuge. After centrifugation, the aqueous phase of the supernatant was transferred to a clean RNase free Eppendorf tube, and RNA precipitated by adding 500 µl to the sample for 5 minutes at R.T. RNA was pelleted by centrifuging for 10 minutes at 13,000 RPM. After discarding the supernatant, the pellet was briefly resuspended in 1 ml of 75% ethanol before being centrifuged for a final time, then the supernatant discarded and pellet air dried. Once completely dry, the pellet was resuspended in fresh RNase free water and concentration and quality assessed by Nanodrop. RNA samples were then cleaned up using an RNAeasy Mini kit (Qiagen) according to the manufacturer's protocols and were then stored at -80ºC until required for cDNA synthesis.

2.11.2 Genomic DNA extraction

Genomic DNA (gDNA) was extracted for qPCR validation of transgene recombination using a commercial QIAmp DNA Micro Kit. Briefly, around ten sections of frozen tissue around 30 µm thick were added to a chilled tube. OCT was washed away with 1 ml PBS followed by 5 minutes of centrifugation at 10,000 RPM at R.T. After discarding supernatant, 180 µL of buffer ATL was added to each sample followed by 20 µl of proteinase K and brief mixing by pulse vortexing. Samples were incubated overnight at 56˚C on an orbital incubator.

The following day, 200 µL of buffer AL was added and mixed before 200 µL of ice cold 96% ethanol was added to each tube for incubation at R.T for 5 minutes. Lysates were then transferred to supplied collection tubes for washing with 500 µl

AW1, spinning, then 500 µL AW2. Tubes were centrifuged for 1 minute at 6000 x g after each wash before discarding previous buffer and adding the spin column to a fresh collecting tube. After discarding the AW2 flowthrough, columns were completely dried by centrifuging at full speed for 3 minutes. DNA was eluted into a clean RNase free tube in 30 µL nuclease free water.

2.11.3 SDS-PAGE

Proteins were extracted from precision cut lung slices using Lysing Matrix D in RIPA buffer (ThermoFisher Scientific), supplemented with protease and phosphatase inhibitors (Roche). Tissue was incubated for 10 minutes on ice in RIPA buffer prior to lysis with Lysing Matrix D (MP Biomedicals, as previous). Lysed samples were then centrifuged at 15,000 x g to pellet cellular debris for 20 minutes at 4˚C. Supernatant was taken and frozen until the protein level could be quantified by BCA assay.

To determine protein concentration, protein lysates were defrosted on ice, then a 1:10 dilution prepared from each. Next, Pierce™ Bicinchoninic acid (BCA) assay was utilised according to manufacturer's protocol for microplate procedure. Briefly, working reagent of BCA was prepared by mixing reagent A: B in the ratio of 50:1, where 1 sample = 200 µL. To a 96 well microplate, 25 µL of bovine serum albumin (BSA) standards (table 2.7) and samples were plated in duplicate, mixed briefly on plate shaker, then incubated for 30 minutes at 37˚C. Plate absorbance was measured near 562 nm using a CLARIOstar plate reader (BMG Labtech).

Table 2. 8 Label and concentration of Bovine Serum Albumin (BSA) standards for Pierce BCA assay.

BSA Vial	Concentration (µg/ mL)
A	2000
B	1500
C	1000
D	750
E	500
F	250
G	125
H	25

I	0 = BLANK

BSA standard values were plotted on the equation:

$$y = mx + C$$

Subsequently rearranged to determine protein concentrations using:

$$\mu g \,/\, \mu L = \frac{(y - c/m)}{100}$$

This equation substitutes the values *m* and *y* from the standard curve, then division by 100 accounts for conversion of units from µg/mL to µg/µL, then subsequent multiplication by 10 to remove the dilution factor. 10 µg of protein were loaded into 12% polyacrylamide gels and resolved at 140 V until satisfactory migration was observed of the loading gel streak.

Gels were removed from the PAGE tank, then washed in transfer buffer (Table 2.9; Tris-NaCl, 20% Methanol) for at least 10 minutes. Simultaneously, polyvinylidene difluoride (PVDF) membranes were activated by submerging in 100% methanol, then added to TBS-T. Transfer cassettes were assembled as standard. Assembled cassettes were places into a transfer tank, filled with transfer buffer, then run at 100 V for 1 hour, on a magnetic stirrer, on an ice tray. Once transfer was complete, cassettes were dis-assembled, and membranes were washed 3 x 5 min in 0.5% TBS-Tween (TBS-T). Next, membranes were blocked in 5% milk (in TBS-T) for 1 hour at R.T, then antibodies added overnight at 4˚C. Membranes were immunolabelled with anti-TROMA I (Krt8; DSHB Hybridoma Bank, 1:100) and GAPDH (Millipore, 1:4000). The next day, membranes were washed 3 x 5 minutes in TBS-T before incubation in secondary antibodies for 1 hour at R.T. (anti-Rat HRP, 1:5000, Anti-mouse HRP, 1:1000).

After antibody incubation, membranes were thoroughly rinsed in TBS-T (3 x 10 minutes). Membranes were incubated in ECL to expose proteins for 5 minutes at R.T. Blots were then sandwiched between plastic sheets and excess ECL removed from the blots. On a ChemiDoc imaging system, a colorimetric image was first taken to visual the membranes, then chemiluminescent images were taken between 1 and 20 seconds. Images were selected that showed the darkest band to be slightly underexposed for later densitometry analysis. Integrated density was used to achieve protein expression quantification for Western blot. In Western blot, rectangular regions of interest were drawn over single lanes, for each sample on the blot, and profiles plotted numerical outputs. Samples were normalised first to the highest housekeeping protein value, then to their respective control sample. In immunofluorescence quantifications.

Table 2. 9 SDS-Page resolving and stacking gel recipe.

Reagents in grey, were added only prior to use as they initiate gel polymerisation. After addition, tubes with gel solutions were briefly inverted to mix and pipetted into casting system.

12% Resolving Gel	
H_2O	2.5 mL
1.5 M Tris/Cl	2.5 mL
50% Glycerol	2 mL
40% Bis-acrylamide	3 mL
10% SDS	100 µL
TEMED	15 µL
10% APS	30 µL

Stacking Gel	
H_2O	3.2 mL
0.5 M Tris/Cl	1.25 mL
40% Bis-acrylamide	500 µL
10% SDS	50 µL
TEMED	5 µL
10% APS	50 µL

Table 2. 10 SDS PAGE buffers.

A

10 X Tris Glycine	
Reagent	Amount
Trizma Base	30.3 g
Glycine	144 g
H_2O	Σ1 L
pH to 8.3 with HCL	

B

1X Tris-glycine Running buffer	
Reagent	Amount
10% SDS	10 mL
10X Tris glycine	100 mL
H_2O	Σ1 L

C

20 X Tris Base	
Reagent	Amount
Trizma Base	24.23 g
NaCl	175.32 g
H_2O	Σ1 L
pH to 8.0 with HCL	

D

Transfer buffer (20%)	
Reagent	Amount
Methanol	200mL
20X Tris Base	50 mL
H_2O	Σ1 L

E

0.5 M Tris (pH6.8)	
Reagent	Amount
Trizma Base	30.29 g
H_2O	Σ 500 mL
pH with HCL	

F

1.5 M Tris (pH8.8)	
Reagent	Amount
Trizma Base	90.85 g
H_2O	Σ 500 mL
pH with HCL	

2.12 Realtime quantitative PCR

2.12.1 Primer Design and validation

To analyse custom gene expression panels, primers were designed and validated from new. Primer BLAST (Ye et al. 2012)was used to generate primers of 20-22 bp length, with a GC content of between 40-60%. Primers had to span exon-exon junctions and have a T_M difference of less than 2˚C. primers were next ordered as DNA oligos (Sigma Aldrich) and resuspended to a stock concentration of 10 µM. Primers were validated by carrying out standard curve assays (1:10 or 1:5) with melt curve analysis. Where standard curves had an efficiency between 90-110%, a unified melt curve, and an R^2 value of >0.99, primers were considered robust and safe to use. Generally, primers were used between 100 to 200 nM in final qPCR reactions.

2.12.2 cDNA synthesis

To generate complementary DNA from extracted RNA, ReadyScript cDNA Synthesis Mix was used (Sigma Aldrich; RDRT-100RXN). In this simple reaction, 100 ng of RNA was added to a 20 µL reaction volume (Table 2.8). cDNA was synthesised by using a thermocycler for minutes at 25˚C, 30 minutes at 42˚C, then finally minutes at 85˚C. Fresh cDNA was produced for each panel and stored at -20˚C prior to use.

2.12.3 qPCR

Reactions for qPCR were set up in 10 µL volumes in MicroAMP Optical 384 well plates (Table 2.9.; Applied Biosystems) in the concentrations described in table 2.8). Gene targets were pipetted in triplicate for at least 4 mice per genotype. The best housekeeping genes were determined using RefFinder (Xie et al. 2012). Briefly, Raw C_t values for the 6 housekeeping genes ACTB, GAPDH, HPRT1, HMBS, GUSB, and TBP (fig 2.3a) were inputted into the RefFinder tool. From this, three formats of identifying best reference genes were calculated: NormFinder (Andersen et al. 2004)(fig 2.3b), GeNorm (Vandesompele et al. 2002)(fig 2.3c), BestKeeper (Pfaffl et al. 2004)(fig 2.3d). In turn, RefFinder provides an analysis of the most stable genes analysed and recommends two for use as normalisation genes (fig 2.3e). In subsequent qPCR experiments, data was normalised to GAPDH and HPRT1.

Data was analysed using the $2^{-\Delta Ct}$ method which reveals relative quantity of transcript found in samples as opposed to $\Delta\Delta C_t$ which reveals fold changes observed. For this method, geometric mean of GAPDH and HPRT1 were subtracted from average C_t values of target genes (ΔC_t). To remove the CT value from fold to relative quantity, $2^{-(\Delta Ct)}$ was calculated.

Table 2. 11 Primers used to screen EphA family members.

Genes were either designed personally, already existed in the lab, or were borrowed from Lee Parry's lab, designed by Non Williams.

Gene Name	Forward (5'-3')	Reverse (5'-3')	Product size
EphA1	GAACGCACCACCAATGTCG	CTTCACCAAACTCCCCTTCTCC	166
EphA2	CTATGGCAAAGGGTGGGACC	AGCTGTTACAGTCTCGCACC	182
EphA2 (-/-)	GGACTGCCAGCGTCAGTATT	CTGTTGGCATCCCCCTTCTT	160
Efna1	TGCTGATTCGAGAGGTTCCG	CATCTGCCACAGAGTCGTCC	106
Efna4	GCTGGGCTTTGAGTTCTTGC	CATGTGATGACCCGCTCTCC	125
GAPDH	CATGGCCTTCCGTGTTCCTA	CTTCACCACCTTCTTGATGTCATC	100
HPRT1	TGGATACAGGCCAGACTTTGTT	CAGATTCAACTTGCGCTCATC	163
HMBS	GATGGGCAACTGTACCTGACTG	CTGGGCTCCTCTTGGAATG	168
GUSB	CCGATTATCCAGAGCGAGTATG	CTCAGCGGTGACTGGTTCG	197
ACTB	GATGTATGAAGGCTTTGGTC	TGTGCACTTTTATTGGTCTC	96
TBP	CAAACCCAGATTGTTCTCCTT	ATGTGGTCTTCCTGAATCCCT	131

Table 2. 12 Reaction mixes for cDNA synthesis.

Reagent	Amount for 1 RXN
ReadyScript	4 µL
RNA	100 ng
DNase RNase free H_2O	Σ20 µL

Table 2. 13 Reaction mixes for a single qPCR reaction. Reaction mixes were scaled by the number of samples in triplicate.

Reagent	Volume for 1 RXN (µL)
2X SyGreen Mix Lo-ROX	5
10 nM Forward Primer	0.1
10 nM Reverse Primer	0.1
cDNA	1
DNase RNase free H_2O	3.8

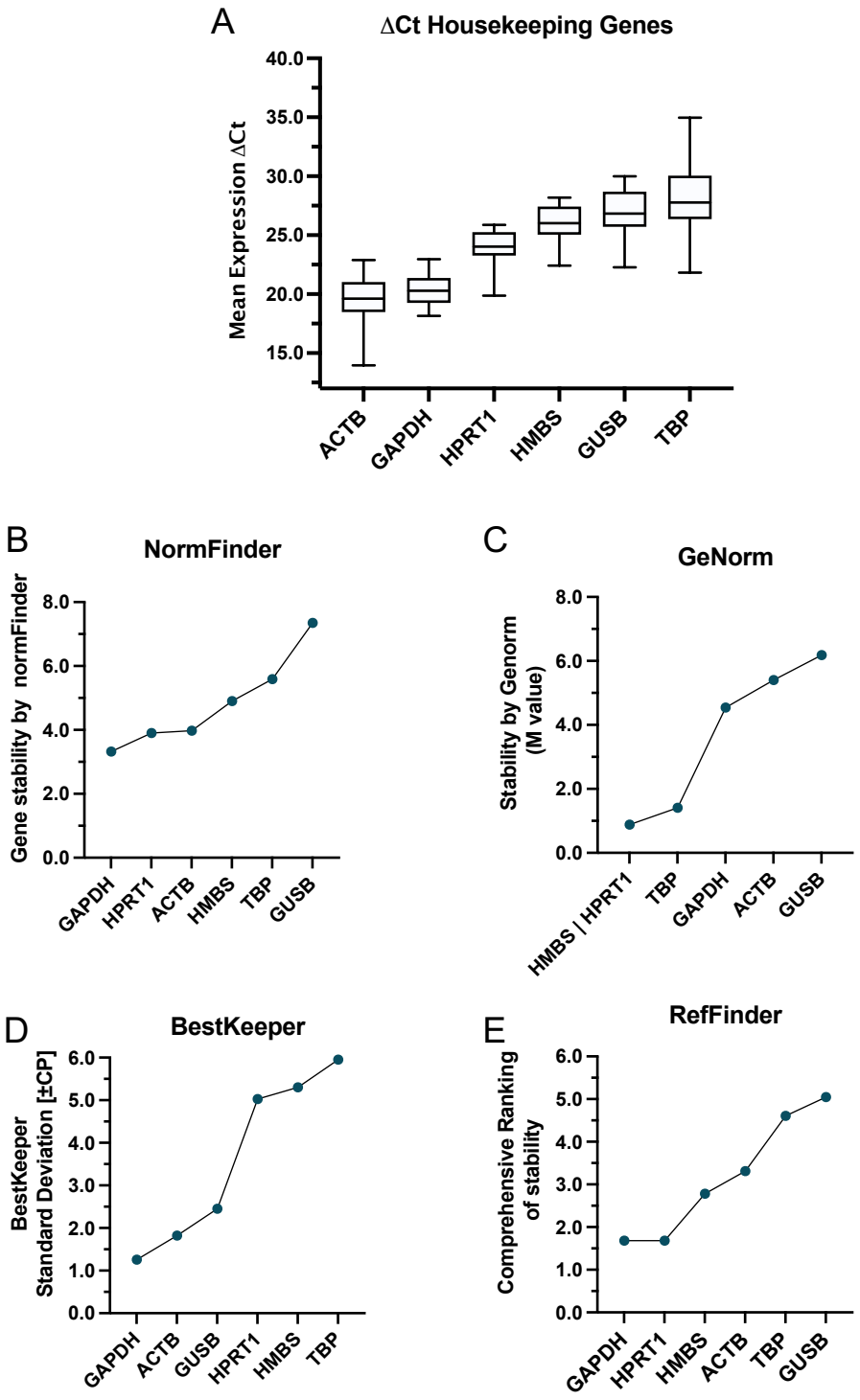

Figure 2. 3 Selection of best housekeeper genes for qPCR normalisation.

A) Raw ΔC_t values from qPCR analysis of housekeeping genes. Box and whiskers represent mean ± SD. B-E) identification of best housekeeper genes for normalisation based on RefFinder analysis. In all results, most stable genes are shown on the left of the plot, in decreasing order. Points represent value calculated from n = 5 WT, EphA2$^{-/-}$ and EphA2$^{+/-}$ animals.

2.13 Statistics

Throughout this thesis, data has been collected from primary mouse tissue. Therefore, statistics has only been carried out where number of mice used was greater than 3 per genotype. Upon analysis, Shapiro-Wilk's test for normality was carried out, and alpha value of $P \geq 0.05$ accepted for normal distribution.

In an effort to be transparent about underlying variability within biological replicates, analyses which make measurements at the cellular level are expressed as superplot figures (Lord et al. 2020). Within these figures, cellular measurements are shown as transparent rings. The colour of these rings corresponds to an opaque circle, which represents the mean of all cellular measurements per mouse from which the tissue was derived. In keeping with the points made in Lord et al.(2020), statistics is only carried out on biological means and not technical means to limit introduction of false power to the calculations.

Where comparisons are made between genotypes only and not between timepoints, Student's t-tests were performed. To compare multiple groups from two different genotypes, Two-way ANOVA with Tukey's post hoc tests were performed. When comparing groups to a singular control, such as in conditioned media Krt8 analyses, One-way ANOVA with Dunnett's multiple comparisons was used.
For analysis of Western blot data, changes in protein between WT and KrasG12D groups were compared by non-parametric T-test with Welch's Correction. In figures where $p > 0.05$ and therefore non-significant, no annotation is shown. *P<0.05, **P<0.01, ***P<0.001, ****P<0.0001.

3 Establishing a model of cell competition in adult mouse lung

3.1 Introduction

As we age our tissues accumulate many mutations that do not result in malignant disease. Studies that have aimed to decipher the genetic landscape of histologically normal tissue and have found that tissues can contain many mutations that have the potential to drive cancer formation. Not-surprisingly, a common finding to all these studies is that incidence of cancer-causing somatic mutations strongly correlates with age (Martincorena et al. 2015; Martincorena et al. 2018; Lawson et al. 2020; Moore et al. 2020; Yoshida et al. 2020; Abascal et al. 2021; Grossmann et al. 2021; Cagan et al. 2022; Huang et al. 2022). Our understanding of why these mutations don't always lead to cancer has grown with our understanding of cell competition. When expressed at low levels in an otherwise normal epithelium, cancer causing mutant cells such as those mutant for KrasG12D (Hill et al. 2021), are eliminated from epithelial tissues over time to restore tissue homeostasis. This largely tumour suppressive mechanism is dependent on heterotypic interactions between normal and mutated cells (Hogan et al. 2009), and functions through repulsion and segregation cues from EphA2 forward signalling to Ras mutant cells (Porazinski et al. 2016; Hill and Hogan 2017; Hill et al. 2021). Loss of function of the EphA2 protein leads to loss of segregation, and fortification of lateral junction complexes between mutant and normal cells (Hill et al. 2021). EphA2 loss has previously been implemented in poor prognostic lung cancer (Yeddula et al. 2015), where loss of EphA2 resulted in greater tumour burden, reduced survival, and progression to lung adenocarcinoma.

Lung cancer is a leading cause of cancer deaths worldwide and has an unmet need for early detection and intervention (Malhotra et al. 2016; Ferone et al. 2020). The largest subgroup of lung cancer, non-small cell lung cancer, accounts for around 85% of lung cancer cases and manifests as distal lung tumours which are histologically positive for ATII cell markers (Mainardi et al. 2014; Sutherland et al. 2014). The predominance of ATII cells in late-stage tumours may indicate that selection processes such as cell competition are driving remodelling of the lung at early stages of disease resulting in a cell of origin.

Multiple studies have demonstrated that the lung has capacity to restore homeostasis via cell competitive mechanisms. When expressed in low numbers throughout the bronchiolar epithelium, HrasV12 mutant cells are extruded from the epithelium by neighbouring wild-type cells (Sasaki et al. 2018; Shirai et al. 2022). Similar work preceding this identified that apoptotic cells are extruded from the epithelium, and further showed that bronchial epithelial cells in culture are capable of eliminating aberrant cells by extrusion (Marshall et al. 2011). Here, dying cells which

were being extruded from the monolayer shifted from apical extrusion to basal extrusion upon silencing of the tumour suppressor *APC*. More recent work has established a role for crowding-induced extrusion as the cause of chest infections following allergic asthma exacerbation (Bagley et al. 2024). The existence of cell competition phenotypes implies that the lung epithelium is capable of moderating homeostasis by extrusion and suggests that cell competition may be pivotal for homeostatic regulation at early timepoints in lung cancer. Current gold standard genetic models of lung cancer overload tissues with genetic mutations or high mutational burden, and/or targeting expression of genetic mutations to specific cell lineages. In addition to this, studies of tumour development have so-far failed to assess the interaction of mutant cells with their relatively normal neighbourhood at early timepoints post oncogene activation.

This chapter aims to establish a model of cell competition that is relevant to lung cancer initiation and assess the role of previously established mechanisms in maintaining lung homeostasis. I hypothesised that KrasG12D mutants would be eliminated by their surrounding normal epithelium, and that a subset of cells that are not eliminated from the distal lung are retained and can drive tumorigenesis.

3.2 Results

3.2.1 Intranasal instillation of Adenoviral Cre drives transgene recombination in mouse lungs.

To study the role of KrasG12D in the adult mouse lung, I made use of the KC mouse. In this model, Cre recombinase drives recombination of floxed STOP codons that precede $Kras^{G12D/+}$ on the *Kras2* locus, and a floxed stop codon that precedes a tandem dimer red fluorescent protein (RFP) in the *Rosa26* locus (Fig.3.1 A). Originally, the mouse is derived from a Pdx1-Cre background so to avoid potential off target effects due to activation of Pdx-1 Cre in other tissues, we aimed to outbreed the line with a WT strain to remove the Pdx1-Cre promoter. Over the course of the project, litters were infrequent so a mixture of Pdx1-Cre positive and negative animals were produced. No difference was observed in pattern of RFP expression or severity of phenotypes between the KrasG12D and WT cohorts and no off-target effects were observed from induction. In experimental cohorts, mice heterozygous for KrasG12D were produced as homozygosity for KrasG12D is embryonically lethal.

To induce transgene expression, we use of a well-described model of producing lung cancer in mice (Jackson et al. 2001; Tuveson et al. 2004; Kim et al. 2005; DuPage et al. 2009). In this model, Cre recombination is driven by the instillation of an Ad5-CMV-iCre (AdCre) virus through the nasal passage. As shown in Figure 3.1 B, intranasal administration led to reliable recombination of bronchiolar airways in the lung (Fig.3.1 Bi). Infection of distal airways was more unreliable, but occasionally patches of recombination were observed (Fig.3.1 Bii-iii).

In order to model normal-mutant cell interactions, I determined the best dose of virus that would infect enough cells to observe an effect, but to maintain sporadic induction throughout the airways. I found that instillation of between 1×10^7 to 1×10^8 particle forming units (PFU) AdCre was sufficient to induce recombination in few cells along the airways and the alveoli (Fig. 3.2).

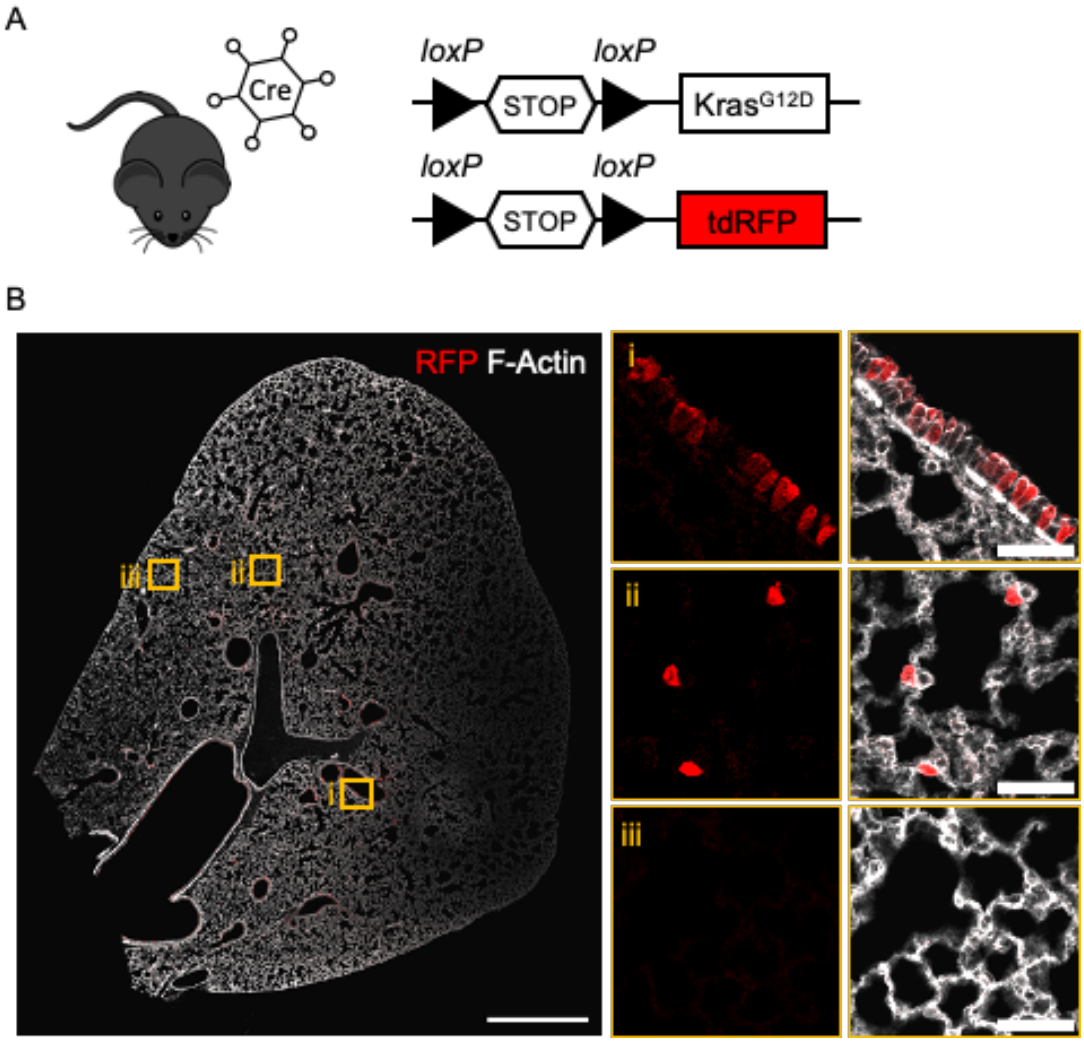

Figure 3. 1 Ad5-CMV-Cre recombinase infection drives transgene expression.

A) Intranasal instillation of adenoviral cre-recombinase results in expression of $Kras^{G12D}$ and a red fluorescent protein reporter. **B)** Adenovirus infection shows robust recombination in bronchiolar regions **(i)** but has a more sporadic infection of distal alveolar lung **(ii-iii).** Red = recombined cells, grey = Filamentous Actin (F-actin). Scale bar in overview image = 1000 µm, scale bar in digital zoom = 50 µm.

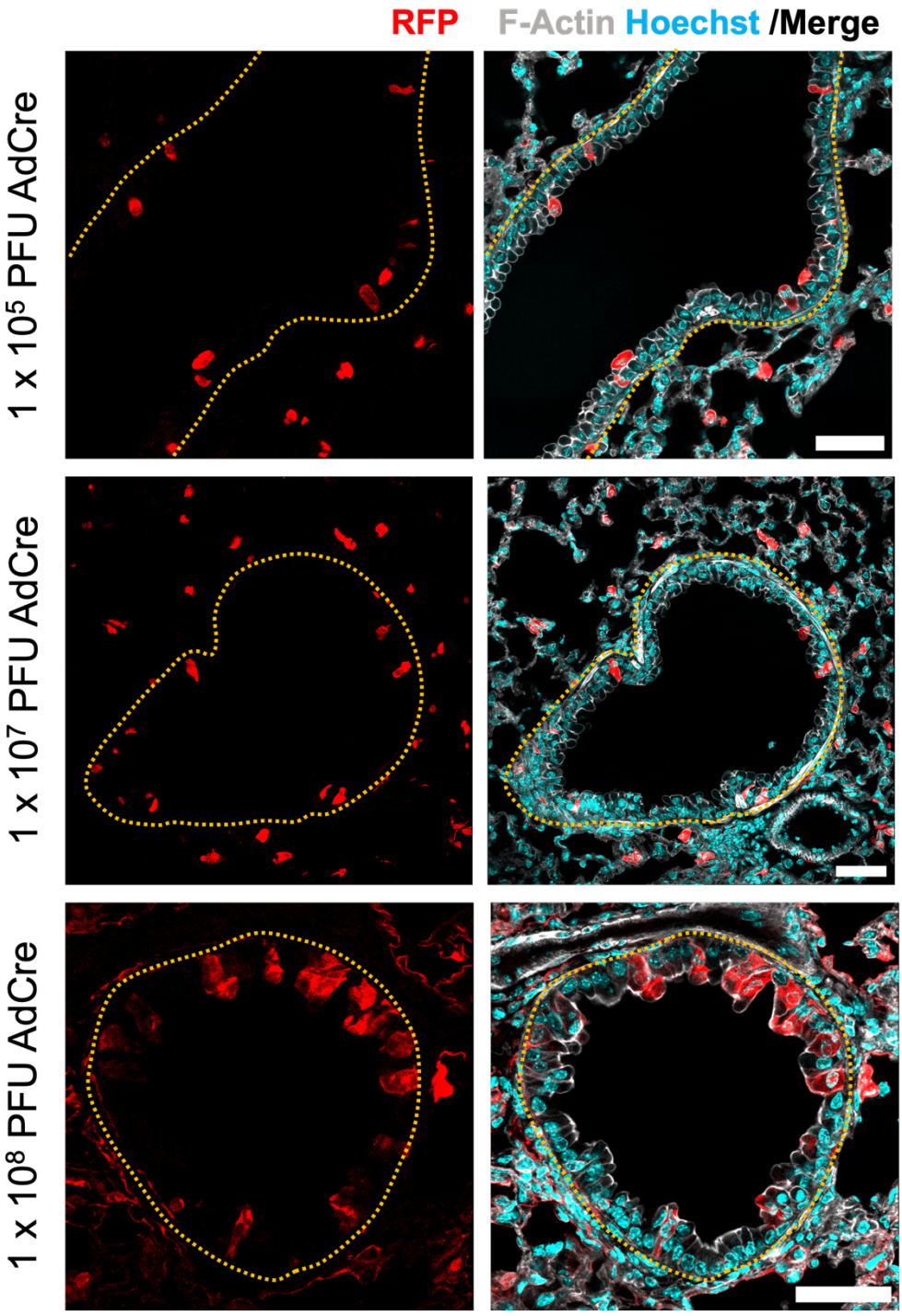

Figure 3. 2 Representative images of viral titres delivered to mice, and subsequent RFP expression in bronchiolar airways.

Mice were instilled with either 1 x 10^5, 1 x 10^7, or 1x10^8 PFU AdCre intranasally. Immunofluorescence microscopy of bronchiolar airways at 2 DPI reveal sufficient mosaic expression of RFP (Red) throughout the lung epithelium. Dashed yellow line depicts boundary between bronchioles and surrounding parenchyma, based on F-actin staining (grey) and Hoechst (cyan). Scale bar = 50 μm throughout.

3.2.2 Low level expression of KrasG12D is sufficient to drive tumorigenesis.

To assess the robustness of this model as a lung-cancer relevant model, it was necessary to confirm that the level of virus administered to animals led to tumour development. Mice were induced with a standard dose of 1 x 10^8 PFU AdCre and allowed to age for ten weeks post induction. Analysis of H&E sections revealed the presence of hyperplastic adenomas in all three KrasG12D mice, where none were present in WT sections (Fig 3.3).

Analysis of histological sections from KRasG12D mice by immunofluorescence revealed presence of distinct stages of adenoma progression throughout the tissue. Using F-actin to label cells, regions of tissue could be identified based on distinct architecture. In KrasG12D lungs, bronchiolar (Fig 3.4 A) and alveolar (Fig 3.4 B) epithelial architecture appeared normal and similar to WT tissue. Here, RFP+ cells were found regularly localised in the epithelium, non-hyperplastic, and staining as expected for pro-surfactant protein C (SPC), an established marker of ATII cells. In the same tissues, I identified regions that possessed histology indicative of KrasG12D cell progression into atypical adenomatous hyperplasia (AAH), with many pro-SPC positive, RFP positive cells found in close proximity to each other, albeit with some resemblance to proper alveolar structure (Fig 4.3 C). Similar to previous reports, KrasG12D activation alone induced cell progression to adenoma. Adenomas were identified in sections based on their compact, cuboidal cell populations that were mostly positive for both RFP and pro-SPC (Jackson et al. 2001; Juul et al. 2023).

These findings confirm that our model holds relevance to lung cancer, and that in our hands, we are able to recapitulate early stages of disease through to lung adenoma.

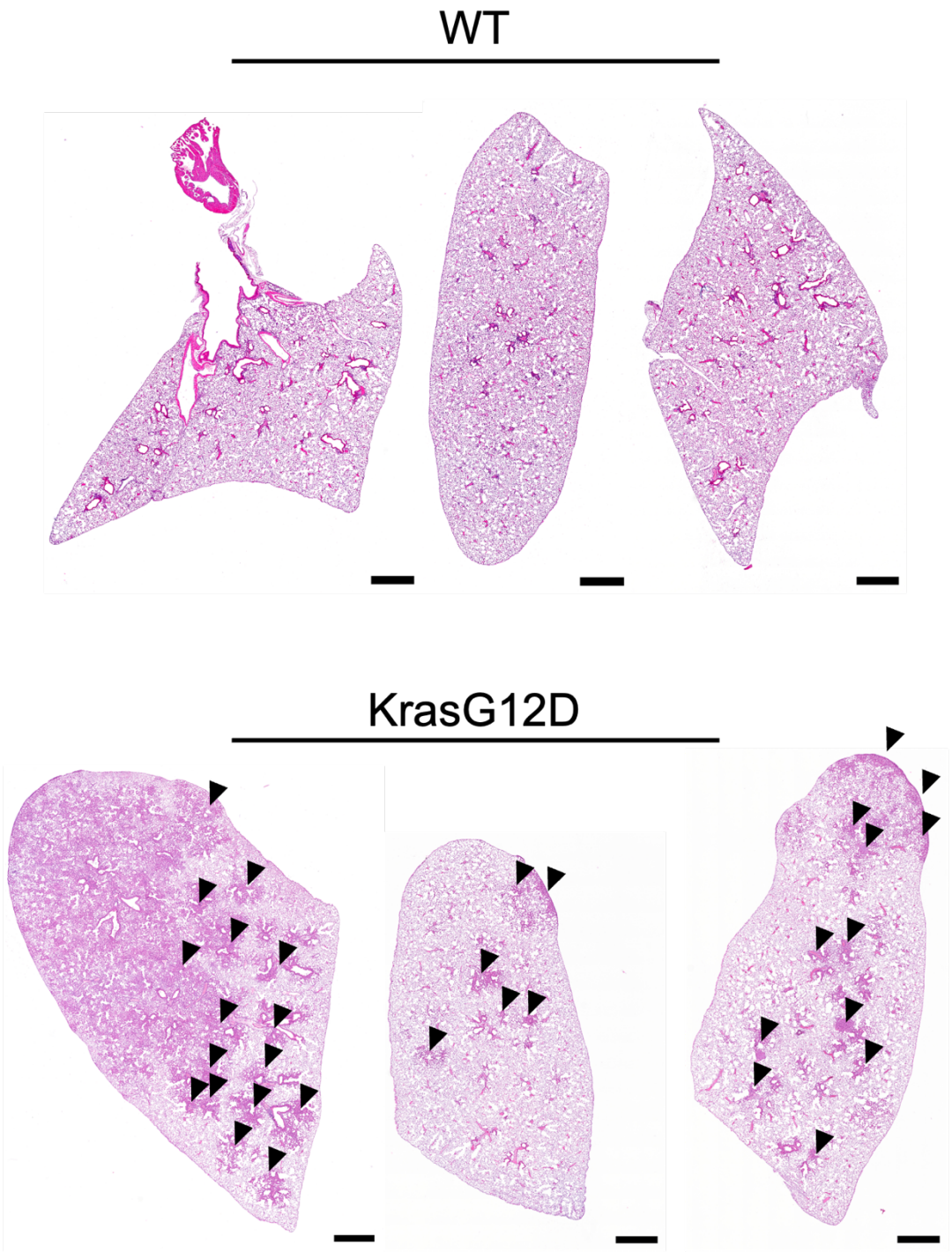

Figure 3. 3 Low level KrasG12D is sufficient to generate tumours by ten weeks post induction.

Induction of 6 to12 week-old mice with 1 x 10^8 PFU AdCre is sufficient to drive adenoma formation in KrasG12D animals. Representative haematoxylin and eosin sections from three wild type (WT) mice, and three KrasG12D mice. Scale bar represents 1 mm. Black arrow heads indicate general area of hyperplasia.

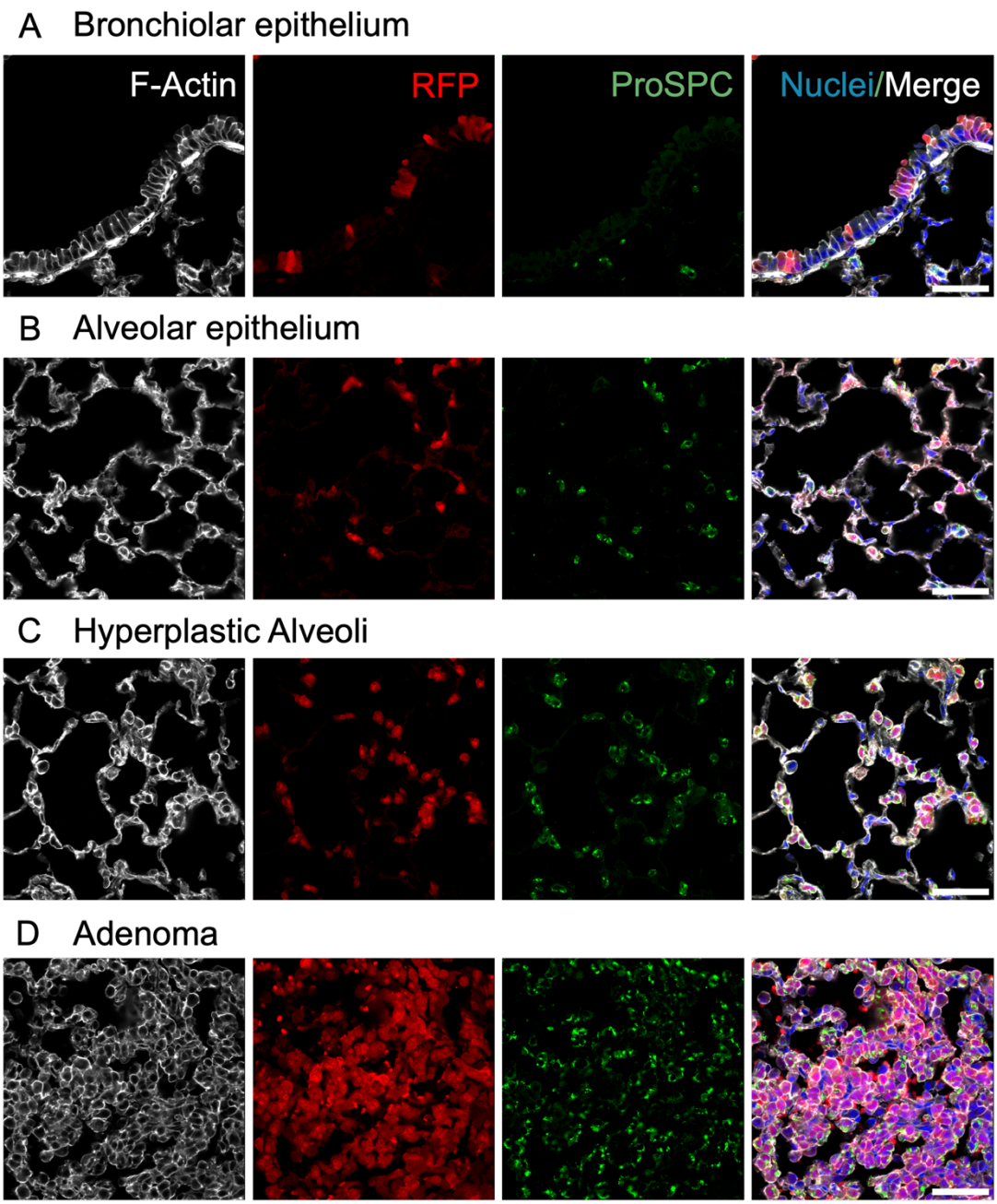

Figure 3. 4 KrasG12D activation mimics histological progression of lung adenocarcinoma.

A-B) Representative images of tumour tissue at 10 weeks post induction. Induction of KrasG12D (and RFP reporter, red) in low numbers of cells does not induce gross cellular changes and some regions of tissue remain morphologically normal with distinct bronchiolar (A) and alveolar (B) architecture. Evidence for **C)** adenomatous atypical hyperplasia, which is the hyperplastic behaviour of ATII cells in the alveolus (green; Pro surfactant protein (Pro-SPC, green) and **D)** adenomas. Scale bar = 50 μm.

3.2.3 AdCre instillation is consistent throughout all lobes of the lung.

Throughout my studies, intranasal administration was the method used to induce my transgenes in mice. Therefore, It was important to consider if viral particles were equally distributed throughout all lobes and in particular, reaching the distal aspects of the lung as this is where the proposed cell of origin for LUAD (Kim et al. 2005; Mainardi et al. 2014; Sutherland et al. 2014). To address this, I turned to flow cytometry to measure the base level of recombination achieved at 2 DPI in the lungs, irrelevant of Kras genotype. Recombined epithelial cells were determined using cell surface staining and flow cytometric analysis (CD45-, CD31-, EPCAM+). Further to this, bronchiolar and alveolar populations could be distinguished based on their relative expression of CD24, with $CD24^{High}$ populations associated with bronchiolar epithelia, and $CD24^{Low}$ populations alveolar (Chen et al. 2012; Nakano et al. 2018).

Following flow cytometric analysis, I found that following 2 days post induction with 1 x 10^8 PFU AdCre, distribution and expression of RFP in both the bronchiolar and the alveolar (Fig 3.5) populations was similar across all lobes. For this analysis, WT (circles) and KrasG12D (diamonds) populations were combined. I found that generally bronchiolar populations contain more RFP positive cells compared to the alveolar region, but no statistical differences were observed. This result confirms that intranasal induction of KrasG12D and RFP is a reliable, non-biased method of inducing transgenes throughout the adult mouse lung.

Consistently, we attained induction of approximately 5% of cells in both regions of the lung (upper vs lower airways, Fig. 3.5). We determined that the level of recombination achieved with 1x10^8 PFU AdCre would be sufficient to observe measurable changes in recombined cells in the epithelium over time.

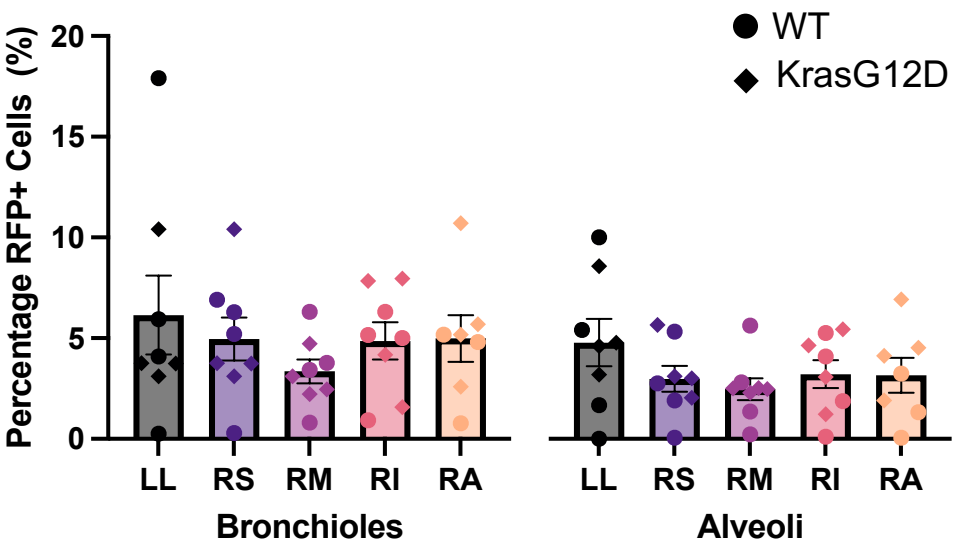

Figure 3. 5 Intranasal instillation of AdCre evenly distributes recombination throughout all lobes of the lung.

Flow cytometric analysis of WT (circles) and KrasG12D (diamonds) animals at 2 DPI reveals that intranasal induction leads to transgene expression throughout the airways and alveolar regions in all lobes. Bars represent mean ± SEM, each data point represents one mouse. LL = left lung lobe, RS = Right superior lobe, RM = Right middle lobe, RI = Right inferior lobe, RA = Right accessory lobe.

3.2.4 KrasG12D mutant cells are not eliminated from the lung epithelium.

To determine whether KrasG12D mutant cells are being eliminated from the lung at expected timepoints, we utilised flow cytometry to quantify changes in RFP+ epithelial cells over time. The benefit of using flow cytometry for this approach is that large tissues such as the lung can be broken down into component parts, single cell suspensions generated, and populations of cells quantified in a non-biased manner. Previous research in the lab, measured changes in global RFP by quantifying the percentage of endogenous RFP expression per tissue area by immunofluorescence microscopy and quantitative imaging tools. I found that this approach was not suitable for lung as lung tissues have massive surface areas relative to the number of RFP events that would be detectable by immunofluorescence, possess lots of empty space and require high quality imaging and magnification for proper analysis meaning that imaging time alone would not permit high throughput quantification. In addition, the lung has high levels of background autofluorescence requiring a different strategy to image.

Using standard gating strategies (Fig 3.6), epithelial cell populations (CD45-, CD31-, EpCAM+) were further resolved into bronchiolar and alveolar airways based on expression of CD24. CD24 (heat stable antigen) has been proposed to mark bronchiolar populations of the murine lung, allowing the distinction between the bronchiolar and alveolar regions of the lung (Chen et al. 2012; Nakano et al. 2018). To account for intralobular variability, each lobe from each mouse was processed separately, allowing us to map the changes in RFP population throughout the entire lung in detail.

Analysis of tissues harvested from WT mice at 2-, 7- and 35- DPI found no significant changes in the amount of RFP+ cells, in $CD24^{Hi}$, or $CD24^{Lo}$ lung populations (Fig. 3.7). In contrast, analysis of tissues harvested from the KrasG12D group showed significant increase in RFP+ cells in the $CD24^{Hi}$ population of every lobe between 2 and 35 DPI (Fig 3.7 A). Similarly, significant increases in RFP+ cells were observed in $CD24^{Lo}$ population of most lobes, except the right accessory lobe (RA; Two-Way ANOVA with Tukey's post hoc, $p = 0.0508$). However, the $CD24^{Lo}$ population of the RA lobe exhibited a non-significant increase in the number of RFP positive cells found with a mean of 34.81 ±32.8% relative to the 9.58 ±8.8% of RFP+ cells in WT animals ($P > 0.05$).

Significant increases were also measured between 7 and 35 DPI in the left lung, right superior (RS), right middle (RM) and right inferior (RI) lobes of $CD24^{Hi}$ population, but not in the RA lobe. In $CD24^{Lo}$ populations, this increase from 7 to 35

DPI was only observed in the RI lobe, however, increases in the percentage of RFP positive cells from 2 to 7 to 35 DPI is evident in both populations of all lobes.

Finally, comparisons made between WT and KrasG12D cohorts show a significant increase in all comparisons, except for the $CD24^{Lo}$ populations of the RA lobe. Once again, the increases that were observed in all groups is evident that KrasG12D activation leads to a robust growth of cells in the adult lung epithelium by 5 weeks post induction, and that early modulation in KrasG12D populations as expected does not occur. Therefore, these data show that cell competitive elimination of KrasG12D mutant cells is not apparent at previously established timepoints. KrasG12D mutations alone are sufficient to permit expansion in the airways as early as 7 DPI, leading to early tumour stages by 35 DPI.

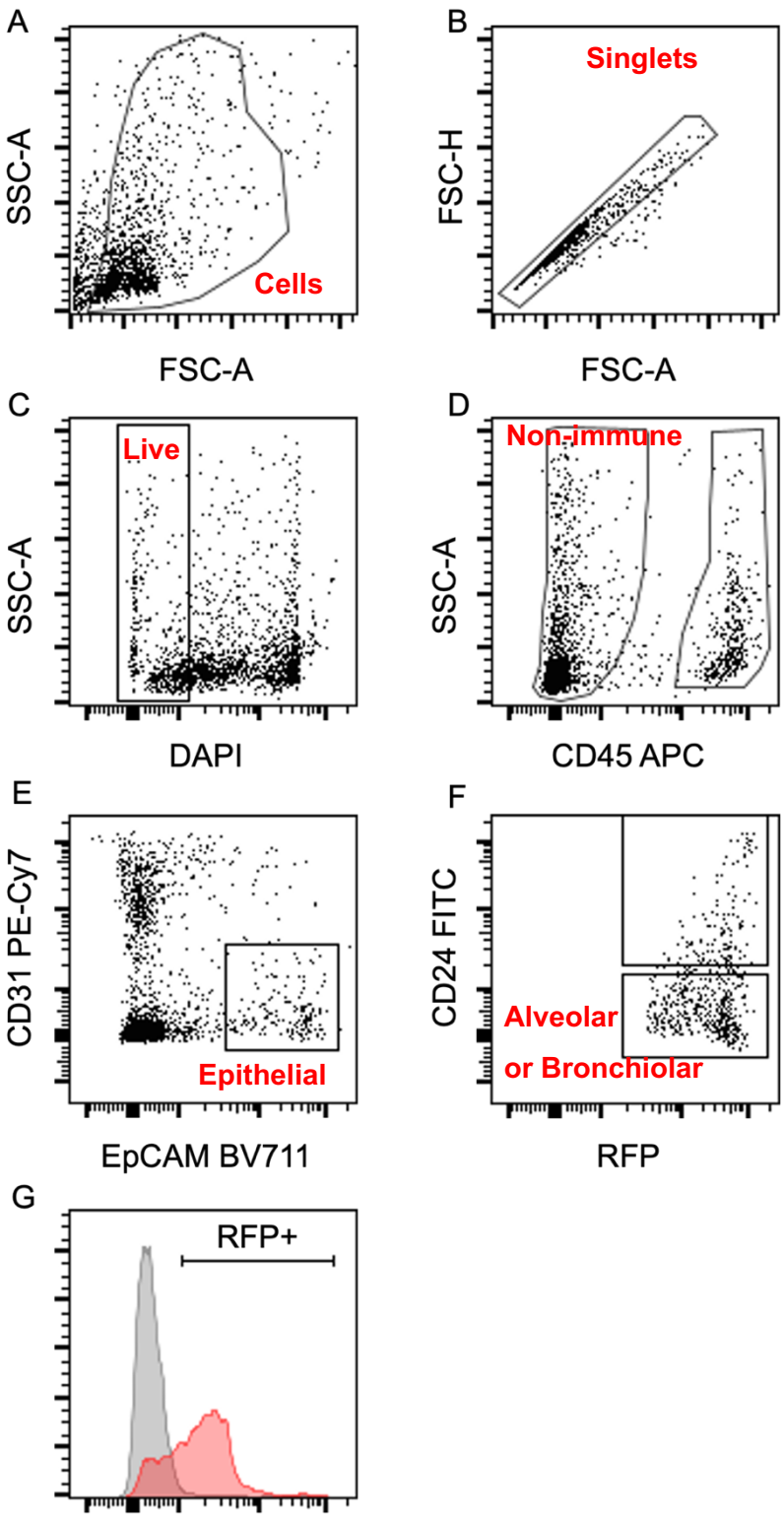

Figure 3. 6 Gating strategy for flow cytometric analysis of lung cell populations.

A-C) Live single cells. D) CD45 positive populations were analysed from this gate. CD45- populations were further resolved. E) CD31- EpCAM positive populations were selected for analysis and further identification with CD24 (F). G) Endogenous RFP expression from AdCre induction was sufficient to track changes in RFP+ populations over time. Histogram plot shows a WT sample at 35 dpi (grey) and a KrasG12D sample at 35 dpi. Expression at 1 x 10^3 taken as positive stain at this level.

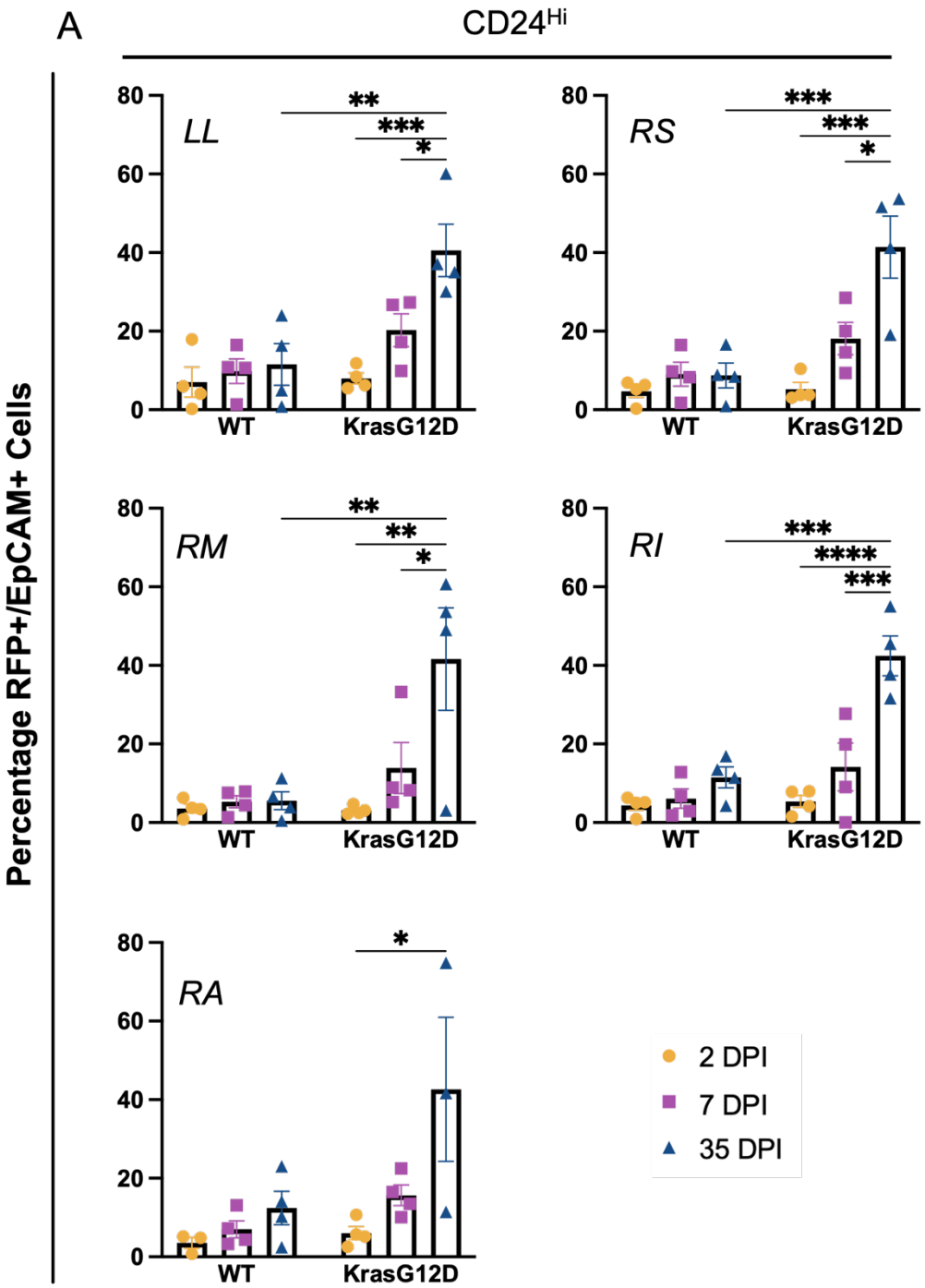

Figure 3.7. (Figure legend on next page.)

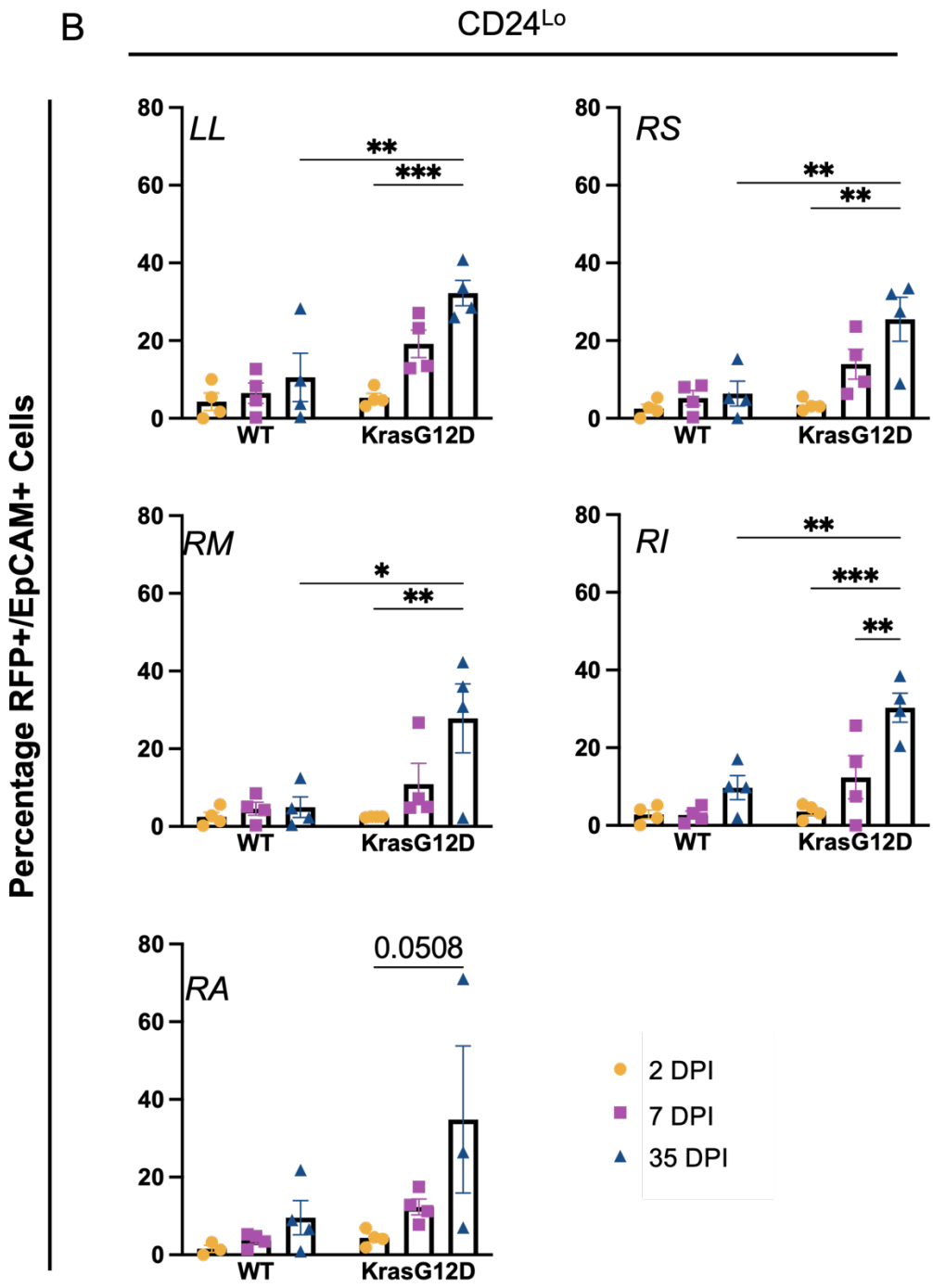

Figure 3. 7 KrasG12D mutant cells expand in the epithelium by 5 weeks post induction.

Lungs were dissected into individual lobes and processed for flow cytometry at 2-, 7- and 35-days post induction. Percentage of RFP+ cells as a total of CD45-, CD31-, EpCAM+ cells are represented by mean ± SEM. Airways and alveoli are further detailed as $CD24^{HI}$ **(A)** airways, and $CD24^{LO}$ **(B)** alveoli. Data points show individual mice at 2 DPI (yellow circle), 7 DPI (purple square) and 35 DPI (blue triangle). Two-Way ANOVA with Tukey's post-hoc tests where *P <0.05, *P <0.01, ***P <0.001, ****P <0.0001. N= 4 per genotype and timepoint. LL = left lung lobe, RS = Right superior lobe, RM = Right middle lobe, RI = Right inferior lobe, RA = Right accessory lobe.

3.2.5 Lung immune cells exhibit low level RFP expression.

Immunohistochemistry of lung tissues is useful to assess cellular morphology in response to KrasG12D induction, and has been a pivotal tool in the competition field for elucidating cell-mediated changes (Hogan et al. 2009; Porazinski et al. 2016; Hill et al. 2021). Upon analysis of RFP immunofluorescence, I witnessed cells that were either no-longer part of the epithelium, or non-epithelial (Fig 3.8 A). Indeed, upon co-staining with anti-RFP and anti-F4/80 (a general marker of murine macrophages - (Hussell and Bell 2014) antibodies, revealed distinct RFP+/ F4/80+ cells were found that appeared to be around the epithelium, but not within it as ATII cells are expected to be. The presence of these cells in the alveoli could introduce error in detecting RFP positive cells by IF, further supporting our decision to use flow cytometric analysis of RFP populations previously.

By referring back to the data acquired in Figure 3.6, quantification of RFP positive macrophages was possible. Using the CD45 positive population of cells (Fig 3.8 A), number of RFP+ cells as per previous gating (Fig 3.8 B) was quantified showing that RFP+ macrophages only account for less than 4% of the total macrophages present in the lung between 2- and 7- days post induction. Two-way ANOVA of WT and KrasG12D CD45+/RFP+ cells at 2 and 7 DPI revealed no significant effect of time post induction, or activation of KrasG12D (Tukey's post hoc test, all $P > 0.05$). These data confirm that a small percentage of RFP positive cells are macrophages and suggests that analysis of fluorescence micrographs will not be skewed by their presence.

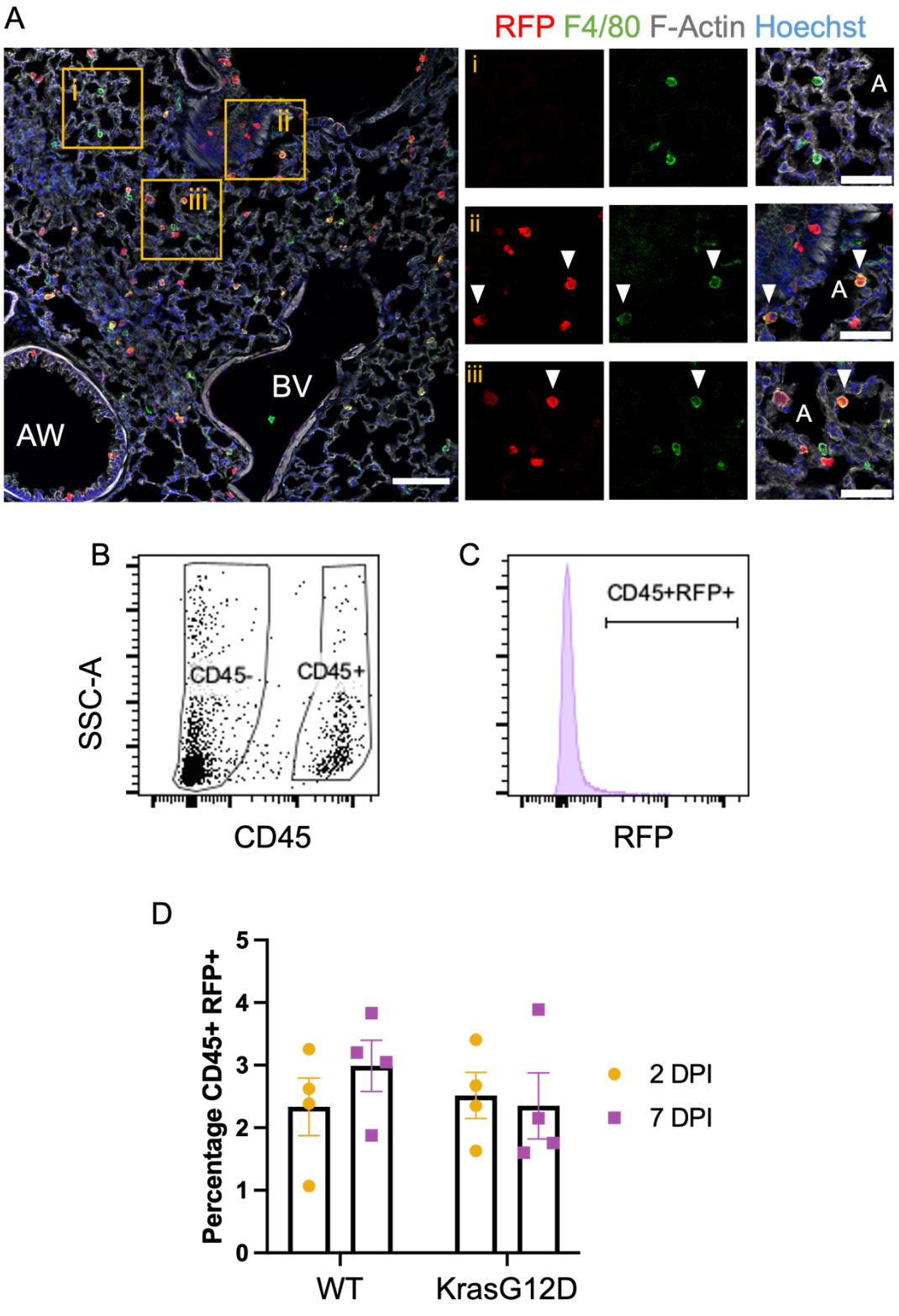

Figure 3. 8 RFP+ macrophages account for less than 4% of total lung myeloid cells.

A) Alveolar macrophages stain positive for RFP in RFP-induced lungs. Confocal imaging of RFP-positive lungs show that alveolar macrophages also stain positive for RFP in induced tissues. Double antibody staining for F4/80 (green) and RFP (red).

Panels i-iii show optical zoom of representative sections of positive cell staining throughout sections: i**)** F4/80 single positive cells, **ii, iii)** single positive RFP and F4/80 cells. White arrowheads depict double positive cells. AW = airway, BV = blood vessel, A = alveolar space. Scale bar, 100 μm in large panel and 50 μm in smaller panels. **B)** Using the flow cytometry data acquired for Fig. 3.6, CD45+ live cells were gated, and cells displayed on a scale of RFP intensity **(C). D)** Analysis of 2- and 7- DPI animals revealed no change in the number of RFP+/ CD45+ cells in either WT or KrasG12D animals. Bars represent mean ±SEM, and data points represent average data from individual lobes from each mouse (n = 4).

3.2.6 KrasG12D mutant cells are not eliminated from the epithelium by apical extrusion.

The next goal was to establish whether KrasG12D mutant cells are eliminated from the bronchiolar airways as has been previously described for HrasV12 mutants (Sasaki et al. 2018; Shirai et al. 2022). RFP+ positive cells can be scored into 3 categories which describe the apical extrusion phenotype (Fig 3.9 A). RFP+ cells that are positioned within the epithelial monolayer with basally located nuclei were classified as not extruding. Translocation of the nucleus to the apical surface of the cell denoted cells extruding. Cells that had lost attachment to the basement membrane, were round in shape and were located on top of the epithelium were classified as extruded (Fig 3.9 A).

When we analyse airways at 2 DPI, we observed a mixed population from all three categories (Fig 3.9 B). The largest proportion was the non-extruding cells which represented 69.27 ±5.5% of WT RFP+ cells, and 69.67 ±3.8% KrasG12D RFP+ cells. Significantly more cells were observed undergoing extrusion in KrasG12D airways compared to WT airways (25.23 ±1.7% versus 18.42 ±0.24 respectively, Welch's t-test, P =0.0039) suggesting that KrasG12D mutants are being extruded from the epithelium. Few cells were observed to undergo full apical extrusion in the 2 DPI samples, with only 5.10 ±2.4% of KrasG12D cells classified as extruded compared to 12.30 ±5.8% of WT RFP+ cells, further suggesting that 2 DPI is the start of the extrusion process.

Analysis of later timepoints at 5- and 7- DPI showed an increase in the percentage of cells not-extruding compared to 2 DPI in both WT and KrasG12D samples (WT 5 DPI: 78.91 ±5.2%, KrasG12D 5 DPI: 79.24 ±8.6%, WT 7 DPI: 79.88 ±2.7, KrasG12D 7 DPI: 81.12±3.4%). Consequently, we observed a reduction in the percentage of cells extruding, with levels returning to those observed for WT 2 DPI in both WT and KrasG12D at 5 DPI (16.80 ±4.6% and 16.39 ±5.83%), as well as WT and KrasG12D at 7 DPI (16.86 ±4.26 and 16.49 ±1.9% respectively). Similar percentages of cells fully extruded can be detected at 5 DPI compared to 2 DPI in KrasG12D samples (4.36 ±3.79%), however at 7 DPI, the percentage of extruded RFP+ KrasG12D cells is reduced to 2.37 ±0.83%. Interestingly, the WT samples exhibit a decreasing trend in the number of extruded cells found (5 DPI = 4.29 ±1.1%, 7 DPI = 3.27 ±1.5%). Overall, my findings suggest that KrasG12D mutant cells are not extruded from the epithelium by interaction with WT neighbours, and that extrusion is not a response to KrasG12D activation as has been observed elsewhere.

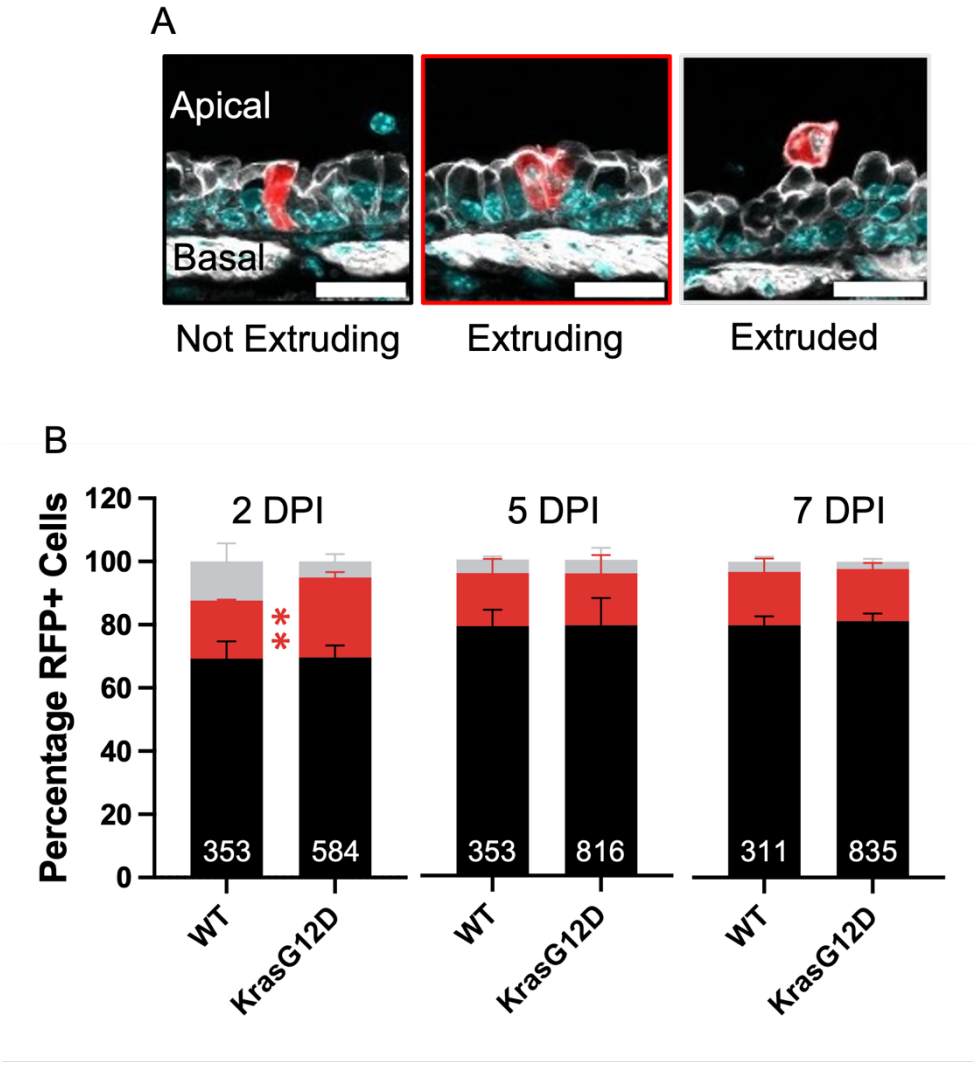

Figure 3. 9 KrasG12D mutant cells are not eliminated by apical cell extrusion in the bronchiolar airways.

A) RFP+ cells can be categorised into 3 phases of extrusion. Cells that retain morphology and a basally located nucleus are not extruding (black). An apical translocation of the nucleus represents cells undergoing extrusion (red), and once all basement membrane attachment is lost the cell is classified as extruded (grey). Scale bar = 20 μm. **B)** Percentage of RFP positive cells classified into the three stages of extrusion across day 2, 5 and 7 post induction. Bars show mean ± SD from n = 3 mice per genotype, number of cells counted in analysis denoted on bar. Welch's T-test, **P <0.01.

3.2.7 $Kras^{G12D}$ mutants are not selected for elimination in the distal lung epithelium.

In the bronchiolar airways, extrusion events can be easily determined because the bronchiole has regular apical-basal polarity and columnar epithelial appearance in tissue sections. However, the distal lung exhibits a far more disorganised appearance when histological sections were analysed. As such, it is more difficult to discern apical-basal polarity and subsequent extrusion phenotypes. To counter this, I used previously established readouts of competition that could indicate whether KrasG12D mutant cells in the alveoli are being recognised by their normal neighbours and selected for elimination (Porazinski et al. 2016; Hill et al. 2021). When a cell is being extruded, it becomes taller on an apico-basal plane as a consequence of contractile forces in the surrounding cells (Hogan et al 2009). Previous work in our lab has identified that EphA2 signalling is required to trigger cell segregation and rounding up of RAS mutant cells fated to become 'losers' (Porazinski et al. 2016; Hill and Hogan 2017; Hill et al. 2021)

To address whether KrasG12D cells respond to normal neighbours in the alveolar epithelium, randomly sampled images were taken of RFP+ alveoli, which were masked using Fiji (Schindelin et al. 2012) with an overlay detected particle sizes greater than 25 μm^2. This was deemed as the minimum area required to eliminate background fluorescence or artefacts that could interfere with morphology readouts. FIJI can generate measurements for cell roundness, perimeter, and area, and expressing the perimeter over area fraction allows us to further validate roundness morphology.

Analysis of changes in cell area across days 2, 5 and 7 post induction, revealed no observable change in cell area in either WT or KrasG12D samples (Fig 3.10 A, B). The average cell area in WT is 77.96 ±6.8 μm^2 at 2 DPI, similarly 74.17 ±7.0 μm^2 at 5 DPI and at 68.00 ±8.6 μm^2 at 7 DPI. In the KrasG12D samples, cells have an average size 70.52 ±2.1 μm^2 at 2 DPI, 85.50 ±3.4 μm^2 at 5 DPI, and 74.49 ±21.82 μm^2 at 7 DPI. Next, I analysed cell roundness to assess whether cells were contractile or segregating away from their neighbouring WT cells. A value of 1 indicates a perfectly round shape. In WT samples, cells had an average roundness of 0.66 ±0.02 at 2 DPI, 0.64 ±0.03 at 5 DPI, and 0.63 ±0.03 at 7 DPI. Interestingly, we observed a significant decrease in roundness in 7 DPI KrasG12D samples (Fig 3.10 C) relative to 2 DPI KrasG12D samples (2 DPI = 0.70 ±0.05, 7 DPI = 0.59 ±0.04; One-Way ANOVA with Dunnett's multiple comparisons. P = 0.0405), indicating that cells were becoming less round when KrasG12D was active for 7 days.

Another readout of a cell's roundness is perimeter to area ratio. A larger perimeter to area ratio indicates a cell that possesses more protrusions or is less round. Similar to roundness measurements, a higher perimeter to area ratio was found in 7 DPI KrasG12D compared to 2 DPI (2 DPI = 0.71 ±0.06, 7 DPI 0.87 ±0.05. Two-way ANOVA with Tukey's post hoc test, P = 0.567 (Fig 3.10 D)). These values were increased compared to WT values of 0.79 ±0.2, 0.76 ±0.1 and 0.72 ±0.08 for 2, 5 and 7 DPI respectively.

These findings strongly suggest that WT cells that surround KrasG12D mutant cells in the alveoli do not detect them as aberrant and initiate segregation responses to prepare for elimination.

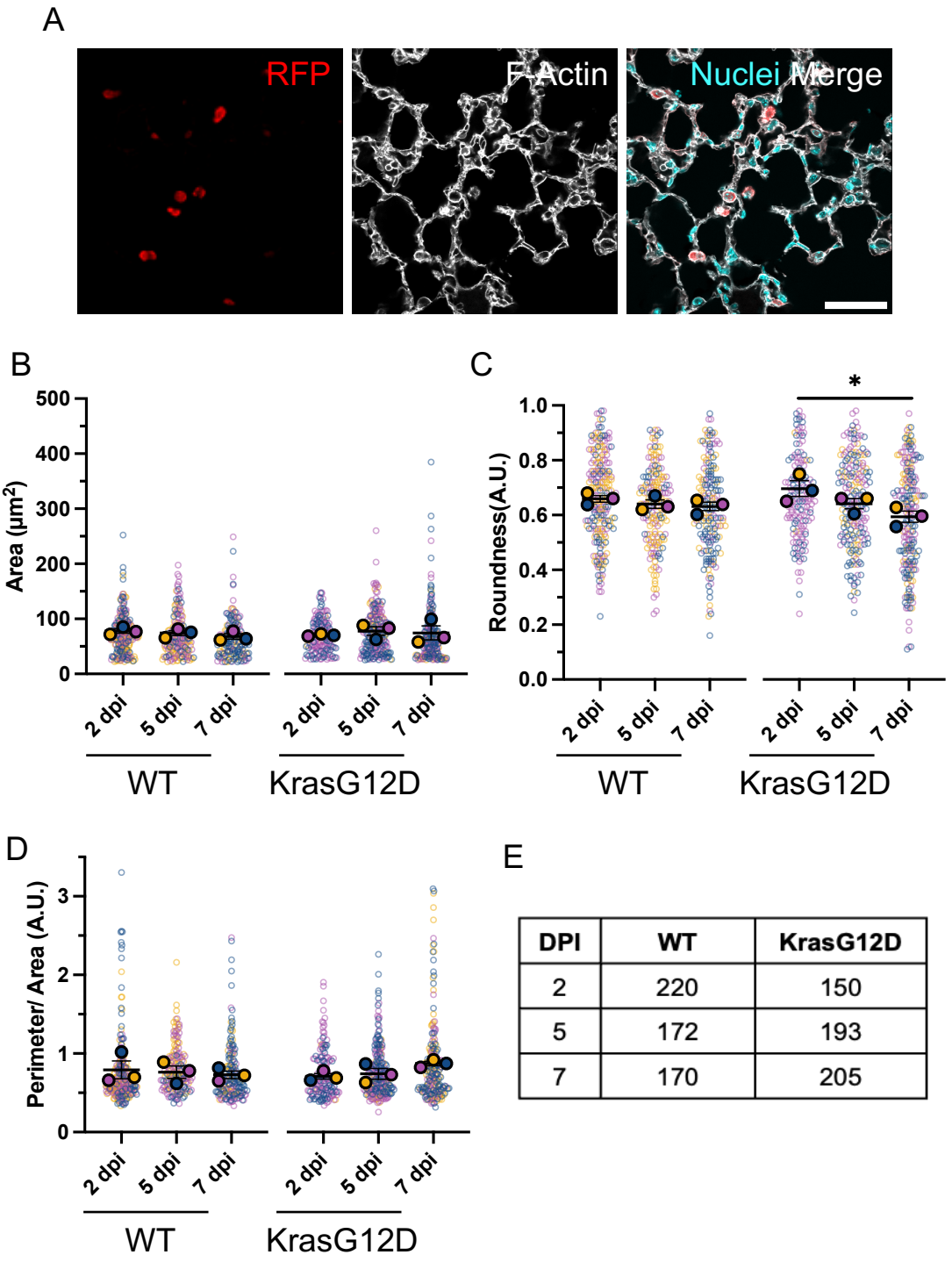

DPI	WT	KrasG12D
2	220	150
5	172	193
7	170	205

Figure 3. 10 Cell morphology readouts of RFP+ alveolar cells.

A) Representative image of alveolar RFP+ cells. **B-D)** Superplots of cell morphological measurements from automated FIJI analysis. **B)** Cell area does not change across 2, 5 and 7 DPI in WT or KrasG12D samples. **C)** Significant decrease in roundness of RFP+ cells in KrasG12D tissues when comparing 2 DPI and 7 DPI timepoints. **D)** Perimeter/ area ratio reveal a trend increase in KrasG12D samples at 7 DPI relative to 2 DPI and WT samples. Transparent rings represent individual cells colour coded to mouse biological replicates. Average biological replicate represented by solid colour circle. Bars represent mean ±SEM. Statistical analyses represents

Two-way ANOVA with Tukey's, *P < 0.05. **E)** Table showing the total number of cells counted per condition from of 3 mice.

3.2.8 Proliferation of KrasG12D mutant cells is apparent by 1 week post induction.

Previous data suggested that cells are expanding in the lung as early as 7 DPI, leading to substantial sized RFP+ populations at 35 DPI. To corroborate this, lung tissue sections were stained for Ki67 antigen, a broad marker of cells in G1-M phase of the cell cycle. To ensure equal inclusion of different regions of the lung, sections were divided in 250 μm by 250 μm grids, and a random number generator used to select 40 sections for quantification. With this approach, sections were stratified (Fig 3.11 A) into normal tissue (Normal), tissue that is hyperplastic or shares a grid with tumour tissue (Edge), and tumour (Tumour) tissue allowing conclusions to be drawn based on a cell's location in the tissue.

Analysis of tissue at 1 week post induction revealed the presence of hyperplastic regions in KrasG12D tissue, but not WT (Fig 3.11 B). In WT lungs, only approximately 0.2233 ±0.07% of cells are positive for Ki67, indicative of the organ's naturally quiescent state. In regions of KrasG12D lungs identified to have normal morphology, this number increased to 0.3533 ±0.06%, and further increased in edge tissue regions (0.6900 ±0.08%; Ordinary One-way ANOVA between WT and edge, p =0.0012) for the two animals that had hyperplastic regions present at 1 week post induction. At 5 weeks post induction (Fig 3.11 C) all lung samples possessed regions of edge tissue, and two samples contained tumour tissue. Morphologically normal tissue regions at 5 weeks post induction possessed a slightly lower number of cells proliferating in both WT and KrasG12D samples (0.1505 ±0.06% and 0.1657 ±0.07% respectively). This number increases to 0.4140 ±0.31% of cells in edge tissue, and further to 0.8700 ±0.55% in tumour regions.

This data displays and corroborates the previous findings that KrasG12D mutant cells are expanding (Fig 3.7) and are not eliminated from the tissue, and further shows that they begin developing towards the hyperplastic phenotype at 1 week post induction.

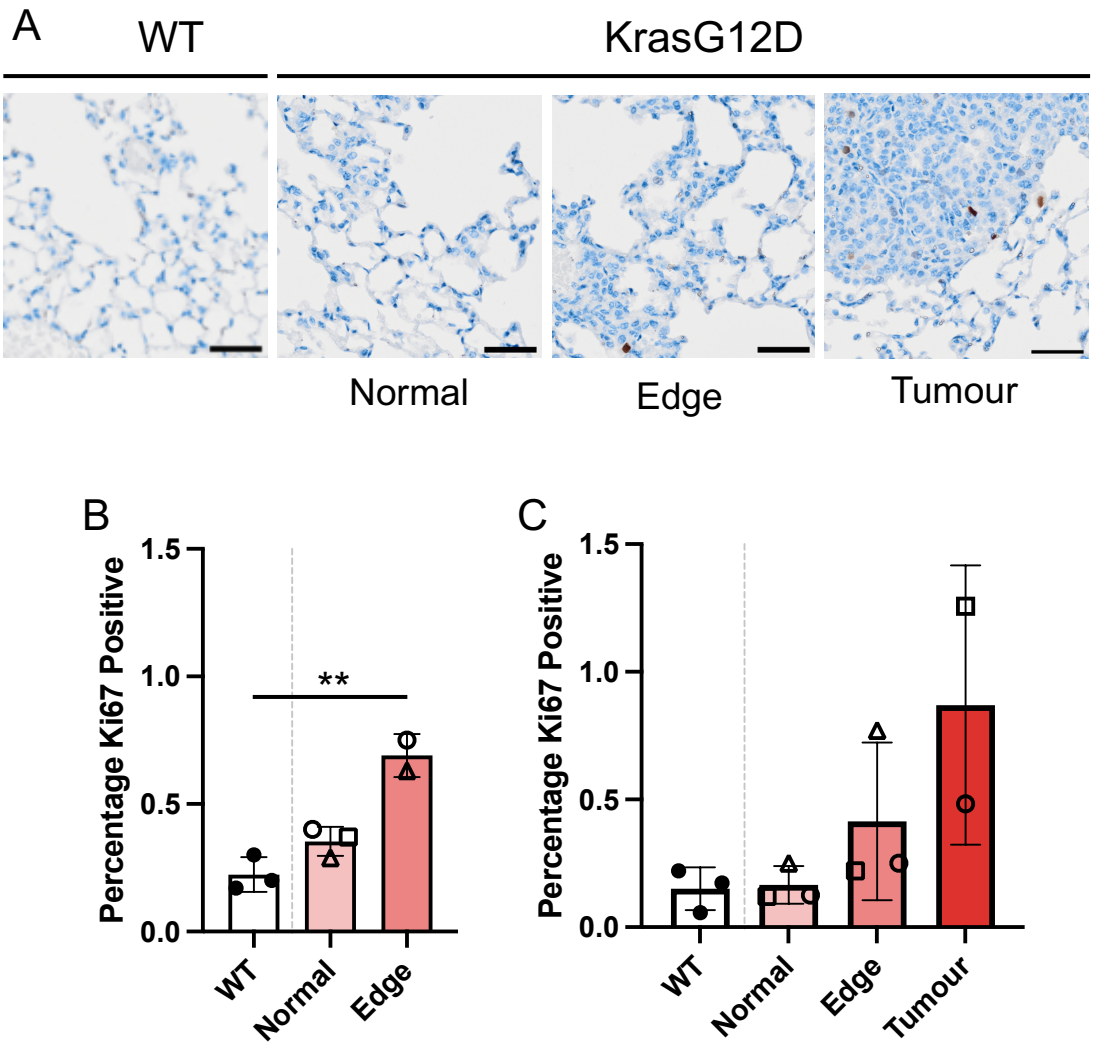

Figure 3. 11 KrasG12D mutant cells are more proliferative at tumour sites compared to normal tissue.

A) Lungs were stained for Ki67 antigen and whole tissue sections imaged by brightfield microscopy. Scale bars, 50 µm. 40 randomly selected 250 µm by 250 µm tiles were selected and stratified into morphologically normal tissue, hyperplastic tissue at the edge of tumours, or tumour sections. **B)** Analysis at 1 week post induction. Hyperplastic regions were only found in 2 animals. **C)** Analysis of sections at 5 weeks post induction. All KrasG12D mice contained hyperplastic regions, but only 2 out of 3 mice possessed tumours. **B-C)** Symbols represent individual mice (total n = 3 per group). Symbol shape in KrasG12D mice (red) identify the same mouse. Bars represent mean ± SD. Ordinary One-way ANOVA between WT and edge, *P <0.01.

3.2.9 EphA2 does not play a pivotal role in lung epithelial homeostasis.

As has been introduced previously, our overarching hypothesis for this chapter was that EphA2 forward signalling was selecting KrasG12D mutant cells for elimination in a conserved manner, as has been previously described in MDCK cell systems, *Drosophila*, and most recently the mouse pancreas (Porazinski et al. 2016; Hill and Hogan 2017; Hill et al. 2021)

To assess the impact of loss of functional EphA2 in KrasG12D cell fate in mouse lungs, I utilised the Pdx1 Cre^{ERT} $Kras^{LSL\text{-}G12D/+}$; $Rosa26^{LSL\text{-}tdRFP}$; $EphA2^{-/-}$ mouse model (Hill et al. 2021) which possesses a truncation in the EphA2 gene at amino acid 426, a region that maps to the extracellular domain of the EphA2 protein (Brantley-Sieders et al. 2004). To assess whether knock-out of EphA2 protein affects the development of the lungs, I used readouts of airspace characteristics to assess if the lungs have successfully formed and properly developed mature airspaces. The first of these readouts is the mean linear intercept (MLI). MLI describes the free distance in the air spaces, or rather, how frequently are alveolar cells encountered in the distal lung (Knudsen et al. 2010; Akram et al. 2019). Analysis of MLI using phalloidin-stained tissue sections from either WT ($EphA2^{+/+}$) or EphA2 knockout ($EphA2^{-/-}$) mice revealed no significant changes (Fig 3.12 A). Both $EphA2^{+/+}$ and $EphA2^{-/-}$ lungs had an average MLI of 45.69 ±4.2 μm^2 or 47.86 ±5.5 μm^2 respectively (P =0.2368).

The second readout of EphA2 function is the number of airspaces observed per mm^2. This readout infers proper patterning of the lungs at later stages of development. In my analyses, I observed no significant differences between $EphA2^{+/+}$ or $EphA2^{-/-}$ samples, with both genotypes presenting similar numbers of airspaces per mm^2 (Fig 3.12 B: +/+ = 121.1 ±20.5 /mm^2, -/- = 123 ±37.3 /mm^2. P =0.8321). These findings indicate that constitutive loss of EphA2 does not cause any overt morphological phenotypes in lungs, in contrast to that seen in other branched organs (Vaught et al. 2009).

With this finding, I hypothesised that there may be some redundancy in EphA2 function, and that other members of the Eph-ephrin signalling family may be accounting for EphA2's loss from the lung. For this, RNA was isolated from total lung tissue and qPCR reactions for *EphA1*, *EphA2*, *Efna1*, and *Efna4* were carried out (Fig 3.12 A-E). Two reactions for EphA2 were performed; one that used primer pairs that annealed prior to the truncation at nucleotide 1372 (Fig 3.13 B), and one primer pair that anneals over the site at 1372 (Fig 3.13 C), which is better representative of EphA2 transcriptional output. Our results indicated that *EphA2* loss coincided with a significant increase in *EphA2* gene transcription (Fig 3.13 A) compared to *EphA2* WT

lungs (P = 0.0049). The second primer set that assessed the truncated gene revealed a stark loss of expression compared to WT mice (Fig 3.13 B). These reactions highlight that our EphA2 loss of function mouse does indeed lack functional transcription, and that initial transcription occurs in excess of that in WT mice. All samples were run as n = 4 mice, however as demonstrated in Figure 3.13b, undetected samples were not represented on the graph.

Eph-ephrins are widely regarded as 'promiscuous' family members, noted for their ability to form receptor complexes with other Eph receptors and, and also their ability to activate or be activated by different ephrin ligands (Noren and Pasquale 2004; Pasquale 2008,2010; Lisabeth et al. 2013). Therefore, it was important to test what happens to other family members in response to EphA2 loss. We found that EphA1 is significantly upregulated in response to EphA2 loss (P = 0.0045), potentially indicating that EphA2 loss is compensated for by EphA1. Analysis of two known ephrin-A ligands that bind EphA2 found general trend increases in $EphA2^{-/-}$ relative to $EphA2^{+/+}$, but this did not achieve significance (Fig 3.13 D; P =0.0528, Fig 3.12 E; P =0.2323). In summary, these expression profiles show that EphA2 loss drives an initial boost in EphA2 transcription possibly by feedback regulation in the tissue, ultimately, no functional transcript is produced which leads to upregulation of EphA1 receptors instead.

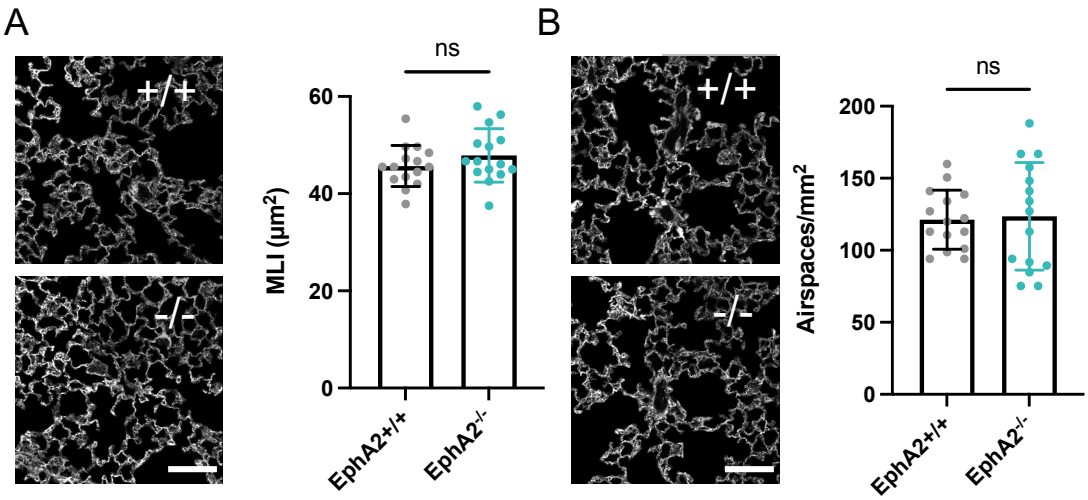

Figure 3. 12 EphA2 loss of function does not affect lung morphology.

A) Mean linear intercept (MLI) is a readout of mean free space in alveoli and not an indicator of alveolar size. No significant changes are observed between EphA2 WT ($EphA2^{+/+}$) and EphA2 homozygous knock-out ($EphA2^{-/-}$). B) Quantitation of airspace number per field of view. No changes observed between genotypes. Data points represent field of view from total n = 3 mice. Bars = mean± SD. Image shows phalloidin stain of F-actin. Scale bar = 50 µm. Unpaired student's T-test, ns = non-significant, P >0.05.

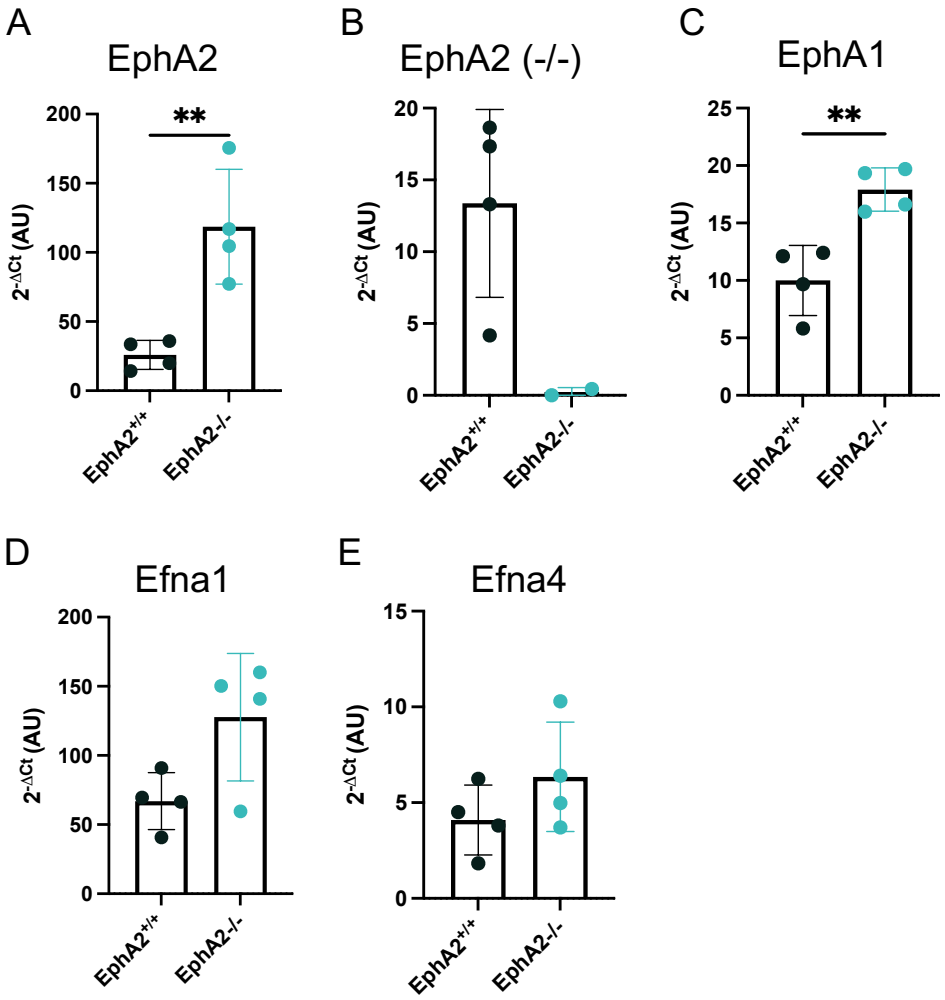

Figure 3. 13 EphA2 knock-out corresponds to an increase in EphA1 transcription.

Quantification of gene expression by qPCR of Eph receptors EphA2 **(A, B)** and EphA1 **(C)**, and EphA2-activating ephrin ligands Efna1 **(D)** and Efna4 **(E).** Bars represent Mean ± SD, and data points represent $2^{-\Delta CT}$ values from n = 4 mice, where Ct values greater than 40 were undetermined and not displayed, signifying low or no expression. Unpaired Student's t-test, **P < 0.01.

3.3 Discussion

3.3.1 KrasG12D mutant cells are not eliminated from the mouse lung epithelium.

In this chapter, we set out to establish if KrasG12D mutant cells undergo competitive interactions with their WT neighbours in the lung epithelium in order to maintain homeostasis via a process known as cell competition. To do this, we employed an established model of Kras-driven tumorigenesis in mice (Jackson et al. 2001; Tuveson et al. 2004; Kim et al. 2005; Kissil et al. 2007; DuPage et al. 2009; Best et al. 2019; Dost et al. 2020), subsequently affirming the suitability of the model for our study. With a single dose of adenoviral Cre recombinase, we were able to observe hyperplastic lesions at 1 week post induction (Fig 3.11 B), expansion of induced KRasG12D populations across a 5-week timeframe (Fig 3.7), and histologically pro-SPC positive, KRasG12D positive tumour lesions at 10-weeks post induction (Fig 3.4), confirming that the model drives a lung adenocarcinoma phenotype.

This model has robustly been shown to initiate tumorigenesis within a relatively short timeframe (around 3 weeks), and singular activating mutations in KrasG12D are sufficient to drive hyperplastic growth from 2 weeks onwards (Jackson et al. 2001; Johnson et al. 2001; Tuveson et al. 2004; Kissil et al. 2007; Best et al. 2019). In our studies we deliver a relatively high dose of AdCre compared to what is necessary for tumour induction; using 1 $x10^8$ PFU AdCre as a standard dose compared to either 5 x 10^5 PFU (Jackson et al. 2001) or 2.5 x 10^7 PFU (DuPage et al. 2009) which both drive hyperplasia at 6 weeks post infection with KrasG12D alone. The aim of this was to generate a large enough sample size to measure interactions between induced and non-induced cells in the airways and distal lung epithelium, ensuring a reliable level of induction from mouse to mouse. We found that 1 x 10^8 PFU was suitable for this as there was a good balance of RFP positive and RFP negative cells in cross sections of bronchioles, however, infection of distal lung cells was somewhat limited throughout our experimental cohorts. This lack of distal lung induction is partially accounted for by the stochastic nature of inducing single cells with a measured number of viral particles which could be overcome by assessing delivery technique.

In their comprehensive analysis of adeno-associated virus (AAV) distribution, Santry et al. (2017) assess the degree of distribution amongst key aspects of the respiratory tract in response to intranasal instillation, a modified intranasal technique

which involves additional closure of the mouth, intratracheal instillation, and an intratracheal injection method. Intranasal administration, either as was performed in this study or with modified technique, resulted in intense staining of the upper respiratory tract, namely the nasal cavity, trachea, and most proximal airways. There was some expansion of the staining into the distal lung, but it's clearly uneven throughout all specimens. When introduced intratracheally however, Santry et al. observed much stronger staining of distal lung and naturally less intense staining in the upper respiratory tract. Even though AAVs are smaller than adenoviruses, these findings demonstrate clearly how intranasal administration may not be the optimal method for delivering a robust volume of virus for transgene induction. Moreover, a potential explanation of the lower levels of induction in the distal lungs is that AdCre could be lost to the nasal cavity and trachea which were not analysed in my cohorts. To distribute virus more evenly across the proximal-distal lung, the current gold standard is an intratracheal instillation, which would be more desirable and uses less virus to achieve similar levels of recombination (DuPage et al. 2009; Yeddula et al. 2015; Sanclemente et al. 2018; Dost et al. 2020; Concepcion et al. 2022). As a consequence of travel restrictions imposed during the 2020 COVID-19 pandemic and subsequent limited training opportunities, intranasal administration was the only option we had which was still sufficient for research aims to be met. Although we achieved success from our model, switching to intratracheal would be a refinement to our model that would ensure a greater degree of recombination *in vivo* in the distal lung, and would better permit the study of early response to KrasG12D activation.

Next, I was able to show that heterotypic interactions between KrasG12D mutant cells and their WT neighbours do not lead to apical elimination from the epithelium as was previously expected (Fig 3.9 B). General observations from this experiment showed a much lower number of cells that were not undergoing extrusion compared to previously published articles (Sasaki et al. 2018; Shirai et al. 2022). This might suggest that compared to the tamoxifen inducible systems, intranasal administration and subsequent adenoviral infection could potentially drive airway shedding regardless of genotype, instead of KRasG12D-driven cell extrusion. Interestingly, I observed that at 2 DPI, more KrasG12D mutant cells were categorised as undergoing the initial stages of extrusion indicated by an apical translocation of the nucleus but had not yet been fully extruded from the epithelium. Relative tissue turnover rate of the lung epithelium is slow (Rawlins and Hogan 2006), therefore, measured changes in population number are unlikely to be an attribute of normal lung physiology. Controversially, airway cells exhibit a strong preference for division along the apical-basal polarity of the cell (El-Hashash and Warburton 2011), with the nucleus

supposedly moving apically in the cell as a part of cell division. This phenomenon could explain such high backgrounds of what I classified to be ‘extruding cells’ and could mean that this metric for analysing competitive elimination is flawed and overshadowed by standard tissue homeostasis. To complement the level of extrusion in the airway epithelium, bronchioalveolar lavage fluid could be taken upon dissection, processed for flow cytometry, and the number of CD45-, CD31-, EpCAM+, RFP+ cells counted as extruded cells free floating in the epithelium. However, this approach may not detect small numbers of cells particularly if the viability of extruded cells is low prior to processing for flow cytometry.

Previous findings have demonstrated HrasV12 mutant cells are extruded apically from epithelia between 3 days to 1 week post induction in the lung, and beyond this time point from the epithelium of the pancreas and mammary gland (Sasaki et al. 2018; Shirai et al. 2022). Though our previous findings are consistent with the latter of these observations (Hill et al. 2021), the current findings presented in this chapter show that apical extrusion is not a mechanism by which KrasG12D mutant cells are eliminated in the lung. Furthermore, any instances of dome-like structures that are proposed to occur in the later stage of HrasV12 activation (Shirai et al. 2022) were not found across the airway epithelium during my analyses. HrasV12 is not frequently found in lung cancers (Prior et al. 2012; Drosten et al. 2017), and is shown to induce a more dramatic oncogene-induced senescence phenotype compared to KrasG12V mutant cells in the lung at early timepoints (Sanclemente et al. 2018). Furthermore, there may be some evidence suggesting that activating KRasG12D mutations have a lower baseline ERK activity than other Kras isoforms such as G12C and Q61R (Gillies et al. 2020). Taken together, these findings may suggest that extrusion of cells from columnar epithelia is dependent on prolific Ras activity and may not be a response to milder activating mutants such as KrasG12D. In future work, it would be interesting to investigate this with the hypothesis that prevalence of different Ras isoforms and orthologs across different tissue types is dictated by the tissue’s inherent response to cope with their burden in the epithelium, inclusive of cell competitive mechanisms and interactions with the surrounding wild-type epithelium.

To support my finding in proximal lungs that KrasG12D mutant cells are not eliminated, I assessed alternative readouts of cell elimination in the alveoli, using predictive morphological changes to assess if KrasG12D mutants were being selected and prepared for elimination. Our lab has previously established a conserved mechanism by which relatively normal cells repel Ras mutant cells by EphA2-

dependent mechanisms in *Drosophila,* murine pancreas and in culture models (Porazinski et al. 2016; Hill and Hogan 2017; Hill et al. 2021). If elimination via previously explored mechanism were to occur, a reduction in cell area and increased rounding up of the cell would be expected. This was not observed for KrasG12D cells when surrounded by normal cells in the lung, suggesting that KRasG12D mutant cell are not detected by normal neighbours and prepared for elimination in the lung, and potentially indicates that EphA2 does not contribute to homeostasis as we hypothesised (Fig 3.10).

Previous work from our lab identified a role for the EphA2 family members in driving repulson of HrasV12 mutant cells away from neighbouring WTs (Porazinski et al. 2016), and showed that *in vivo*, KrasG12D mutant cell area decreases, and a mutant cluster of cells circularity increases in an EphA2 dependent manner (Hill et al. 2021). Therefore, if this mechanism was conserved in the lung, these metrics would potentially be readouts of EphA2-dependent responses in normal-mutant cell-cell interactions. A limitation of these analyses is that lack of validation of proteins in the mammalian tissue. Early on, we encountered issues pertaining to visualising EphA2 protein as we aimed to assess the degree to which it is expressed in the lung epithelium, whether different cell types have different levels, and if there was a regional specificity to the protein. However, numerous attempts with many of the currently available EphA2 antibodies yielded poor results and specificity compared to $EphA2^{-/-}$ tissues and subsequently it EphA2 could not be located in the lung epithelium. Similar issues were encountered when trying to measure total protein concentration of EphA2 using Western blotting.

We sought to further explore the role of EphA2 in the lung, and whether or not its function is redundant, as we do not observe any competition phenotype that would indicate otherwise. Analysis of the EphA2 gene and EphA- ephrin-A family members revealed a potential compensatory upregulation of *EphA1* in $EphA2^{-/-}$ lungs (Fig 3.13 C). EphA receptors are known for their ability to bind to multiple ephrin-A ligands to initiate signalling events (Lisabeth et al. 2013). Another implied function of EphA2 is its role in branching morphogenesis in development, particularly a role in breast mammary gland branching (Vaught et al. 2009). I postulated that if this mechanism was conserved in the lung, and Epha2 was functionally required from development perhaps lung architecture would be influenced in $EphA2^{-/-}$ mice. By looking at readouts of postnatal development such as mean linear intercept and airspace number I concluded that EphA2 is not required for proper patterning of the developing lung (Fig 3.12 A and B).

3.3.2 KrasG12D mutant cells undergo morphological changes akin to transient cell states in lung fibrosis.

Contrastingly to what we hypothesised, KrasG12D mutant cells became less rounded and exhibited a trend towards being more spread out in the tissue (Fig 3.10 B-C). Interestingly, this phenotype suggests a differentiation response from ATII cell morphology (smaller area, mostly cuboidal and therefore small P: A ratio, and high roundness) into ATI cells (squamous epithelial cell, high P: A, low roundness). This phenotype has previously been identified in response to lung injury pathways, specifically where aberrant populations of ATII cells in the distal lung transdifferentiate into a Krt8+ subpopulation, exhibiting decreased sphericity and ATI cell-type markers (Strunz et al. 2020). This fits into a broader category of interest in the lung homeostasis field whereby lung injury and epithelial perturbation drives remodelling of ATII to ATI cells in the lung (Riemondy et al. 2019; Choi et al. 2020; Toth et al. 2023). Further support for this hypothesis comes from a recent study that shows a mechanism by which p53 activity ushers KrasG12D mutant cells into ATI-like cells, which upon loss of p53 leads to more severe adenocarcinoma progression from adenomas (Kaiser et al. 2023). Therefore, these findings suggest that upon KrasG12D activation the lung epithelium is unable to get of rid of problematic cells and must therefore repurpose them to less-influential cell types such as the progenitor-like ATII cells into quiescent ATI cells. With this in mind, it would be plausible that abrogation of p53 in our model would lead to loss of these morphological changes.

3.3.3 Summary and future directions.

In summary, my findings presented here hint towards a mechanism of selective homeostasis that prioritises mutant cell elimination on a danger-to-benefit system, whereby potentially slow-killer mutants like KrasG12D may not pose an initial threat to the airways and are therefore retained to maintain tissue barrier integrity. In the alveoli, KrasG12D mutants may be set aside in a similar way by p53 dependent mechanisms which aim to preserve functionality of the gas exchange surface. Following this work, I set out to identify whether the induction of oncogenic KrasG12D in the alveolar lung induces an injury-like response whereby mutant ATII cells are changed in the days following oncogenic insult.

4 Developing an *ex vivo* tool to model epithelial dynamics in the alveoli following KrasG12D activation.

4.1 Introduction

Technological advances in science in recent years have given rise to a wealth of models that are regularly used in lung research. Many of these address lineage tracing in the lung whether via Cre promoter-driven induction as in the *Scgb1a1*, *HOPX* and *Sftpc* lines, or by modifying approaches such as intratracheal or intranasal instillation to drive specific tropism of adenoviral vectors to CC10 or SPC positive cells. However, these models still suffer from the caveats that limit the use GEMMs to explore complex cell biology process in real time, *in situ*. Furthermore, the capacity to perform live imaging experiments *in vivo* is restricted by the infrastructure and licensing in place at research facilities making it the less amenable option for experimentation. Ultimately, the lung is notoriously tricky to model faithfully, and all-encompassing models are still not present in the field.

2D cell culture models have been extensively used to evaluate cellular processes in research, outside of the context of the body. 2D cultures can be derived from primary tissues from mice or humans and can be cultured within a few hours. Alternatively, immortalised cultures can be purchased from large repositories such as the American Type Culture Collection (ATCC). Out of 39 lung epithelial cell lines available on the ATCC, only 7 are derived from normal, non-diseased tissues. Some of these lines such as BEAS-2B and various human bronchial epithelial cells are regularly used, however they lack mature cell types and fail to recapitulate the epithelial arrangement of cells in submerged culture.

To achieve this added level of detail, bronchial epithelial cells can be cultured at the air liquid interface (ALI), whereby progenitor basal cells in the culture differentiate when exposed to air and give rise to goblet cells, club cells, and ciliated cells (Bluhmki et al. 2020). ALIs demonstrate relatively normal proximal airway functionality such as a working mucociliary beat, mucous secretion, and high trans-epithelial electrical resistance, indicative of strong epithelial integrity. ALIs can be generated as part of a co-culture, with some studies demonstrating endothelial, differentiated epithelial and macrophage co-cultures to model a more complete picture of the proximal airways *in vitro* (Klein et al. 2013). Though they are better representative of the arrangement of cells in the epithelial layer, and more importantly reciprocate polarity at the air-liquid interface, there are major drawbacks to ALI that limit their use in research. Established cell lines introduce limitations depending on the cell line used, for example BEAS-2B cells do not for tight junctions, and the normal human bronchial epithelial cells (16HBE) have less mucous production compared to primary derived bronchial epithelial cells (Upadhyay and Palmberg 2018). Alternatively, commercially available ALI cultures have a lifetime of 3-12 months but

are often more difficult to customise and manipulate genetically, not to mention more expensive than in-house ALI development (Zscheppang et al. 2018).

Organoids possess the greatest level of versatility in *in vitro* models of lung. Currently, most regions of the lung can be recapitulated in organoid form, either as bronchospheres, tracheospheres, alveolar organoids, and bronchiolar organoids derived from mice or human lungs (Lu et al. 2021). Furthermore, organoids are ideal for co-culture scenarios, genetic manipulation, and standard research techniques such as microscopy, molecular biology, and histology. However, organoids do not faithfully capture the organisation of cells in 3D space as they exist *in vivo*, which is a key aspect in the lungs ability to respond to injury and other insults. Our research question required analysis of cellular responses in real time, understanding how spatial relationships between the epithelial compartment and other parts of the lung influence response to acute KrasG12D activation. Therefore, we opted for a precision cut lung slices (PCLS) model.

Precision cut lung slices are an easily-implemented system, making use of existing mouse models in the lab. Sectioning live lung tissues and culturing them in standard conditions has permitted the observation of developmental stages (Akram et al. 2019), acute lung injury processes (Kim et al. 2021), as well as investigating the lung *ex vivo* following chronic fibrosis by bleomycin *in vivo* (Strunz et al. 2020). PCLS can be used for quantitative live-cell imaging, 2D and 3D microscopy, molecular biology analysis, and airway physiology (Akram et al. 2019; Strunz et al. 2020; Kim et al. 2021; Cheong et al. 2023; Dean and Cheong 2023; Bagley et al. 2024). A pitfall of PCLS models is the limited time that they can be cultured, and whether resident immune cells are present at the time of extraction, without air-liquid interface culture. In the chapter, we aimed to establish what occurs in the distal lung in response to KrasG12D activation. We set out to achieve this by first generating a PCLS model of early tumorigenesis using our existing genetic mouse line, then optimised protocols for immunofluorescence microscopy in 2D, 3D, and live time-lapse.

4.2 Results

4.2.1 Generating precision cut lung slices

To address questions raised in the previous chapter, we opted to establish an *ex vivo* model of distal lung biology in collaboration with Dr Charlotte Dean (Imperial College) and with the help of Ellis Jones, a Cardiff University MSc project student in the lab. In the first iterations of PCLS experiments, the main objective was to establish a robust system for generating slices with equipment that was available to us in Cardiff. From dissection, lungs were inflated with, and embedded in 2% low melting point agarose (Fig 4.1 A). Left lung lobe blocks were trimmed into trapezoidal shapes to ensure a wide base for providing structure when cutting, and to expose the top and bottom of the tissue. This secured the tissue to the vibratome stage, and reduced time spent cutting unnecessary sections of tissue.

On the vibratome, two lobes could be prepped simultaneously based on positioning of the blocks on the stage and careful transfer of slices from the vibratome basin (Fig 4.1B) to a prepped 24-well plate with media (Fig 4.1 C). Slices were generated from the middle 2/3rds of the left lung, sectioned transversely to ensure even sizing of consecutive slices (Fig 4.1 C). Following experimental culturing conditions outlined by our collaborator (Akram et al. 2019), slices were cultured in serum-free DMEM, supplemented with 1% Penicillin/streptomycin mix and 1% GlutaMAX. Upon sectioning, slices were incubated for 1 hour at 37˚C, before performing two washes in fresh, pre-heated media, and transfer to a fresh, sterile 24 well plate.

A benefit of using an *ex vivo* system such as PCLS is that all structures of the lung are represented in slices when processed correctly. To assess our success in this task, we stained PCLS with a primary antibody against Epithelial Cell Adhesion Molecule (EpCAM) conjugated to FITC (EpCAM-FITC) to reveal epithelial structures in the slice (Fig 4.2 A). A closer look at some stand-out structures revealed the presence of bronchoalveolar ductal junctions (Fig 4.2 Ai), large bronchiolar airways (Fig 4 Aii), and depending on the location in the tissue, bifurcating airways (Fig 4.2 Aiii). As EpCAM is epithelium-specific, endothelial cells were not directly observed in Figure 4.2 A, however, the negative imprint of their presence could be seen in the autofluorescence of the tissue such as in Figure 4.2 Aii, left of the airway which is expected of larger bronchioles. The endothelial cells of the lung are closely associated to parenchymal structures, particularly the alveoli, where intricate innervation of the gas exchange surface permits efficient gas exchange. Therefore, we stained slices

with a CD31-APC antibody which is compatible with live-cell imaging, revealing a network of EpCAM-, CD31+ cells that closely resemble the structure of alveoli (Fig 4.2 B). Finding these structures in PCLS samples demonstrates the suitability of the model to study interactions in a systems relevant way.

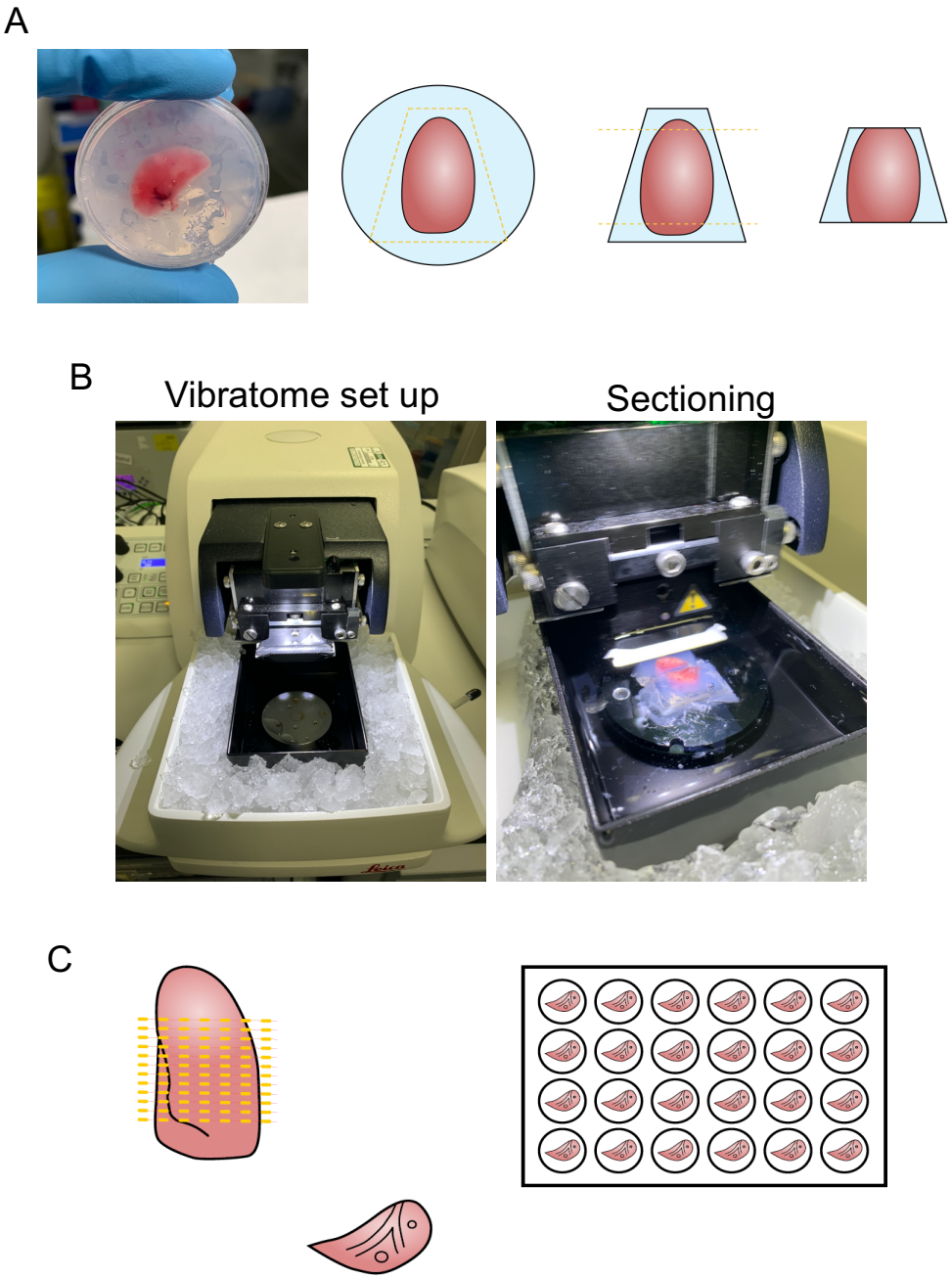

Figure 4. 1 Generation of Precision Cut Lung Slices using vibratome-based tissue sectioning.

A) Left lung lobes are inflated and embedded in low melting point agarose gels (2%), then trimmed to trapezoidal blocks for sectioning, ensuring the top and bottom of the tissue are exposed. **B)** Tissue blocks are mounted to a vibratome, submerged in ice-cold HBSS, and sectioned at 300 µm thick. **C)** Lungs were cut along the transverse plane, and slices generated from the middle 2/3rds of the tissue in order to generate evenly sized slices (yellow dashed lines). Slices were then incubated in DMEM substituted with 1% Pen/Strep and 1% GlutaMAX.

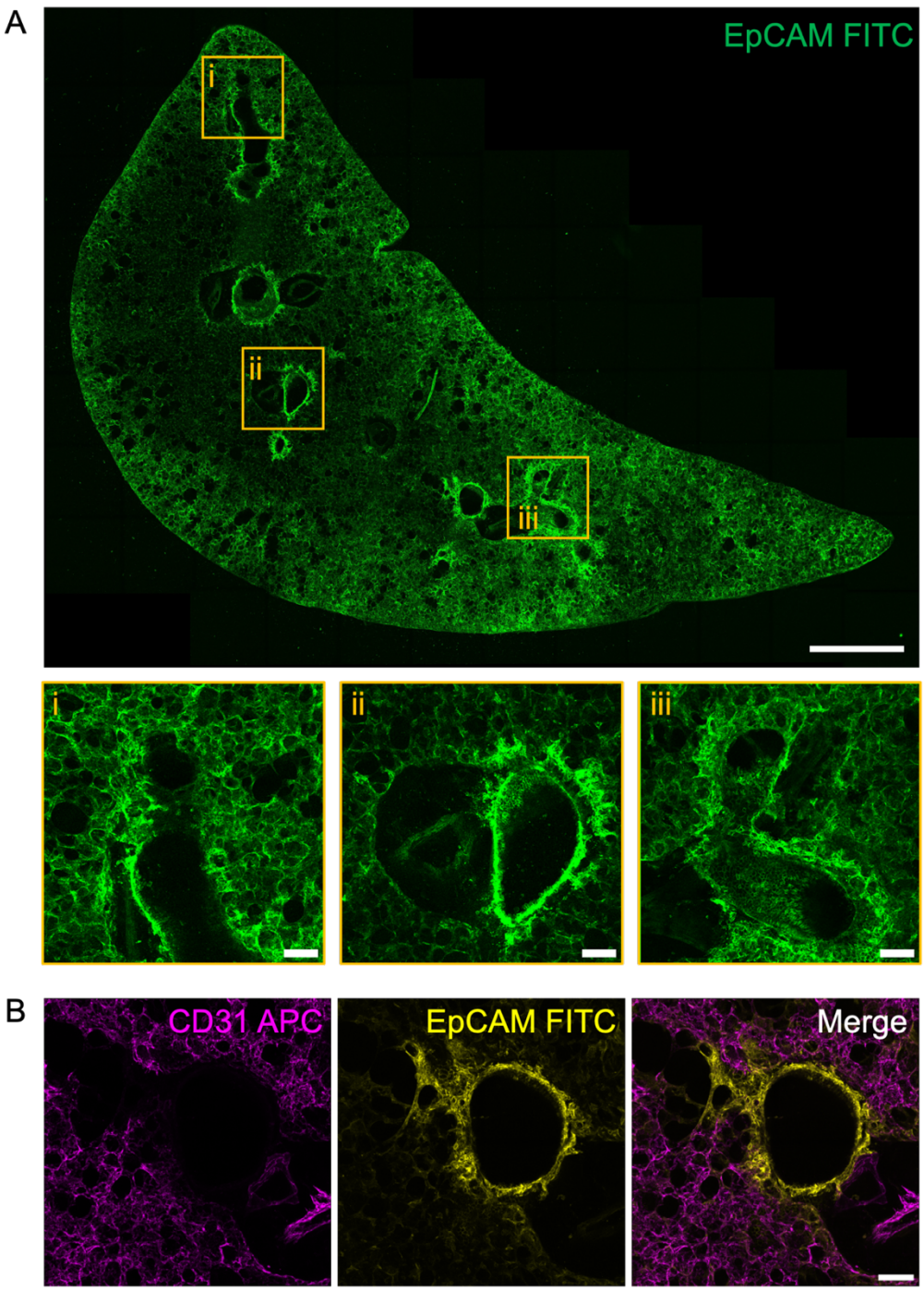

Figure 4. 2 Fluorescence staining of live PCLS reveal range of tissue architecture throughout the transverse section.

A) Whole section tile scan, taken as a z-stack and presented as a maximum intensity projection. Green lookup table represents EpCAM FITC, a general stain for epithelium. Yellow boxes show **i)** bronchioalveolar ductal junction and surrounding alveolar parenchyma, **ii)** an EpCAM+ airway directly adjacent to an EpCAM- blood vessel and **iii)** across section of a bifurcating airway with surrounding alveoli. **B)** Staining of endothelial cells using anti-CD31 APC antibody (magenta) and EpCAM FITC (yellow) shows specificity of stain, and integrity of structures in PCLS. Scale bar in large image represents 1000 µm, and small insets and B) 100 µm.

4.2.2 *Ex vivo* induction of PCLS with Adenoviral Cre recombinase.

After establishing that the slices remain visibly intact and contain key structures, I next aimed to assess the metabolic viability of PCLS in culture, with or without induction. PCLS present a key opportunity to study the dynamic changes that occur in the distal lung epithelium, therefore we experimented with inducing PCLS *ex vivo*, assuring more ATI cells would be targeted by AdCre compared to *in vivo*. To induce RFP transgenes, PCLS were generated, then incubated in 1 $x10^8$ PFU AdCre, a high viral titre relative to the amount of tissue being induced. Next, to assess viability I made use of an MTT assay (Section 2.6.3) on day 2 and 7 of culture, in uninfected PCLS and PCLS which had been infected with 1 x 10^8 PFU AdCre for 16 hours (Fig. 4.3 A). This dose was used as the highest sustainable dose of AdCre that could be delivered without exhausting viral stocks, and is the same dose as delivered to the entire lung *in vivo*. PCLS were checked daily, and no degradation of tissue or architectural changes were noted by brightfield microscopy (Fig 4.3 B).

Analysis with MTT assay first revealed that between 2 and 7 DPI, uninfected PCLS absorbance and therefore viability remain unchanged across 7 days of culture ($p = 0.2794$). Similarly, no negative changes in viability were observed in viability across 7 days of culture in infected PCLS, suggesting that PCLS are viable upon infection with AdCre for at least 7 DPI (Fig 4.3 C). At 2 DPI, infected PCLS have a significant reduction in viability compared to uninfected PCLS (Fig 4.3C, $P =0.0187$). A similar reduced viability is observed at 7 DPI ($P =0.0372$), however stability of viability across 7 days is enough remain confident that PCLS are viable upon AdCre infection. Comparison of infected and uninfected PCLS to PCLS that were incubated in 100% methanol for 2 minutes reveals the extent to which the PCLS are still viable after induction. Methanol fixed slices had next to no measured absorbance and could be described as no longer viable in culture. Therefore, although PCLS take an initial hit in viability upon AdCre infection, they remain viable for further experimentation for at least 7 days post infection.

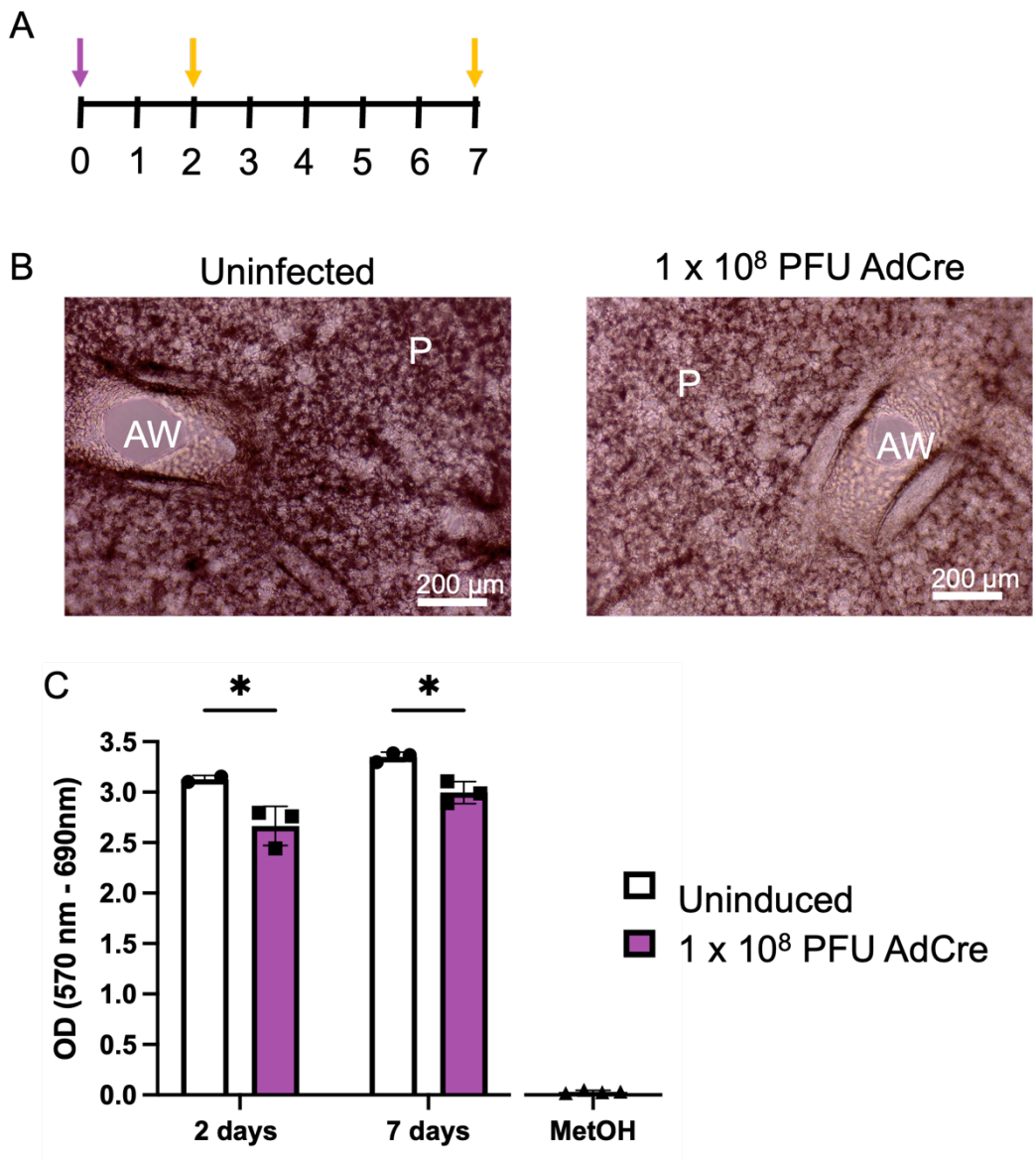

Figure 4. 3 PCLS infected with AdCre remain viable in culture for at least 7 DPI.

A) Schematic diagram for testing viability of PCLS in culture. Slices were generated and infected with 1 x 10^8 PFU on day 0 (yellow arrow). Assays were carried out on day 2 of culture, and on day 7 (red arrows). **B)** Representative images of PCLS 2 days in culture, one uninfected (left) and one infected with 1 x 10^8 PFU of AdCre. AW = airway, P = parenchymal tissue. **C)** MTT assays were carried out 2 days post-infection, and 7 days post-infection on both uninfected and PCLS. To portray what a dead slice looks like, PCLS were treated with 100% methanol (triangles; MetOH) for 2 minutes prior to the first incubation steps. Absorbance was measured at 570 nm and corrected at 690 nm, revealing that there is a small decrease in viability in infected tissue, but this does not pose a viability problem by day 7. Two-way ANOVA with Bonferroni's post-hoc test. *P<0.05. Bars are Mean ±SD. N = 1 mouse, each data point represents a PCLS. Scale bars = 200 µm.

4.2.3 Bronchioles are not reliable in our system of PCLS

Recently PCLS have been used to explore airway responsiveness to allergic exacerbation (Bagley et al. 2024), therefore we were curious whether airways in our PCLS could potentially bridge a gap between induction and timepoints analysed *in vivo*. Indeed, imaging of bronchiolar airways revealed typical patterning of the bronchiolar epithelium with F-actin, and interestingly highlighted striated smooth muscle fibres encasing the bronchioles (Fig 4.4A). In induced PCLS, RFP positive cells could be detected throughout the epithelium, expressed in a mosaic fashion between un-induced cells (Fig 4.4B). This would indicate that *Ex vivo* induction drives sufficient recombination of airways for good mosaic patterning. However, observing airway structures with brightfield microscopy when PCLS are in culture revealed that airways become denuded with observed shedding of bronchial cells within days of starting culture (Fig 4.5). Shedding was observed in both WT (Fig 4.5 A) and KrasG12D PCLS (Fig 4.5 B), with clusters of presumed epithelial cells were found free floating in airway lumen. At other times, I observed no epithelial cells connected to the stroma (Fig 4.5, white dashed lines). These changes to the airway were only made partially visible by the presence of some cells that remain in place.

Therefore, it was decided that PCLS were an unreliable system for analysis of potentially rare extrusion events in the bronchioles due to the rate of detachment seen *ex vivo*, and we instead focused on alveolar lung tissue compartments in PCLS experiments.

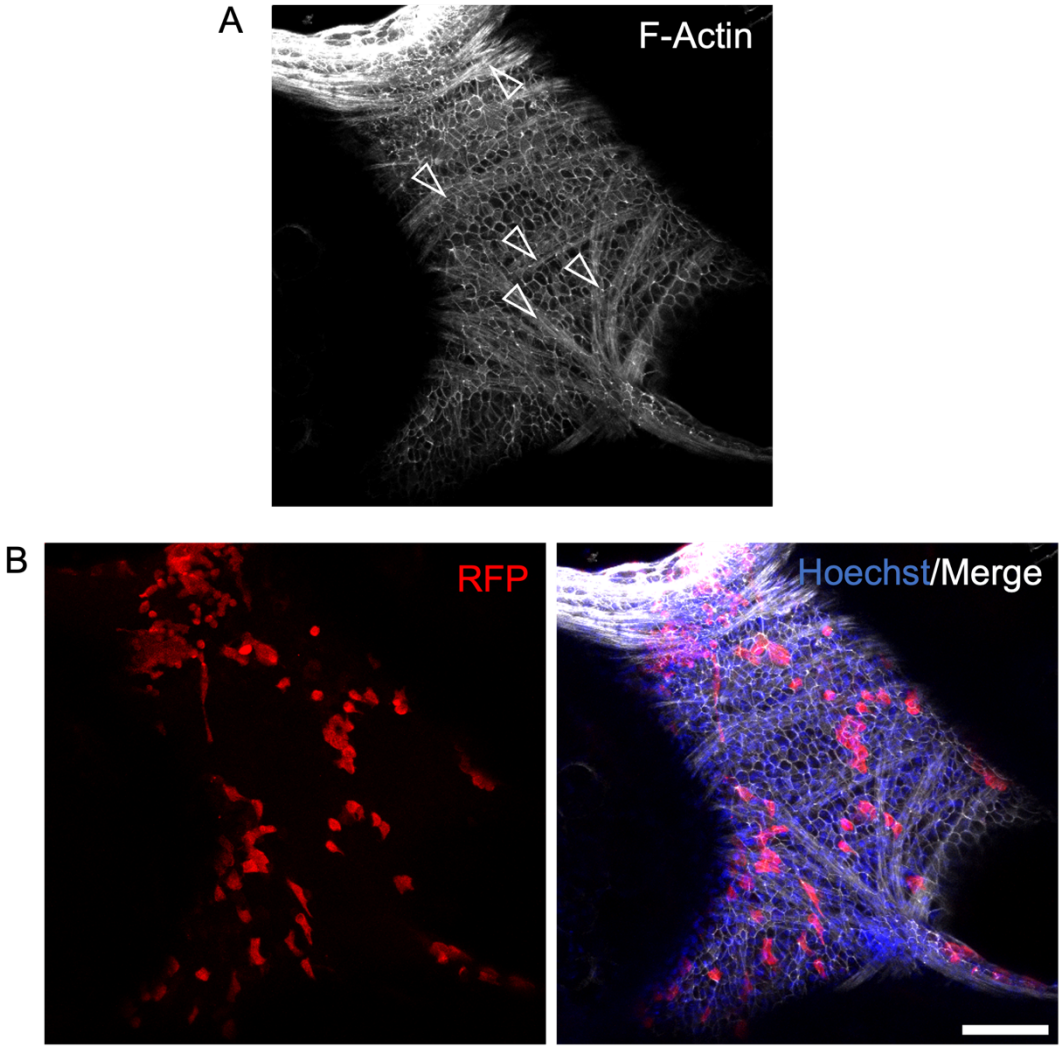

Figure 4. 4 Bronchiolar airways are present in PCLS.

A) Phalloidin staining of filamentous actin (F-actin) in PCLS. Staining reveals cobblestone epithelial layer, but also the presence of striated smooth muscle bands around the outside of the bronchiole (white arrow heads). Banding patterns indicate a bifurcation or domain branch of the bronchiole. **B)** In the same image, induction with 1 x 10^7 PFU induces mosaic patterns of recombined cells of the airways. RFP (red), Hoechst stained nuclei (blue) and F-actin (grey). Scale bar, 100 μm. Maximum intensity projection of image acquired at 20X magnification.

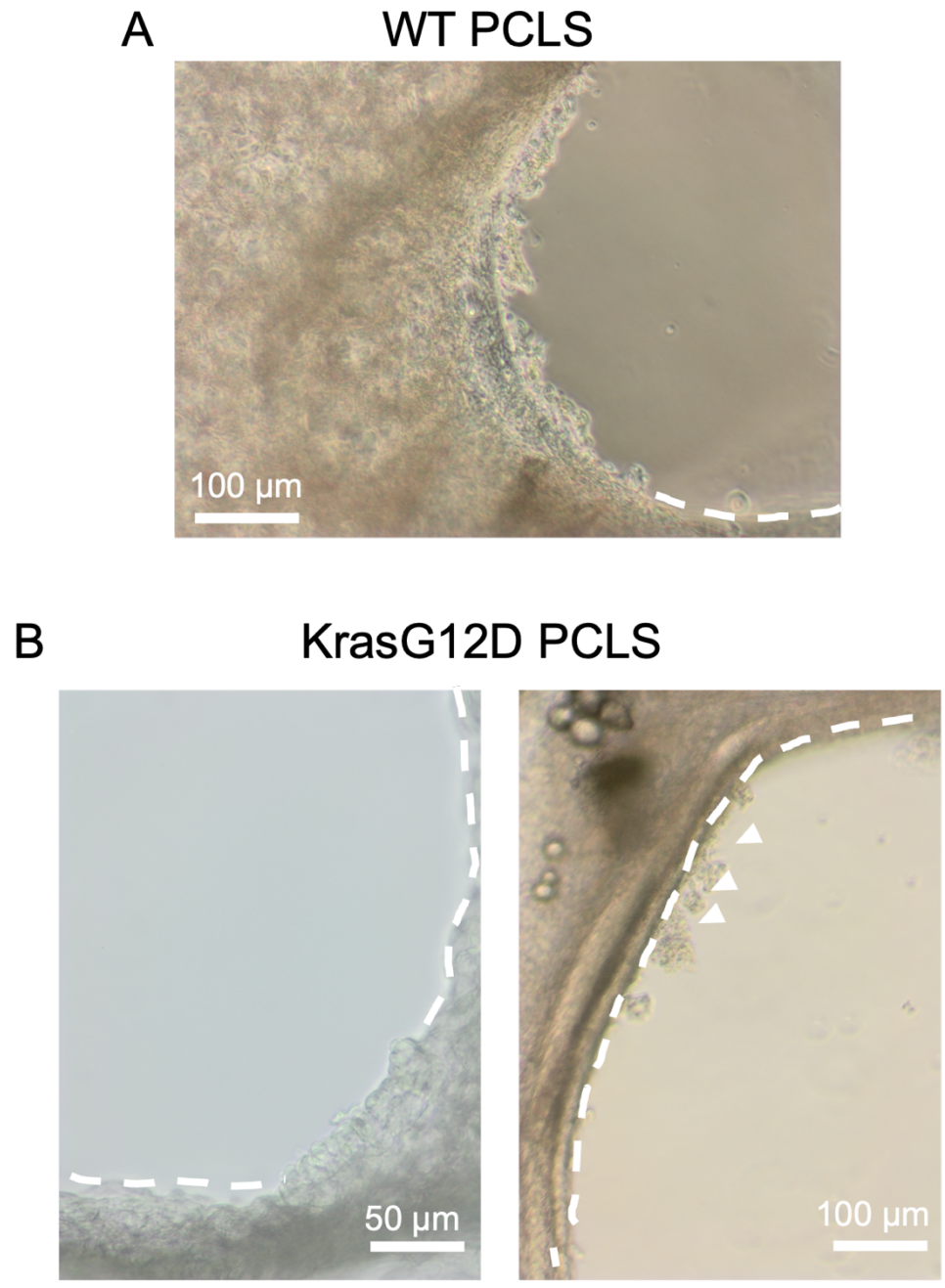

Figure 4. 5 Bronchiolar airways are not well maintained in PCLS.

Viewing airways of PCLS in culture reveal that airways are denuded from at 2 days in culture independently of KRasG12D genotype. Dotted white lines demarcate airways that have shed their cellular epitheliumin **A)** WT airways, and **B)** KrasG12D airways. White arrowheads point towards buckeled or denuded airways that will eventually be shed from the airway.

4.2.4 Determining an optimal titre of AdCre to achieve sufficient transgene induction.

We next set out to establish a protocol that would ensure induction of RFP in a mosaic pattern throughout the alveolar epithelium. To do this, PCLS were infected with a range of AdCre titres from 1 x 10^8 PFU down to 1 x 10^1 PFU AdCre.

Images were acquired as Z-stacks to permit volumetric analysis of PCLS. Slices were infected for 16 hours overnight, then cultured to 2 DPI. Analysis was carried out by measuring RFP volume as a percentage of F-actin volume. Using this measurement, we observed that 1 x10^7 PFU drove the most robust response out of all doses (6.31 ±1.62%) (Fig 4.6A), even greater than 1 x 10^8 PFU (4.64 ±2.74%). Interestingly, 1 x 10^6 PFU appears to be the lowest that AdCre could be titred, having a mean RFP percentage of 3.34 ±2.56%. After this, 1 x 10^5, 1 x 10^4, 1 x 10^2, and 1 x 10^1 PFU all induced RFP in less than 1% of the PCLS (Fig 4.6A). At 2 DPI, this titre appeared to represent a good distribution of RFP+ cells in the alveoli (Fig 4.6B), and around 40-60 µm depth could regularly be achieved at 40X objective with oil immersion. As a result of this experiment, 1 x 10^7 PFU was selected as the optimal dose to induce Cre recombination events in tissues.

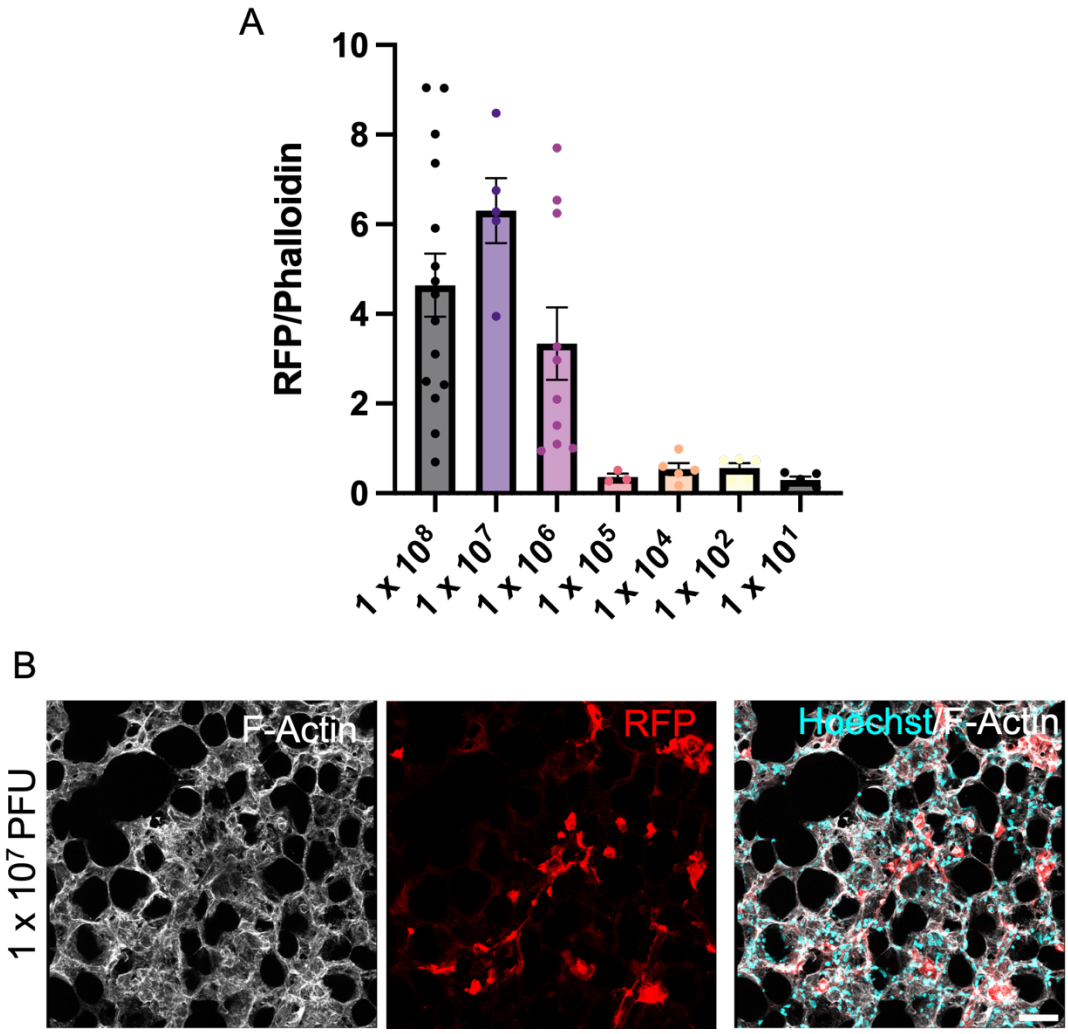

Figure 4. 6 1 x 10^7 PFU Adcre drives best recombination.

A) A range of viral titres from 1 x 10^8 PFU down to 1 x 10^1 PFU were tested on slices overnight. At 2 DPI, slices were fixed, stained and imaged in 3D for phalloidin and RFP. Data is presented as total RFP volume as a total percentage of phalloidin volume. Bars are Mean ±SEM, and data points represent fields of view used for analysis. **B)** Representative image of the 1 x 10^7 PFU dose which gave most stable and highest RFP expression at 2 DPI. RFP = red, F-actin = grey. Scale bar = 50µm, maximum intensity projection.

4.2.5 KrasG12D activation does not promote changes in RFP expression.

Next, I set out to establish what happens to the alveolar niche within the first week of induction *ex vivo*. PCLS were fixed at 2-, 5- and 7-DPI, stained for RFP and F-actin, and the number of RFP+ cells quantified as a percentage of total cells. Between WT and KrasG12D PCLS, no changes were observed at specified timepoints, and levels of RFP were comparable at 2 DPI (WT = 9.19 ±1.75%, KrasG12D = 10.38 ±2.48%), 5 DPI (WT = 23.77 ±10.45%, KrasG12D = 14.76 ±4.11%), and 7 DPI WT = 29.40 ±4.31%, KrasG12D = 28.66 ±8.00%) (Fig 4.7A). However, a significant effect across time was observed (Two-Way ANOVA, P =0.0013), with levels of RFP significantly increased in WT slices (Tukey's post hoc, P = 0.0344). Significance was not achieved, but RFP levels increased in KrasG12D PCLS (P = 0.0608) (Fig 4.7A).

This trend suggests that across the course of a week, more cells begin expressing RFP getting stronger by 7 DPI, or that baseline levels of proliferation in the slices results in greater RFP compared to 2 DPI. Representative images of WT and KrasG12D PCLS at 7DPI reveals the degree to which RFP expression is similar between the samples, and also the spatial distribution of RFP+ cells in the alveoli (Fig 4.7B).

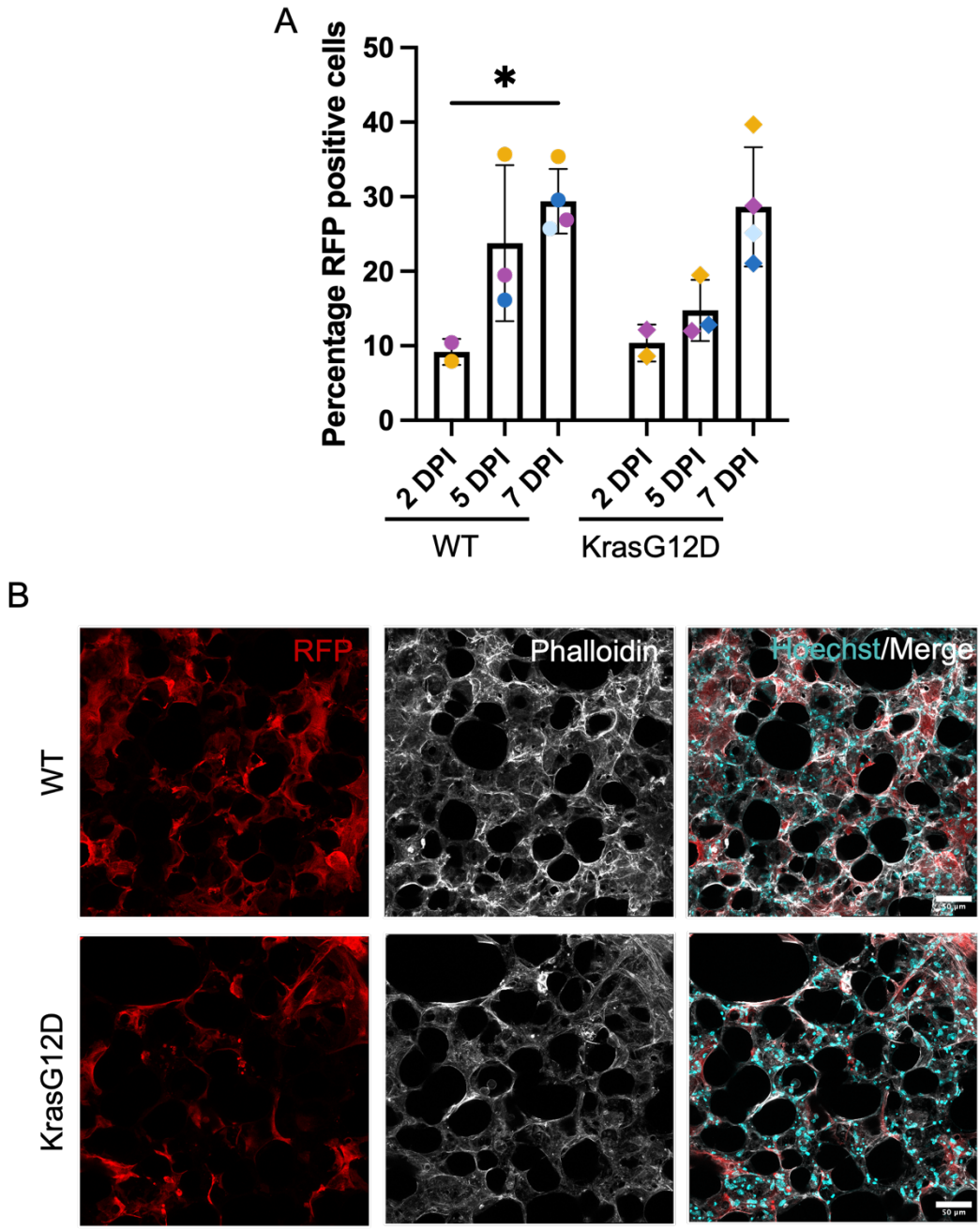

Figure 4. 7 RFP-expressing populations of cells do not change in response to KrasG12D activation.

A) Analysis of RFP+ cell numbers over the first week post induction at 2- 5- and 7-DPI, for both WT (circles) and KRasG12D (diamonds) PCLS. Data represent mean ±SD of percentage RFP+ cells per total cells. **B)** Representative images to show level of induction observed at 7 DPI in WT and KrasG12D PCLS. RFP (red), F-actin (grey), and Hoechst (cyan) shown as maximum intensity projections. Scale bar, 50 µm. N = 2 at 3 DPI, 3 at 5 DPI, and 4 at 7 DPI. PCLS generated from the same WT or KrasG12D mice are colour matched.

4.2.6 KrasG12D does not drive proliferation at 7 DPI *ex vivo*.

I next sought to identify if there was latency in RFP expression leading to the increases in RFP+ cells observed in the previous section, or whether this was driven by proliferation in the PCLS. To do this, I performed immunofluorescence microscopy of 7 DPI PCLS stained with Ki67, a general marker of cells between G1-M of the cell cycle. Analysis of total numbers of cells proliferating per field of view revealed similar levels of total cell proliferation at 7 DPI (Fig 4.8A), with 6.6 ±3.4% of WT cells positive for Ki67, and 6.7±0.7% of cells in KrasG12D PCLS (Unpaired T-test with Welch's correction, P =0.9726). Further stratification of these Ki67 positive cells into RFP+ and RFP negative revealed that 29.8±12.9% of Ki67+ cells in WT PCLS were also RFP+, and that 41.01±5.9% of Ki67 positive cells in KrasG12D PCLS were RFP+ (Fig 4.8B). These data suggest that potentially KrasG12D drives slightly more proliferation in KrasG12D PCLS, but this is not significant at 7 DPI (Welch's T-test, P = 0.4163). I did not observe proliferation with hyperplastic regions of tissue, and populations are evenly represented in all images such as in Figure 4.8 C. Another characteristic of KrasG12D activation in the distal lung is inevitably the hyperproliferation of ATII cells that will later develop into lung lesions, positively expressing the ATII cell marker Pro-SPC. Therefore, I carried out another immunohistochemistry on 7 DPI PCLs to view the levels of pro-SPC positive cells. Interestingly, the percentage of positive detected cells decreased in KrasG12D PCLS relative to WT PCLS (Fig 4.8D 27.41% to 20.18%). This unexpected result could suggest ATII cells are being lost from the tissue, or that KRasG12D mutant cells are losing their mature cell marker expression in a KrasG12D-dependent manner at 7 DPI. In summary, there is no indication that KrasG12D activation is driving hyperplastic responses in the epithelium at 7 DPI in PCLS. Immunohistochemistry of proliferation and mature ATII cells in 7 DPI PCLS.

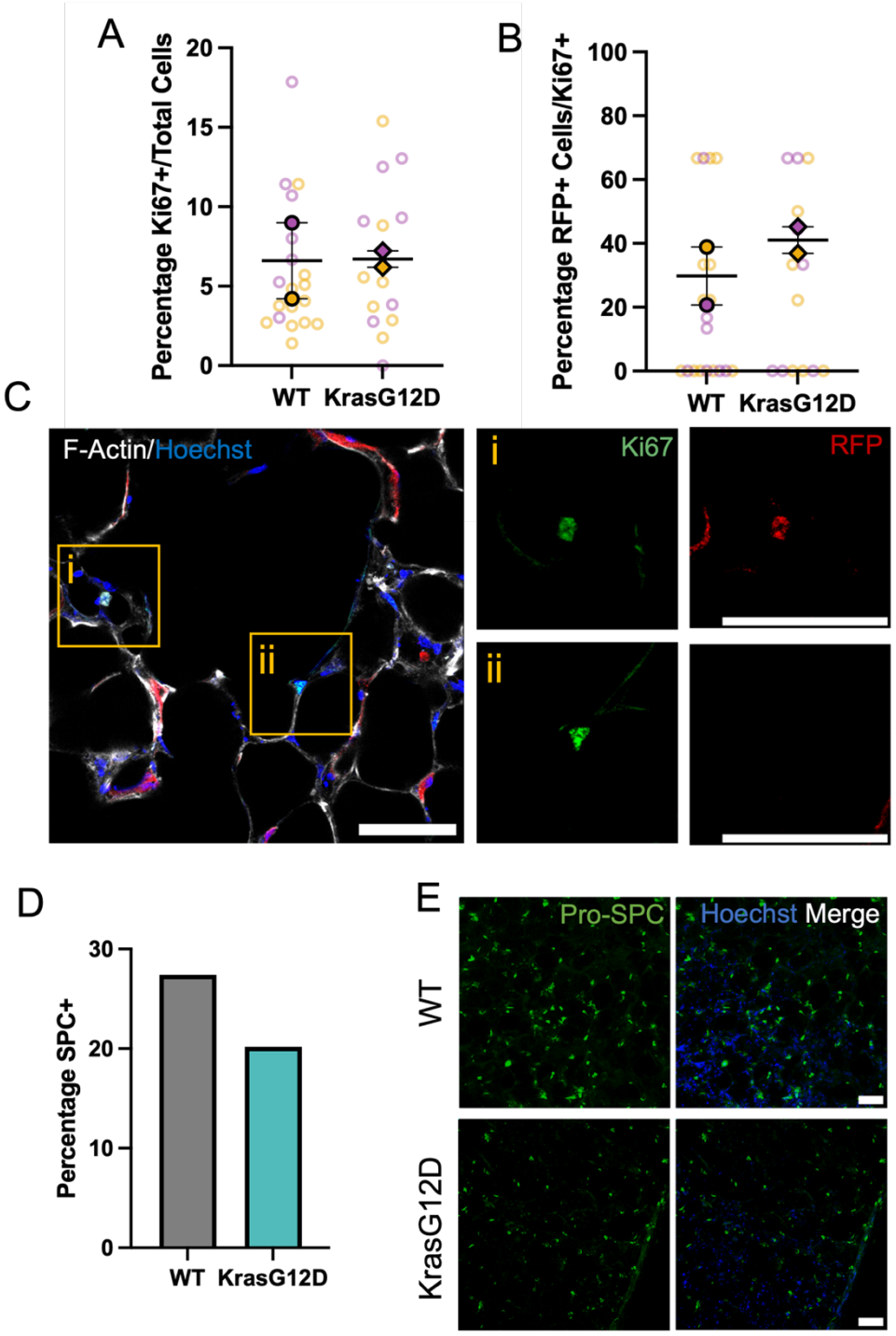

Figure 4. 8 Expression of KrasG12D does not drive excess proliferation of ATII cell hyperplasia.

A) Percentage of Ki67+ cells/total cells at 7 DPI. **B)** Percentage of Ki67+ cells stained positive for RFP. **C)** Representative images of proliferating cells stained positive (**i)** for Ki67 (green) and RFP (red). Some Ki67+ cells were negative for RFP **(ii). D)** Pro-surfactant protein C (ProSPC) quantification per total cell count. E) Representative image of Pro-SPC (green). Scale bars = 50 μm. Data represent Mean±SD. Solid data points show number of mice, coloured rings are corresponding fields of view that were counted. **D)** mean percentage SPC+ from n =1 mouse.

4.2.7 KrasG12D activation leads to a reduction in CD45+ cell migration.

We next established live imaging of induced slices to observe real-time changes in the lung microenvironment in response to KrasG12D activation. To do this, live PCLS were stained for 30 minutes in live imaging compatible antibodies (APC-CD45 and EpCAM FITC). Slices were next adhered to glass-bottom 6 well plates using a thin layer of 2% agarose. Alongside CD45 to image immune cells and EpCAM to visualise epithelial structures, I found that endogenous RFP could be used to visualise the cells that had been induced with AdCre. 5 DPI PCLS were imaged for 12 hours, with single tile z-stacks acquired every 30 minutes (Fig 4.9A, B, Supplementary Movie 1-4).

Compilation of images into movies revealed a dynamic environment of epithelial and immune cells. Cells expressing endogenous levels of RFP could be clearly identified in all samples (Supplementary Movies 1-4, Fig 4.9). CD45 APC labelled CD45+ pan-haematopoietic populations with high specificity. Live cell imaging showed that RFP+ cells are dynamic and highly mobile (Supplementary Movies 1 and 2). Throughout all movies, distinct CD45+ RFP+ cell can be observed. This is similar to our observation *in vivo*, suggesting that our previous observations were not caused by immune staining artefacts. RFP populations which represented KrasG12D activated cells were somewhat more hyperactive than their WT counterparts. In Supplementary Movie 4, the yellow box highlights an RFP positive cell extending a long cell process to a neighbouring RFP+ cell (Fig 4.10 A).

In all movies, CD45+ populations appeared to adopt typical and expected cell behaviours, e.g., engulfment of apoptotic cells (Supplementary Movie 2, yellow box; Fig 4.10 B). From side-by side comparison of WT and KrasG12D PCLS, it was immediately clear that the CD45+ populations were a lot less motile than CD45+ cells in WT PCLS movies (Supplementary Movies 3 and 4). In Supplementary Movie 3, a CD45+ cells can be observed dynamically moving between a cluster of RFP positive cells, even itself appearing RFP+. Conversely, the These observations suggest that expression of KrasG12D in epithelial cells affects immune-epithelial cell behaviours and cell interactions in the distal lung.

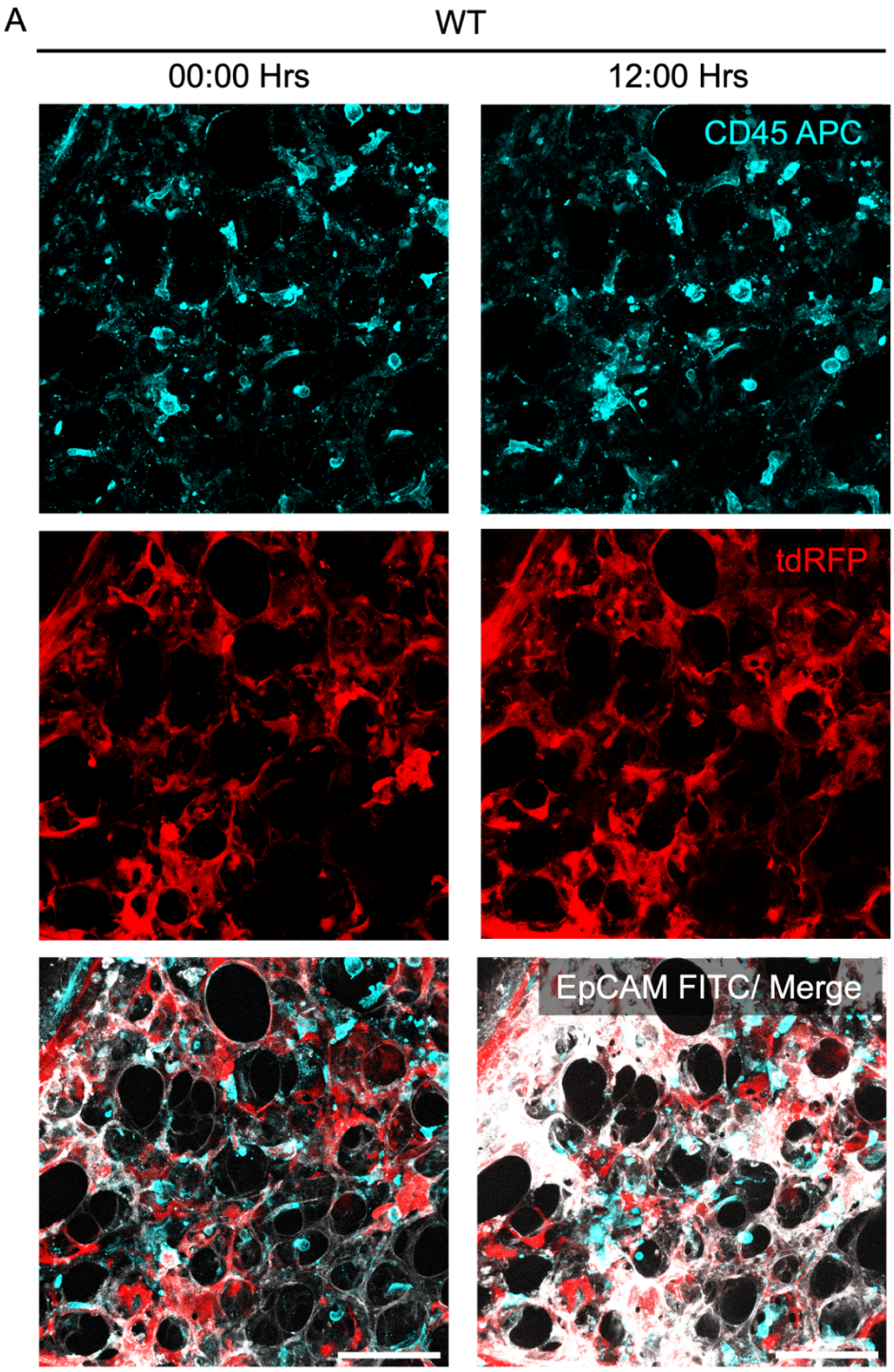

Figure 4. 9 Live cell imaging of precision cut lung slices.

PCLS were generated from **A)** WT and **B)** KrasG12D lungs (next page), infected as previous, and cultured until 5 DPI. At 5 DPI, PCLS were stained with CD45 APC (cyan) EpCAM FITC (grey) and embedded in 2% agarose in a glass-bottomed dish. PCLS were next imaged as single FOV as Z-stacks, every 30 minutes for 12 hours. Slices remain visibly viable across the 12 hours imaging period evidenced by frames from the start of the timelapse (00:00 Hrs) and at the end (12:00 Hrs). Scale bar 100 µm.

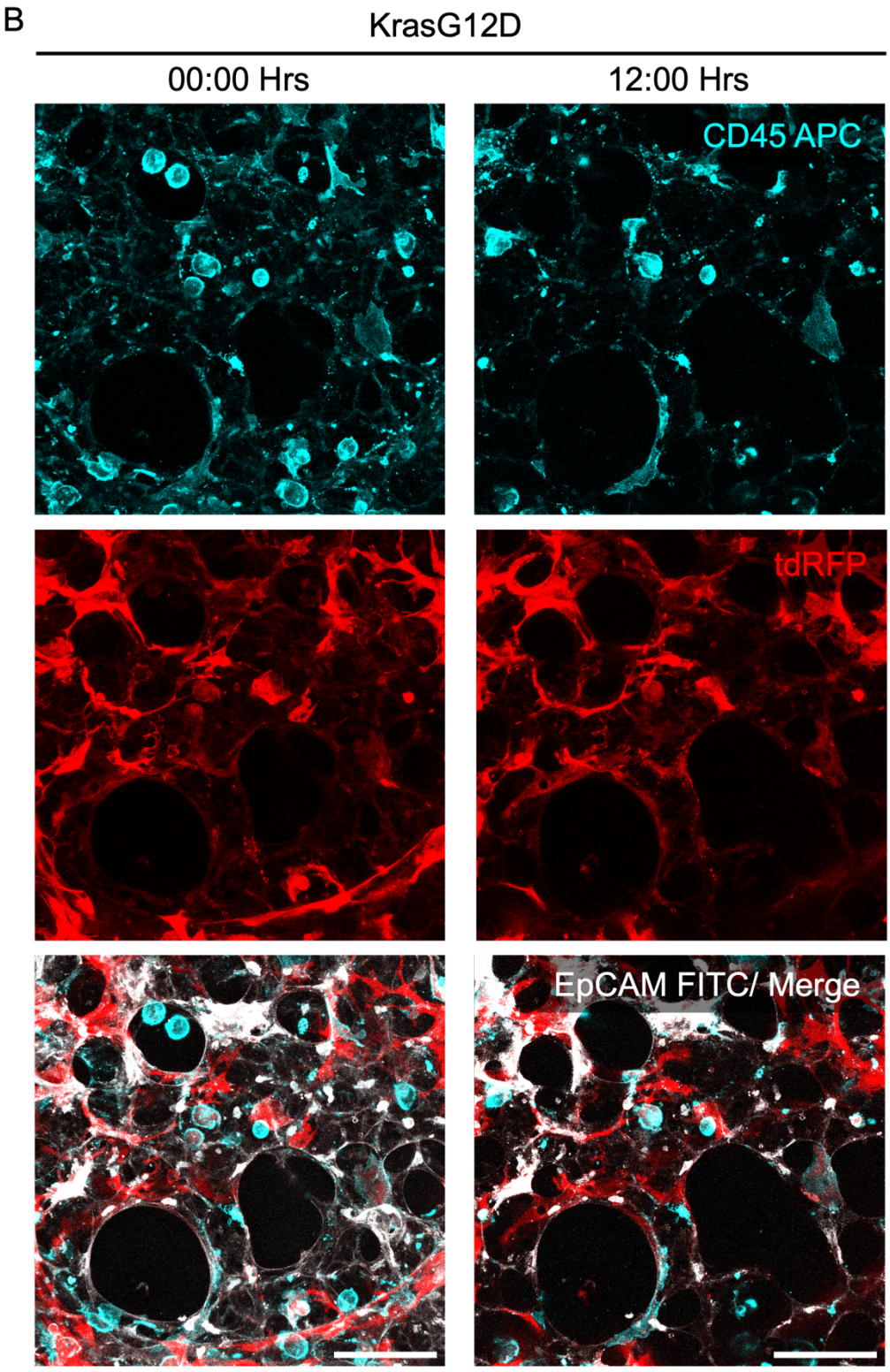
B
KrasG12D
00:00 Hrs
12:00 Hrs
CD45 APC
tdRFP
EpCAM FITC/ Merge

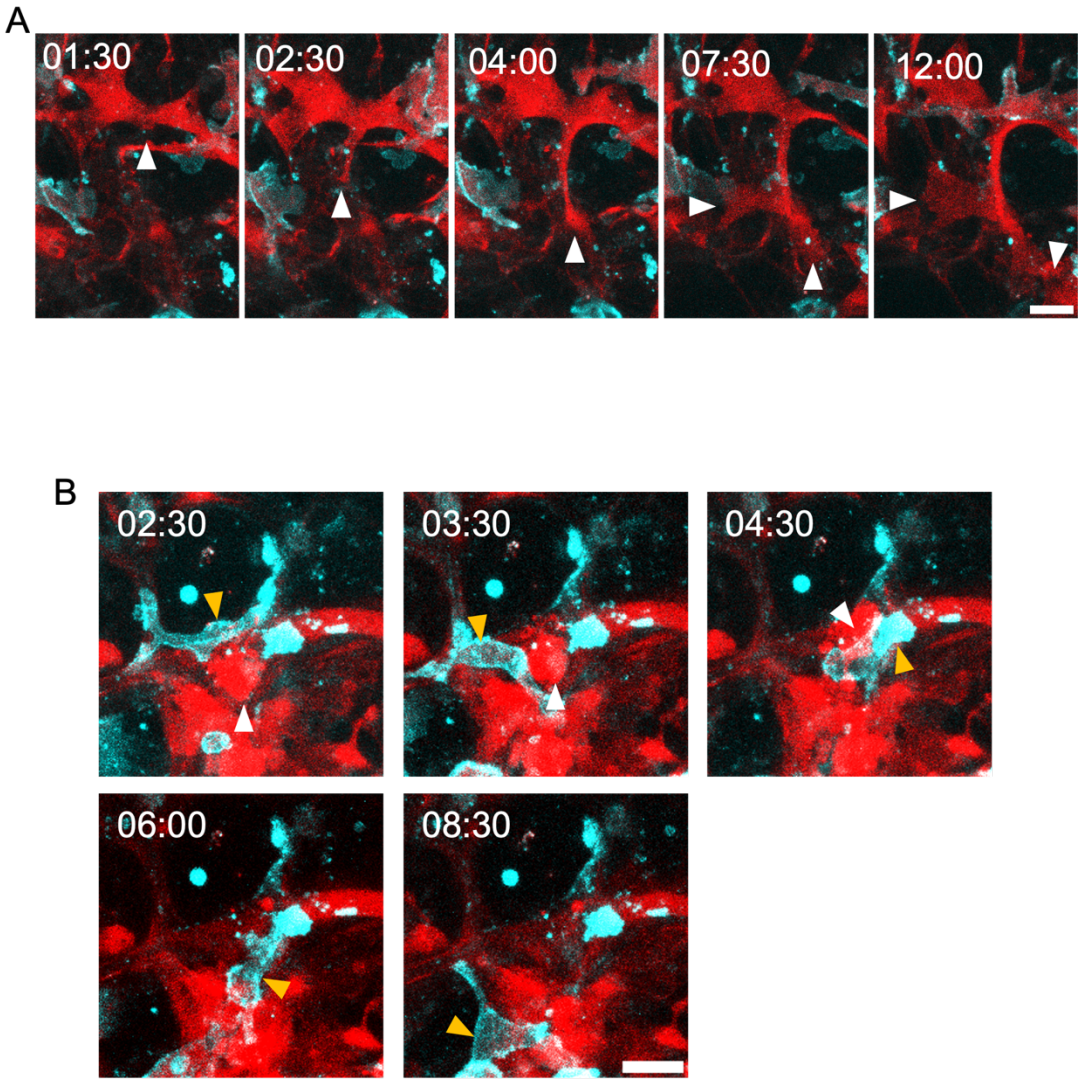

Figure 4. 10 PCLS allow epithelial-immune cell interactions to be observed at high resolution.

Snapshot images of **A)** supplementary movie 4, and **B)** supplemental movie 2. **A)** An RFP+ cell in a KrasG12D PCLS can be observed extending a long protrusion between 1:30 hours (white arrowhead), which extends until the end of imaging (12:00 hours) where it appears to meet another RFP+ cell. **B)** A CD45+ (cyan, yellow arrowhead) cell moves around a potentially apoptotic cell which is expressing RFP (red, white arrowhead) in a WT PCLS. At approximately 6 hours into imaging, the RFP+ apoptotic cell disappears and CD45+ cell moves on to another location. Numbers are time as hh: mm. Scale bars = 20 μm.

To explore this possible phenomenon in greater detail, time series Z-stacks were rendered in Imaris to produce traceable CD45+ cells. As a part of ensuring the quality of analyses, bright, small puncta of staining in the CD45-APC channel were excluded from the timeseries, and cell traces manually validated. Tracks refer to the data generated across the entire time-series, between each frame to generate 3D data in time. Cell track displacement was measured from 0 to 12 hours, then starting coordinates normalised to 0 μm. Presentation of these results in the X-Y axis shows that CD45+ cell tracks were more displaced in WT relative to CD45+ cell tracks in KrasG12D PCLS. Here, CD45+ cell tracks remained clustered at the centre of the graph, indicating a lack of cell migration (Fig 4.11A, Fig 4.11B). When the axes are rotated along the X-axis to show X-Z migration, a similar trend was observed (Fig 4.11C and D). The extent of CD45+ cell migration is demonstrated in Figure 4.11E, whereby images are colour coded to the time-series. Presentation of the data in this format showed that WT images are less sharp than KrasG12D images, suggesting that cell migration between frames is higher in WT compared to Kras slices.

A quantitative analysis of supplementary movies 1-4 revealed that CD45+ cells have a reduced track length in KrasG12D PCLS compared to WT PCLS (31.33±4.12 μm vs. 38.67±12.57 μm respectively; Fig 4.12A). Similarly, the mean speed of cells in KrasG12D PCLS was also reduced relative to WT (WT = 0.001485 m/s, Kras = 0.001311 μm/s). This reduction is modest, however CD45+ cells in WT PCLS exhibit a greater variation in cell speed (Fig 4.12 B) than CD45+ cells in KrasG12D PCLS. This, in combination with the broad range of cell types detected with anti-CD45 highlight the need for more informative immunostaining panels.

Next, I wanted to assess whether CD45+ cells were being recruited to KrasG12D mutant cells *ex vivo*. To do this, the number of CD45+ cells were assessed in each field of view across the 12 hour time-series, measuring the average number of CD45+ cells present across 24 frames (Fig 4.12 C). The number of CD45+ cells was found to be higher in WT PLCS (30.88±11 cells/FOV) compared to 8.8±4.24 cells/FOV in KrasG12D PCLS. In addition to this, the number of cells tracked through the length of the time course supported the observed difference, showing that the total number of CD45+ cells was higher in WT PCLS than KrasG12D (54±7 and 16±3 respectively). A potential explanation to this is that more cells are migrating into and out of the imaging plane in WT PCLS, whereas the less motile CD45+ cells in KrasG12D PCLS do not. Alternatively, fewer CD45+ cells were present in the fields of view selected for analysis.

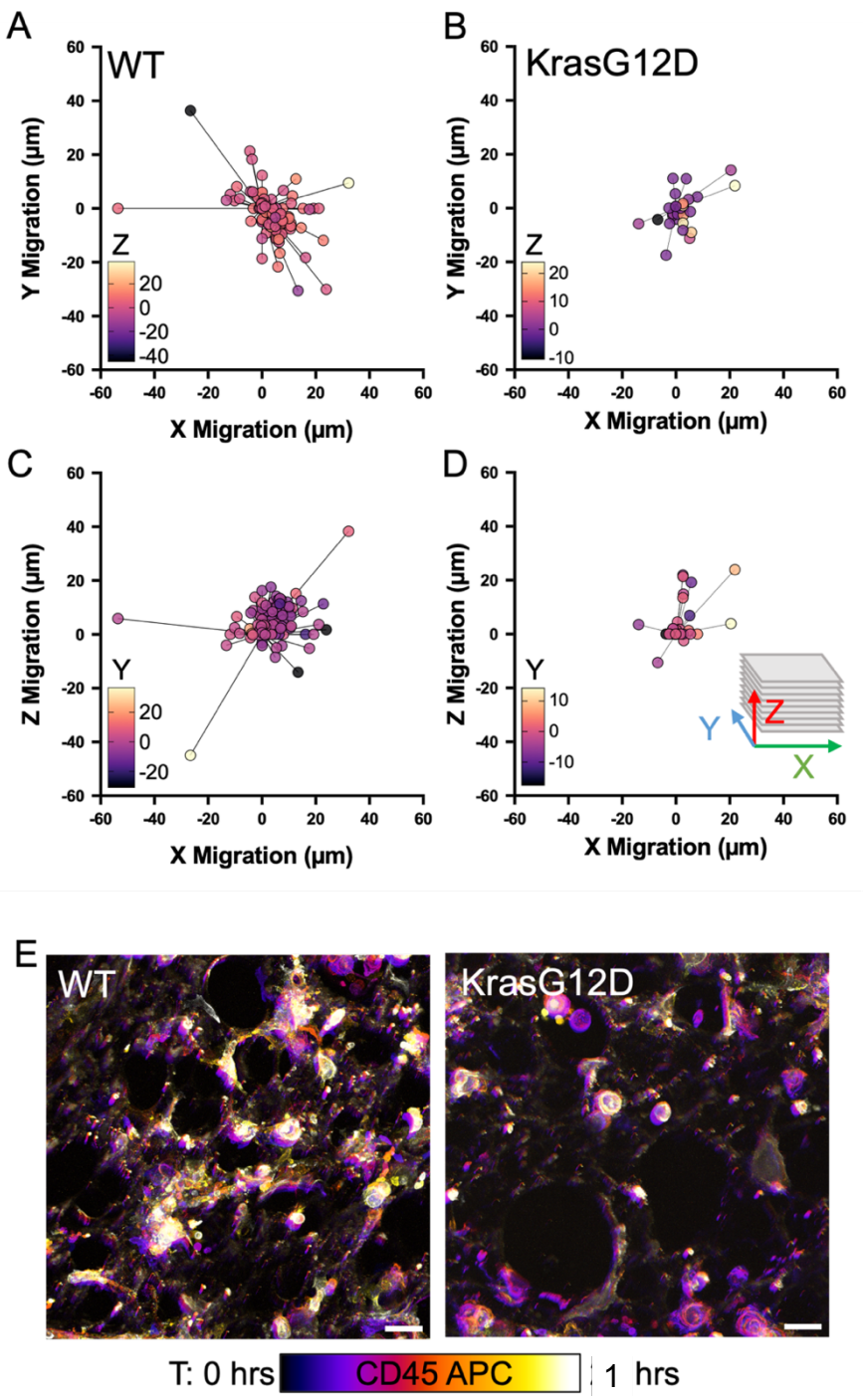

Figure 4. 11 CD45+ cells are less migratory in the presence of KrasG12D mutant cells.

A-D) Analysis of average cell displacement in WT **(A, C)** or KrasG12D **(B, D)** PCLS over a 12 hour live imaging experiment at 5-6DPI. **A, B)** XY migration shown by position of transparent data points relative to 0,0 origin. Colour of circles indicates Z-migration. **C, D)** different angle of cell displacement (XZ), where colour indicates migration in Y. **E)** Time-scale composite image of all 25 frames overlayed for CD45-APC stain. Colour represents the time from which the frame was taken, and sharpness of the image semi-representative of the amount of cell movement over time. Scale bar, 20 µm.

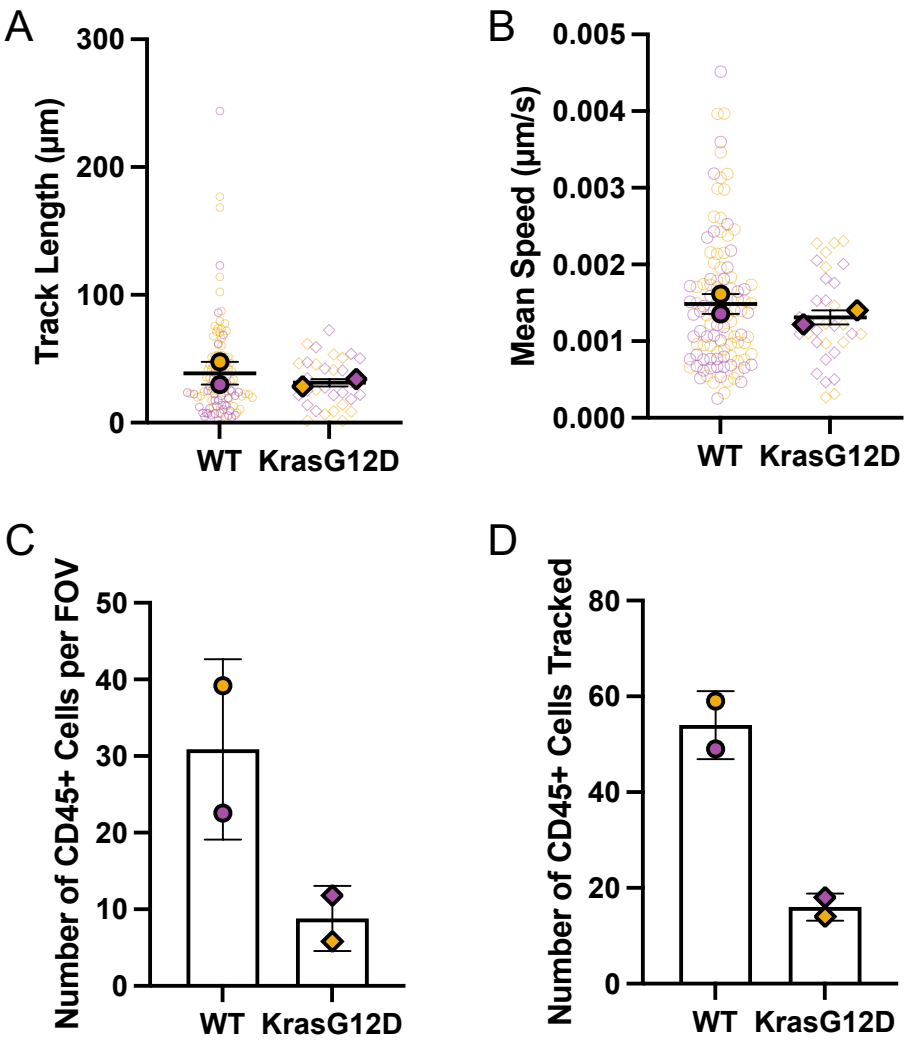

Figure 4. 12 CD45+ cells are more present and migratory in WT PCLS than KrasG12D PCLS.

A) analysis of track length over 24 hours for CD45+ cells. **B)** Average speed of CD45+ cells in PCLS across 12 hours (25 frames every 30 minutes). **C)** Average number of CD45+ cells detected in each frame of the timecourse irrelevant of tracking. **D)** Number of tracked cells across the timecourse. Data represent mean±SEM. **A,B)** empty rings represent individual cells tracked across timecourse in each slice (colour). **A-D)** Solid shape represents average for each slice, two slices from n = 2 PCLS from 1 mouse per genotype.

4.3 Discussion

4.3.1 Generating a viable model of early tumorigenesis with PCLS.

In this chapter, we were excited about the prospect of establishing a new tool to investigate the early stages of primary lung tumorigenesis in an *ex vivo* PCLS model, which to our knowledge, has not yet been attempted. We demonstrated that in our hands, PCLS remain structurally intact with major tissue compartments localised *in situ* (Fig 4.2). This is an improvement on current organoid approaches which heavily rely on sorting dissociated epithelial cell populations from lungs and reconstituting them as organoids (Choi et al. 2020; Dost et al. 2020; Hill et al. 2023; Lim et al. 2023). An advantage of PCLS is that ATI cells become more available for induction with AdCre, as opposed to *in vivo,* where virus particles must first travel along the nasal passageway, trachea, and intrapulmonary bronchioles before hitting the distal lung. However, assessment of PCLS viability following AdCre induction showed a reduced viability of PCLS at 2 DPI but not at 7 DPI (Fig 4.4 C). This indicated that generating PCLS, then infecting with AdCre overnight in a low volume of culture media has a minimal effect on viability.

We determined $1x10^7$ PFU to be an optimal viral titre for transgene induction (Fig 4.6), which appears to be a substantial volume of virus considering we used $1x10^8$ PFU to induce the lung *in vivo* (Chapter 3). These data indicate that AdCre induction of PCLS *ex vivo* may causing damage to the tissues, and using large amounts of virus which can be costly and inefficient. Recent studies that aimed to improve *ex vivo* tissue culture practices implemented the use of a cell permeable TAT-Cre peptide. TAT-Cre efficiently drove transgene recombination in *R26R – EYFP* reporter animals with no effect on PCLS viability compared to uninduced controls (Cheong et al. 2023). Furthermore, use of TAT-Cre peptide showed a robust induction in all cell types of the lung, including epithelial, stromal, and immune compartments. Ultimately, a comparison of induced and uninduced PCLS to methanol treated PCLS demonstrated that PCLS were sufficiently viable for our studies.

Following this, we assessed the degree of recombination that could be observed in our PCLS. We found that bronchiolar airways were quite difficult to image in good detail, but when it was possible, good mosaic induction of RFP could be observed (Fig 4.4). Contrastingly, brightfield imaging of PCLS daily as part of cell culture procedures revealed some denuding of bronchioles *ex vivo* irrespective of Kras genotype (Fig 4.5). Interestingly, another study has demonstrated that PCLS can be successfully used to observe bronchiolar airway responses to allergic asthma

exacerbation (Bagley et al. 2023; Bagley et al. 2024). Here, authors show that in response to methacholine (a muscarinic receptor agonist that drives airway smooth muscle contraction), distinct epithelial extrusion events could be observed in response to tissue over-crowding. Furthermore, they demonstrate that priming of airways using a house dust-mite allergy model *in vivo* prior to PCLS production, airways become hypersensitive to methacholine and causes severe pathological cell shedding. Comparison of methodologies between our study and Bagley et al. reveal that both studies use protocols from Akram et al. (2019), but with modification to the culture media. We followed Akram et al. (2019) by using serum-free DMEM as this reportedly induces less cell death than in M199 media supplemented with FBS. However, Bagley et al. supplemented DMEM with 10% FBS and observed relatively viable bronchioles for up to 7 days in culture, suggesting growth factors present in FBS could help maintain epithelial cell attachment to the basement membrane of airways. In our study, we ultimately decided this variable was not robust enough to analyse potentially rare events in the bronchioles and found that our system was more suitable for study of alveolar regions of PCLS.

4.3.2 PCLS capture the early alveolar lung environment following KrasG12D activation.

Our study aimed to understand develop a tool to recapitulate the events that occur in the distal lung in response to KrasG12D activation. We observed in Chapter 3 that cells are not being eliminated from the adult lung *in vivo*, but instead exhibit plasticity and differentiation phenotypes before turning hyperplastic. We show that our findings *in vivo* are conserved *ex vivo*, where RFP+ cells are not lost at 7 DPI (Fig 4.7 A). Instead, we show an estimated 3-fold increase in the percentage of RFP+ cells in PCLS in both WT and KrasG12D conditions, suggesting either latency of viral transduction, or a biproduct of normal cell proliferation in the PCLS. Analysis of Ki67 in our *ex vivo* PCLs at 7 DPI revealed no significant changes in the total number of proliferating cells (Fig 4.8 A), nor the percentage of proliferating cells that are also RFP+ (Fig 4.8 B). Our values for total proliferating cells align very closely with the values observed in control PCLS (Kim et al. 2021), validating our technique, and our finding that KrasG12D mutant cells are not hyperproliferative aligns with data that suggests 1 week is too early post expression to start seeing expansion (Dost et al. 2020). Preliminary data presented on Pro-SPC stained ATII cells revealed a trend decrease in the percentage of Pro-SPC positive cells observed in KrasG12D PCLS (Fig 4.8 D, E). This finding is also supported by recent literature which has identified

that ATII cells lose mature cell identity markers such as Pro-SPC in response to KrasG12D activation (Dost et al. 2020; Wang et al. 2021), and is suggestive of the injury-driven remodelling of ATII cells we describe in the next chapter (Choi et al. 2020; Strunz et al. 2020).

4.3.3 Potential for viewing live interactions with immune cells *Ex vivo*.

We attempted live cell timelapse microscopy of PCLS that were immunostained to detect CD45+ cells along with endogenous RFP (Fig 4.9). As a pilot experiment, the aim was primarily to see whether live cell imaging was feasible. We were successful in this attempt and were able to describe an interesting phenotype whereby CD45+ immune cells are less migratory (Fig 4.10, 4.11 A) with reduced cell speed (Fig 4.11 B) in KrasG12D mutant PCLS. Unfortunately, the experiments are underpowered following attempts to add to the data were technically unsuccessful. Furthermore, CD45 as a marker of immune cell populations does not reveal enough detail to make precise inferences of epithelial-immune cell dynamics and cell-cell interactions following expression of KrasG12D. Better resolution of immune populations could be achieved by using anti-Ly6G to stain neutrophils, CD68 for general macrophages, CD206 to distinguish M1 (CD206-) or M2 (CD206+) macrophages, and Siglec F to determine whether macrophages are resident alveolar ($CD206^{HI,}$ SiglecF+), or interstitial ($CD206^{Intermediate}$, SiglecF-) (Hussell and Bell 2014; Larionova et al. 2020). Other groups have demonstrated that in combination with PCLS models, multiplex immunofluorescence using high Stoke shift antibodies can be used to profile immune cells in a similar way to flow cytometry (Raffo-Iraolagoitia et al. 2023). Overall, our PCLS has excellent potential to help characterise the early epithelia-immune interactions that occur in response to KrasG12D activation.

4.3.4 Strengths of the PCLS model.

Generally, the main benefit of using a PCLS model is that all component parts of the lung are preserved in the same sample, without the need for co-culture, cell sorting or special supplementation to preserve cell types. We have demonstrated here that existing mouse models that have been used to study *in vivo* phenotypes can be further utilised with *ex vivo* induction, or potentially with *in vivo* induction for *ex vivo* culture. PCLS technology has been applied to a range of different species including human (Neuhaus et al. 2017; Temann et al. 2017), sheep (Lambermont et al. 2014), guinea pig (Ressmeyer et al. 2006), and chicken (Bryson et al. 2020), in addition to mouse PCLS. Additionally, PCLS are generated as 300 μm thick sections which

presents the opportunity to study cell biology in a 3D model that is more representative of *in situ* architecture as opposed to organoid models which only loosely model this (Choi et al. 2020; Dost et al. 2020; Lim et al. 2023).

I present in this thesis that PCLS can be used to further elucidate mechanisms that would not usually be possible in *in vivo* studies, applying more classical cell biology approaches such as conditioned media studies and live cell imaging. Furthermore, PCLS introduce the possibility of refining animal usage for short term studies by generating many samples from a single lung that can be used to observe the effect of different drugs, inhibitor experiments, agonist studies and more.

4.3.5 Limitations of the PCLS model.

The biggest limitation of PCLS is the limited culture time where they remain viable. As PCLS are cultured past 7 dpi, they may start to exhibit degradation in structure, and become less reliable to model cellular interactions within the tissue. Furthermore, studies that aim to explore biology beyond 7 dpi require alternative methods of modelling, or by using a combination of *in vivo* induction prior to PCLS generation. As discussed in this chapter, variable results are achieved regarding bronchiolar airways. In our experiments, PCLS are limited to study airways, suggesting the need for alternative approaches such as co-culture systems and air liquid interface (ALI; (Silva et al. 2023), or epithelioid culture (Herms et al. 2023).

As PCLS are derived from primary lung tissue, a drawback is that immune cells that are detected in each PCLS are only representative of the cells that were present at the time of harvest. As this is true for both the WT and KrasG12D PCLS this is a comparable parameter which can be accounted for by incorporating more fields of view and ensuring a set number of cells are measured per cohort. For more reductive approaches, researchers have regularly used macrophage-organoid co-culture systems to model epithelial-immune relationships *ex vivo* (Choi et al. 2020; Hill et al. 2023; Lim et al. 2023).

4.3.6 Summary and future directions.

In summary, I established a PCLS model system to study KrasG12D cell fate ex vivo. can be used in conjunction with our KrasG12D GEMM to generate and *Ex vivo* PCLS model of early KrasG12D activation in the distal lung. I demonstrated successfully that PCLS can be combined with immunofluorescence microscopy in 2D and 3D, in addition to live cell timelapse microscopy to generate qualitative and quantitative data. In the process of characterising our PCLS model, I found that KrasG12D activation

leads to an interesting immune cell phenotype that should be better characterised in the future, using multi-plex live cell fluorescence microscopy. Additionally, future work should aim to prolong the viability of PCLS *ex vivo* to assess when KrasG12D mutant cells become pathogenic in the alveoli.

5 KrasG12D drives alveolar cell remodelling.

5.1 Introduction

Our lungs are exposed to a constant barrage of insults as we age. The prevalence of pulmonary lung diseases such as fibrosis, COPD, emphysema, and lung cancer are therefore not surprising, especially considering that key driving forces of these diseases like pollution, infections and other environmental factors are on the rise. As with any tissue, homeostatic repair pathways in the lung that aim to resolve injury often become dysregulated and lead to aberrant repair pathways that contribute to disease progression. Recent studies have highlighted this by the discovery of aberrant populations of epithelial alveolar cells in the distal lung, which express distinct gene signatures and lack mature cell phenotypes (Choi et al. 2020; Kobayashi et al. 2020; Strunz et al. 2020).

In a mouse model of fibrosis, aberrant Krt8+ alveolar populations arose 10 days after injury, appeared distinct from ATI and ATII cells, and resolved over a 56-day timeframe (Strunz et al. 2020). A key characteristic of these Krt8+ alveolar differentiation intermediate (Krt8+ ADI) populations is that over time they lose expression of ATII cell markers such as pro-SPC, becoming less cuboidal and more squamous in the tissues. Other articles at the time found that injuring mouse lungs by exposing them to LPS gave rise to aberrant transitional state populations that were characterised by expression of *Cldn4, Sox4, Lgals3* and *Fn1*, further showing that these cells corresponded to the Krt8+ ADI observed in bleomycin lungs (Kobayashi et al. 2020; Strunz et al. 2020). Kobayashi et al. demonstrated that these transitional populations are derived from ATII progenitor cells in the alveoli, presenting evidence of direct ATII to ATI differentiation by lineage tracing and Cldn4 immunostaining, subsequently naming them Pre-Alveolar Transitional State cells (PATS). In a third study that identified aberrant repair populations (Damage Associated Transient Progenitors; DATP), a significant increase in interstitial macrophage populations was observed in conjunction with DATP cell signatures, further identifying IL-1β to be the key driver of cell differentiation in the alveolar lung (Choi et al. 2020).

Within these DATP, PATS and Krt8+ ADI populations, commonly upregulated pathways include p53 signalling, cellular senescence, and HIF-1α signalling (Choi et al. 2020; Kobayashi et al. 2020; Strunz et al. 2020). Upregulation of these pathways is suggestive of process that underpin the initiation of cancer (Serrano et al. 1997; Ferbeyre et al. 2002). A recent study highlighted that induction of oncogenic KrasG12D in ATII cells is accompanied by loss of ATII cell identity, acquisition of developmental gene signatures such as *Hmga2* and *NKX2-1* (Dost et al. 2020). This potential link between aberrant repair pathways is supported by recent research (published after defining my initial hypothesis), where lineage tracing of ATII cells

identified marked ATI populations indicating that KrasG12D positive ATII cells can directly give rise to ATI cells (Chaudhary et al. 2023). With these comparative phenotypes to consider, I hypothesised that in the absence of competitive elimination of KrasG12D mutant cells from the alveoli, other tumour preventative mechanisms must be at play to remove potentially tumorigenic ATII cells from their progenitor state, into a more quiescent bystander population. I hypothesised this may occur via conserved injury-repair mechanisms in the lung, via transitional cell states that have been observed in pulmonary fibrotic lung models.

To dissect this potential mechanism, my aims were to:

1) Use our established PCLS model of early lung tumorigenesis to screen for transitionary cell states at early timepoints post KrasG12D induction.
2) Determine the cellular responses following KrasG12D induction, including an analysis of how cells that neighbour KrasG12D mutants also respond.
3) Investigate whether conserved cellular changes also observed *in vivo*, at 35 DPI of KrasG12D expression.

5.2 Results

5.2.1 Identification of lung injury response markers in KrasG12D mutant lungs

Following my initial findings (section 3.2.6: Fig 3.8 B-D), it became apparent that the hypothesis pertaining to cell competition was not correct; cells were not being eliminated from the epithelium, nor were they exhibiting phenotypes that would indicate mechanisms of normal-mutant cell competition. KrasG12D mutants appeared to undergo changes in morphology that were similar to those observed in models of pulmonary fibrosis (Strunz et al. 2020). Following injury, alveolar cells differentiate from cuboidal ATII cells to squamous ATI cells, incompletely remodelling and becoming contributing to hyperplastic foci in fibrosis (Strunz et al. 2020).

To assess whether any markers of lung injury were relevant to human lung cancer cases, I used the Gene Expression Profiling Interactive Analysis (GEPIA2) resource to explore if Cytokeratin 8 (Krt8) is found in human non-small cell lung cancer (NSCLC), specifically in lung adenocarcinoma (LUAD) and lung squamous cell carcinoma (LUSC) samples. Indeed, expression profiles of tumour samples from both LUAD and LUSC revealed a highly significant increase in Krt8 expression in tumours compared to normal samples from the same dataset (Fig 5.1A; One-way ANOVA, $P < 0.0001$). Other signatures associated with injury-associated transitional cell states were additionally found to be upregulated in both LUAD and LUSC, particularly *SFN, Cldn4, Sox4,* and *TP53* (Fig 5.1 B-E; One-way ANOVA, $P < 0.0001$). Furthermore, the developmental marker that defines lung identity was found to be reduced in LUSC (One-way ANOVA, $P < 0.0001$), but unchanged in LUAD (Fig 5.1 F). Data from tumour samples only reveals that injury-associated transcriptomes are conserved; however, this only gives an insight into late stage disease and not the pre-neoplastic tissue.

To assess this question, we turned to our *Ex vivo* model and anlaysed total protein from PCLS at 7 DPI. Immunoblotting for Krt8 protein revealed expression in both WT and KrasG12D slices (Fig 5.2A). Presence of a triple protein band around 54.5 kDa is in keeping with previously published work that uses the same antibody (Strunz et al. 2020), and therefore densitometry quantification was performed on all three bands. Quantification revealed a distinct increase in Krt8 in KrasG12D PCLS relative to WT PCLS (Fig 5.2 B; Unpaired t-test with Welch's correction, $P = 0.0148$). These findings indicated that KrasG12D may be driving an injury response phenotype in the alveoli.

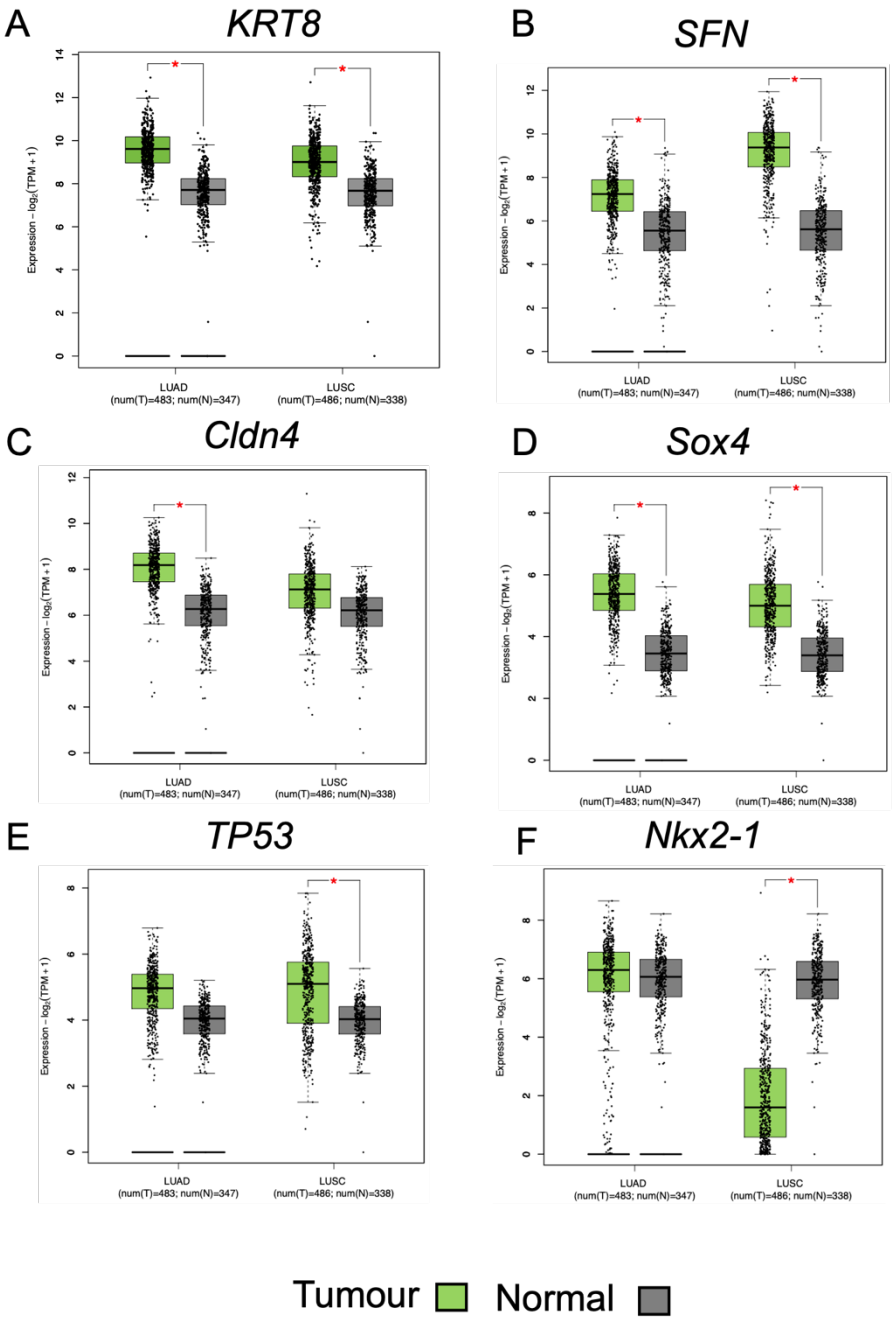

Figure 5. 1 Presence of lung injury response markers in LUAD and LUSC samples.

Using GEPIA 2 to screen for injury response markers found in fibrosis in human tumour data sets. **A-E)** Gene expression of markers upregulated in fibrotic transitional cell types are upregulated in both lung adenocarcinoma (LUAD) and lung squamous cell carcinoma (LUSC). **F)** the developmental lineage determinant Nkx2-1 is found to be downregulated in LUSC, but unchanged in LUAD. One-way ANOVA comparing tumour to normal samples, *P <0.0001. LUAD: tumour n = 483, normal n = 347. LUSC: tumour n = 486, normal n = 338.

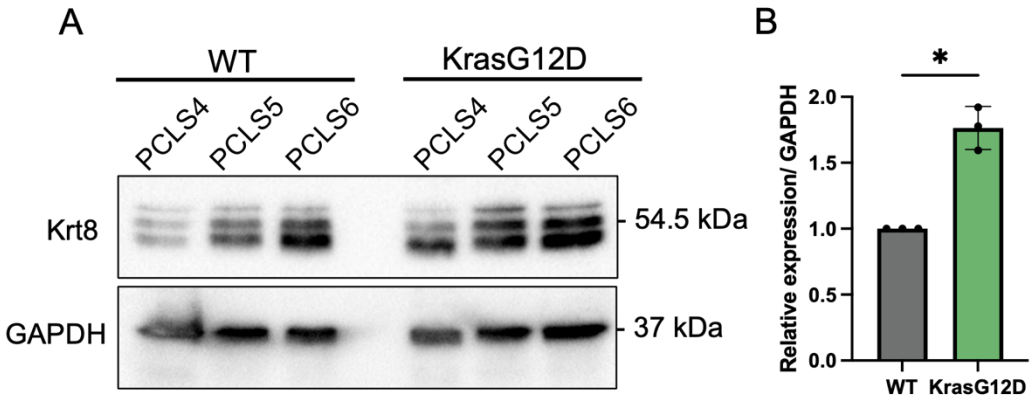

Figure 5. 2 Western Blot analysis of Krt8 in *ex vivo* PCLS.

A) Western blot for PCLS induced with $1x10^7$ AdCre and harvested at 7 DPI. PCLS4-5 refer to slices generated from WT and KrasG12D lungs at the same time, and lysates generated from 3 pooled slices. **B)** Quantification of Krt8 expression by densitometry. Protein expression normalised to GAPDH, made relative to each WT. Unpaired t-test with Welch's correction, *P <0.05, n = 3.

5.2.2 Krt8+ cells increase in tissue in the presence of KrasG12D

KrasG12D drives an increase in the expression of Krt8 at 7 DPI. It was next important to establish how long after the onset of KrasG12D expression Krt8 begins to be expressed. To do this, PCLS were fixed at 2 and 7 DPI, stained for anti-Krt8, RFP and Hoechst. Immediately upon viewing PCLS stains (Fig 5.3A), it was clear that expression of Krt8 increased over time. At 2 DPI, Krt8 protein appeared to be diffusely expressed across the alveoli, and at low levels, potentially localising to ATII cells. This assumption is based on the largely cuboidal shaped staining which does not align with the squamous ATI morphology. This pattern of staining was consistent in both WT and KrasG12D slices. In WT PCLS at 7 DPI, the expression of Krt8 was similar to that observed at 2 DPI. Contrastingly, KrasG12D PCLS Krt8 was expressed at higher levels in cells and Krt8+ cells appeared more squamous and spread in the epithelium.

To quantify these changes, numbers of Krt8+ cells were counted by looking for nuclear association with a Krt8 stain. Krt8+ cells were counted when cells were intact and positive staining associated with nuclei. Krt8 is a cytoskeletal intermediate filament, therefore staining would be expected around the nucleus and cytoplasm. Comparing Krt8 positivity in WT versus KrasG12D PCLS at 2 DPI, a trend increase in the percentage of Krt8 positive cells was observed (Fig 5.3B; WT =10.68 ±2.00% vs. KrasG12D = 18.94 ±3.08, Two Way ANOVA, P =0.2556). Analysis of Krt8+ cells per FOV in WT PCLS over time revealed no significant change in the percentage of cells positive for Krt8, with the mean expression at 13.22 ±4.73% (P =0.8914). Comparison of WT and KrasG12D PCLS at 7 DPI found a greater but non-significant percentage of Krt8 positive cells in KrasG12D PCLS than WT counterparts (19.57 ±419%, P =0.2944). This number resembles the percentages seen at 2 DPI (P =0.9978), strongly suggesting that presence of KrasG12D alone is sufficient to induce a greater number of Krt8 expressing cells in *ex vivo*.

To determine whether KrasG12D cells also express higher amounts of Krt8 than WT cells, I scored Krt8 levels in cells. Fluorescence readings were normalised to background fluorescence, then mean change in Krt8 integrated density analysed. As expected, integrated density of Krt8 was increased near three-fold in Krt8+ cells in KrasG12D PCLS compared to WT PCLS (Fig 5.3 C; WT = 3042 ±1495 a.u. vs. KrasG12D = 11140 ±3292 a.u., unpaired t-test, P =0.0178). These data imply that in response to KrasG12D activation, cells start expressing Krt8 as early as 2 DPI, and over time express a greater amount of total protein.

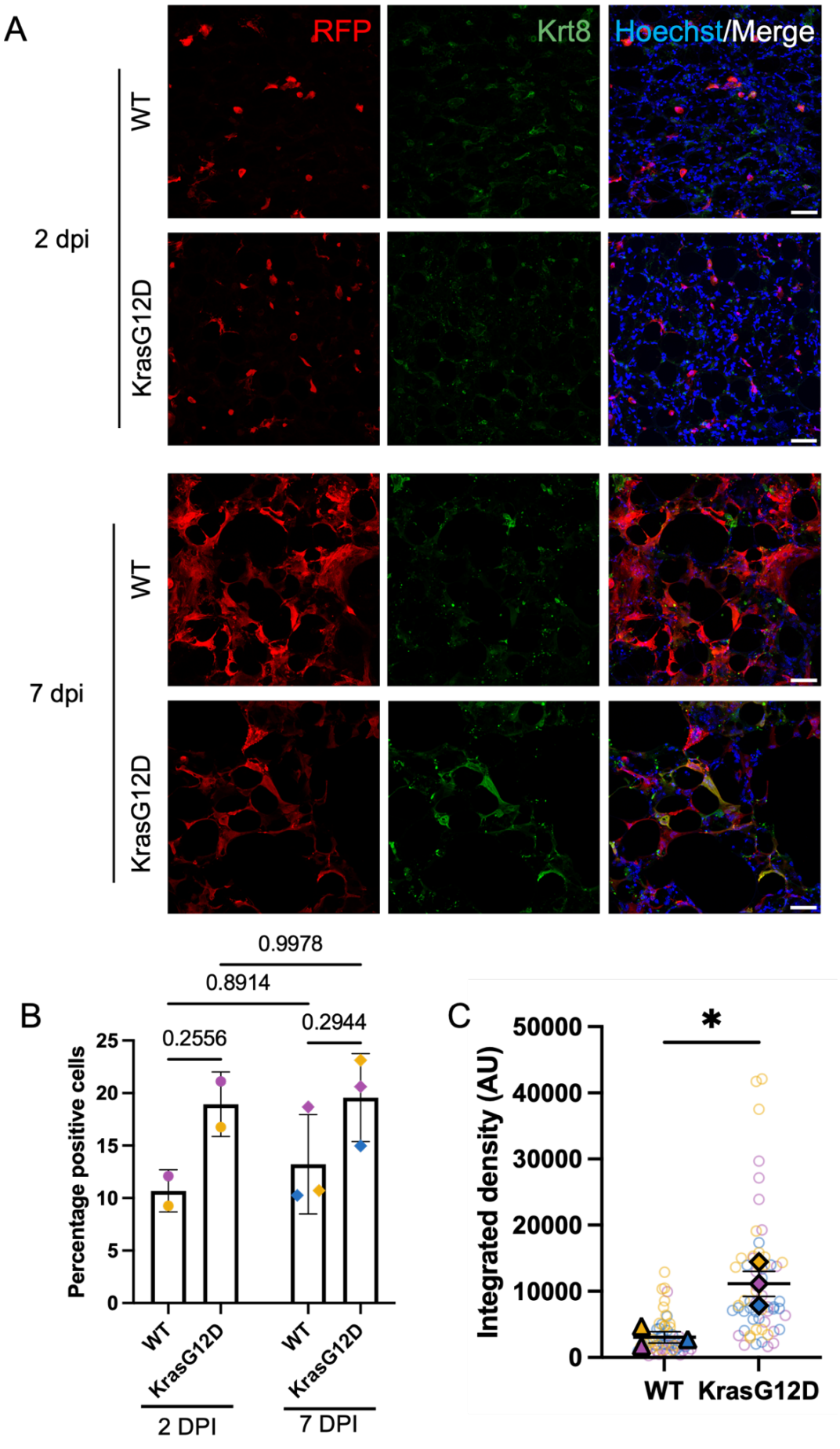
A
RFP
Krt8
Hoechst/Merge
WT
KrasG12D
2 dpi
7 dpi
B
0.9978
0.8914
0.2556
0.2944
Percentage positive cells
25
20
15
10
5
0
WT
KrasG12D
WT
KrasG12D
2 DPI
7 DPI
C
*
Integrated density (AU)
50000
40000
30000
20000
10000
0
WT
KrasG12D

Figure 5. 3 Krt8 is expressed in alveoli in response to expression of KrasG12D.

A) Representative images of WT and KrasG12D PCLS at 2 DPI and 7 DPI. Immunostaining with anti-RFP (red), anti-cytokeratin 8 (Krt8, green) antibodies and merged with Hoechst (blue). Images are maximum intensity projections, scale bar = 50µm. **B)** Quantification of the percentage of Krt8+ cells/total cells at 2 and 7 DPI in WT and KrasG12D PCLS. Data represent mean±SD, data points show biological replicates with 3 slices per mouse (WT n =2, KrasG12D n = 3). Two-Way ANOVA with Tukey's post hoc tests. P values of multiple comparisons are noted above relevant bars. **C)** Quantification of Krt8 immunofluorescence (integrated density) at 7 DPI in WT (triangles) and KrasG12D (diamonds) PCLS. Solid shapes represent biological means, and corresponding transparent shapes represent the individual cells quantified for each group. WT n = 58 cells, KrasG12D n = 62 cells. Data represent biological means ±SEM. Unpaired t-test, *P < 0.05.

5.2.3 Krt8 expression is increased in WT cells neighbouring KrasG12D mutant cells.

To further characterise the changes that occur at 7 days post KrasG12D activation, PCLS cells were counted and populations of cells further sub-categorised into RFP+/Krt8- (Fig 5.4A), Krt8+/RFP- (Fig 5.4B), and then the percentage of RFP+ cells that expressed Krt8 analysed (Fig 5.4C). Quantification of this revealed a slight decrease in the percentage of RFP positive, Krt8 negative cells at 7 DPI from 17.21 ±2.5% to 12.88 ±3.36% in KrasG12D PCLS (Fig 5.4A, P =0.1537). Percentage of Krt8 positive, RFP negative cells was greater in KrasG12D PCLS (WT = 5.32 ±1.07% KrasG12D =11.25 ±4.72%, P =0.1555), suggesting that cells that are KrasG12D also switch on Krt8 expression in response to their mutant neighbours (Fig 5.4B). Finally, quantification of the percentage of RFP positive cells that express Krt8 reveals an overall increase from 17.73 ±8.8% in WT PCLS to 29.10 ±11.1% in KrasG12D PLCS, demonstrating further that KrasG12D drives expression of Krt8 at 7 DPI.

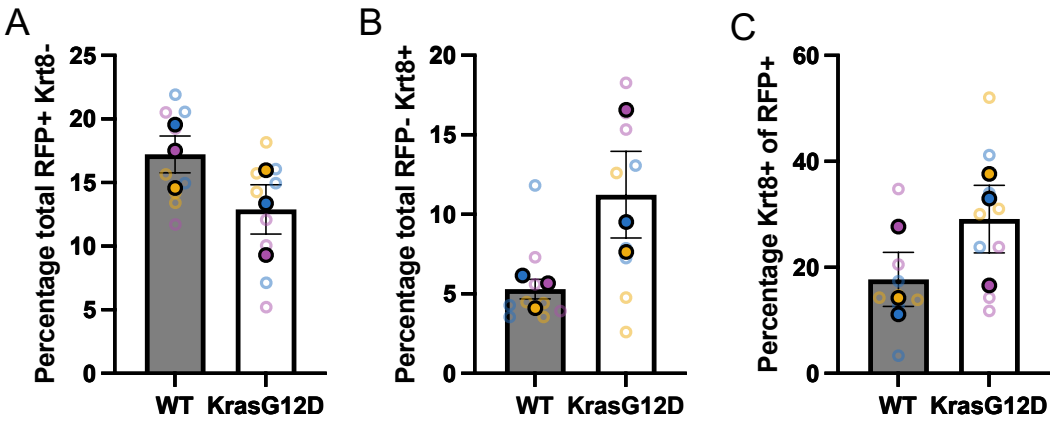

Figure 5. 4 Krt8 is expressed in WT and KrasG12D mutant cells in KrasG12D expressing PCLS.

A) Quantification of the percentage of RFP positive but Krt8 negative cells/total cells and **B)** percentage RFP negative but Krt8 positive cells/total cells. **C)** Percentage of RFP+ cells that are Krt8 positive. Data represent mean ±SEM for WT PCLS (grey) and KrasG12D PCLS (clear) at 7 DPI, solid circles are biological means of all images counted (transparent rings in corresponding colour). N = 3 mice per group, colour of circles represent the same mouse across A-C

.

5.2.4 KrasG12D mutant Krt8+ cells exhibit morphological changes seen in differentiation.

Krt8 signatures in the lung have been implicated in fibrotic lung responses, with a key aspect being the differentiation and cell shape changes observed over time. To investigate whether Krt8 mutant cells were responding in a similar way, Imaris (Bitplane) was used to separate double positive Krt8+/RFP+ cells from Krt8+/RFP- cells and determine cell descriptors in 3D images.

In keeping with the findings seen at 7 DPI in section 3.2.6, Figure 3.8, I hypothesised that KrasG12D cells would potentially display a shift from smaller volume cuboidal cells to a more spread and less spherical morphology in Krt8+ cells. Analysis of cell volume revealed that the mean volume of WT Krt8+/RFP- cells was 605.8 ±133.6 μm^3 (Fig 5.6 A). WT Krt8+/RFP+ cells had a slightly lower volume at 481±249.4 μm^3, but this difference was not significant (Two-Way ANOVA, P =0.9102). KrasG12D Krt8+/RFP- cells had an average volume of 499.6 ±218.2 μm^3 (WT vs. KrasG12D Krt8+/RFP- P =0.9875), similar to Krt8+ cells in WT slices. Analysis of Krt8+/RFP+ cells in KrasG12D-expressing PCLS showed a significant increase in cell volume to 926.5 ±342.7 μm^3 when compared to Krt8+/RFP- cell volume (P =0.0400), and a non-significant increase compared to cell volume of double positive cells in WT PCLS (P =0.0629; Fig. 5.6 A).

Next, sphericity of Krt8 positive cells was analysed. Similar to volume measurements, Krt8+/RFP- cells exhibited very similar values of 0.77 ±0.028 a.u. and 0.756 ±0.041 a.u. in from WT- and KrasG12D –expressing PCLS, respectively (Fig 5.6B; P =0.9837). No significant differences were observed between Krt8+/RFP- and double positive cells in WT PCLS (WT Krt8+/RFP+ =0.674 ±0.103 a.u., P =0.2668). In contrast, Krt8+/RFP+ cells had a reduced sphericity of 0.593 +0.044 a.u. in KrasG12D-expressing PCLS which was significantly different to sphericity of Krt8+/RFP- cells (P =0.0466)). Taken together, these data show that KrasG12D activation induces an injury response and cellular remodelling, which is not observed following an injury response alone. Whether or not this is a distinct cellular mechanism or one that takes advantage of a conserved pathway is still unclear.

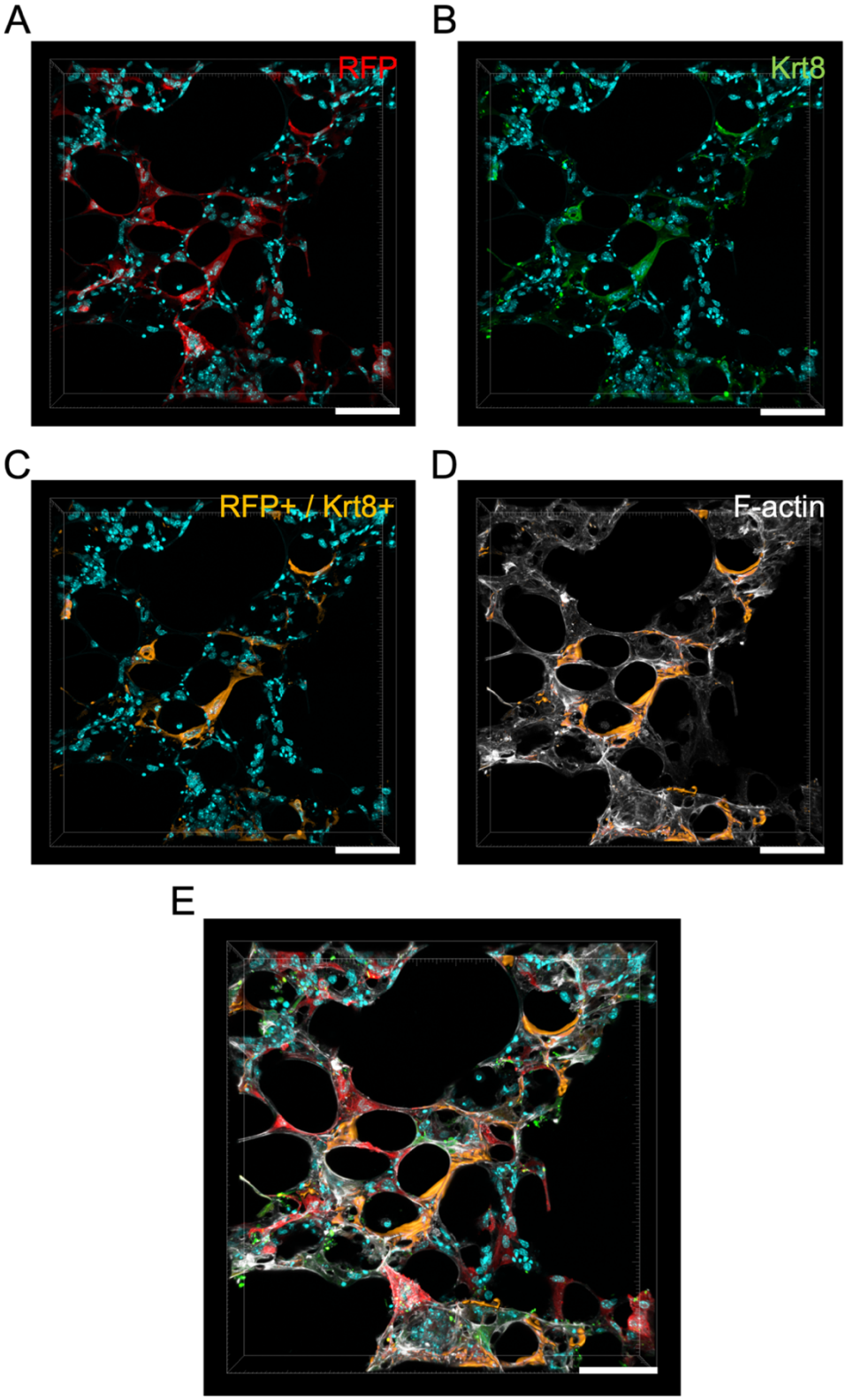

Figure 5. 5Example images of Imaris-rendered surfaces.

A, B) Imaris projections of images immunolabelled for RFP (red) and Krt8 (green) and stained with Hoechst (blue). **C)** Co-localisation channel generated from RFP and Krt8 projections, with non-colocalised cells removed. **D)** Rendering of C as a surface layer with F-actin. **E)** Merge of A, B and D. Scale bars,50µm.

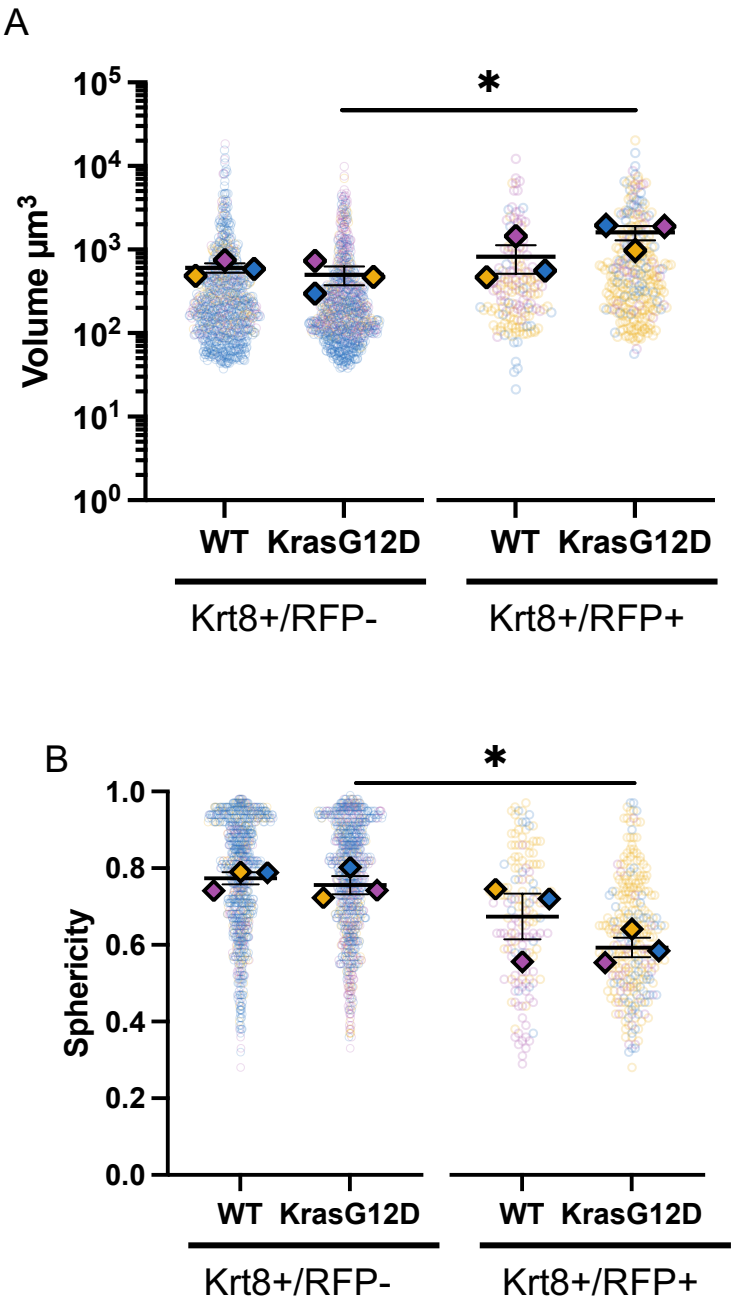

Figure 5. 6 Volumetric analysis of Krt8+ cells in PCLS.

A) Measurement of Krt8+/RFP- and Krt8+/RFP- cells volume at 7 DPI in WT and KrasG12D PCLS. data represent mean±SEM. Data is not transformed, just presented on a $\log_{10}$ axis to better visualise the spread of cell volumes. **B)** Measurement of cellular sphericity, where 1 is most spherical. Data represent mean±SEM, opaque coloured data points are biological replicate means, corresponding in colour to the cells measured in the analysis. Two-Way ANOVA with Tukey's post hoc test. *P<0.05. Data derived from n=3 mice per genotype, 3 PCLS per mouse.

5.2.5 ATII cell remodelling via a Krt8+ transitional state is driven partly by KrasG12D.

Our data suggested that KrasG12D is driving Krt8-mediated remodelling in the alveolar lung, and the number of RFP negative Krt8 positive cells increased at 7 DPI in KrasG12D-expressing tissues compared to WT (5.2.3). therefore, I postulated that KrasG12D mutant cells may be secreting factors that are inducing an injury-like response in the surrounding WT cells. To test this theory, conditioned media experiments were carried out.

PCLS were generated, infected with 1 x 10^7 PFU AdCre, and cultured to 7 DPI as previous. Media present on PCLS at 7 DPI was taken from 4 wells, mixed 50:50 with fresh DMEM, then added to WT PCLS. WT PCLS were either incubated with conditioned media from WT PCLS (WT+CM(WT)), or with conditioned media from KrasG12D expressing PCLS (WT+CM(KrasG12D)). As control samples, PCLS from WT and KrasG12D lungs were given a fresh media at 7 DPI in place of conditioned media (WT+F and KrasG12D+F respectively). All PCLS in this experiment were then cultured for an extra 2 days before fixation at day 9 post induction. Fixed PCLS were immunolabelled for Krt8 and RFP as previously described (Fig 5.7 A).

At 9 DPI 17.25 ±1.71% of cells were positive for Krt8 in WT plus fresh media (Fig 5.7 B, Fig 5.8 A). This is substantially increased compared to previously observed numbers of Krt8 in WT PCLS (Fig 5.3 B), indicating that PCLS undergo further injury post 7 DPI. The percentage of Krt8+ cells significantly increased to 31.67 ±4.933% in KrasG12D+F compared to the WT+ Fresh condition (P =0.0384). Though we observe greater proportions of cells expressing Krt8 in WT PCLS, a significant increase in percentage Krt8+ cells were observed in KrasG12D + F media at 9 DPI indicating that KrasG12D expression is still promoting cellular trans-differentiation (Fig 5.7 B, Fig 5.8 B). Unexpectedly, we observed an increase in Krt8+ cells in WT+CM PCLS from 17% to 29 ±10.33% (Fig 5.7 B, Fig 5.8 C); however, this was not significantly different (P=0.072). Analysis of WT+CM(KC) PCLS showed that KrasG12D conditioned media induced a significant increase in Krt8+ cells in WT PCLS to 35.5 ±2.082% compared to WT+CM(WT) (P =0.0056) (Fig 5.7 B, Fig 5.8 D).

Together these findings show that our initial hypothesis was correct, and that KrasG12D mutant cells generate secreted products that promote remodelling events in WT cells in KrasG12D-expressing PCLS.

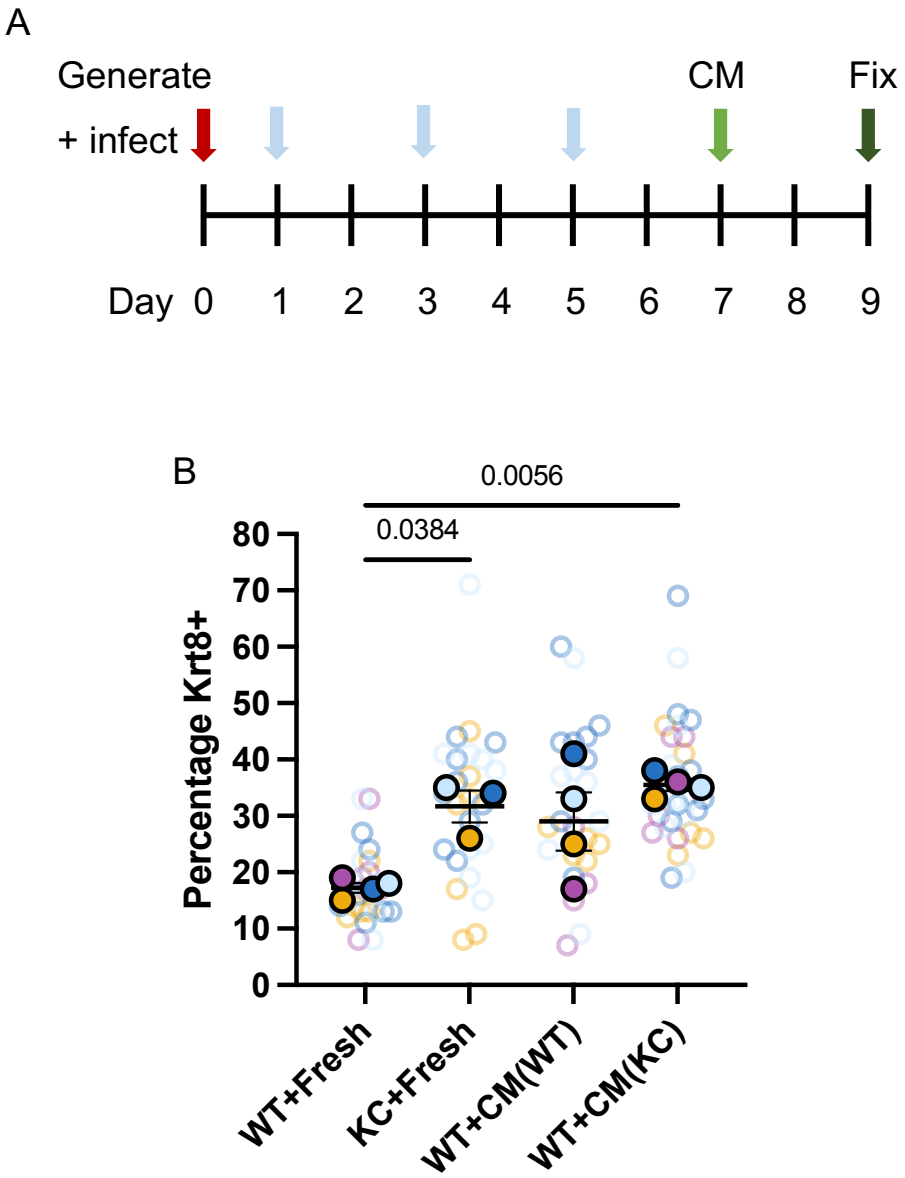

Figure 5. 7. Conditioned media from KrasG12D PCLS drives Krt8 expression in WT PCLS.

A) Schematic for conditioned media experiments. PCLS generation, infection (red arrow), media changes across the 7 days of culture (blue arrows) addition of CM to slices at 7 DPI (green arrow), fixation on 9 DPI (dark green arrow). **B)** Percentage of total cells that express Krt8 at 9 DPI. Data represent mean ±SEM, with solid data points representing technical repeats from at least 3 mice (1 slice per mouse, per condition). Corresponding coloured rings represent fields of view from which cells were counted. One-Way ANOVA with Bonferroni's multiple comparison relative to WT+Fresh. P <0.05 shown on graph. P >0.05/ non-significance is not shown.

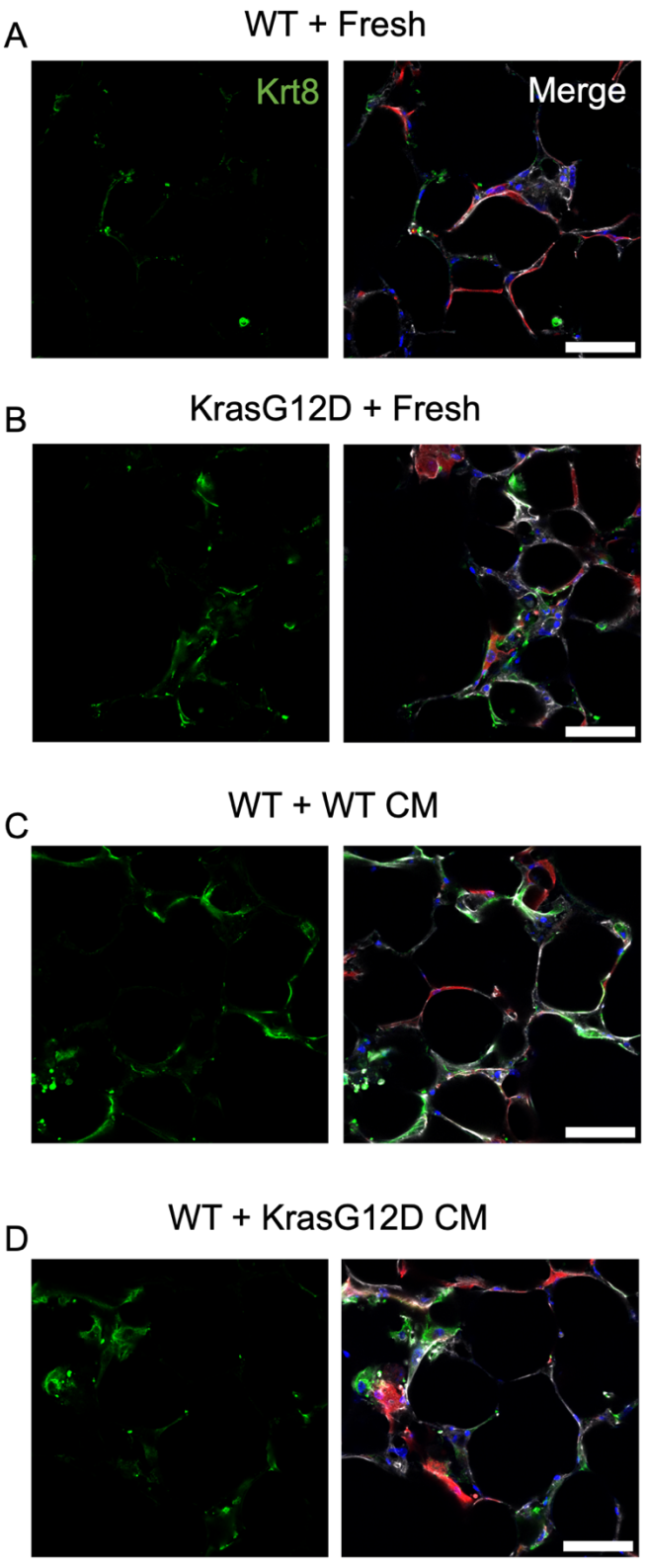

Figure 5. 8 Representative images of conditioned media PCLS.

A-D) Representative images at 9 DPI for PCLS immunostained with anti-Krt8 (green; left panels), along with anti-RFP (red), and stained with phalloidin for F-actin (grey), and Hoechst for nuclei (blue) in merge images (right panels). Optical sections of Z-stacks. Scale bar, 50μm.

5.2.6 KrasG12D induced inflammatory cytokine response in the alveolar epithelium.

To investigate potential secreted factors from KrasG12D mutant cells, dot blot inflammatory cytokine arrays were employed due to their high throughput and easy-to-use protocols. We opted to screen 40 inflammatory cytokines (see methods section) for each of the conditioned media conditions at 9 DPI. Using 1 mL of culture media as per manufacturer's instructions revealed the signature of several pro-inflammatory cytokines and soluble factors (Fig 5.9A). It is possible that concentration of factors in the media were too strong and some sensitivity in the assay may be lost as a result, this is evidenced by the fact that exposure of the blots was stopped before positive control arrays reached saturation due to high expression of three signatures.

Despite this, the arrays revealed a striking pro-inflammatory signature in KrasG12D CM, (Fig 5.9B-K). From the 10 strong signatures observed on the blots, 4 had a less than 2-fold increase in the WT+CM(KC) blot relative to the WT+F: Eotaxin-2(1.077), MIP-1γ (1.31), sTNF RI (1.36), sTNFII (1.69) (Figures 5.8B, I, J and K respectively). A substantial fold change was observed in the remaining 6: G-CSF (2.48), CM-CSF (3.28), IL-6 (2.93), KC (4.95), LIX (3.92), and MIP-1α (5.47). If driven by KrasG12D expression, similar responses should be observed between the KrasG12D+Fresh and WT+CM(KC) conditions. However, this was not the case, suggesting that conditioned media influenced both cytokine and Krt8 expression in conditioned media samples (Fig 5.7 B, Fig 5.8 C and D, Fig 5.9). We hypothesised that culturing PCLS past day 7 post induction led to tissue decay and skewed the result of the conditioned media assays. Therefore, conditioned media experiments were repeated, instead introducing conditioned media to respective PCLS at 5 DPI, and culturing until 7 DPI.

In this second experiment, several interesting targets were once again detected (Fig 5.10A), in addition to two new targets. Quantification of densitometry data from cytokine arrays revealed fewer strong hits compared to the previous array (Fig 5.10). In KrasG12D conditioned media we observed an increase in Eotaxin 2 (1.25), IL-6 (1.59), KC (1.42), LIX (1.32), MIP-1γ (1.4), RANTES (1.11), sTNF RI (1.62) and sTNF RII (1.57) (Figure 5.9 B-I). Targets that were enriched previously (Fig 5.9 C, D and H) including GM-CSF, G-CSF, and MIP-1α were not found in this second array. Consistently, levels of Eotaxin-2, IL-6, KC, LIX, MIP-1γ, and soluble TNF receptors I and II were detected in both experiments, suggesting an important pro-inflammatory role of these factors following KrasG12D expression in PCLS cultures.

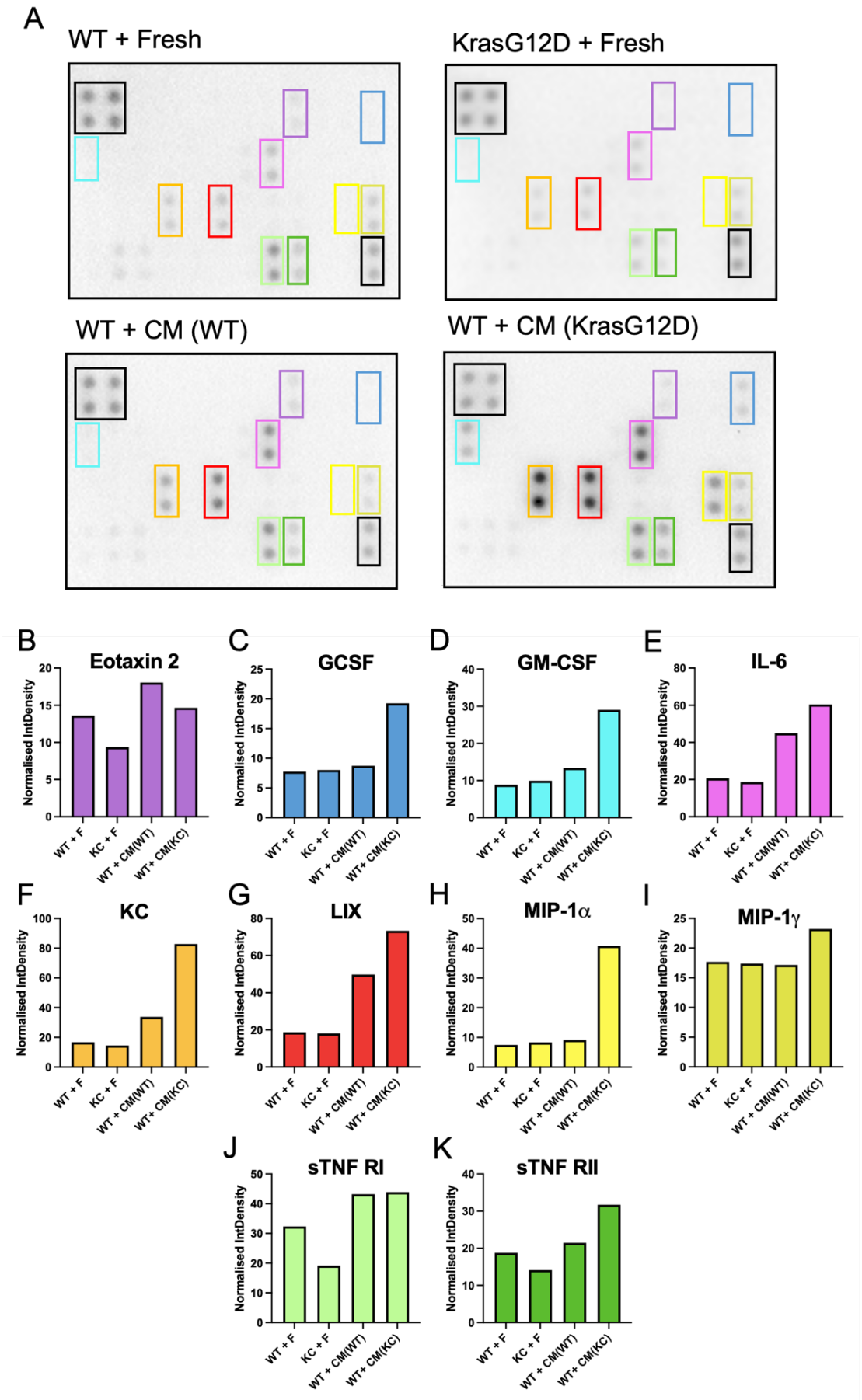

Figure 5. 9 Dot blot inflammatory cytokine array at 9 DPI.

A) Cytokine Array dot blots used to screen conditioned media from PCLS at 9 DPI. Targets are arranged in vertical pairs, and coloured boxes correspond to semi-quantified graphs B-K. Positive control blots are outlined in black. **B-K**) Bars represent integrated density of cytokine array targets normalised to positive control for each respective condition WT PCLS + Fresh media (WT +F), KrasG12D PCLS + Fresh media (KC+F), WT PCLS + WT-conditioned media (WT+CM(WT)), and WT+ KrasG12D-conditioned media (WT+CM(KC)).

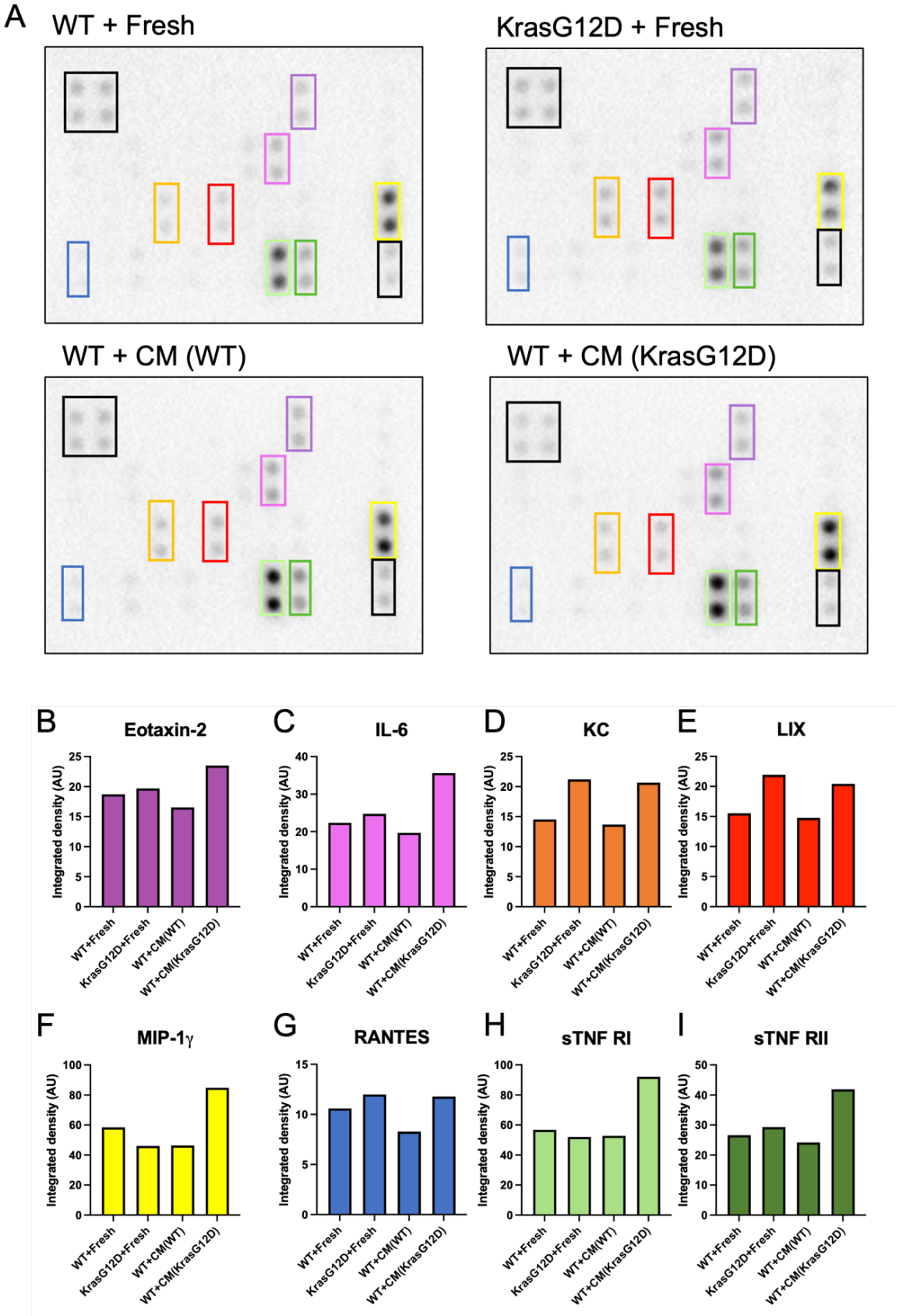

Figure 5. 10 Dot blot Inflammatory cytokine array at 7 DPI.

A) Cytokine Array dot blots used to screen conditioned media from PCLS at 9 DPI. Targets are arranged in vertical pairs, and coloured boxes correspond to semi-quantified graphs B-I. Positive control blots are outlined in black. **B-I**) Bars represent integrated density of cytokine array targets normalised to positive control for each respective condition WT PCLS + Fresh media (WT +Fresh), KrasG12D PCLS + Fresh media (KrasG12D +Fresh), WT PCLS + WT-conditioned media (WT+CM(WT)), and WT+ KrasG12D-conditioned media (WT+CM(KrasG12D)).

5.2.7 Krt8 phenotypes are present and stratify with histological severity of lungs at 35 DPI.

We next aimed to assess whether the Krt8 phenotype we observed *ex vivo* was recapitulated *in vivo*. At 7 DPI, RFP positivity was relatively low throughout the lung (Fig 5.11 A). In contrast, at 35 DPI lungs showed a range of histological changes that were consistent with normal tissue, early hyperplastic tissue, and late-stage adenomatous tissue. From a small experimental cohort used (n=3 WT and n=3 KrasG12D), only 2/3 KrasG12D animals had successful inoculations with AdCre, meaning analysis of 35 DPI tumour tissue was unfortunately limited to 2 mice. Within these 2 mice, histological changes were identified by viewing H&E (not shown) and RFP staining. For our analysis, tissue was sub-stratified into broad categories based on RFP expression and tissue architecture; normal tissue (Normal), tissue adjacent to hyperplastic regions (Adjacent), Low hyperplasia regions that still contained airspaces, but showed thickening of alveolar walls and RFP staining (Low), medium hyperplastic regions that were determined by more densely packed RFP-positive tissue (Mid) and highly hyperplastic regions that resembled the most dense, tumour-like tissue that stained positive for RFP (High).

Firstly, levels of RFP in the tissue were analysed to consolidate previous information from flow cytometry experiments (3.2.3), and to see if our stratification of tissue held some accuracy. We found that in WT and KrasG12D normal tissues, percentage of RFP+ cells remained consistently low with 2.83 ±2.4% of WT (Fig 5.11A and B, “WT Normal”), and 2.52 ±0.92% of KrasG12D cells positive for RFP and (Fig 5.11A and B, “KrasG12D Normal”; One-Way ANOVA, P >0.9999). Tissue adjacent to hyperplastic tissues in KrasG12D had a greater percentage of RFP (13.60 ±3.75%, Fig 5.11 A and B, “Adjacent”) compared to regions of histologically normal tissue, but this was not significantly different (P =0.8780). In our stratifications, hyperplastic regions all exhibit similar levels of RFP (Fig 5.11 A and B “Low” = 40.57 ±20.10, “Mid” = 38.79 ±20.34, “High” = 33.24 ±22.75), which further resemble our previous findings from flow cytometry. FFPE serial sections were stained for Krt8 by immunofluorescence, and the regions previously selected in RFP IHC were found and sampled for estimations of RFP level and Krt8 expression. Unsurprisingly, no significant change was observed between WT and KrasG12D normal tissue, with 10.90 ±2.1% Krt8 positive cells in WT tissue (Fig 5.11 A and C), and 5.89 ±2.29% Krt8 positive cells in KrasG12D normal tissue (Fig 5.11 A and C, P =0.3635). Similarly, no significant change was observed between KrasG12D adjacent and WT normal tissue, where 14.9 ±5.75% of cells were Krt8+ (Fig 5.11A and C, P =0.5457). Interestingly,

KrasG12D “adjacent” tissue had a roughly 2.5-fold times greater Krt8 population than KrasG12D “normal” tissue (Fig 5.11 A and C), suggesting that proximity to hyperplasia may be driving Krt8 expression. In low hyperplastic regions, Krt8 expression spiked drastically to 54.81 ±1.97% (Fig 5.11 C), starkly contrasting the previous analyses. More interestingly, Krt8 expression increased in accordance with sub stratification of hyperplastic regions, climbing to 67.20 ±2.12% in Mid, and then peaking at 77.02 ±3.22% in high hyperplastic fields of view (Fig 5.11C, all $P < 0.0001$). These data suggest that KrasG12D development into hyperplasia is associated with increased expression of Krt8, highlighting a potential role for ATII cell differentiation in KrasG12D-driven tumorigenesis.

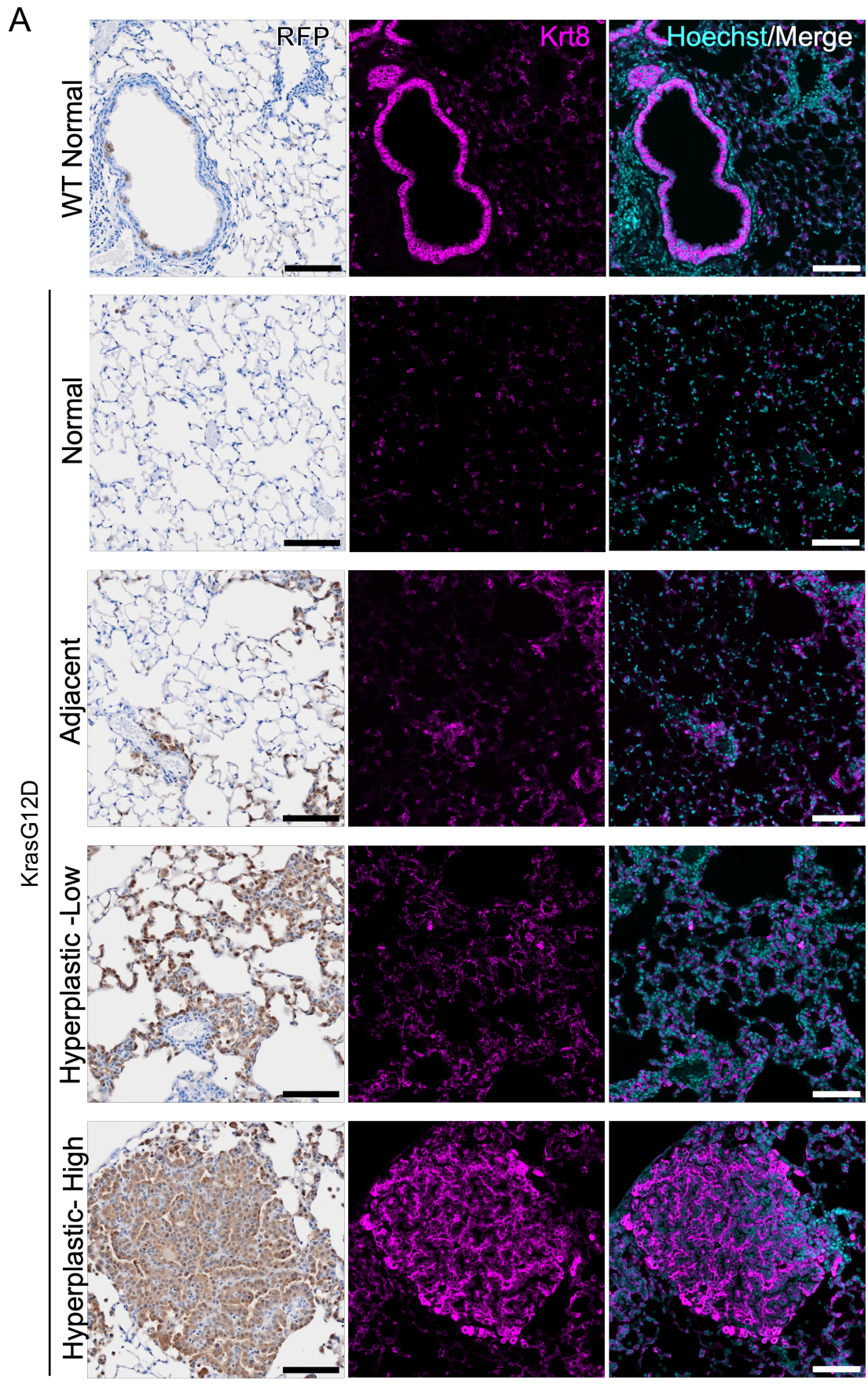
A
RFP
Krt8
Hoechst/Merge
WT Normal
KrasG12D
Normal
Adjacent
Hyperplastic -Low
Hyperplastic- High

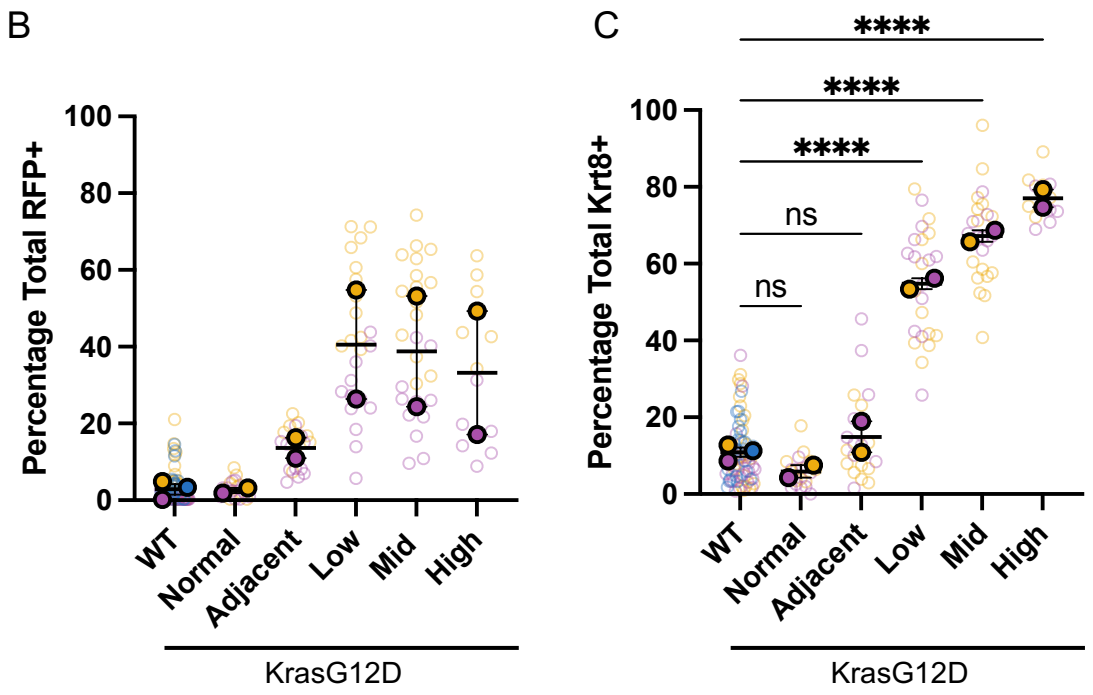

Figure 5. 11 Krt8 phenotype stratifies with the severity of hyperplasia.

A) Representative images of stratification groups starting with normal tissue from both WT and KrasG12D animals at 35 DPI. These display clear airspaces, non-buckled airways and look relatively healthy. In KrasG12D tissues, adjacent tissue refers to samples taken either next to hyperplastic tissue or contain very little RFP+ cells within the image. Hyperplastic tissue was identified based on RFP+ staining, then sub-stratified into low hyperplasia, mid hyperplasia, and high hyperplasia based on both RFP expression and severity of alveolar disorganisation. Serial sectioned FFPE slides were stained for RFP (brown, DAB), and Krt8 (magenta). Scale bars,100 μm. Slides prepared and images acquired by Daisy Moyers (undergraduate project student at Cardiff University). **B)** Quantification of RFP+ cells as a percentage of total cells per field of view. KrasG12D mice at 35 DPI. **C)** Quantification of Krt8+ cells as a percentage of total cells per field of view. Number of fields counted are shown by transparent rings, corresponding to the biological mean (solid circle) from n = 3 WT mice, and n = 2. Lines and error bars represent mean± SEM. One-Way ANOVA with Dunnett's multiple comparisons relative to WT. P>0.05 = non-significant (ns), ****P<0.0001.

5.3 Discussion

5.3.1 KrasG12D drives injury-like remodelling of the alveolar lung via Krt8+ transitional cell states.

Cytokeratin 8 is an intermediate filament protein that is expressed across a range of tissues in many cell types. In the lung, it has recently been described as a marker of mature cell differentiation in response to stress and injury (Riemondy et al. 2019; Choi et al. 2020; Kobayashi et al. 2020; Strunz et al. 2020; Toth et al. 2023). Furthermore, recent studies into lung carcinogenesis have highlighted distinct expression of Krt8 in adenocarcinomas in keeping with the results of our screening of available human tumour databases (Fig 5.1A) (Fukunaga et al. 2002; Hill et al. 2023; Yang et al. 2023; Li et al. 2024). This raises the question of what triggers lung regeneration, and where the borders between lung injury and oncogenic insult intersect. Expression of KrasG12D in PCLS led to a general increase in the amount of Krt8 in the tissue *ex vivo* (Fig 5.1B). Further analysis showed that not only do more cells start to express Krt8, but the amount of Krt8 expressed within cells also increased relative to levels seen in WT PCLS over the first week post induction (Fig 5.3A-C). Krt8 positivity is now regarded as an expected phenotype in tumour tissues, however we find novelty in showing expression of Krt8 at early timepoints and show that Krt8 expression is not limited to KrasG12D expressing cells in the alveoli (Fig 5.4).

We observed that a large percentage of KrasG12D expressing cells are additionally positive for Krt8 (Fig 5.4), and also show that a surprising number of cells that neighbour KrasG12D mutant cells also express Krt8 to a greater extent than in WT control experiments (Fig 5.4B). Using 3D rendering of Krt8 positive PCLS (Fig 5.5), we showed that KrasG12D mutant cells undergo morphological changes that resemble trans-differentiation from ATII cells into ATI – that is, becoming larger in volume, and decrease in sphericity (Fig 5.6). This reflects what is currently understood about injury-driven remodelling of alveolar cells. Kobayashi et al. (2020) demonstrate that pre-alveolar type I transitional cell state (PATS) cells arise when ATII cells differentiate into ATI cells upon LPS and bleomycin injury. Moreover, Krt8+ cells that arise in bleomycin-injured mouse lungs exhibit loss of Pro-SPC positive cells, lose sphericity, and do not become fully differentiated to mature ATI cells (Strunz et al. 2020). Expression of mature cell type markers have not been observed in intermediate cell populations (Choi et al. 2020; Kobayashi et al. 2020; Strunz et al. 2020), which interestingly aligns with a study which analysed KrasG12D-mediated

changes in ATII-cell derived organoids. Here the authors found that ATII differentiation markers such as *Sftpc, Nkx2-1, Lyz2 and Cd74* were downregulated in response to KrasG12D mutation, and in turn, developmental signatures like *Sox9*, *Hmga2* and *Ly6a* were upregulated (Dost et al. 2020). It is possible that Krt8+ cells detected in our system can be further associated to one of the core injury phenotypes (PATS, Krt8+ ADI and DATPs (Xie et al. 2022)), however the timeframe permitted by this project, antibody incompatibilities, and a series of equipment and reagent shortages meant that unfortunately this could not be carried out. The directionality of this phenotype is well described in ATII to ATI differentiation, but recent findings show that it is possible to reprogramme ATI cells back to ATII cells (Juul et al. 2023; Yang et al. 2023).

Using a mouse model that drives KrasG12D expression in ATI cells (HOPX CreERT), Juul et al.(2023) were able to show appearance of cuboidal ATII-like cells in the lung after 13 months. These cells which were labelled as ATI cells and expressed characteristic markers of ATII cell fate such as *Abca3*, *Sftpb* and *Sftpc*, eventually giving rise to lepidic adenocarcinomas which are histologically distinct from adenocarcinomas which originate from SFTPC CreERT; KrasG12D mice (ATII cell driver). Another study which used a different model of ATI-driven KrasG12D expression (*Gramd2* CreERT2), showed that tumour lesions arise predominantly as papillary adenocarcinoma, with lepidic adenocarcinoma and early hyperplasia present in tissues too (Yang et al. 2023). Both studies demonstrate that ATI to ATII cell transitions present with Krt8 expression, indicating a conserved pathways of repair and progenitor relationships in the distal lung. Amounting evidence from lung studies suggest that the Krt8 state is an emergency transition in response to lineage misspecification, oncogenic insult, epithelial damage, and infection. Loss of NKX2-1 from alveolar epithelium progenitor (AEP) derived organoids leads to an irreversible Krt8+/Cldn4+ cell state (Toth et al. 2023). The extent to which NKX2-1 is removed from these cells determines whether Krt8 transitional states resolve; when NKX2-1 is partially lost, Krt8 states resolve as seen in fibrosis (Choi et al. 2020; Kobayashi et al. 2020; Strunz et al. 2020), or become permanently stressed proliferative cells when NKX2-1 is completely deleted from mice (Toth et al. 2023). Furthermore, recent investigations have uncovered the presence of gastric cell type signatures in KrasG12D-driven tumours (Juul et al. 2023), further suggesting the function of NKX2-1 potential regulator of the cell of origin in KrasG12D disease, whereby status of NKX2-1 in mutant cells may prove tumour suppressive or promoting.

5.3.2 Cytokine release from KrasG12D mutant cells account for WT cell trans-differentiation.

In our model, we switched on expression of oncogenic KrasG12D which promoted aberrant Ras/MAPK signalling and increased phosphorylated ERK (Jackson et al. 2001; Cisowski et al. 2016). Aberrant self-renewal driven by oncogenic KrasG12D leads to p53 mediated cell cycle arrest and downregulation of ATII cell maturity gene signatures, and the differentiation of cells through transitional cell states observed in lung fibrosis repair programmes (Kaiser et al. 2023) In line with this, we observe a KrasG12D-associated increase in Krt8+ cell states, suggesting a conserved p53-dependent mechanism. These new ATI-like cells may well contribute to early cancerous lesions in the lung, but they would not contribute to adenocarcinoma formation as expected until p53 is rendered non-functional. This aligns with what we show in this study and explains part of the known dogma that additional loss of tumour suppressors is required for full progression from adenoma to adenocarcinoma. I hypothesise that if PCLS were derived from KrasG12D, $p53^{fl/fl}$ lungs, we would not observe Krt8 signatures as we do here.

Upon finding that non-mutant cells start expressing Krt8 in KrasG12D PCLS, we postulated that secreted factors may be contributing to landscape remodelling in the alveoli. Subsequent transplantation of KrasG12D-conditioned media onto *ex vivo* PCLS was sufficient to induce Krt8 expression in WT PCLS (Fig 5.7-7). Similar studies have implemented co-culture systems with alveolar organoids and macrophages (Choi et al. 2020; Hill et al. 2023) finding that inflammatory signals such as IL-1β from macrophages drive ATII cell remodelling *in vitro*, and that competent immune systems are required for EGFR-driven tumorigenesis *in vivo* (Hill et al. 2023). At the core of this was the idea that inflammatory processes associated with lung injury were driving immune cell recruitment to the cells of origin, providing the necessary signals for the next stages of morphogenesis. These findings instructed the next steps of our experiments in which we screened PCLS media for inflammatory pathways to try and decipher how KrasG12D is driving remodelling *ex vivo*. By implementing dot blot arrays (Fig 5.9 and 5.10). we identified a number of potential innate immune system modifiers that were consistently changed as a result of KrasG12D conditioning of media: IL-6, KC, LIX, MIP 1γ, sTNF RI and sTNF RII (Fig 5.9 E, F, G, I, J, K; Fig 5.10 C, D, E, F, H, I). Surprisingly, IL-1β which seems to be an expected driver of cellular differentiation (Choi et al. 2020) does not appear differentially regulated by conditioned media, potentially indicating that IL-1β signalling arises as a downstream

event to the initial inflammatory processes caused by KrasG12D activation and subsequent recruitment of immune cells to the early oncogenic niche.

KrasG12D activation leads to the upregulation of IL-6, KC and LIX directly (Ji et al. 2006; Ancrile et al. 2007), subsequently leading to recruitment of the innate immune system to the KrasG12D-mutant niche (Deng et al. 2019; Hamarsheh et al. 2020). These innate immune cells feed into the pro-inflammatory cascade that drive tumour cell expansion, angiogenesis, further immune recruitment, extracellular matrix remodelling and anti-tumorigenic immune evasion (Tamori et al. 2010; Deng et al. 2019; Hamarsheh et al. 2020). In our study, we did not have a great enough resolution to our flow cytometry panels to assess changes in populations of immune cells retrospectively. Based on the work of others, suitable parameters to include would screen for alveolar (CD45+, EpCAM-, $CD64^{High}$, SiglecF+) and interstitial (CD45+, EpCAM-, $CD64^{High}$, SiglecF-) macrophages, and neutrophils (CD45+, CD11b+, Ly6G +) (Hill et al. 2023). Similarly, in PCLS recruitment of innate immune cells is not possible due to the lack of pools to draw from, leaving only small number of resident immune cells that were present at the point of generation if they survived for long enough. One way to address this shortcoming would be to set up a co-culture system as in the organoid platforms used by Choi et al. (2020) and Hill et al.(2023). As a result of this, the panel of cytokines found in our study are credible, and the lack of IL-1β in the screen can be explained by low level expression in *ex vivo* PCLS.

5.3.3 KrasG12D mediated expression of Krt8 is observed in 35 DPI tumour sections in mice.

To examine whether our *ex vivo* phenotype was preserved *in vivo* we set out to analyse different stages of tumorigenesis in 35-DPI tissue (Fig 5.11). We found that we could loosely stratify hyperplastic tissue regions based on RFP level and how crowded and non-normal the alveoli looked. We observed an upper limit to the amount of RFP+ cells we could count (Fig 5.11B), which reassuringly aligned closely to what we observe in section 3.2.3, and further provide a context to our findings in that section. Based on our assumptions on severity, Krt8 staining of serial sections confirmed our hypothesis that cellular differentiation as a potential response to cancer stress is compounded with tumour histology, with the greatest Krt8 expression observed in the most severe hyperplasia (Fig 5.11C). The next step for this work that would fortify our findings *in vivo* was to screen for immune cell populations that could be driving differentiation. Unfortunately, we were not successful in characterising the cells that were present, only finding confounding results from flow cytometry data (not

shown). Another route to study would be pERK levels and p53, and how this stratified with Krt8 intensity. Increased p53 staining, reduced pERK and Krt8+ staining would indicate that KrasG12D mutant cells undergo differentiation as in Kaiser et al. To substantiate our hypothesis that KrasG12D is driving local changes to WT epithelia, regions of interest were chosen around hyperplastic regions and analysed across RFP and Krt8 IHC staining (Fig 5B and 5C). We observed that percentage positive Krt8 staining far exceeded the percentage RFP positive staining in comparative sections of the tissue suggesting that hyperplastic RFP positive cells are influencing the WT neighbourhood as we observe *ex vivo*.

5.3.4 Summary and future directions.

To conclude, the data presented here highlights a potential mechanism by which KrasG12D mutant cells undergo morphological changes that are reminiscent of recent advances in the field. We show that two potential mechanisms may be occurring simultaneously – one in which p53 mediates KrasG12D mutant cell transition (Fig 5.12 B), and one driven by inflammatory signalling and subsequent innate immune cell recruitment to the niche (Fig 5.12 C). We have mostly shown this using our *ex vivo* PCLS model of early tumorigenesis, highlighting the tool as valuable way to discover readouts of cancer cell biology in a controlled system, and present a case for using PCLS to further understand how a cell of origin is determined in the alveolar lung. We demonstrate that KrasG12D driven transitional cell states are preserved *in vivo*, and demonstrate that with worsening histological severity, total Krt8 levels also increase.

Future work on this aspect should aim to identify fully the population of cells that are undergoing trans-differentiation, additionally identifying two mechanisms by which cells are transitioning. A general hypothesis is that in the first instance, KrasG12D mutant ATII cells are undergoing p53 mediated transition, and loss of p53 would result in loss of transition. Using an SPC-Cre virus to induce ATII-cell specific KrasG12D would permit the live-imaging of ATII cell differentiation in culture.

Furthermore, we used our new *ex vivo* model of interrogating early KrasG12D biology in the alveoli, showing that KrasG12D mutant cells secrete pro-inflammatory cytokines into the media, leading to expression of transitional cell markers in non-KrasG12D populations. To further expand on this work, ideal experiments would aim to promote alveolar cell differentiation by supplementing PCLS media with IL-1β. Alternatively, identifying key cytokines that promote innate immune cell recruitment can be achieved by blocking some of the candidates we identified here.

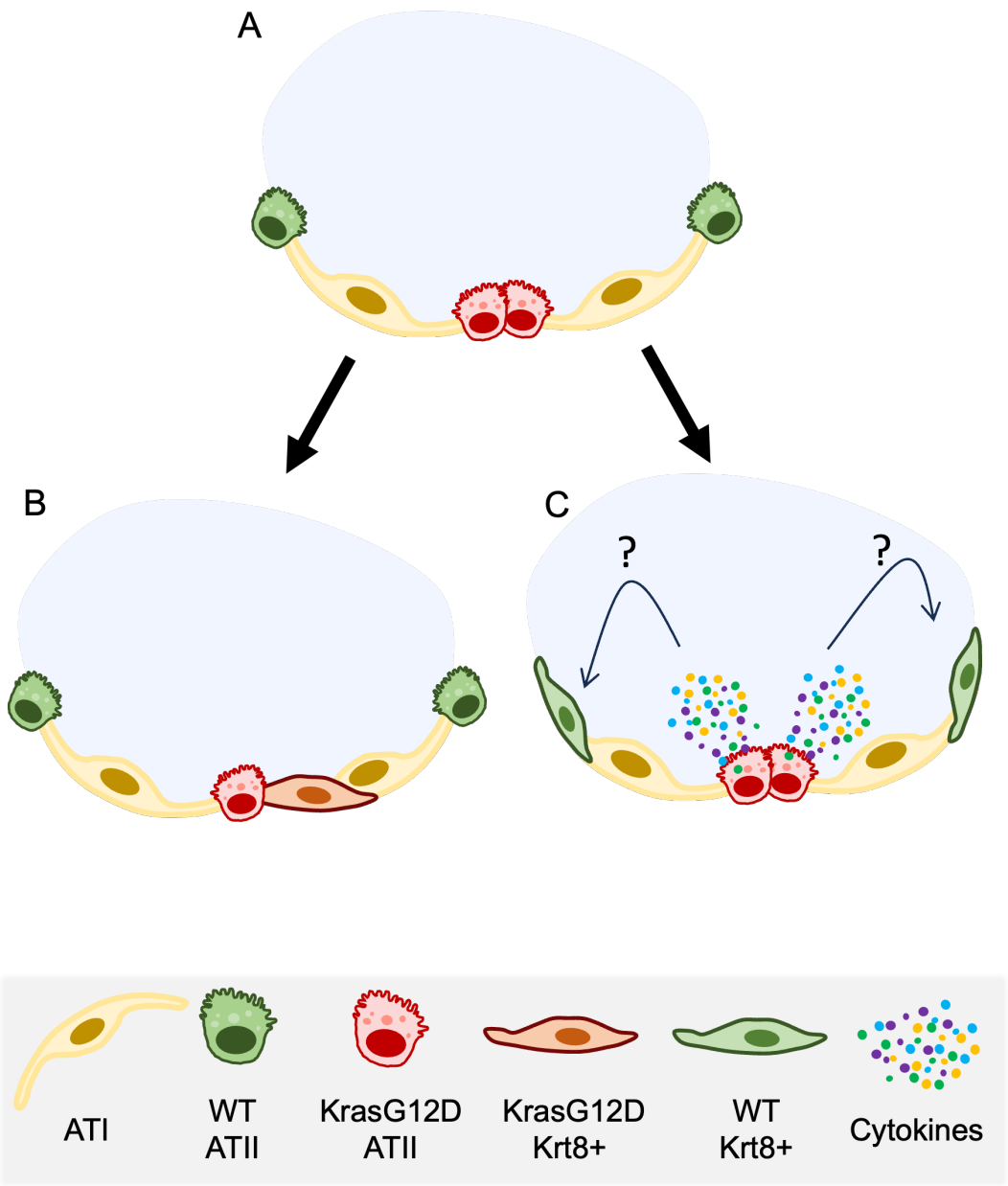

Figure 5. 12 KrasG12D drives two potential mechanisms of cell trans-differentiation in the alveoli.

When KrasG12D is activated in the alveoli **(A)** transitional states associated with epithelial injury repair is initiated. **B)** KrasG12D mutant cells undergo morphological changes, becoming less cuboidal and more squamous, and start to express cytokeratin 8 (Krt8). **C)** KrasG12D mutant cells secrete pro-inflammatory cytokines that potential regulate innate immune cell populations in the lung, subsequently leading to remodelling of wild-type (WT) cells into damage associated transitional cell states, also expressing Krt8.

6 General Discussion.

Our tissues harbour and accumulate somatic mutations over time. However, the presence of potentially dangerous mutant cells in tissues does not necessarily mean that they will develop tumours. There are now many studies demonstrating how oncogenic cells can be eliminated from tissues based on interactions with their relatively more-healthy neighbouring cells (Hogan et al. 2009; Kajita et al. 2010; Kajita et al. 2014; Kajita and Fujita 2015; Porazinski et al. 2016; Kon et al. 2017; Sasaki et al. 2018; Hill et al. 2021; Shirai et al. 2022). In other tissues such as the intestinal stem cell compartment, these interactions may tip in the favour of the mutant cells, leading to the elimination of normal cells and expansion of mutant populations (Kolahgar et al. 2015; Suijkerbuijk et al. 2016; Flanagan et al. 2021; van Neerven et al. 2021). In the lung, there are limited studies identifying competitive elimination of HrasV12 mutant cells from the bronchiolar epithelium (Sasaki et al. 2018; Shirai et al. 2022), but elimination of cells carrying disease relevant mutations such as KrasG12V or KrasG12D is not described.

KrasG12D mutations account for ~ 30% of NSCLC cases and are sufficient to drive severe disease progression in mice by 5 weeks post induction (Jackson et al. 2001; Johnson et al. 2001; DuPage et al. 2009). By exploring an existing lung cancer model and adapting transgene induction and analysis for cell competition, I found that KrasG12D mutant cells are neither extruded from the proximal lung epithelium, nor are they removed from the alveolar epithelium at early timepoints as was hypothesised. Analysis of alternative cell competition readouts that indicate selection and preparation for elimination suggested that KrasG12D mutant cells are not recognised by neighbouring WT cells, and subsequently remain in the epithelium to drive hyperplastic growth. Further to this, I identified that cells in the alveoli undergo morphological changes reported to occur in fibrotic lung disease.

I established an *ex vivo* tool to further explore this phenotype and discovered that KrasG12D mutant cells express Krt8 which is a prominent marker of ATII to ATI cell differentiation in fibrotic lung disease (Choi et al. 2020; Kobayashi et al. 2020; Strunz et al. 2020). Using 3D analysis of PCLS, I identified that Krt8+ KrasG12D-expressing cells undergo morphological changes from cuboidal to squamous cells, suggestive of a transition from ATII to ATI cell fate *ex vivo*. Finally, analysis of conditioned media from PCLS experiments identified a potential role for pro-inflammatory cytokines in the recruitment of innate immune cells to the alveolar epithelium which further drives differentiation of non-transformed cells. Together these data corroborate recent findings that explore the potentially shared role for injury repair pathways in fibrosis and cancer, further refining how the plasticity of certain cells in the lung can give rise to a cell of origin for cancer.

6.1. Cell competition is not a contributing factor to homeostasis of the lung epithelium following KrasG12D activation.

During cell competition, several processes occur that ensure epithelial integrity is maintained. One such mechanism identified by our lab is EphA2 forward signalling, required for the segregation and subsequent elimination of Ras mutant cells *in vitro* and *in vivo* (Hogan et al. 2009; Hill and Hogan 2017; Hill et al. 2021).Hyperactivity of Ras-MAPK signalling in cells results in the increased expression of EphA2 receptor at the cell membrane. Increased EphA2 receptor expression increases ligand binding and subsequent receptor phosphorylation which induces a series of downstream processes that aim to segregate the cell from WT neighbours, destabilise E-cadherin junctions, and reorganise the actin cytoskeleton to prepare for extrusion(Porazinski et al. 2016; Hill and Hogan 2017; Hill et al. 2021). Following this, mutant cells undergo predictable morphological changes that indicate their apical extrusion from the epithelium. This has been documented both *in vitro* and *in vivo* (Hogan et al. 2009; Porazinski et al. 2016; Sasaki et al. 2018; Shirai et al. 2022).

In Chapter 3, I set out to identify competitive cell extrusion events at early timepoints in the proximal airways as published evidence suggested that this occurs within 3 days of HrasV12 expression (Shirai et al. 2022). My analysis revealed that a small proportion of cells can be seen in the initial stages of extrusion but found no evidence that mutant cells are fully extruded. As my findings did not support my cell competition hypothesis, I did not pursue a role for EphA2 in lung epithelial homeostasis. Future work could include a thorough analysis of molecular readouts of apical extrusion of Ras mutant cells, described by our lab and others, including stability of E-cadherin junctions (Hill et al. 2021), accumulation of F-actin between KrasG12D cells in clusters (Hogan et al. 2009), and accumulation of filamin and vimentin in WT cells surrounding KrasG12D mutants (Kajita et al. 2014). These readouts would aim to further support that KrasG12D mutant cells in the proximal lung are not recognised for elimination by surrounding WT cells, permitting them to stay in the epithelium. These experimental readouts could also apply to the alveolar lung where we observed no evidence for cell competition *in vivo*.

The disparities observed between my study and others may suggest alternative responses to different Ras mutations in the lung epithelium. However, as the mode of driving transgene expression differed between this thesis and both Sasaki et al. (2018) and Shirai et al. (2022) prevent direct comparison of my findings. Fortunately, I was able to find a study that utilised KrasG12D oncogene in the Krt19-Cre^{ERT} model which can be used to support my hypothesis (Ray et al. 2011). At 6

months post induction, KrasG12D drove lung adenomas and dense papillary hyperplasia (Ray et al. 2011). Similar histological findings were not observed in the HrasV12 lungs driven by the Krt19 promoter (Shirai et al. 2022), which suggests that HrasV12 mutations do not contribute to lung tumorigenesis in the same way that KrasG12D mutations do. This is in keeping with the finding that Hras mutations are rarely found in lung cancer cases (Prior et al. 2012). Is it due to cell competition that Hras mutations do not drive tumorigenesis, but Kras mutants do as they are able to evade loser cell fate? This may indicate that other somatic mutations that are found in tissues but do not drive disease are designated as loser cells and are subsequently lost from the lung epithelium. This would be an interesting angle to identify EDAC targets in the lung to better understand the process.

6.2. A proposed mechanism of KrasG12D-driven Injury-associated ATII cell differentiation.

From the work carried out in Chapter 4 and Chapter 5, I propose an updated mechanism of how conserved injury repair pathways dictate KrasG12D mutant cell fate in the epithelium at early timepoints. In homeostasis, ATII cell identity and self-renewal is maintained by RAS/MAPK signalling (Desai et al. 2014). In keeping with our current understanding of molecular pathways underpinning ATII-to-ATI cell differentiation, aberrant activation of KrasG12D leads to increased ATII cell self-renewal (Chaudhary et al. 2023), as well as metabolic changes that consequently activate p53 signalling targets such as increased Hif1α (Kikuchi et al. 2009; Kang et al. 2014; Kaiser et al. 2023). Induction of p53 signalling pathways leads to cell cycle arrest in ATII cells, as well as the loss of ATII cell mature signatures (Fig 6.1), subsequently promoting differentiation of ATII cells via transitional cell states to ATI cells (Choi et al. 2020; Kobayashi et al. 2020; Strunz et al. 2020; Kaiser et al. 2023). As was discovered in this thesis, KrasG12D positive cells expressing Krt8 (one of the conserved transitional state markers) undergo morphological changes that indicate metaplasia from ATII cells to squamous ATI cells *ex vivo* (Fig 6.1). This similarity is found between fibrotic lung populations expressing Krt8 which are themselves derived from ATII cells *in vivo* (Strunz et al. 2020).

In parallel to direct KrasG12D-mutant ATII cell differentiation, a population of Kras non-transformed cells also begin expressing Krt8 in the presence of KrasG12D mutant cells. KrasG12D expression drives the expression and subsequent release of pro-inflammatory cytokines into the local environment (Ji et al. 2006; Ancrile et al. 2007) including KC, LIX, IL-6, and GM-CSF which have been shown to promote

recruitment of innate immune cells such as interstitial macrophages to the site of mutation (Deng et al. 2019; Hamarsheh et al. 2020). We describe here that in the presence of KrasG12D-expressing cells, CD45+ immune cells slow down and become less migratory, either as a suggesting that they recognise, and focus on transformed cells in the alveoli. This phenotype has been observed in studies of the pre-metastatic lung in breast cancer, revealing that expression of CD18 on neutrophils leads to arrested motility in response to G-CSF production (Fercoq et al. 2024).

Recent published works have identified that interstitial macrophages release IL-1β following recruitment and activation to the alveoli (Choi et al. 2020; Hill et al. 2023). A population of WT ATII cells express interleukin-1 receptor 1 (Il1r1) that are epigenetically primed to respond to inflammatory signalling respond to the sudden influx of innate immune cells, and in turn, downregulate ATII identity gene expression, enter cell cycle arrest and undergo Hif1α mediated differentiation into transient progenitor cells that express Krt8 (Choi et al. 2020). Due to chronic inflammatory responses and lack of inflammatory resolution, Krt8+ cells are restrained as intermediates and do not become ATI cells (Park et al. 2011; Kobayashi et al. 2020).

I have shown that Krt8 positive cells accumulate in conjunction with disease progression through histological stages and this correlates with number of RFP+ (and therefore KrasG12D expressing) cells. Human lung tissues expressing oncogenic *KRAS* have a highly significant correlation with presence of Krt8+ intermediate cells (Han et al. 2024). Furthermore, regions surrounding tumours *in vivo* exhibit more *Krt8*-associated gene signatures than normal tissue further away from tumour regions, supporting a prolonged role for chronic inflammation and its effect on non-transformed cells in the lung (Han et al. 2024). As early as 2 weeks post KrasG12D induction, hyperplastic regions in the lung take on histological characteristics akin to lepidic expansion in the alveoli (Jackson et al. 2001; Desai et al. 2014). I have shown at 7 DPI that KrasG12D-expressing cells morphologically similar to ATII cells exhibit morphological features that precede lepidic expansion in the alveoli. Furthermore, I propose that injury-associated differentiation through transitional cell states is a failed tumour-suppressive mechanism which further drives loss of lung function and ultimately fails to prevent expansion of ATII-derived cells in adenocarcinoma. What is unclear from current studies is how and when aberrant Krt8+ cells switch fate and become tumorigenic (Fig 6.1). This process needs to be further studied.

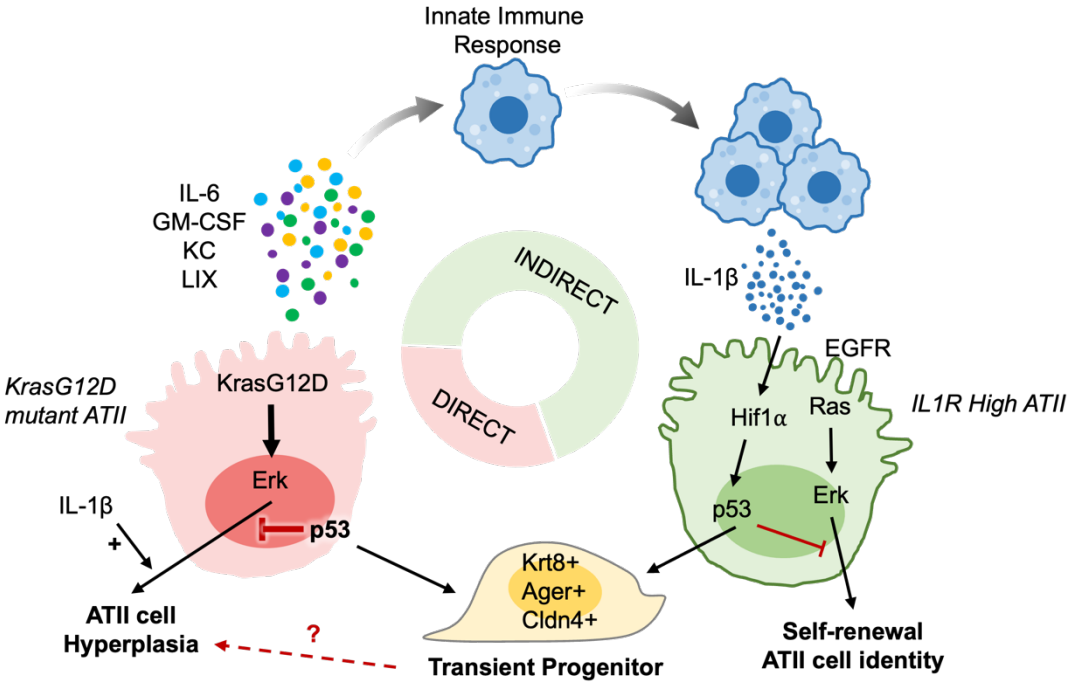

Figure 6. 1. A Proposed mechanisms of KrasG12D-induced changes in ATII cell fate in the alveoli.

Direct: Expression of KrasG12D in ATII cells is sufficient to drive cell cycle arrest and subsequent trans-differentiation to canonical transient progenitor states defined by a set of conserved markers.
Indirect: Parallel to direct differentiation pathways, KrasG12D mutant cells produce pro-inflammatory cytokines that influence and recruit innate immune cells to the alveolar lung. Approximately 15% of ATII cells identified by their expression of IL1R1 are primed to respond to IL-1β delivered by recruited immune cells, in turn, downregulate ATII transcriptional signatures and progress to transient progenitor states. Chronic exposure to IL-1β is reported to prevent resolution of transient progenitors to functional ATI cells and is also shown to drive hyperplasia of ATII cells *in vivo* and *in vitro*. From our current understanding, the oncogenic switch between transient progenitor and hyperplastic tumours is not defined (red dashed arrow).

6.3. Future directions.

The data presented in this thesis raise many interesting avenues for future research. Competitive cell elimination of KrasG12D mutant cells is not conserved in the lung, therefore further work should aim to identify the different outputs driven by the range of Ras mutations and isoforms. Firstly, a comparable model of driving tumorigenesis should be tested by delivering AdCre intranasally to $Hras^{LSL\text{-}G12V}$ mice then similar timepoints and analyses carried out. This would identify whether the differences are caused by differential Ras signalling or as a consequence of driving transgene recombination via viral infection or Cre-driver. In conjunction with this, it would be interesting to test how well competitive cell elimination is preserved across a larger range of Ras mutations such as those found on Kras codons 12, 13 and 61 (Prior et al. 2012).

The goal behind exploring cell competition is to better understand the innate homeostatic processes that help maintain our tissue, and to better understand how interruption of these processes can contribute to disease. Previously, our lab has identified that KrasG12D mutant cells in the pancreas adopt a loser cell fate at the early stages of KrasG12D activation and that improper clearance of these cells permits the growth of pre-cancerous lesion that continue to grow and accumulate mutations with age (Hill et al. 2021). Here I have shown that the lung does not clear KrasG12D mutant cells from its epithelia, but instead uses conserved injury repair processes, partially driven by pro-inflammatory cytokine pathways *ex vivo*. Further work should explore the role of pro-inflammatory signals *in vivo*, using blocking experiments to target pro-inflammatory cytokines identified here, alongside immune-deficient mice to understand what happens in the pre-hyperplastic alveoli.

The analysis and characterisation of lung immune responses to KrasG12D are not fully explored in this thesis, and much work is needed to confidently assign a role for innate immune cells in the KrasG12D-mediated differentiation of WT cells. This includes more stringent flow cytometry panels that resolve different immune cell populations, better readouts of cytokine concentrations both *in vivo* and *ex vivo*, as well as better immunohistochemical staining to show where immune cells are located *in situ*. I hypothesise that in the absence of a. functional immune system, only KrasG12D-expressing cells will undergo Krt8+ differentiation. Studies have revealed that when inflammation resolves, differentiating ATII cells become ATI cells and do not contribute to pathogenesis *in vivo* (Choi et al. 2020; Kobayashi et al. 2020). By alleviating chronic inflammation in KrasG12D lungs, would the onset of tumorigenesis be prolonged?

Another important aspect of future research is to explore the role of p53 signalling as this has been shown to drive the cell cycle arrest of KrasG12D-ATII cells and promote the differentiation pathways (Kaiser et al. 2023). I hypothesise that in the absence of p53 signalling, KrasG12D mutant cells do not undergo differentiation *ex vivo*, instead switching to hyperplastic states and accelerating the development of lung tumours both *ex vivo* and *in vivo*.

Recent revelations in the field of tissue homeostasis and cell competition have shown a protective role for tissue injury and somatic heterogeneity *in vivo*. Activating mutations in Ras are capable of driving squamous cell carcinoma in the skin of mice (Brown et al. 2017; Park et al. 2017; Pineda et al. 2019; Gallini et al. 2023). Live imaging of transformed cells in wounded ear skin revealed the loss of competitive advantage of both HrasV12 and KrasG12 heterozygous cells *in vivo* (Gallini et al. 2023). This study showed that tissue repair process in non-transformed cells overpowered tumorigenic processes in the skin. This has already been assessed to some extent in the lung, with specific ablation of certain cell types leading to field cancerisation from mutant progenitor populations (Kim et al. 2005; Desai et al. 2014). What is unclear is whether chronic inflammatory processes prior to KrasG12D activation would work to promote tumorigenesis, or drive differentiation processes that reduce potential cells of origin. This could be achieved by using low dose bleomycin for alveolar injury, naphthalene for airway injury.

Investigations into oesophageal tumour initiation regularly make use of DEN to induce a spectrum of mutations across the epithelium (Colom et al. 2020; Colom et al. 2021). Competitive interactions between different mutant populations give rise to largely homogeneous tumour populations, where less fit mutant cells are outcompeted by more fit mutant populations (Colom et al. 2021). This method of driving tumorigenesis is reminiscent of how somatic mutations arise in the lung in humans, whereby exposure to carcinogenic materials drive mutagenesis and subsequent accumulation of somatic mutations. Tobacco smoke is a potent carcinogen which causes 80-90% of lung cancer deaths (Yoshida et al. 2020). In spite of this, tobacco-driven lung cancer is relatively infrequent, with only 10-20% of smokers developing cancer in their lifetimes (Crispo et al. 2004; Huang et al. 2022). The effect of pre-exposing lung to cigarette smoke and then later inducing KrasG12D and RFP would be an interesting study to see how changing the relative fitness of the lung epithelium would affect KrasG12 mutant cell dynamics.

6.4. Conclusions

To conclude, I have revealed that KrasG12D mutant cells are not eliminated from the lung epithelium as was hypothesised, indicating that cell competition is not as conserved as we initially believed. Moreover, I have provided evidence to suggest that at the onset of KrasG12D activation, mutant cells in the alveolar epithelium undergo differentiation into a transient population of cells that can persist as hyperplastic foci in the alveoli and generate a pro-inflammatory environment. I have established an *ex vivo* model of the lung alveoli which can be used to track epithelial dynamics of lung epithelial and immune cells at early timepoints following activation of oncogenic KrasG12D. This work helps to further our understanding of what occurs at early timepoints following oncogene activation, as well as understanding how conserved repair pathways of the lung help shape the epithelium at the early stages of tumorigenesis. Eventually, we hope that this work will lead to the discovery of new strategies to detect lung cancer cases at earlier timepoints to improve treatment and prognosis.

List of References

Abascal, F. et al. 2021. Somatic mutation landscapes at single-molecule resolution. *Nature* 593(7859), pp. 405-410. doi: 10.1038/s41586-021-03477-4

Adams, T. S. et al. 2020. Single-cell RNA-seq reveals ectopic and aberrant lung-resident cell populations in idiopathic pulmonary fibrosis. *Sci Adv* 6(28), p. eaba1983. doi: 10.1126/sciadv.aba1983

Adderley, H., Blackhall, F. H. and Lindsay, C. R. 2019. KRAS-mutant non-small cell lung cancer: Converging small molecules and immune checkpoint inhibition. *EBioMedicine* 41, pp. 711-716. doi: 10.1016/j.ebiom.2019.02.049

Akram, K. M. et al. 2019. Live imaging of alveologenesis in precision-cut lung slices reveals dynamic epithelial cell behaviour. *Nat Commun* 10(1), p. 1178. doi: 10.1038/s41467-019-09067-3

Alcolea, M. P., Greulich, P., Wabik, A., Frede, J., Simons, B. D. and Jones, P. H. 2014. Differentiation imbalance in single oesophageal progenitor cells causes clonal immortalization and field change. *Nat Cell Biol* 16(6), pp. 615-622. doi: 10.1038/ncb2963

Amato, K. R. et al. 2014. Genetic and pharmacologic inhibition of EPHA2 promotes apoptosis in NSCLC. *J Clin Invest* 124(5), pp. 2037-2049. doi: 10.1172/JCI72522

Amato, K. R. et al. 2016. EPHA2 Blockade Overcomes Acquired Resistance to EGFR Kinase Inhibitors in Lung Cancer. *Cancer Res* 76(2), pp. 305-318. doi: 10.1158/0008-5472.CAN-15-0717

Ancrile, B., Lim, K. H. and Counter, C. M. 2007. Oncogenic Ras-induced secretion of IL6 is required for tumorigenesis. *Genes Dev* 21(14), pp. 1714-1719. doi: 10.1101/gad.1549407

Andersen, C. L., Jensen, J. L. and Ørntoft, T. F. 2004. Normalization of real-time quantitative reverse transcription-PCR data: a model-based variance estimation approach to identify genes suited for normalization, applied to bladder and colon cancer data sets. *Cancer Res* 64(15), pp. 5245-5250. doi: 10.1158/0008-5472.CAN-04-0496

Ardain, A., Marakalala, M. J. and Leslie, A. 2020. Tissue-resident innate immunity in the lung. *Immunology* 159(3), pp. 245-256. doi: 10.1111/imm.13143

Bagley, D. C. et al. 2023. Bronchoconstriction damages airway epithelia by excess crowding-induced extrusion. *bioRxiv*, doi: 10.1101/2023.08.04.551943

Bagley, D. C. et al. 2024. Bronchoconstriction damages airway epithelia by crowding-induced excess cell extrusion. *Science* 384(6691), pp. 66-73. doi: 10.1126/science.adk2758

Barkauskas, C. E. et al. 2013. Type 2 alveolar cells are stem cells in adult lung. *J Clin Invest* 123(7), pp. 3025-3036. doi: 10.1172/jci68782

Basil, M. C. and Morrisey, E. E. 2020. Lung regeneration: a tale of mice and men. *Semin Cell Dev Biol* 100, pp. 88-100. doi: 10.1016/j.semcdb.2019.11.006

Best, S. A. et al. 2019. Distinct initiating events underpin the immune and metabolic heterogeneity of KRAS-mutant lung adenocarcinoma. *Nat Commun* 10(1), p. 4190. doi: 10.1038/s41467-019-12164-y

Bluhmki, T. et al. 2020. Development of a miniaturized 96-Transwell air-liquid interface human small airway epithelial model. *Sci Rep* 10(1), p. 13022. doi: 10.1038/s41598-020-69948-2

Brantley-Sieders, D. M., Caughron, J., Hicks, D., Pozzi, A., Ruiz, J. C. and Chen, J. 2004. EphA2 receptor tyrosine kinase regulates endothelial cell migration and vascular assembly through phosphoinositide 3-kinase-mediated Rac1 GTPase activation. *J Cell Sci* 117(Pt 10), pp. 2037-2049. doi: 10.1242/jcs.01061

Brantley-Sieders, D. M. et al. 2008. The receptor tyrosine kinase EphA2 promotes mammary adenocarcinoma tumorigenesis and metastatic progression in mice by amplifying ErbB2 signaling. *J Clin Invest* 118(1), pp. 64-78. doi: 10.1172/jci33154

Brown, S. et al. 2017. Correction of aberrant growth preserves tissue homeostasis. *Nature* 548(7667), pp. 334-337. doi: 10.1038/nature23304

Brumby, A. M. and Richardson, H. E. 2003. scribble mutants cooperate with oncogenic Ras or Notch to cause neoplastic overgrowth in Drosophila. *EMBO J* 22(21), pp. 5769-5779. doi: 10.1093/emboj/cdg548

Bryson, K. J. et al. 2020. Precision cut lung slices: a novel versatile tool to examine host-pathogen interaction in the chicken lung. *Vet Res* 51(1), p. 2. doi: 10.1186/s13567-019-0733-0

Cagan, A. et al. 2022. Somatic mutation rates scale with lifespan across mammals. *Nature* 604(7906), pp. 517-524. doi: 10.1038/s41586-022-04618-z

Cayuso, J., Xu, Q., Addison, M. and Wilkinson, D. G. 2019. Actomyosin regulation by Eph receptor signaling couples boundary cell formation to border sharpness. *Elife* 8, doi: 10.7554/eLife.49696

Cayuso, J., Xu, Q. and Wilkinson, D. G. 2015. Mechanisms of boundary formation by Eph receptor and ephrin signaling. *Dev Biol* 401(1), pp. 122-131. doi: 10.1016/j.ydbio.2014.11.013

Celebi Sözener, Z., Cevhertas, L., Nadeau, K., Akdis, M. and Akdis, C. A. 2020. Environmental factors in epithelial barrier dysfunction. *J Allergy Clin Immunol* 145(6), pp. 1517-1528. doi: 10.1016/j.jaci.2020.04.024

Chan, M. and Liu, Y. 2022. Function of epithelial stem cell in the repair of alveolar injury. *Stem Cell Res Ther* 13(1), p. 170. doi: 10.1186/s13287-022-02847-7

Chaudhary, P. et al. 2023. Activation of KrasG12D in Subset of Alveolar Type II Cells Enhances Cellular Plasticity in Lung Adenocarcinoma. *Cancer Res Commun* 3(11), pp. 2400-2411. doi: 10.1158/2767-9764.CRC-22-0408

Chen, H. et al. 2012. Airway epithelial progenitors are region specific and show differential responses to bleomycin-induced lung injury. *Stem Cells* 30(9), pp. 1948-1960. doi: 10.1002/stem.1150

Cheng, C., Ansari, M. M., Cooper, J. A. and Gong, X. 2013. EphA2 and Src regulate equatorial cell morphogenesis during lens development. *Development* 140(20), pp. 4237-4245. doi: 10.1242/dev.100727

Cheong, S. S., Luis, T. C., Stewart, M., Hillier, R., Hind, M. and Dean, C. H. 2023. A method for TAT-Cre recombinase-mediated floxed allele modification in ex vivo tissue slices. *Dis Model Mech* 16(11), doi: 10.1242/dmm.050267

Chevallier, M., Borgeaud, M., Addeo, A. and Friedlaender, A. 2021. Oncogenic driver mutations in non-small cell lung cancer: Past, present and future. *World J Clin Oncol* 12(4), pp. 217-237. doi: 10.5306/wjco.v12.i4.217

Chiba, T. et al. 2016. MDCK cells expressing constitutively active Yes-associated protein (YAP) undergo apical extrusion depending on neighboring cell status. *Sci Rep* 6, p. 28383. doi: 10.1038/srep28383

Chioccioli, M. et al. 2024. Stem cell migration drives lung repair in living mice. *Dev Cell*, doi: 10.1016/j.devcel.2024.02.003

Choi, J., Park, J. E., Tsagkogeorga, G., Yanagita, M., Koo, B. K., Han, N. and Lee, J. H. 2020. Inflammatory Signals Induce AT2 Cell-Derived Damage-Associated Transient Progenitors that Mediate Alveolar Regeneration. *Cell Stem Cell* 27(3), pp. 366-382.e367. doi: 10.1016/j.stem.2020.06.020

Cisowski, J., Sayin, V. I., Liu, M., Karlsson, C. and Bergo, M. O. 2016. Oncogene-induced senescence underlies the mutual exclusive nature of oncogenic KRAS and BRAF. *Oncogene* 35(10), pp. 1328-1333. doi: 10.1038/onc.2015.186

Colom, B. et al. 2020. Spatial competition shapes the dynamic mutational landscape of normal esophageal epithelium. *Nat Genet* 52(6), pp. 604-614. doi: 10.1038/s41588-020-0624-3

Colom, B. et al. 2021. Mutant clones in normal epithelium outcompete and eliminate emerging tumours. *Nature* 598(7881), pp. 510-514. doi: 10.1038/s41586-021-03965-7

Concepcion, C. P. et al. 2022. Inactivation Promotes Lineage-Specific Transformation and Early Metastatic Features in the Lung. *Cancer Discov* 12(2), pp. 562-585. doi: 10.1158/2159-8290.CD-21-0248

Couraud, S., Zalcman, G., Milleron, B., Morin, F. and Souquet, P. J. 2012. Lung cancer in never smokers--a review. *Eur J Cancer* 48(9), pp. 1299-1311. doi: 10.1016/j.ejca.2012.03.007

Cowan, C. A. and Henkemeyer, M. 2001. The SH2/SH3 adaptor Grb4 transduces B-ephrin reverse signals. *Nature* 413(6852), pp. 174-179. doi: 10.1038/35093123

Crispo, A. et al. 2004. The cumulative risk of lung cancer among current, ex- and never-smokers in European men. *Br J Cancer* 91(7), pp. 1280-1286. doi: 10.1038/sj.bjc.6602078

CRUK, C. R. U. 2024. *Lung cancer*. https://www.cancerresearchuk.org/about-cancer/lung-cancer: Available at: [Accessed: 21 April 2024].

Danopoulos, S., Shiosaki, J. and Al Alam, D. 2019. FGF Signaling in Lung Development and Disease: Human Versus Mouse. *Front Genet* 10, p. 170. doi: 10.3389/fgene.2019.00170

Davis, J. D. and Wypych, T. P. 2021. Cellular and functional heterogeneity of the airway epithelium. *Mucosal Immunol* 14(5), pp. 978-990. doi: 10.1038/s41385-020-00370-7

de la Cova, C., Abril, M., Bellosta, P., Gallant, P. and Johnston, L. A. 2004. Drosophila myc regulates organ size by inducing cell competition. *Cell* 117(1), pp. 107-116. doi: 10.1016/s0092-8674(04)00214-4

Dean, C. H. and Cheong, S. S. 2023. Simple Models of Lung Development. *Adv Exp Med Biol* 1413, pp. 17-28. doi: 10.1007/978-3-031-26625-6_2

Deng, S., Clowers, M. J., Velasco, W. V., Ramos-Castaneda, M. and Moghaddam, S. J. 2019. Understanding the Complexity of the Tumor Microenvironment in K-ras Mutant Lung Cancer: Finding an Alternative Path to Prevention and Treatment. *Front Oncol* 9, p. 1556. doi: 10.3389/fonc.2019.01556

Desai, T. J., Brownfield, D. G. and Krasnow, M. A. 2014. Alveolar progenitor and stem cells in lung development, renewal and cancer. *Nature* 507(7491), pp. 190-194. doi: 10.1038/nature12930

Desideri, E., Cavallo, A. L. and Baccarini, M. 2015. Alike but Different: RAF Paralogs and Their Signaling Outputs. *Cell* 161(5), pp. 967-970. doi: 10.1016/j.cell.2015.04.045

Di Federico, A., De Giglio, A., Parisi, C. and Gelsomino, F. 2021. STK11/LKB1 and KEAP1 mutations in non-small cell lung cancer: Prognostic rather than predictive? *Eur J Cancer* 157, pp. 108-113. doi: 10.1016/j.ejca.2021.08.011

Dost, A. F. M. et al. 2020. Organoids Model Transcriptional Hallmarks of Oncogenic KRAS Activation in Lung Epithelial Progenitor Cells. *Cell Stem Cell* 27(4), pp. 663-678.e668. doi: 10.1016/j.stem.2020.07.022

Downward, J. 2003. Targeting RAS signalling pathways in cancer therapy. *Nat Rev Cancer* 3(1), pp. 11-22. doi: 10.1038/nrc969

Drosten, M. et al. 2017. H-Ras and K-Ras Oncoproteins Induce Different Tumor Spectra When Driven by the Same Regulatory Sequences. *Cancer Res* 77(3), pp. 707-718. doi: 10.1158/0008-5472.CAN-16-2925

DuPage, M., Dooley, A. L. and Jacks, T. 2009. Conditional mouse lung cancer models using adenoviral or lentiviral delivery of Cre recombinase. *Nat Protoc* 4(7), pp. 1064-1072. doi: 10.1038/nprot.2009.95

Dye, B. R. et al. 2015. In vitro generation of human pluripotent stem cell derived lung organoids. *Elife* 4, doi: 10.7554/eLife.05098

El-Hashash, A. H. and Warburton, D. 2011. Cell polarity and spindle orientation in the distal epithelium of embryonic lung. *Dev Dyn* 240(2), pp. 441-445. doi: 10.1002/dvdy.22551

Ellis, S. J., Gomez, N. C., Levorse, J., Mertz, A. F., Ge, Y. and Fuchs, E. 2019. Distinct modes of cell competition shape mammalian tissue morphogenesis. *Nature* 569(7757), pp. 497-502. doi: 10.1038/s41586-019-1199-y

Enomoto, M., Takemoto, D. and Igaki, T. 2021. Interaction between Ras and Src clones causes interdependent tumor malignancy via Notch signaling in Drosophila. *Dev Cell* 56(15), pp. 2223-2236.e2225. doi: 10.1016/j.devcel.2021.07.002

Fadul, J. et al. 2021. KRas-transformed epithelia cells invade and partially dedifferentiate by basal cell extrusion. *Nat Commun* 12(1), p. 7180. doi: 10.1038/s41467-021-27513-z

Ferbeyre, G., de Stanchina, E., Lin, A. W., Querido, E., McCurrach, M. E., Hannon, G. J. and Lowe, S. W. 2002. Oncogenic ras and p53 cooperate to induce cellular senescence. *Mol Cell Biol* 22(10), pp. 3497-3508. doi: 10.1128/MCB.22.10.3497-3508.2002

Fercoq, F. et al. 2024. Integrin inactivation slows down neutrophils congesting the pre-metastatic lung in a model of breast cancer. *bioRxiv*, p. 2024.2003.2019.585724. doi: 10.1101/2024.03.19.585724

Fernandez-Antoran, D., Piedrafita, G., Murai, K., Ong, S. H., Herms, A., Frezza, C. and Jones, P. H. 2019. Outcompeting p53-Mutant Cells in the Normal Esophagus by Redox Manipulation. *Cell Stem Cell* 25(3), pp. 329-341.e326. doi: 10.1016/j.stem.2019.06.011

Ferone, G., Lee, M. C., Sage, J. and Berns, A. 2020. Cells of origin of lung cancers: lessons from mouse studies. *Genes Dev* 34(15-16), pp. 1017-1032. doi: 10.1101/gad.338228.120

Ferrer, I., Zugazagoitia, J., Herbertz, S., John, W., Paz-Ares, L. and Schmid-Bindert, G. 2018. KRAS-Mutant non-small cell lung cancer: From biology to therapy. *Lung Cancer* 124, pp. 53-64. doi: 10.1016/j.lungcan.2018.07.013

Flanagan, D. J. et al. 2021. NOTUM from Apc-mutant cells biases clonal competition to initiate cancer. *Nature* 594(7863), pp. 430-435. doi: 10.1038/s41586-021-03525-z

Fukunaga, Y. et al. 2002. Expression of cytokeratin 8 in lung cancer cell lines and measurement of serum cytokeratin 8 in lung cancer patients. *Lung Cancer* 38(1), pp. 31-38. doi: 10.1016/s0169-5002(02)00109-5

Gallini, S. et al. 2023. Injury prevents Ras mutant cell expansion in mosaic skin. *Nature* 619(7968), pp. 167-175. doi: 10.1038/s41586-023-06198-y

George, J. et al. 2015. Comprehensive genomic profiles of small cell lung cancer. *Nature* 524(7563), pp. 47-53. doi: 10.1038/nature14664

Ghimessy, A. et al. 2020. Current therapy of KRAS-mutant lung cancer. *Cancer Metastasis Rev* 39(4), pp. 1159-1177. doi: 10.1007/s10555-020-09903-9

Gillies, T. E., Pargett, M., Silva, J. M., Teragawa, C. K., McCormick, F. and Albeck, J. G. 2020. Oncogenic mutant RAS signaling activity is rescaled by the ERK/MAPK pathway. *Mol Syst Biol* 16(10), p. e9518. doi: 10.15252/msb.20209518

Graf, J., Trautmann-Rodriguez, M., Sabnis, S., Kloxin, A. M. and Fromen, C. A. 2023. On the path to predicting immune responses in the lung: Modeling the pulmonary innate immune system at the air-liquid interface (ALI). *Eur J Pharm Sci* 191, p. 106596. doi: 10.1016/j.ejps.2023.106596

Grossmann, S. et al. 2021. Development, maturation, and maintenance of human prostate inferred from somatic mutations. *Cell Stem Cell* 28(7), pp. 1262-1274.e1265. doi: 10.1016/j.stem.2021.02.005

Gu, Y., Forostyan, T., Sabbadini, R. and Rosenblatt, J. 2011. Epithelial cell extrusion requires the sphingosine-1-phosphate receptor 2 pathway. *J Cell Biol* 193(4), pp. 667-676. doi: 10.1083/jcb.201010075

Gu, Y. et al. 2015. Defective apical extrusion signaling contributes to aggressive tumor hallmarks. *Elife* 4, p. e04069. doi: 10.7554/eLife.04069

Hamaoka, Y., Negishi, M. and Katoh, H. 2016. EphA2 is a key effector of the MEK/ERK/RSK pathway regulating glioblastoma cell proliferation. *Cell Signal* 28(8), pp. 937-945. doi: 10.1016/j.cellsig.2016.04.009

Hamarsheh, S., Groß, O., Brummer, T. and Zeiser, R. 2020. Immune modulatory effects of oncogenic KRAS in cancer. *Nat Commun* 11(1), p. 5439. doi: 10.1038/s41467-020-19288-6

Han, G. et al. 2024. An atlas of epithelial cell states and plasticity in lung adenocarcinoma. *Nature* 627(8004), pp. 656-663. doi: 10.1038/s41586-024-07113-9

Hay, J., Shahzeidi, S. and Laurent, G. 1991. Mechanisms of bleomycin-induced lung damage. *Arch Toxicol* 65(2), pp. 81-94. doi: 10.1007/BF02034932

Hewitt, R. J. and Lloyd, C. M. 2021. Regulation of immune responses by the airway epithelial cell landscape. *Nat Rev Immunol* 21(6), pp. 347-362. doi: 10.1038/s41577-020-00477-9

Hill, W. and Hogan, C. 2017. Normal epithelial cells trigger EphA2-dependent RasV12 cell repulsion at the single cell level. *Small GTPases* 10(4), pp. 305-310. doi: 10.1080/21541248.2017.1324940

Hill, W. et al. 2023. Lung adenocarcinoma promotion by air pollutants. *Nature* 616(7955), pp. 159-167. doi: 10.1038/s41586-023-05874-3

Hill, W. et al. 2021. EPHA2-dependent outcompetition of KRASG12D mutant cells by wild-type neighbors in the adult pancreas. *Curr Biol*, doi: 10.1016/j.cub.2021.03.094

Hogan, C. et al. 2009. Characterization of the interface between normal and transformed epithelial cells. *Nat Cell Biol* 11(4), pp. 460-467. doi: 10.1038/ncb1853

Hong, K. U., Reynolds, S. D., Watkins, S., Fuchs, E. and Stripp, B. R. 2004. Basal cells are a multipotent progenitor capable of renewing the bronchial epithelium. *Am J Pathol* 164(2), pp. 577-588. doi: 10.1016/S0002-9440(10)63147-1

Huang, L., Guo, Z., Wang, F. and Fu, L. 2021. KRAS mutation: from undruggable to druggable in cancer. *Signal Transduct Target Ther* 6(1), p. 386. doi: 10.1038/s41392-021-00780-4

Huang, Z. et al. 2022. Single-cell analysis of somatic mutations in human bronchial epithelial cells in relation to aging and smoking. *Nat Genet* 54(4), pp. 492-498. doi: 10.1038/s41588-022-01035-w

Hunter, J. C., Manandhar, A., Carrasco, M. A., Gurbani, D., Gondi, S. and Westover, K. D. 2015. Biochemical and Structural Analysis of Common Cancer-Associated KRAS Mutations. *Mol Cancer Res* 13(9), pp. 1325-1335. doi: 10.1158/1541-7786.MCR-15-0203

Hussell, T. and Bell, T. J. 2014. Alveolar macrophages: plasticity in a tissue-specific context. *Nat Rev Immunol* 14(2), pp. 81-93. doi: 10.1038/nri3600

Innes, B. A. and Dorin, J. R. 2001. Submucosal gland distribution in the mouse has a genetic determination localized on chromosome 9. *Mamm Genome* 12(2), pp. 124-128. doi: 10.1007/s003350010244

Ishikawa, M. et al. 2012. Higher expression of EphA2 and ephrin-A1 is related to favorable clinicopathological features in pathological stage I non-small cell lung carcinoma. *Lung Cancer* 76(3), pp. 431-438. doi: 10.1016/j.lungcan.2011.12.004

Issigonis, M., Tulina, N., de Cuevas, M., Brawley, C., Sandler, L. and Matunis, E. 2009. JAK-STAT signal inhibition regulates competition in the Drosophila testis stem cell niche. *Science* 326(5949), pp. 153-156. doi: 10.1126/science.1176817

Jackson, E. L., Olive, K. P., Tuveson, D. A., Bronson, R., Crowley, D., Brown, M. and Jacks, T. 2005. The differential effects of mutant p53 alleles on advanced murine lung cancer. *Cancer Res* 65(22), pp. 10280-10288. doi: 10.1158/0008-5472.CAN-05-2193

Jackson, E. L. et al. 2001. Analysis of lung tumor initiation and progression using conditional expression of oncogenic K-ras. *Genes Dev* 15(24), pp. 3243-3248. doi: 10.1101/gad.943001

Ji, H. et al. 2006. K-ras activation generates an inflammatory response in lung tumors. *Oncogene* 25(14), pp. 2105-2112. doi: 10.1038/sj.onc.1209237

Johnson, L., Mercer, K., Greenbaum, D., Bronson, R. T., Crowley, D., Tuveson, D. A. and Jacks, T. 2001. Somatic activation of the K-ras oncogene causes early onset lung cancer in mice. *Nature* 410(6832), pp. 1111-1116. doi: 10.1038/35074129

Judd, J. et al. 2021. Characterization of KRAS Mutation Subtypes in Non-small Cell Lung Cancer. *Mol Cancer Ther* 20(12), pp. 2577-2584. doi: 10.1158/1535-7163.MCT-21-0201

Juul, N. H. et al. 2023. KRAS(G12D) drives lepidic adenocarcinoma through stem-cell reprogramming. *Nature* 619(7971), pp. 860-867. doi: 10.1038/s41586-023-06324-w

Kaiser, A. M. et al. 2023. p53 governs an AT1 differentiation programme in lung cancer suppression. *Nature* 619(7971), pp. 851-859. doi: 10.1038/s41586-023-06253-8

Kajita, M. and Fujita, Y. 2015. EDAC: Epithelial defence against cancer-cell competition between normal and transformed epithelial cells in mammals. *J Biochem* 158(1), pp. 15-23. doi: 10.1093/jb/mvv050

Kajita, M. et al. 2010. Interaction with surrounding normal epithelial cells influences signalling pathways and behaviour of Src-transformed cells. *J Cell Sci* 123(Pt 2), pp. 171-180. doi: 10.1242/jcs.057976

Kajita, M. et al. 2014. Filamin acts as a key regulator in epithelial defence against transformed cells. *Nat Commun* 5, p. 4428. doi: 10.1038/ncomms5428

Kang, R. et al. 2014. RAGE is essential for oncogenic KRAS-mediated hypoxic signaling in pancreatic cancer. *Cell Death Dis* 5(10), p. e1480. doi: 10.1038/cddis.2014.445

Karasuyama, H., Miyake, K., Yoshikawa, S. and Yamanishi, Y. 2018. Multifaceted roles of basophils in health and disease. *J Allergy Clin Immunol* 142(2), pp. 370-380. doi: 10.1016/j.jaci.2017.10.042

Kikuchi, H., Pino, M. S., Zeng, M., Shirasawa, S. and Chung, D. C. 2009. Oncogenic KRAS and BRAF differentially regulate hypoxia-inducible factor-1alpha and -2alpha in colon cancer. *Cancer Res* 69(21), pp. 8499-8506. doi: 10.1158/0008-5472.CAN-09-2213

Kim, C. F. et al. 2005. Identification of bronchioalveolar stem cells in normal lung and lung cancer. *Cell* 121(6), pp. 823-835. doi: 10.1016/j.cell.2005.03.032

Kim, H., Kim, M., Im, S. K. and Fang, S. 2018. Mouse Cre-LoxP system: general principles to determine tissue-specific roles of target genes. *Lab Anim Res* 34(4), pp. 147-159. doi: 10.5625/lar.2018.34.4.147

Kim, H. T. et al. 2019. WNT/RYK signaling restricts goblet cell differentiation during lung development and repair. *Proc Natl Acad Sci U S A* 116(51), pp. 25697-25706. doi: 10.1073/pnas.1911071116

Kim, S. Y. et al. 2021. The acid injury and repair (AIR) model: A novel ex-vivo tool to understand lung repair. *Biomaterials* 267, p. 120480. doi: 10.1016/j.biomaterials.2020.120480

Kissil, J. L. et al. 2007. Requirement for Rac1 in a K-ras induced lung cancer in the mouse. *Cancer Res* 67(17), pp. 8089-8094. doi: 10.1158/0008-5472.CAN-07-2300

Klein, S. G., Serchi, T., Hoffmann, L., Blömeke, B. and Gutleb, A. C. 2013. An improved 3D tetraculture system mimicking the cellular organisation at the alveolar barrier to study the potential toxic effects of particles on the lung. *Part Fibre Toxicol* 10, p. 31. doi: 10.1186/1743-8977-10-31

Knudsen, L., Weibel, E. R., Gundersen, H. J., Weinstein, F. V. and Ochs, M. 2010. Assessment of air space size characteristics by intercept (chord) measurement: an accurate and efficient stereological approach. *J Appl Physiol (1985)* 108(2), pp. 412-421. doi: 10.1152/japplphysiol.01100.2009

Kobayashi, Y. et al. 2020. Persistence of a regeneration-associated, transitional alveolar epithelial cell state in pulmonary fibrosis. *Nat Cell Biol* 22(8), pp. 934-946. doi: 10.1038/s41556-020-0542-8

Kolahgar, G., Suijkerbuijk, S. J., Kucinski, I., Poirier, E. Z., Mansour, S., Simons, B. D. and Piddini, E. 2015. Cell Competition Modifies Adult Stem Cell and Tissue

Population Dynamics in a JAK-STAT-Dependent Manner. *Dev Cell* 34(3), pp. 297-309. doi: 10.1016/j.devcel.2015.06.010

Kon, S. et al. 2017. Cell competition with normal epithelial cells promotes apical extrusion of transformed cells through metabolic changes. *Nat Cell Biol* 19(5), pp. 530-541. doi: 10.1038/ncb3509

Konishi, S. et al. 2016. Directed Induction of Functional Multi-ciliated Cells in Proximal Airway Epithelial Spheroids from Human Pluripotent Stem Cells. *Stem Cell Reports* 6(1), pp. 18-25. doi: 10.1016/j.stemcr.2015.11.010

Konkimalla, A. et al. 2022. Multi-apical polarity of alveolar stem cells and their dynamics during lung development and regeneration. *iScience* 25(10), p. 105114. doi: 10.1016/j.isci.2022.105114

Konstantinopoulos, P. A., Karamouzis, M. V. and Papavassiliou, A. G. 2007. Post-translational modifications and regulation of the RAS superfamily of GTPases as anticancer targets. *Nat Rev Drug Discov* 6(7), pp. 541-555. doi: 10.1038/nrd2221

Krotenberg Garcia, A. et al. 2021. Active elimination of intestinal cells drives oncogenic growth in organoids. *Cell Rep* 36(1), p. 109307. doi: 10.1016/j.celrep.2021.109307

Lambermont, V. A. et al. 2014. Comparison of airway responses in sheep of different age in precision-cut lung slices (PCLS). *PLoS One* 9(9), p. e97610. doi: 10.1371/journal.pone.0097610

Larionova, I. et al. 2020. Tumor-Associated Macrophages in Human Breast, Colorectal, Lung, Ovarian and Prostate Cancers. *Front Oncol* 10, p. 566511. doi: 10.3389/fonc.2020.566511

Lavoie, H., Gagnon, J. and Therrien, M. 2020. ERK signalling: a master regulator of cell behaviour, life and fate. *Nat Rev Mol Cell Biol* 21(10), pp. 607-632. doi: 10.1038/s41580-020-0255-7

Lavoie, H. and Therrien, M. 2015. Regulation of RAF protein kinases in ERK signalling. *Nat Rev Mol Cell Biol* 16(5), pp. 281-298. doi: 10.1038/nrm3979

Lawson, A. R. J. et al. 2020. Extensive heterogeneity in somatic mutation and selection in the human bladder. *Science* 370(6512), pp. 75-82. doi: 10.1126/science.aba8347

Lee, D. D. H., Petris, A., Hynds, R. E. and O'Callaghan, C. 2020. Ciliated Epithelial Cell Differentiation at Air-Liquid Interface Using Commercially Available Culture Media. *Methods Mol Biol* 2109, pp. 275-291. doi: 10.1007/7651_2019_269

Lee-Six, H. et al. 2019. The landscape of somatic mutation in normal colorectal epithelial cells. *Nature* 574(7779), pp. 532-537. doi: 10.1038/s41586-019-1672-7

Leitch, A. E., Duffin, R., Haslett, C. and Rossi, A. G. 2008. Relevance of granulocyte apoptosis to resolution of inflammation at the respiratory mucosa. *Mucosal Immunol* 1(5), pp. 350-363. doi: 10.1038/mi.2008.31

Leroi, A. M., Koufopanou, V. and Burt, A. 2003. Cancer selection. *Nat Rev Cancer* 3(3), pp. 226-231. doi: 10.1038/nrc1016

Leung, C. T. and Brugge, J. S. 2012. Outgrowth of single oncogene-expressing cells from suppressive epithelial environments. *Nature* 482(7385), pp. 410-413. doi: 10.1038/nature10826

Lewis, A. E., Kuwahara, A., Franzosi, J. and Bush, J. O. 2022. Tracheal separation is driven by NKX2-1-mediated repression of Efnb2 and regulation of endodermal cell sorting. *Cell Rep* 38(11), p. 110510. doi: 10.1016/j.celrep.2022.110510

Li, G. et al. 2024. Keratin gene signature expression drives epithelial-mesenchymal transition through enhanced TGF-β signaling pathway activation and correlates with adverse prognosis in lung adenocarcinoma. *Heliyon* 10(3), p. e24549. doi: 10.1016/j.heliyon.2024.e24549

Li, J. Y. et al. 2019. S897 phosphorylation of EphA2 is indispensable for EphA2-dependent nasopharyngeal carcinoma cell invasion, metastasis and stem properties. *Cancer Lett* 444, pp. 162-174. doi: 10.1016/j.canlet.2018.12.011

Lim, K. et al. 2023. Organoid modeling of human fetal lung alveolar development reveals mechanisms of cell fate patterning and neonatal respiratory disease. *Cell Stem Cell* 30(1), pp. 20-37.e29. doi: 10.1016/j.stem.2022.11.013

Lisabeth, E. M., Falivelli, G. and Pasquale, E. B. 2013. Eph receptor signaling and ephrins. *Cold Spring Harb Perspect Biol* 5(9), doi: 10.1101/cshperspect.a009159

Liu, N. et al. 2019a. Stem cell competition orchestrates skin homeostasis and ageing. *Nature* 568(7752), pp. 344-350. doi: 10.1038/s41586-019-1085-7

Liu, Q. et al. 2019b. Lung regeneration by multipotent stem cells residing at the bronchioalveolar-duct junction. *Nat Genet* 51(4), pp. 728-738. doi: 10.1038/s41588-019-0346-6

Liu, Z., Yee, P. P., Wei, Y., Kawasawa, Y. I. and Li, W. 2019c. Differential YAP expression in glioma cells induces cell competition and promotes tumorigenesis. *J Cell Sci* 132(5), doi: 10.1242/jcs.225714

Lord, S. J., Velle, K. B., Mullins, R. D. and Fritz-Laylin, L. K. 2020. SuperPlots: Communicating reproducibility and variability in cell biology. *J Cell Biol* 219(6), doi: 10.1083/jcb.202001064

Lu, T., Cao, Y., Zhao, P., Shen, S. and Xi, Y. 2021. Organoid: a powerful tool to study lung regeneration and disease. *Cell Regen* 10(1), p. 21. doi: 10.1186/s13619-021-00082-8

Luche, H., Weber, O., Nageswara Rao, T., Blum, C. and Fehling, H. J. 2007. Faithful activation of an extra-bright red fluorescent protein in "knock-in" Cre-reporter mice ideally suited for lineage tracing studies. *Eur J Immunol* 37(1), pp. 43-53. doi: 10.1002/eji.200636745

Luster, A. D., Alon, R. and von Andrian, U. H. 2005. Immune cell migration in inflammation: present and future therapeutic targets. *Nat Immunol* 6(12), pp. 1182-1190. doi: 10.1038/ni1275

Mack, N. A., Whalley, H. J., Castillo-Lluva, S. and Malliri, A. 2011. The diverse roles of Rac signaling in tumorigenesis. *Cell Cycle* 10(10), pp. 1571-1581. doi: 10.4161/cc.10.10.15612

Macmillan Cancer Support. 2024. *Lung cancer*. https://www.macmillan.org.uk/cancer-information-and-support/lung-cancer: Available at: [Accessed: 21 April 2024].

Macrae, M. et al. 2005. A conditional feedback loop regulates Ras activity through EphA2. *Cancer Cell* 8(2), pp. 111-118. doi: 10.1016/j.ccr.2005.07.005

Mainardi, S., Mijimolle, N., Francoz, S., Vicente-Dueñas, C., Sánchez-García, I. and Barbacid, M. 2014. Identification of cancer initiating cells in K-Ras driven lung adenocarcinoma. *Proc Natl Acad Sci U S A* 111(1), pp. 255-260. doi: 10.1073/pnas.1320383110

Malhotra, J., Malvezzi, M., Negri, E., La Vecchia, C. and Boffetta, P. 2016. Risk factors for lung cancer worldwide. *Eur Respir J* 48(3), pp. 889-902. doi: 10.1183/13993003.00359-2016

Marshall, T. W., Lloyd, I. E., Delalande, J. M., Näthke, I. and Rosenblatt, J. 2011. The tumor suppressor adenomatous polyposis coli controls the direction in which a cell extrudes from an epithelium. *Mol Biol Cell* 22(21), pp. 3962-3970. doi: 10.1091/mbc.E11-05-0469

Martincorena, I. 2019. Somatic mutation and clonal expansions in human tissues. *Genome Med* 11(1), p. 35. doi: 10.1186/s13073-019-0648-4

Martincorena, I. and Campbell, P. J. 2015. Somatic mutation in cancer and normal cells. *Science* 349(6255), pp. 1483-1489. doi: 10.1126/science.aab4082

Martincorena, I. et al. 2018. Somatic mutant clones colonize the human esophagus with age. *Science* 362(6417), pp. 911-917. doi: 10.1126/science.aau3879

Martincorena, I. et al. 2015. Tumor evolution. High burden and pervasive positive selection of somatic mutations in normal human skin. *Science* 348(6237), pp. 880-886. doi: 10.1126/science.aaa6806

Meng, X., Cui, G. and Peng, G. 2023. Lung development and regeneration: newly defined cell types and progenitor status. *Cell Regen* 12(1), p. 5. doi: 10.1186/s13619-022-00149-0

Merlos-Suárez, A. and Batlle, E. 2008. Eph-ephrin signalling in adult tissues and cancer. *Curr Opin Cell Biol* 20(2), pp. 194-200. doi: 10.1016/j.ceb.2008.01.011

Metzger, R. J., Klein, O. D., Martin, G. R. and Krasnow, M. A. 2008. The branching programme of mouse lung development. *Nature* 453(7196), pp. 745-750. doi: 10.1038/nature07005

Meuwissen, R., Linn, S. C., van der Valk, M., Mooi, W. J. and Berns, A. 2001. Mouse model for lung tumorigenesis through Cre/lox controlled sporadic activation of the K-Ras oncogene. *Oncogene* 20(45), pp. 6551-6558. doi: 10.1038/sj.onc.1204837

Miao, H. et al. 2009. EphA2 mediates ligand-dependent inhibition and ligand-independent promotion of cell migration and invasion via a reciprocal regulatory loop with Akt. *Cancer Cell* 16(1), pp. 9-20. doi: 10.1016/j.ccr.2009.04.009

Min, H. Y. and Lee, H. Y. 2023. Cellular Dormancy in Cancer: Mechanisms and Potential Targeting Strategies. *Cancer Res Treat* 55(3), pp. 720-736. doi: 10.4143/crt.2023.468

Mo, J. et al. 2020. Effect of EphA2 knockdown on melanoma metastasis depends on intrinsic ephrinA1 level. *Cell Oncol (Dordr)* 43(4), pp. 655-667. doi: 10.1007/s13402-020-00511-x

Moeller, A., Ask, K., Warburton, D., Gauldie, J. and Kolb, M. 2008. The bleomycin animal model: a useful tool to investigate treatment options for idiopathic pulmonary fibrosis? *Int J Biochem Cell Biol* 40(3), pp. 362-382. doi: 10.1016/j.biocel.2007.08.011

Montoro, D. T. et al. 2018. A revised airway epithelial hierarchy includes CFTR-expressing ionocytes. *Nature* 560(7718), pp. 319-324. doi: 10.1038/s41586-018-0393-7

Moore, L. et al. 2020. The mutational landscape of normal human endometrial epithelium. *Nature* 580(7805), pp. 640-646. doi: 10.1038/s41586-020-2214-z

Morata, G. and Ripoll, P. 1975. Minutes: mutants of drosophila autonomously affecting cell division rate. *Dev Biol* 42(2), pp. 211-221. doi: 10.1016/0012-1606(75)90330-9

Moreno, E. and Basler, K. 2004. dMyc transforms cells into super-competitors. *Cell* 117(1), pp. 117-129. doi: 10.1016/s0092-8674(04)00262-4

Moreno, E., Basler, K. and Morata, G. 2002. Cells compete for decapentaplegic survival factor to prevent apoptosis in Drosophila wing development. *Nature* 416(6882), pp. 755-759. doi: 10.1038/416755a

Morris, J. P., Wang, S. C. and Hebrok, M. 2010. KRAS, Hedgehog, Wnt and the twisted developmental biology of pancreatic ductal adenocarcinoma. *Nat Rev Cancer* 10(10), pp. 683-695. doi: 10.1038/nrc2899

Moya, I. M. et al. 2019. Peritumoral activation of the Hippo pathway effectors YAP and TAZ suppresses liver cancer in mice. *Science* 366(6468), pp. 1029-1034. doi: 10.1126/science.aaw9886

Mullassery, D. and Smith, N. P. 2015. Lung development. *Semin Pediatr Surg* 24(4), pp. 152-155. doi: 10.1053/j.sempedsurg.2015.01.011

Nakano, H., Nakano, K. and Cook, D. N. 2018. Isolation and Purification of Epithelial and Endothelial Cells from Mouse Lung. *Methods Mol Biol* 1799, pp. 59-69. doi: 10.1007/978-1-4939-7896-0_6

Neuhaus, V. et al. 2017. Assessment of long-term cultivated human precision-cut lung slices as an ex vivo system for evaluation of chronic cytotoxicity and functionality. *J Occup Med Toxicol* 12, p. 13. doi: 10.1186/s12995-017-0158-5

Nikolić, M. Z., Sun, D. and Rawlins, E. L. 2018. Human lung development: recent progress and new challenges. *Development* 145(16), doi: 10.1242/dev.163485

Noguchi, M., Furukawa, K. T. and Morimoto, M. 2020. Pulmonary neuroendocrine cells: physiology, tissue homeostasis and disease. *Dis Model Mech* 13(12), doi: 10.1242/dmm.046920

Noren, N. K. and Pasquale, E. B. 2004. Eph receptor-ephrin bidirectional signals that target Ras and Rho proteins. *Cell Signal* 16(6), pp. 655-666. doi: 10.1016/j.cellsig.2003.10.006

Norman, M. et al. 2012. Loss of Scribble causes cell competition in mammalian cells. *J Cell Sci* 125(Pt 1), pp. 59-66. doi: 10.1242/jcs.085803

Ostedgaard, L. S. et al. 2020. Lack of airway submucosal glands impairs respiratory host defenses. *Elife* 9, doi: 10.7554/eLife.59653

Padhye, A., Ungewiss, C., Fradette, J. J., Rodriguez, B. L., Albritton, J. L., Miller, J. S. and Gibbons, D. L. 2019. A novel ex vivo tumor system identifies Src-mediated invasion and metastasis in mesenchymal tumor cells in non-small cell lung cancer. *Sci Rep* 9(1), p. 4819. doi: 10.1038/s41598-019-41301-2

Park, E. C., Cho, G. S., Kim, G. H., Choi, S. C. and Han, J. K. 2011. The involvement of Eph-Ephrin signaling in tissue separation and convergence during Xenopus gastrulation movements. *Dev Biol* 350(2), pp. 441-450. doi: 10.1016/j.ydbio.2010.12.012

Park, S. et al. 2017. Tissue-scale coordination of cellular behaviour promotes epidermal wound repair in live mice. *Nat Cell Biol* 19(2), pp. 155-163. doi: 10.1038/ncb3472

Pasquale, E. B. 2008. Eph-ephrin bidirectional signaling in physiology and disease. *Cell* 133(1), pp. 38-52. doi: 10.1016/j.cell.2008.03.011

Pasquale, E. B. 2010. Eph receptors and ephrins in cancer: bidirectional signalling and beyond. *Nat Rev Cancer* 10(3), pp. 165-180. doi: 10.1038/nrc2806

Peto, R., Roe, F. J., Lee, P. N., Levy, L. and Clack, J. 1975. Cancer and ageing in mice and men. *Br J Cancer* 32(4), pp. 411-426. doi: 10.1038/bjc.1975.242

Pfaffl, M. W., Tichopad, A., Prgomet, C. and Neuvians, T. P. 2004. Determination of stable housekeeping genes, differentially regulated target genes and sample integrity: BestKeeper--Excel-based tool using pair-wise correlations. *Biotechnol Lett* 26(6), pp. 509-515. doi: 10.1023/b:bile.0000019559.84305.47

Pineda, C. M. et al. 2019. Hair follicle regeneration suppresses Ras-driven oncogenic growth. *J Cell Biol* 218(10), pp. 3212-3222. doi: 10.1083/jcb.201907178

Plasschaert, L. W. et al. 2018. A single-cell atlas of the airway epithelium reveals the CFTR-rich pulmonary ionocyte. *Nature* 560(7718), pp. 377-381. doi: 10.1038/s41586-018-0394-6

Porazinski, S. et al. 2016. EphA2 Drives the Segregation of Ras-Transformed Epithelial Cells from Normal Neighbors. *Curr Biol* 26(23), pp. 3220-3229. doi: 10.1016/j.cub.2016.09.037

Prior, I. A., Lewis, P. D. and Mattos, C. 2012. A comprehensive survey of Ras mutations in cancer. *Cancer Res* 72(10), pp. 2457-2467. doi: 10.1158/0008-5472.CAN-11-2612

Raffo-Iraolagoitia, X. et al. 2023. *γδ T cells impair airway macrophage differentiation in lung adenocarcinoma*. BioRxiv:

Rawlins, E. L. and Hogan, B. L. 2006. Epithelial stem cells of the lung: privileged few or opportunities for many? *Development* 133(13), pp. 2455-2465. doi: 10.1242/dev.02407

Rawlins, E. L. et al. 2009. The role of Scgb1a1+ Clara cells in the long-term maintenance and repair of lung airway, but not alveolar, epithelium. *Cell Stem Cell* 4(6), pp. 525-534. doi: 10.1016/j.stem.2009.04.002

Ray, K. C., Bell, K. M., Yan, J., Gu, G., Chung, C. H., Washington, M. K. and Means, A. L. 2011. Epithelial tissues have varying degrees of susceptibility to Kras(G12D)-initiated tumorigenesis in a mouse model. *PLoS One* 6(2), p. e16786. doi: 10.1371/journal.pone.0016786

Ressmeyer, A. R., Larsson, A. K., Vollmer, E., Dahlèn, S. E., Uhlig, S. and Martin, C. 2006. Characterisation of guinea pig precision-cut lung slices: comparison with human tissues. *Eur Respir J* 28(3), pp. 603-611. doi: 10.1183/09031936.06.00004206

Riemondy, K. A. et al. 2019. Single cell RNA sequencing identifies TGFβ as a key regenerative cue following LPS-induced lung injury. *JCI Insight* 5(8), doi: 10.1172/jci.insight.123637

Rock, J. R. et al. 2009. Basal cells as stem cells of the mouse trachea and human airway epithelium. *Proc Natl Acad Sci U S A* 106(31), pp. 12771-12775. doi: 10.1073/pnas.0906850106

Rohani, N., Parmeggiani, A., Winklbauer, R. and Fagotto, F. 2014. Variable combinations of specific ephrin ligand/Eph receptor pairs control embryonic tissue separation. *PLoS Biol* 12(9), p. e1001955. doi: 10.1371/journal.pbio.1001955

Rosenblatt, J., Raff, M. C. and Cramer, L. P. 2001. An epithelial cell destined for apoptosis signals its neighbors to extrude it by an actin- and myosin-dependent mechanism. *Curr Biol* 11(23), pp. 1847-1857. doi: 10.1016/s0960-9822(01)00587-5

Rosigkeit, S. et al. 2021. Definitive evidence for Club cells as progenitors for mutant Kras/Trp53-deficient lung cancer. *Int J Cancer* 149(9), pp. 1670-1682. doi: 10.1002/ijc.33756

Rudin, C. M., Brambilla, E., Faivre-Finn, C. and Sage, J. 2021. Small-cell lung cancer. *Nat Rev Dis Primers* 7(1), p. 3. doi: 10.1038/s41572-020-00235-0

Salvador-Barbero, B., Alatsatianos, M., Morton, J. P., Sansom, O. J. and Hogan, C. 2024. Oncogenic KRAS cells use Ant signalling and cell dormancy to override homeostatic cell elimination mechanisms in adult pancreas. BioRxiv.

Sanclemente, M. et al. 2018. c-RAF Ablation Induces Regression of Advanced Kras/Trp53 Mutant Lung Adenocarcinomas by a Mechanism Independent of MAPK Signaling. *Cancer Cell* 33(2), pp. 217-228.e214. doi: 10.1016/j.ccell.2017.12.014

Santry, L. A., Ingrao, J. C., Yu, D. L., de Jong, J. G., van Lieshout, L. P., Wood, G. A. and Wootton, S. K. 2017. AAV vector distribution in the mouse respiratory tract following four different methods of administration. *BMC Biotechnol* 17(1), p. 43. doi: 10.1186/s12896-017-0365-2

Sasaki, A. et al. 2018. Obesity Suppresses Cell-Competition-Mediated Apical Elimination of RasV12-Transformed Cells from Epithelial Tissues. *Cell Rep* 23(4), pp. 974-982. doi: 10.1016/j.celrep.2018.03.104

Schindelin, J. et al. 2012. Fiji: an open-source platform for biological-image analysis. *Nature Methods* 9(7), pp. 676-682. doi: 10.1038/nmeth.2019

Schyns, J., Bureau, F. and Marichal, T. 2018. Lung Interstitial Macrophages: Past, Present, and Future. *J Immunol Res* 2018, p. 5160794. doi: 10.1155/2018/5160794

Serrano, M., Lin, A. W., McCurrach, M. E., Beach, D. and Lowe, S. W. 1997. Oncogenic ras provokes premature cell senescence associated with accumulation of p53 and p16INK4a. *Cell* 88(5), pp. 593-602. doi: 10.1016/s0092-8674(00)81902-9

Shirai, T. et al. 2022. Basal extrusion of single-oncogenic mutant cells induces dome-like structures with altered microenvironments. *Cancer Sci* 113(11), pp. 3710-3721. doi: 10.1111/cas.15483

Shreenivas, A., Janku, F., Gouda, M. A., Chen, H. Z., George, B., Kato, S. and Kurzrock, R. 2023. ALK fusions in the pan-cancer setting: another tumor-agnostic target? *NPJ Precis Oncol* 7(1), p. 101. doi: 10.1038/s41698-023-00449-x

Silva, S., Bicker, J., Falcão, A. and Fortuna, A. 2023. Air-liquid interface (ALI) impact on different respiratory cell cultures. *Eur J Pharm Biopharm* 184, pp. 62-82. doi: 10.1016/j.ejpb.2023.01.013

Simanshu, D. K., Nissley, D. V. and McCormick, F. 2017. RAS Proteins and Their Regulators in Human Disease. *Cell* 170(1), pp. 17-33. doi: 10.1016/j.cell.2017.06.009

Skoulidis, F. et al. 2015. Co-occurring genomic alterations define major subsets of KRAS-mutant lung adenocarcinoma with distinct biology, immune profiles, and therapeutic vulnerabilities. *Cancer Discov* 5(8), pp. 860-877. doi: 10.1158/2159-8290.CD-14-1236

Slattum, G., Gu, Y., Sabbadini, R. and Rosenblatt, J. 2014. Autophagy in oncogenic K-Ras promotes basal extrusion of epithelial cells by degrading S1P. *Curr Biol* 24(1), pp. 19-28. doi: 10.1016/j.cub.2013.11.029

Slattum, G., McGee, K. M. and Rosenblatt, J. 2009. P115 RhoGEF and microtubules decide the direction apoptotic cells extrude from an epithelium. *J Cell Biol* 186(5), pp. 693-702. doi: 10.1083/jcb.200903079

Slattum, G. M. and Rosenblatt, J. 2014. Tumour cell invasion: an emerging role for basal epithelial cell extrusion. *Nat Rev Cancer* 14(7), pp. 495-501. doi: 10.1038/nrc3767

Strunz, M. et al. 2020. Alveolar regeneration through a Krt8+ transitional stem cell state that persists in human lung fibrosis. *Nat Commun* 11(1), p. 3559. doi: 10.1038/s41467-020-17358-3

Suijkerbuijk, S. J., Kolahgar, G., Kucinski, I. and Piddini, E. 2016. Cell Competition Drives the Growth of Intestinal Adenomas in Drosophila. *Curr Biol* 26(4), pp. 428-438. doi: 10.1016/j.cub.2015.12.043

Sun, S., Schiller, J. H. and Gazdar, A. F. 2007. Lung cancer in never smokers--a different disease. *Nat Rev Cancer* 7(10), pp. 778-790. doi: 10.1038/nrc2190

Sutherland, K. D., Proost, N., Brouns, I., Adriaensen, D., Song, J. Y. and Berns, A. 2011. Cell of origin of small cell lung cancer: inactivation of Trp53 and Rb1 in distinct cell types of adult mouse lung. *Cancer Cell* 19(6), pp. 754-764. doi: 10.1016/j.ccr.2011.04.019

Sutherland, K. D., Song, J.-Y., Kwon, M. C., Proost, N., Zevenhoven, J. and Berns, A. 2014. Multiple cells-of-origin of mutant K-Ras–induced mouse lung adenocarcinoma. *Proceedings of the National Academy of Sciences* 111(13), pp. 4952-4957. doi: 10.1073/pnas.1319963111

Tamori, Y. et al. 2010. Involvement of Lgl and Mahjong/VprBP in cell competition. *PLoS Biol* 8(7), p. e1000422. doi: 10.1371/journal.pbio.1000422

Tata, P. R. et al. 2013. Dedifferentiation of committed epithelial cells into stem cells in vivo. *Nature* 503(7475), pp. 218-223. doi: 10.1038/nature12777

Tavares, L. P., Peh, H. Y., Tan, W. S. D., Pahima, H., Maffia, P., Tiligada, E. and Levi-Schaffer, F. 2020. Granulocyte-targeted therapies for airway diseases. *Pharmacol Res* 157, p. 104881. doi: 10.1016/j.phrs.2020.104881

Temann, A., Golovina, T., Neuhaus, V., Thompson, C., Chichester, J. A., Braun, A. and Yusibov, V. 2017. Evaluation of inflammatory and immune responses in long-term cultured human precision-cut lung slices. *Hum Vaccin Immunother* 13(2), pp. 351-358. doi: 10.1080/21645515.2017.1264794

Toth, A. et al. 2023. Alveolar epithelial progenitor cells require Nkx2-1 to maintain progenitor-specific epigenomic state during lung homeostasis and regeneration. *Nat Commun* 14(1), p. 8452. doi: 10.1038/s41467-023-44184-0

Tuveson, D. A. et al. 2004. Endogenous oncogenic K-ras(G12D) stimulates proliferation and widespread neoplastic and developmental defects. *Cancer Cell* 5(4), pp. 375-387. doi: 10.1016/s1535-6108(04)00085-6

Udayakumar, D., Zhang, G., Ji, Z., Njauw, C. N., Mroz, P. and Tsao, H. 2011. EphA2 is a critical oncogene in melanoma. *Oncogene* 30(50), pp. 4921-4929. doi: 10.1038/onc.2011.210

Upadhyay, S. and Palmberg, L. 2018. Air-Liquid Interface: Relevant In Vitro Models for Investigating Air Pollutant-Induced Pulmonary Toxicity. *Toxicol Sci* 164(1), pp. 21-30. doi: 10.1093/toxsci/kfy053

van Neerven, S. M. et al. 2021. Apc-mutant cells act as supercompetitors in intestinal tumour initiation. *Nature* 594(7863), pp. 436-441. doi: 10.1038/s41586-021-03558-4

Vandesompele, J., De Preter, K., Pattyn, F., Poppe, B., Van Roy, N., De Paepe, A. and Speleman, F. 2002. Accurate normalization of real-time quantitative RT-PCR data by geometric averaging of multiple internal control genes. *Genome Biol* 3(7), p. RESEARCH0034. doi: 10.1186/gb-2002-3-7-research0034

Varner, V. D. and Nelson, C. M. 2017. Computational models of airway branching morphogenesis. *Semin Cell Dev Biol* 67, pp. 170-176. doi: 10.1016/j.semcdb.2016.06.003

Vaught, D., Chen, J. and Brantley-Sieders, D. M. 2009. Regulation of mammary gland branching morphogenesis by EphA2 receptor tyrosine kinase. *Mol Biol Cell* 20(10), pp. 2572-2581. doi: 10.1091/mbc.e08-04-0378

Vigil, D., Cherfils, J., Rossman, K. L. and Der, C. J. 2010. Ras superfamily GEFs and GAPs: validated and tractable targets for cancer therapy? *Nat Rev Cancer* 10(12), pp. 842-857. doi: 10.1038/nrc2960

Vincent, J. P., Kolahgar, G., Gagliardi, M. and Piddini, E. 2011. Steep differences in wingless signaling trigger Myc-independent competitive cell interactions. *Dev Cell* 21(2), pp. 366-374. doi: 10.1016/j.devcel.2011.06.021

Virk, H., Arthur, G. and Bradding, P. 2016. Mast cells and their activation in lung disease. *Transl Res* 174, pp. 60-76. doi: 10.1016/j.trsl.2016.01.005

Wang, D., Haviland, D. L., Burns, A. R., Zsigmond, E. and Wetsel, R. A. 2007. A pure population of lung alveolar epithelial type II cells derived from human embryonic stem cells. *Proc Natl Acad Sci U S A* 104(11), pp. 4449-4454. doi: 10.1073/pnas.0700052104

Wang, Z. et al. 2021. Deciphering cell lineage specification of human lung adenocarcinoma with single-cell RNA sequencing. *Nat Commun* 12(1), p. 6500. doi: 10.1038/s41467-021-26770-2

Wang, Z. N. and Tang, X. X. 2020. New Perspectives on the Aberrant Alveolar Repair of Idiopathic Pulmonary Fibrosis. *Front Cell Dev Biol* 8, p. 580026. doi: 10.3389/fcell.2020.580026

Watson, J. K. et al. 2015. Clonal Dynamics Reveal Two Distinct Populations of Basal Cells in Slow-Turnover Airway Epithelium. *Cell Rep* 12(1), pp. 90-101. doi: 10.1016/j.celrep.2015.06.011

Wculek, S. K., Cueto, F. J., Mujal, A. M., Melero, I., Krummel, M. F. and Sancho, D. 2020. Dendritic cells in cancer immunology and immunotherapy. *Nat Rev Immunol* 20(1), pp. 7-24. doi: 10.1038/s41577-019-0210-z

Wu, M., Zhang, X., Lin, Y. and Zeng, Y. 2022. Roles of airway basal stem cells in lung homeostasis and regenerative medicine. *Respir Res* 23(1), p. 122. doi: 10.1186/s12931-022-02042-5

Xie, F., Xiao, P., Chen, D., Xu, L. and Zhang, B. 2012. miRDeepFinder: a miRNA analysis tool for deep sequencing of plant small RNAs. *Plant Mol Biol*, doi: 10.1007/s11103-012-9885-2

Xie, T., Lynn, H., Parks, W. C., Stripp, B., Chen, P., Jiang, D. and Noble, P. W. 2022. Abnormal respiratory progenitors in fibrotic lung injury. *Stem Cell Res Ther* 13(1), p. 64. doi: 10.1186/s13287-022-02737-y

Xu, X. et al. 2012. Evidence for type II cells as cells of origin of K-Ras-induced distal lung adenocarcinoma. *Proc Natl Acad Sci U S A* 109(13), pp. 4910-4915. doi: 10.1073/pnas.1112499109

Yang, M. et al. 2023. Alveolar type I cells can give rise to KRAS-induced lung adenocarcinoma. *Cell Rep* 42(12), p. 113286. doi: 10.1016/j.celrep.2023.113286

Yang, Y. et al. 2008. Phosphatidylinositol 3-kinase mediates bronchioalveolar stem cell expansion in mouse models of oncogenic K-ras-induced lung cancer. *PLoS One* 3(5), p. e2220. doi: 10.1371/journal.pone.0002220

Ye, J., Coulouris, G., Zaretskaya, I., Cutcutache, I., Rozen, S. and Madden, T. L. 2012. Primer-BLAST: A tool to design target-specific primers for polymerase chain reaction. *BMC Bioinformatics* 13(1), p. 134. doi: 10.1186/1471-2105-13-134

Yeddula, N., Xia, Y., Ke, E., Beumer, J. and Verma, I. M. 2015. Screening for tumor suppressors: Loss of ephrin receptor A2 cooperates with oncogenic KRas in promoting lung adenocarcinoma. *Proc Natl Acad Sci U S A* 112(47), pp. E6476-6485. doi: 10.1073/pnas.1520110112

Yoshida, K. et al. 2020. Tobacco smoking and somatic mutations in human bronchial epithelium. *Nature* 578(7794), pp. 266-272. doi: 10.1038/s41586-020-1961-1

Yuan, F. et al. 2023. Transgenic ferret models define pulmonary ionocyte diversity and function. *Nature* 621(7980), pp. 857-867. doi: 10.1038/s41586-023-06549-9

Yum, M. K. et al. 2021. Tracing oncogene-driven remodelling of the intestinal stem cell niche. *Nature* 594(7863), pp. 442-447. doi: 10.1038/s41586-021-03605-0

Zacharias, W. J. et al. 2018. Regeneration of the lung alveolus by an evolutionarily conserved epithelial progenitor. *Nature* 555(7695), pp. 251-255. doi: 10.1038/nature25786

Zenonos, K. and Kyprianou, K. 2013. RAS signaling pathways, mutations and their role in colorectal cancer. *World J Gastrointest Oncol* 5(5), pp. 97-101. doi: 10.4251/wjgo.v5.i5.97

Zscheppang, K. et al. 2018. Human Pulmonary 3D Models For Translational Research. *Biotechnol J* 13(1), doi: 10.1002/biot.201700341

Appendix

Supplemental Movie 1. Timelapse of WT PCLS 1.

Live cell timelapse microscopy of 5 DPI WT PCLS immunostained with Anti-CD45 APC (cyan), and endogenous expression of red fluorescent protein (RFP; red). Time series was acquired over a 12 hour period, with Z-stacks acquired at 30 minute intervals. Movies are maximum intensity projections (MIP), scale bar, 50 μm.

Supplemental Movie 2. Visualising active CD45+ cell populations *ex vivo*.

In this WT PCLS, cells stained positive for anti-CD45 APC (cyan) appear moving around the lung epithelium, around RFP+ cells (red). Some evidence of regulated cell death of an RFP+ cell can be seen (yellow box) with a CD45+ cell actively moving around it before it's loss from the tissue. MIP, scale bar 50μm.

Supplemental Movie 3. CD45+ cell migration appears more subdued in KrasG12D PCLS.

In this KrasG12D PCLS, CD45+ cells (cyan) appear less frequently, and appear to be less migratory than their counterparts in WT PCLS. CD45+ cells appear more localised to clusters of KrasG12D-expressing, RFP+ cells (red). Some cells appear to be working around multiple RFP+ cells, extending protrusions and moving between cell bodies (yellow box). MIP, scale bar 50μm.

Supplemental Movie 4. KrasG12D-expressing cells are migratory.

In this KrasG12D PCLS, an RFP+ cell (red) can be seen extending a long protrusion across the timeseries (yellow box). Between 08:00 and 12:00 hours, this protrusion appears to find another RFP+ cell and becomes seamless, implying cell contact. CD45+ cells (cyan), are more abundant in this movie, but still appear less migratory and frantic. MIP, scale bar 50μm.